DEUTSCHES ELEKTRONEN-SYNCHROTRON DESY

DESY 81-012
March 1981

REVIEW OF ELECTRON-POSITRON PHYSICS AT PETRA

by

P. Duinker

National Institute for Nuclear and High Energy Physics,
Amsterdam, The Netherlands

NOTKESTRASSE 85 · 2 HAMBURG 52

To be sure that your preprints are promptly included in the
HIGH ENERGY PHYSICS INDEX ,
send them to the following address (if possible by air mail) :

DESY
Bibliothek
Notkestrasse 85
2 Hamburg 52
Germany

DESY 81-012
March 1981

e^+e^- PHYSICS AT PETRA [+)]

P. Duinker

National Institute for Nuclear and High Energy Physics,
Amsterdam, The Netherlands

CONTENTS

[+)] Review Lecture given at the International School of Subnuclear Physics, Erice, Italy, 1980

1. INTRODUCTION

These lectures review the experimental results up to the middle of 1980 obtained with PETRA, the worlds highest energy electron-positron colliding beam storage ring, at DESY in Hamburg, Germany.

Five experiments (CELLO, JADE, MARK-J, PLUTO and TASSO) were approved in 1976 and at the end of 1978 the first measurements were taken. The machine has been running with beam energies ranging from 6 to 18 GeV. The general features and the performance of PETRA are given in section 2. The experiments are discussed in section 3, starting with an overall view of the goals of the physics program in section 3.1, a description of the principal components of the detectors in section 3.2. Section 3 ends with a brief discussion of the Monte Carlo simulation programs in use for the various processes and some aspects of the radiative correction calculations.

Tests of Quantum Electrodynamics (QED) and the universality of the charged leptons are given in sections 4.1 and 4.2. The measurements of the asymmetry in the production of muon pairs and the first tests of models of the electro-weak interaction with one or more neutral bosons are presented in sections 4.2, 4.3 and 4.5.

PETRA offers for the first time the possibility to study the two photon exchange reaction in a systematic way with events samples comparable to the single photon annihilation channel, and the results obtained so far are described in section 5.

The general characteristics of hadron events such as the total hadronic cross section, jet analysis, searches for the top quark in hadronic events with and without a muon, the searches for new particles other than quarks, multiplicity distributions, particle

spectra and particle yields are presented in section 6.

The tests of Quantum Chromodynamics and the detailed analysis of an event topology by the JADE, MARK-J, PLUTO and TASSO Collaborations which led to the discovery of three jet events arising from the radiation of hard non-collinear gluons are reviewed in section 7.

Section 8 closes this review with a summary of the main results.

2. THE e^+e^- MACHINE PETRA

PETRA[1] (Positron Elektron Tandem Ringbeschleuniger Anlage) began operation in the fall of 1978 as the world's highest energy e^+e^- colliding beam machine. Since it's commissioning, PETRA beams have been available for physics runs 60% of the time, with the remaining time being devoted to machine development and maintenance periods[2].

The ring, with a circumference of 2.3 kilometers, has eight long straight sections of which two are reserved for the RF accelerating cavities. At present only four of the experimental areas are occupied. The remaining two experimental areas are reserved for second generation experiments.

The original injection scheme utilized both of the existing DESY facilities, DESY and DORIS. Electrons, inititally accelerated in LINAC I (see Fig. 1) are injected into DESY (Deutsches Elektronen Synchrotron) where they are further accelerated to 6 GeV and injected into PETRA. Positrons follow a somewhat more complicated path: after initital acceleration in LINAC II, positrons are injected via DESY into DORIS (Doppel-Ring-Speicher), where they are accumulated at an energy of 2.2 GeV. Stored positron bunches in DORIS are then tranferred back to DESY for further acceleration to 6 GeV, the minimum PETRA injection energy.

With the discovery of the upsilon (Υ) resonance in 1977 at FNAL[3] and the confirmation in e^+e^- interactions[4], the need to

operate DORIS as a storage ring independent of PETRA was realized. Consequently, in the fall of 1977 the decision was made to construct a Positron Intensity Accumulator (PIA)[5] to free DORIS for physics runs. In this new injection scheme, positrons are accumulated in PIA after acceleration in LINAC II. Twenty successive LINAC bunches are injected into PIA, compressed in phase space, and transferred to DESY for acceleration and injection into PETRA. PIA was assembled in record time and since the summer of 1979 has served as the injector for both DORIS and PETRA.

The average luminosity is $3 \times 10^{30}\ cm^{-2}\ sec^{-1}$ at beam energies of 17.5 GeV. The time-integrated luminosity per month obtained in the intersection point of the S-W Hall with the MARK-J detector since the beginning of 1979 is shown in Fig. 2. The months without any luminosity are the periods of the major machine shut downs which were used to install additional cavities and RF power to increase the energy of the circulating $e^{\pm}$ beams. It is expected that the luminosity will increase by a factor ~ 2 in the near future with the installation of mini-beta quadrupoles in the four intersection regions.

Recently the vertical polarization of the beams caused by the synchrotron radiation has been observed by the PETRA-polarimeter[6]. Figure 3 shows the arrangement in the N-E Hall which is used to measure the polarization of the electron beam by detecting a back-scattered circularly polarized photon beam. The detector measures the difference in counting rates between the scattered left and right handed photons as function of the converter position.

In Figure 4 the counting rate for 100% polarization is compared with the measured asymmetry values V where,

$$V = {}^1/_2 \left(\frac{N_R - N_L}{N_R + N_L} \right)_{Z=a} - {}^1/_2 \left(\frac{N_R - N_L}{N_R + N_L} \right)_{Z=-a}$$

N_R = measured counting rate for right handed photons
N_L = measured counting rate for left handed photons.
The two terms in brackets in the expression for V are measured at the positions for the converter of Z=a and Z=-a, respectively.

At 15.3 GeV the polarization is essentially zero or very small due to the influence of a nearby depolarizing machine resonance. At 15.2 GeV, however, the electron beam is polarized up to about (40 ± 10)%. Sofar the polarization has been detected under certain beam conditions when beam-beam interactions were not present. The aim of the future measuring program will be to investigate the polarization as a function of those machine parameters which are decisive for the effect.

To summarize this section one can say that in the first two years of operation of PETRA the energy range has been from 12 to 36.6 GeV and that it has run reliably with very little failures. The stability of the machine was the major reason why all the groups at PETRA have been able to perform their experiments satisfactorily.

FIGURE CAPTIONS

Figure 1 Layout of the DESY site at Hamburg, W. Germany with the PETRA e^+e^- Storage Ring showing the locations of the detectors. The N-E Hall with PLUTO (now replaced by CELLO), the S-E Hall with TASSO, the S-W Hall with MARK-J and the N-W Hall with the JADE detectors respectively.

Figure 2 The integrated luminosity per month obtained with the MARK-J detector since the beginning of 1979 as function of time.

Figure 3 Layout of the system to measure the polarization of the PETRA beams.

Figure 4 Difference in counting rates between right and left handed circularly polarized light (asymmetry) as a function of the position of the converter. The solid line shows the expected asymmetry for 100% polarization. The open circles are the measurements for a beam energy of 15.3 GeV and the black circles the ones at 15.2 GeV.

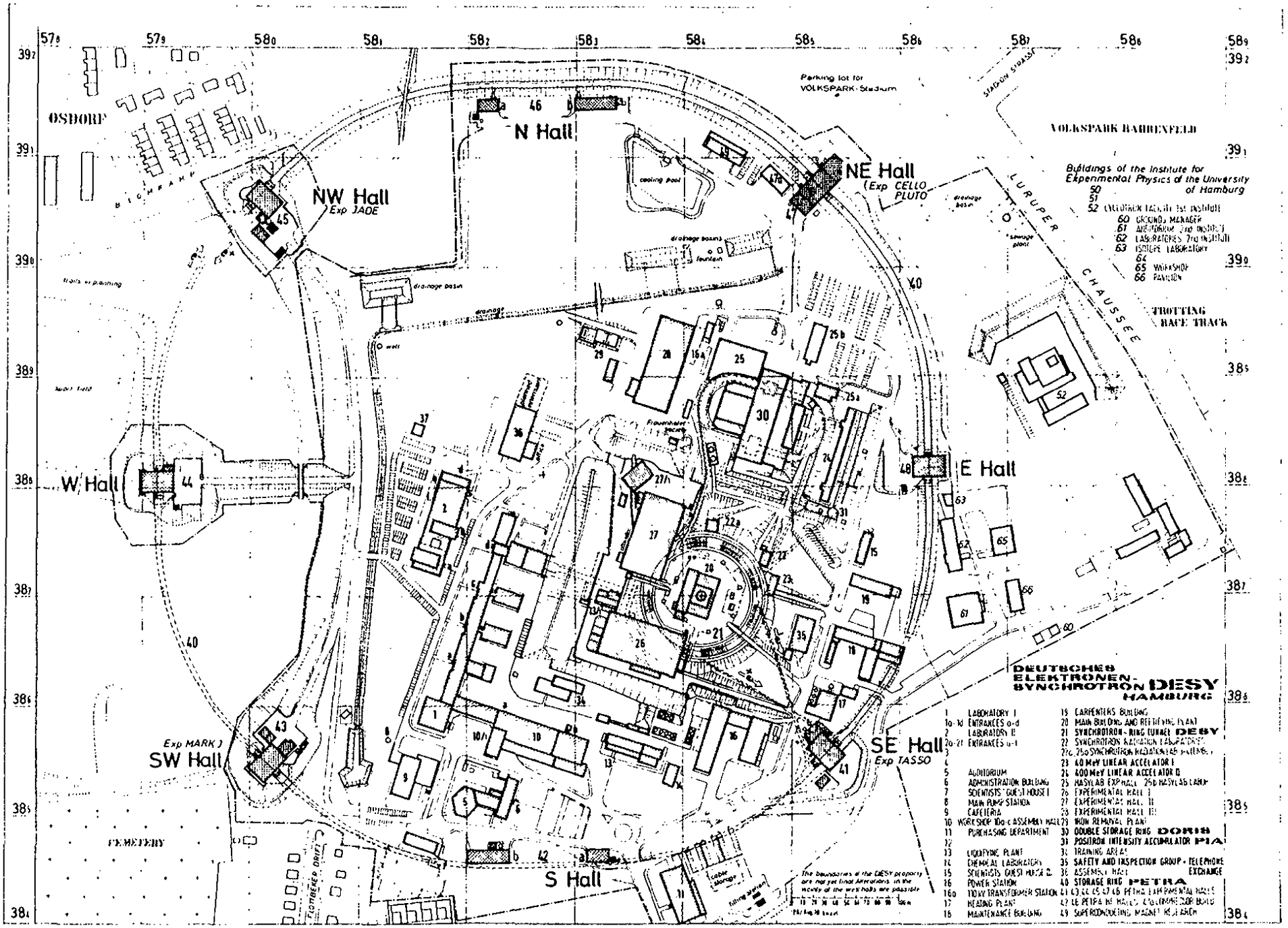
N Hall
NE Hall
(Exp CELLO PLUTO
NW Hall
Exp JAOE
E Hall
W Hall
SW Hall
Exp MARK J
SE Hall
Exp TASSO
S Hall
OSDORF
VOLKSPARK BAHRENFELD
Parking lot for VOLKSPARK-Stadium
Buildings of the Institute for Experimental Physics of the University of Hamburg
TROTTING RACE TRACK
CEMETERY
DEUTSCHES ELEKTRONEN-SYNCHROTRON DESY HAMBURG
1 LABORATORY I
2 LABORATORY II
10-10 ENTRANCES a-d
20-21 ENTRANCES a-i
5 AUDITORIUM
6 ADMINISTRATION BUILDING
7 SCIENTISTS' GUEST HOUSE I
8 MAIN PUMP STATION
9 CAFETERIA
10 WORKSHOP 10a-c ASSEMBLY HALL
11 PURCHASING DEPARTMENT
13 LIQUIFYING PLANT
14 CHEMICAL LABORATORY
15 SCIENTISTS' GUEST HOUSE II
16 POWER STATION
16a 10 kV TRANSFORMER STATION
17 HEATING PLANT
18 MAINTENANCE BUILDING
19 CARPENTERS BUILDING
20 MAIN BUILDING AND REFUELING PLANT
21 SYNCHROTRON - RING TUNNEL DESY
22 SYNCHROTRON RADIATION LABORATORY
23 40 MeV LINEAR ACCELERATOR I
24 400 MeV LINEAR ACCELERATOR II
25 HASYLAB EXPHALL 25b HASYLAB LAB
26 EXPERIMENTAL HALL I
27 EXPERIMENTAL HALL II
28 EXPERIMENTAL HALL III
29 IRON REMOVAL PLANT
30 DOUBLE STORAGE RING DORIS
31 POSITRON INTENSITY ACCUMULATOR PIA
32 TRAINING AREA
34 SAFETY AND INSPECTION GROUP - TELEPHONE EXCHANGE
35 ASSEMBLY HALL
40 STORAGE RING PETRA
49 SUPERCONDUCTING MAGNET RESEARCH
The boundaries of the DESY property are not yet final. Alterations in the vicinity of the work halls are possible.

Fig. 1

Fig. 2

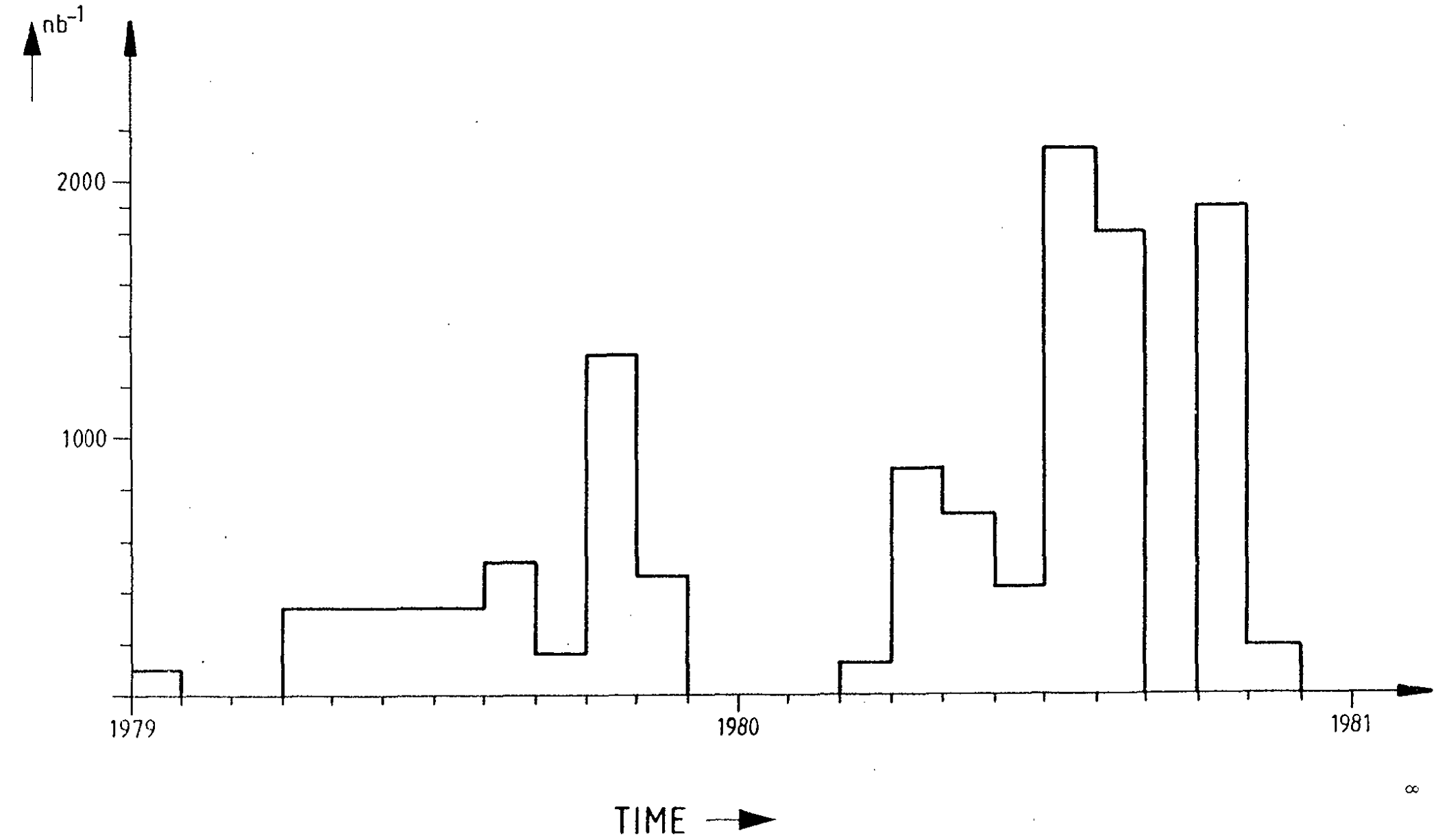

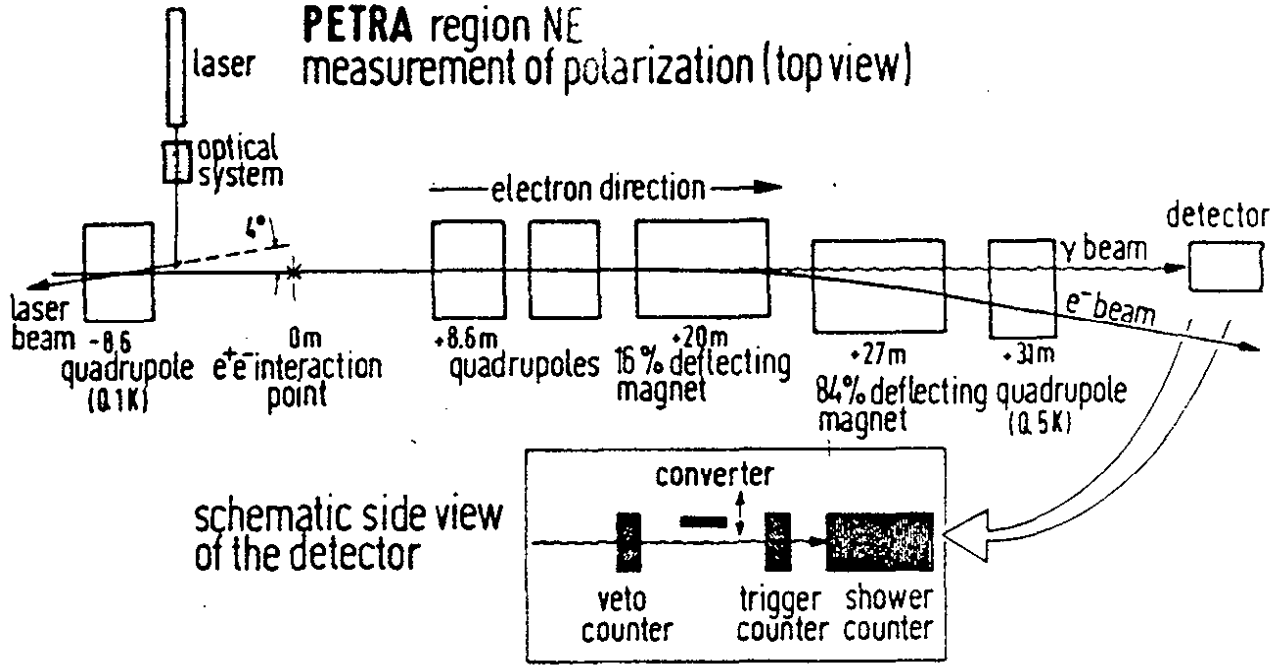
PETRA region NE
measurement of polarization (top view)
laser
optical system
electron direction
detector
γ beam
e⁻ beam
laser beam
-8.6 quadrupole (Q 1K)
0m e⁺e⁻ interaction point
+8.6m quadrupoles
+20m 16% deflecting magnet
+27m 84% deflecting magnet
+31m quadrupole (Q 5K)
schematic side view of the detector
converter
veto counter
trigger counter
shower counter

Fig. 3

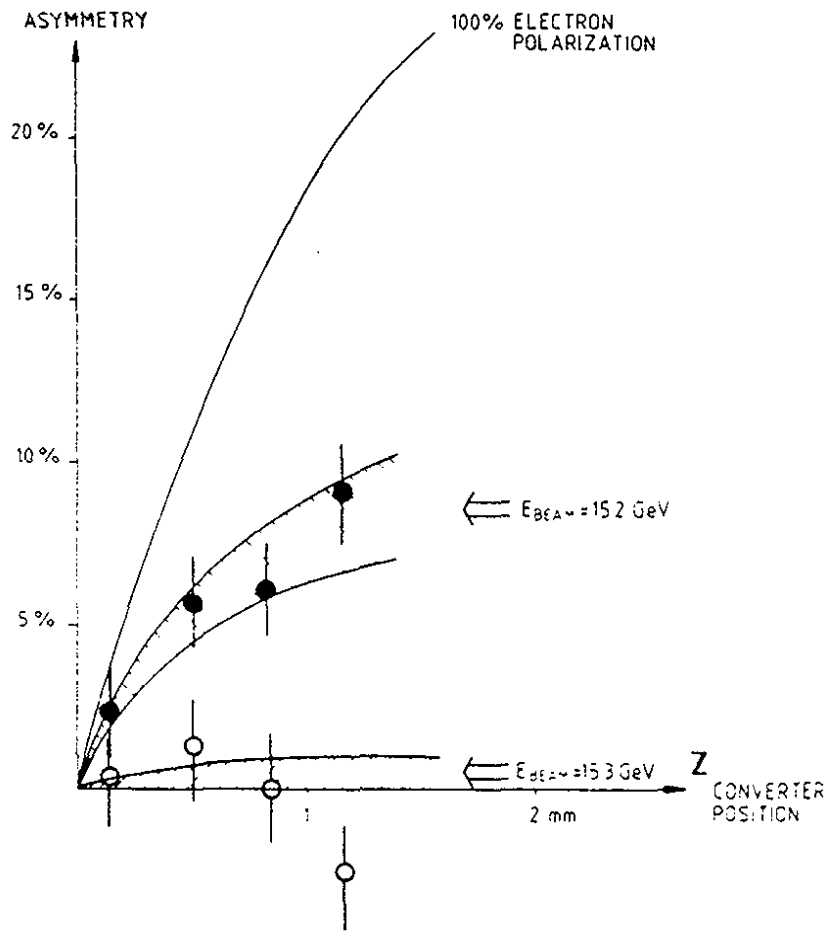
PETRA BEAM POLARIZATION
ASYMMETRY
100% ELECTRON POLARIZATION
20 %
15 %
10 %
5 %
E_BEAM = 15.2 GeV
E_BEAM = 15.3 GeV
Z
CONVERTER POSITION
1
2 mm

Fig. 4

3. THE PETRA EXPERIMENTS

3.1 Physics Objectives

Some of the prime physics goals of the experiments are:

(1) To study the various QED processes shown in Fig. 5a and b, and to study the universality of the known charged leptons in their electromagnetic interactions. At PETRA the maximum available c.m. energy at the moment is $\sqrt{s}$ = 36.6 GeV (q^2 up to 1300 GeV^2). Since first order QED processes exhibit a 1/s cross section dependence one can probe the validity of QED with an order of magnitude greater sensitivity than that previously available in earlier colliding beam experiments performed at storage rings at SLAC, DESY, ADONE and CEA in the range of $q^2 \leq 50\ GeV^2$.

(2) To measure the charge asymmetry expected from the interference of weak and electromagnetic interactions in the production of $\mu^+\mu^-$ pairs. As shown in Fig. 6, diagrams in which a virtual photon is exchanged or in which a Z^o vector boson is exchanged both contribute to $\mu^+\mu^-$ production. The interference can be understood in terms of a variety of models based on the weak interaction Lagrangian

$$L_{int} = i\,\bar{\mu}\,\gamma^\tau\,(g_V - g_A\gamma^5)\,\mu\,Z_\tau .$$

In the simple V-A model for example, one assumes $g_V = g_A = g$, where $g^2/M^2_Z = G/\sqrt{2}$, and where G is the Fermi coupling constant. In the now standard Glashow-Weinberg-Salam (GWS) model[7] the couplings are expressed in terms of the single parameter θ_w, the Weinberg angle:

$$g_V = {}^1/_4\ g\ \cos\theta_w\ (3\ \tan^2\theta_w - 1), \text{ and } g_A = {}^1/_4\ g\ \sec\theta_w .$$

In order to distinguish between theoretical hypotheses, we can use the forward-backward charge asymmetry

$$A \equiv \frac{\sigma^- - \sigma^+}{\sigma^- - \sigma^+}$$

where σ_- (σ_+) corresponds to the cross section for events which have the μ^- (μ^+) appearing in the forward hemisphere. At $\sqrt{s}$ = 30 GeV, with a total time-integrated luminosity of 10^{38} cm^{-2}, one obtains $\sim 10^4$ events in a 4π detector, leading to a 10 standard deviation asymmetry effect in the V-A model and a 5 standard deviation effect in the GWS model.

One notes that before the direct observation of the Z^o, the precise determination of the charge asymmetry arising from weak-electromagnetic interference is the most important verification of the idea of the unified electromagnetic and weak theory.

(3) To test models of the electro-weak interaction with the QED processes shown in Fig. 5a. At the highest PETRA energies the weak interactions effects become noticeable and limits on the vector and axial vector coupling constants can be obtained in a model independent way. Models of the weak interaction with a larger symmetry group than the standard GWS model can be tested and the two neutral boson masses which appear in those models can be restricted.

(4) To study the photon-photon scattering process as shown in Figure 7. The theoretical work on this subject started in the nineteen thirties[8] and it was revived in the sixties[9] and early seventies[10]. The first events were observed at ADONE[11] and later some measurements were obtained at DORIS[12] and SPEAR[13]. Since the advent of PETRA the two-photon exchange channels $\gamma\gamma \rightarrow$ hadrons can be studied in a systematic way with a number of events which is compatible with the number obtained from the single photon annihilation.

(5) To measure the total hadronic cross section (Fig. 8) and thereby the structure and energy dependence of the total cross section, in order to search for new thresholds in the hadronic final state continuum, and to search directly for more J-like particles which appear as sharp resonances.

(6) To search for new quark flavors by studying the shape

distributions of the hadronic events without and with inclusive muons (Fig. 9a).

(7) Using the distributions of the μe, μh and hh final states shown in Fig. 9b to search for the existence of new charged leptons heavier than the tau.

(8) To study the topology of hadronic events by measuring the direction and energy of charged and neutral particles. In particular, at PETRA energies, the fragmentation of hard gluons emitted in association with quark - antiquark pairs leads to the creation of additional gluons and quarks, resulting in the production of multi-jet events. Study of the properties of these jets enables one to make a direct comparison with the predictions of QCD[14]. The rate of 3-jet events relative to 2-jet events is a direct measure of the strong interaction coupling constant α_s.

3.2 The Detectors

The Collaborations who built the five large detectors for the experiments at PETRA are:

CELLO : DESY-Karlsruhe-München-ORSAY-Paris-SACLAY.

JADE : DESY-Hamburg-Heidelberg-Lancaster-Manchester-Rutherford-Tokyo.

MARK-J : Aachen-DESY-MIT-NIKHEF-Peking.

PLUTO : Aachen-DESY-Hamburg-Bergen-Maryland-Siegen-Wuppertal.

TASSO : Aachen-Bonn-DESY-Hamburg-London-Oxford-Rutherford-Weizmann-Wisconsin.

Table I summarizes the main characteristics of the four track detectors CELLO, JADE, PLUTO, and TASSO. The radius of the cylindrical chambers with the magnetic fields of the solenoids and the various detection devices for the energy measurements of photons and electrons are given. The setting errors obtained for the charged tracks are listed in the last column (for detailed descriptions of these detectors see reference (15).

The relation between the length L of a track in the central chamber, the B-field in KGauss, the number of measurements N along

a charged track and the momentum resolution is given by: (when Coulomb scattering can be neglected)

$$\frac{\Delta p}{p} = \frac{p}{0.03} \frac{\sigma}{L^2 B} \{ A_N, (N+5)^{-1} \}^{1/2}$$

where A_N, is a constant (A_N, = 750) and σ is the setting error.

The CELLO detector (Fig. 10) was moved into the beam in the fall of 1979 replacing PLUTO. A thin superconducting coil (0.5 radiation lengths thick) provides a ~ 13 KG solenoidal magnetic field. The inner detector measuring the trajectories of charged particles consists of separate concentric cylindrical packages containing a total of 12 layers of proportional and drift chambers. The solid angle covered by this part of the detector is 87% of 4π. The r and ϕ measurements of the cylindrical chambers is complemented by r-z measurements along the charged tracks using the information by cathode strips running at 90° and 30° relative to the beam direction. The coil is surrounded by a lead-liquid argon electromagnetic calorimeter consisting of 16 modules and supplemented by two symmetric end cap modules. Each of the 16 modules is a stack of 41 layers of ~ 20 radiation lengths thick. The information of the shower development is obtained from 2 cm strips running at 0°, 90° and 45° to the beam direction. The resolution for electrons at 18 GeV is found to be 3%. The inner detectors are surrounded by the iron return yoke followed by large drift chambers to identify and measure muon tracks.

The JADE detector is shown in Fig. 11. It has a conventional coil producing a field of 5 KGauss. The cylindrical drift chamber is pressurized to increase the track resolution and to measure the energy loss, dE/dX, of a charged track in the gas. 48 dE/dX samples along the track are measured and provide a means to identify particles in certain momentum regions. The coil is surrounded by about 2700 lead glass blocks (12.5 radiation lengths thick) to

measure the electromagnetic showers. Time of flight counters inside the coil and outside, a μ detector array of loaded concrete interleaved with drift chambers complete the set-up. Figure 12 shows the visible energy as measured by the JADE detector as function of the momentum imbalance. In Fig. 12b the visible energy is plotted. The two-photon annihilation events from the reaction $e^+e^- \to e^+e^-$ + hadrons cluster at low visible energy and are well separated from the hadron events caused by the e^+e^- annihilation.

The PLUTO detector (Fig. 13) consists of a superconducting coil which produces a magnetic field of 17 KGauss. A set of cylindrical proportional chambers detects the tracks of charged particles. Outside the iron flux return yoke proportional tube chambers are used to identify muons. An additional iron absorber outside the magnet yoke provides additional absorption length for the separation of the hadrons from the muons. The solid angle covered for the muon detection is 83% of 4π with a punch through and decay probability of less than three percent up to a muon momentum of 5 GeV.

To investigate the two-photon events, two forward spectrometers enable electron detection in the angular region between 23 and 250 mrad. Each spectrometer contains a small angle tagger (SAT) covering the angular range up to 68 mrad. Finely segmented arrays of lead glass blocks and two sets of proportional chambers complete this part of the set-up. The remaining part of the forward angular range is covered by the large angle tagger (LAT) which uses a lead scintillator sandwich preceeded by a layer of proportional tubes. The r.m.s. energy resolution in the SAT and LAT is $8.4\%/\sqrt{E}$ and $11\%/\sqrt{E}$, respectively. Similar systems of forward spectrometers have been installed by the CELLO, JADE and TASSO groups.

The TASSO detector is shown in Fig. 14. The central detector consists of a cylindrical drift chamber, time of flight system, magnet, liquid argon shower counters and the top and bottom muon

chambers. The conventional coil provides a solenoidal field of 5 KGauss. Inside this field a large cylindrical drift chamber with 15 sense wire planes, 9 radial and 6 with a stereo angle of $\pm 4^{\circ}$ is placed. The single wire resolution is 220 microns which yields a momentum resolution of $\Delta p/p = 2\%.p$, (p in GeV) for the muon tracks. A 4-gap proportional chamber aids the pattern recognition and the z-reconstruction.

Two spectrometer arms in the central region for detailed particle identification with 3 different Cerenkov counter systems followed by time of flight counters, shower counters, hadron absorber and muon chambers complete the detector. A hadron event as reconstructed by the TASSO pattern recognition program is displayed in Fig. 15. A total of 14 tracks are reconstructed for this particular event. In Fig. 16 the distribution of the sum of the momenta of the charged tracks for a sample of hadron events is plotted. Below 10 GeV the events are due to two photon events. The background from beam gas events in this region is small as is indicated by the hatched part of the histogram. The solid line is a Monte Carlo prediction for the momentum distribution of hadronic events produced by the single photon annihilation process and as can be seen the two photon and single photon events are readily separated.

The MARK-J detector is shown in Figure 17. It is designed to distinguish charged hadrons, electrons, muons, neutral hadrons and photons and to measure their directions and energies. It covers a solid angle of $\phi = 2\pi$ and $\theta = 12^{\circ}$ to 168° (θ is the polar and ϕ is the azimuthal angle). The detector, which consists of five magnetized iron toroids built around a non-magnetic inner detector complemented by end caps, was designed to be insensitive to the effects of synchrotron radiation. The detector layer structure is best understood be referring to Fig. 18.

The beam pipe is surrounded by a four layer inner track

detector composed of 992 drift tubes. The tubes, which are arranged perpendicular to the beam line, reconstruct the position of the event vertex along the beam line to an accuracy of two millimeters. The distribution of event vertices obtained using the drift tubes is shown in Fig. 19. The observed r.m.s. width of 1.27 cm is compatible with that expected from the known bunch length of the machine.

Particles then pass through 18 radiation lengths of shower counters used to identify and measure the energy of electrons, photons, charged and neutral hadrons. This inner calorimeter is divided into three layers of shower counters (labelled A, B, and C in Fig. 17). Since every shower counter is viewed by one phototube at each end, the longitudinal (z) position of particle trajectories can be determined by comparing the relative pulse heights from each end of the counter. Timing information provides another measure of the longitudinal position.

Twelve planes of drift chambers (labelled S and T) measure the angles of particles penetrating the inner electromagnetic calorimeter. The energy sampling elements of the calorimeter K, shown in Fig. 17, are 192 scintillation counters arranged in four layers. The main body of the calorimeter is composed of the magnetized iron plates which are also used to momentum-analyze muons . Hadrons penetrating the inner shower counter layers, and secondary particles produced by hadronic showers initiated in the inner layers, deposit most of their remaining energy in the calorimeter K.

Muons are identified by their ability to penetrate the iron of the hadron calorimeter. The low-momentum cut-off is about 1.3 GeV/c at normal incidence. The initial muon trajectory is measured in the S and T chambers and in the drift tubes.

The bend angle and position of muons exiting from the calorimeter are mesured in 10 planes of drift chambers, labelled R and P

in Fig. 17. The total thickness of the iron is 87 cm and it has a bending power of approximately 17 kG-meters. The typical bend angle for a 15 GeV muon is 30 mrad.

An additional 2 layers of drift chambers (Q chambers) are situated amidst the iron layers to measure the muon tracks in the bending plane. Adjacent to these chambers are the 32 muon trigger counters marked (D) used to trigger on single and multiple muon events and to reject cosmic rays.

For hadronic events the r.m.s. resolution in the total observed energy is ~ 20% as can be seen in Fig. 20a. From counter tracks the total missing energies in the directions parallel and perpendicular to the beam, which are used in the event selection, may be computed. The observed distributions of these quantities are shown in Figures 20b and 20c for high energy hadronic events.

3.3 Monte Carlo Simulation

A large part of the analysis effort of the experimental groups is devoted to the development and use of Monte Carlo programs. This simulation of events proceeds in three steps.

1. Event Generation
2. Detector Simulation
3. Event Coding

The event generators produce simulated events for a wide variety of e^+e^- reactions. The momenta, masses, charges, and the spatial distribution of the final state particles are generated according to the physics hypothesis appropriate to each process.

Hadron production by e^+e^- annihilation

$$e^+e^- \rightarrow \text{hadrons}, \qquad (1)$$

is treated in the framework of quantum chromodynamics (QCD), where the final state hadrons are viewed as composite particles made up

of quarks (and antiquarks) bound by a force mediated by gluons. Process (1) proceeds through the production of a quark-antiquark ($q\bar{q}$) pair, accompanied by the possible final state radiation of one or two gluons (denoted by g or gg) or in rare cases by the production of an additional $q\bar{q}$ pair. The quarks and gluons then fragment, meaning that they pull additional $q\bar{q}$ pairs from the sea with limited P_t with respect to the quark or gluon directions, forming jets of hadrons. Reaction (1) thus includes the following sub-processes:

$$e^+e^- \rightarrow q\bar{q} \rightarrow \text{hadrons} \quad (1a)$$
$$e^+e^- \rightarrow q\bar{q}g \rightarrow \text{hadrons} \quad (1b)$$
$$e^+e^- \rightarrow q\bar{q}gg \rightarrow \text{hadrons} \quad (1c)$$
$$e^+e^- \rightarrow q\bar{q}q\bar{q} \rightarrow \text{hadrons} \quad (1d)$$

As an example, Figure 21 shows a $q\bar{q}g$ final state, accompanied by radiation of an initital state photon, which leads to multi-jets. For the search for the existence of new heavy quark flavors such as the top quark t, the reaction

$$e^+e^- \rightarrow t\bar{t} \rightarrow \text{hadrons} \quad (1e)$$

is simulated as a special case of process (1a - 1d).

Pair production of the charged leptons and two-photon production, through the reactions

$$e^+e^- \rightarrow e^+e^- \quad (2)$$
$$e^+e^- \rightarrow \mu^+\mu^- \quad (3)$$
$$e^+e^- \rightarrow \tau^+\tau^- \rightarrow \text{hadrons and leptons} \quad (4)$$
$$e^+e^- \rightarrow \gamma\gamma \quad (5)$$

is also simulated. The analysis of computer generated final states for reactions (2) - (5) is a major part of the QED tests discussed in Section 4.1. . Other processes simulated include the "two-photon processes"

$$e^+e^- \rightarrow e^+e^-e^+e^- \quad (6)$$
$$e^+e^- \rightarrow e^+e^-\mu^+\mu^- \quad (7)$$

and

$$e^+e^- \rightarrow e^+e^- + \text{hadrons} \qquad (8)$$

Event types (1a) - (1e) are generated in most cases using a slightly modified version of the computer program recently implemented by A. Ali, E. Pietarinen, G. Kramer, and J. Willrodt[16], which provides a detailed model of hadron production by e^+e^- annihilation in the framework of QCD. In general, $q\bar{q}$ pairs are produced in fractions proportional to the square of the quark charges for flavors up, down, strange, charm, and bottom (denoted u,d,s,c, and b respectively). The fragmentation procedure used to transform quarks into hadrons is similar to that used by Feynman and Field[17]. The fragmentation functions used are $zD(z) = (1 - z)^2$ for u,d, and s quarks and $zD(z)$ = constant for c and b quarks, where z represents the fraction of the quark momentum carried away by the hadron formed at each stage of the fragmentation process (see Ref. 17). Heavy quarks (c and b) are allowed to decay weakly according to the usual six quark model[18], and the light quarks produced in the decay sometimes fragment independently, forming additional jets. Since gluon fragmentation functions are unknown, gluons simply fragment to quark pairs which in turn fragment according to the normal procedure. The $q\bar{q}g$ events in which hard non-collinear gluons are radiated (see Fig. 21) are generated according to the perturbative QCD matrix elements which includes the effects of non-zero quark mass[19]. Events of this type are required to have a thrust (Section 6.3.1) less than 0.95 before fragmentation in order to avoid the singularity for soft or collinear gluon emission[16]. Checks are made to insure the results do not depend strongly on the value of this cut.

Events from the higher order QCD processes $q\bar{q}gg$ and $q\bar{q}q\bar{q}$ are treated in a similar way to those from $q\bar{q}g$. The principal difference is that instead of applying the thrust cut, the requirement of acoplanarity greater than 0.05 is imposed, where acoplanarity is

defined as

$$A = \min \Sigma \, |\vec{E}_i \cdot \vec{n}_3| \; / \; \Sigma \, |\vec{E}_i|$$

and $\vec{E}_i$ is the vector energy and $\vec{n}_3$ is chosen to minimize A. This implies that none of the four partons can be soft and that no two are collinear. It does, however, reject planar events which are not near a singularity in the matrix element. A $t\bar{t}$ generator[19], which proceeds in the same way as for other heavy quarks, is used to study the effects that will be useful in searching for the top quark. All of the first four event generators use a (QED) radiative correction generator[20].

Bhabha scattering, μ pair production, τ pair production and $\gamma\gamma$ events are currently generated according to lowest order distributions and radiative corrections are applied externally for the first three processes using the programs of Berends et al.[20], (see Section 4.). Two-photon event generation for $e^+e^- \to e^+e^-e^+e^-$ and $e^+e^- \to e^+e^-\mu^+\mu^-$ is done using the program of Vermaseren[21] which is exact to order α^4 in the cross section.

The output of the Monte Carlo generators is used by the detector simulation programs. This latter program proceeds for the MARK-J detector in the following way. Particles are tracked through the detector and interaction points with counter and chamber planes are computed. The amount of energy in each hit counter is determined from tables that give the dependence on penetration depth, angle, and particle energy. Energy resolution and longitudinal shower fluctuations are also simulated using tabulated information. The above-mentioned tables were generated from the test beam data taken with electrons and pions at energies from 0.5 to 10 GeV, from experimental calorimeter studies[22] and from shower Monte Carlo programs[23].

Hits in the drift chamber and drift tubes are digitized. The chamber performance is simulated in detail including background,

inefficiency, multiple hits, cross talk and δ-rays. The full chamber survey information is used as provided on an input file. The somewhat complicated drift distance versus drift time function is also reproduced.

Finally the counter ADC and TDC information is digitized. Pulse heights are corrected for attenuation in the scintillator and times are corrected for particle flight time, scintillation light transit time and time slewing due to varying pulse height. Multiple hits are also treated.

To summarize, the detector is simulated in detail so that Monte Carlo events can be treated in the same way as actual data. To complete this process, the information described above is then coded into a form that resembles the raw data format. These events are stored on tape or disk so they may be read by the various analysis programs. This is useful for many purposes such as calculation of acceptance for a process, computation of background, and determination of detector effects on measured quantities. In particular, the MARK-J group uses Monte Carlo simulation, and the appropriate event generator, to produce expected distributions in variables that can be compared to data. Similar methods have been used by the other groups, taking into account the various components of their detectors.

3.4 Radiative Corrections

The luminosity of PETRA in the intersections is monitored by measuring the rate of Bhabha events in the central detectors and the small angle luminosity monitors. We assume that a present energies and small q^2 the absolute rate of the Bhabha scattering process is well described by QED and it may thus be used as an absolute monitor. The large q^2 Bhabha scattering covered by the central detectors as described in Section (3.2) is also well described by QED and can be used as an independent monitor. Neverthe-

less, care must be exercised to take proper account of radiative corrections which may be as large as 20% for some final state configurations in for example the MARK-J detector.

The measured rate for Bhabha scattering (reaction (2)) receives contributions from all orders in the pertubation expansion of QED. Furthermore, given the finite energy and position resolution of the detector, some events in which a hard photon is radiated

$$e^+e^- \rightarrow e^+e^- \gamma \qquad (9)$$

are also detected and attributed to Bhabha scattering.

It is therefore necessary to evaluate the contribution to the total Bhabha scattering cross section to order α^3. Higher order corrections are difficult to compute and have not yet been calculated exactly. Fortunately, they are small since the result of the α^3 correction is already only a few percent.

The calculations described below were first carried out by Berends and Gastmans[20], and the most recent version of their computer program is used by several of the groups. The cross section for Bhabha scattering can be written as

$$d\sigma/d\Omega = d\sigma_o/d\Omega \ (1 + \delta\{\theta, \phi\})$$

where $d\sigma_o/d\Omega$ is the lowest order (α^2) cross section and δ represents the radiative correction to order α^3. Following the notation of Berends, we write

$$\delta = \delta_b + \delta_v$$

were δ_b is due to real bremsstrahlung and receives contributions from the eight diagrams in Figure 22 and δ_v is due to virtual bremsstrahlung which is the contribution of the interference between the lowest order diagrams and the diagrams in which one closed loop occurs (due to virtual photons, virtual electron-positron pairs, $\mu^+\mu^-$ or $\tau^+\tau^-$ pairs) shown in Figure 22.

Renormalization removes the ultraviolet divergence of δ_v, and one is left with an infrared divergence which is exactly cancelled by the infrared divergence occuring in δ_b; δ is then finite.

A further correction which could have been included in δ_v is the hadron contribution to vacuum polarization. It can be thought of as quark-antiquark loops occuring in the photon propagator and is similar to lepton loops. Those contributions have been calculated by Berends and Komen[20] using experimental knowledge of R, the ratio of the cross section for $e^+e^- \to$ hadrons to the cross section of the point-like process $e^+e^- \to \mu^+\mu^-$.

At 90° with respect to the beam axis the contribution from quark loops to δ is of the order of +4% at $\sqrt{s}$ = 17 GeV and slowly increases with energy. The procedure followed by the MARK-J group is described in some detail in the next paragraphs. The other PETRA groups use similar calculations in determining the radiative corrections.

i) Small Angle Radiative Corrections

The radiative corrections for the small angle Bhabha scattering require careful treatment since the differential cross section is strongly peaked in this region. Ripken[24] has overcome the technical difficulties of numerical computation in the small angle region by using Gaussian integration techniques, and he has applied his program to the case of the MARK-J using a matrix element provided by Berends. At angles smaller than 5° with respect to the beam axis, all electron muon and tau loop diagrams and the hadronic contribution to vacuum polarization are small and neglected.

In the small angle luminosity monitoring stations of the MARK-J detector pairs comprising one small scintillator and one opposite large scintillator define the acceptance. The geometry of these counters has been incorporated into the radiative corrections in the following fashion. For the hard photon part of the cross section electron-positron-photon triplets are generated where one

of the leptons is within the acceptance of a small scintillator and the other lepton is required to pass within the boundaries of the large scintillator diametrically opposite. The soft photon part is incorporated analytically. These corrections are very sensitive to the relative position of the small scintillator with respect to the larger one. The residual uncertainty in the positions of the scintillators contributes a relative systematic error in the calculation of δ of about 30%. Since the value of δ is -8%, the radiative corrections contribute an error of 2.5% to the total luminosity measured in the small angle monitor.

ii) Large Angle Radiative Corrections

For large angle Bhabha scattering the phase space for real bremsstrahlung can be experimentally characterized by two simple boundaries:

E_{th} : an energy threshold for the outgoing electron and positron,

ξ : a limit on the angle in space between the electron direction and the direction at 180° to the positron direction (acollinearity cut).

Figure 23 shows δ plotted as a function of θ over the A counter acceptance at $\sqrt{s}$ = 27.4 GeV for various combinations of the cuts.

With the knowledge of δ one may integrate the differential cross section over the detector acceptance to find the Bhabha rate expected in the central detector.

One finds that the luminosity measurement with the central detector agrees within ~ 3% with the measurement made with the small angle luminosity counters (see Fig. 24). As will be described in Section 4.4, precise knowledge of the overall normalization plays an important role in the g_V and g_A determinations because the weak interaction modifications of QED predictions are small.

An experimental check on the calculations of the radiative corrections is the distribution of the measured angle ξ compared with the QED prediction. In Fig. 25 the acollinearity angle ξ for the MARK-J data for the Bhabha events is shown. The agreement between the measurements and the recent calculations by F.A.Berends and R. Kleiss[24] is good. The JADE data for the same angular distribution is shown in the next figure (Fig. 26), and also here the agreement over a wide range of acollinearity angles (up to 120°) between the data and the QED predictions are very good.

TABLE I

Main Characteristics of the Track Detectors.

	radius in meter	length in meter	B-field in KGauss	Photon detection	$\sigma(r, \phi)$ in microns
P L U T O	0.70	1.0	17.0	shower counters	~ 1000
C E L L O	0.75	3.5	13.0	liquid argon	210
J A D E	1.00	3.6	5.0	lead glass	180
TASSO	1.35	4.5	5.0	liquid argon plus shower counters	220

FIGURE CAPTIONS

Fig. 5a) Electron, muon and tau pair production in lowest order.
b) Photon Photon production in lowest order.

Fig. 6 First order electromagnetic and weak processes contributing to the reaction $e^+e^- \to \mu^+\mu^-$.

Fig. 7 The two-photon mechanism in an e^+e^- interaction.

Fig. 8 The reaction $e^+e^- \to$ hadrons in lowest order.

Fig. 9a) Diagram for production and decay of heavy quarks in e^+e^- annihilation.
b) Diagram for production and decay of heavy leptons in e^+e^- annihilation.

Fig. 10 The CELLO detector.

Fig. 11 The JADE detector.

Fig. 12a) The visible energy (charged tracks and neutral electromagnetic energy as measured by the JADE detector plotted as function of the momentum balance.
b) The distribution of the visible energy as measured by the same detector. The solid line represents the prediction for photon-photon events of the process $e^+e^- \rightarrow e^+e^-$ hadrons. The hatched area are the events of the process $e^+e^- \rightarrow$ hadrons.

Fig. 13 Side view of the PLUTO detector.

Fig. 14 End and top view of the TASSO detector.

Fig. 15 A hadronic event at 35.8 GeV c.m. energy as seen by the central cylindrical chambers of the TASSO detector. The black points represent the wires which fired, the solid lines are the track reconstructions by the pattern recognition program. Also indicated are the time of flight counters which were hit.

Fig. 16 Distribution of the total visible momentum of charged tracks from hadron events as measured by the TASSO detector. Beam gas events are indicated by the hatched part of the histogram. The solid line is a Monte Carlo prediction for hadron production through one-photon annihilation in the $q\bar{q}$ model.

Fig. 17 The MARK-J detector in end view. Beam pipe (1), drift tubes (DT), shower counters (A,B,C), inner drift chambers (S,T), calorimeter counters (K), outer drift chambers (Q,P,R), and magnetized iron (2).

Fig. 18 The layer structure of the MARK-J detector as seen by a particle emerging from the interaction point at a right angle to the beam axis.

Fig. 19 Distribution of event vertices along the beam direction reconstructed using the drift tube tracks of the MARK-J detector.

Fig. 20 Energy measurement at $\sqrt{s}$ = 30 GeV. The solid lines are predictions of Monte Carlo computations.
a) Visible energy spectrum for hadronic events.
b) Energy imbalance $E_\perp$ in the direction transverse to the beam.
c) Energy imbalance $E_{//}$ in the beam direction.

Fig. 21 Gluon bremsstrahlung from the final state of e^+e^- annihilation into quark-antiquark pairs.

Fig. 22 Radiative diagrams for the process $e^+e^- \to e^+e^-$.

Fig. 23 Radiative corrections δ as a function of the scattering angle θ for different acceptance cuts for the central part of the MARK-J detector.

Fig. 24 Luminosity measured with the central MARK-J detector (L_C) and with the luminosity monitor (L_G) during energy scans.

Fig. 25 Acollinearity distribution for Bhabha scattering events observed in the central detector of the MARK-J. The data are compared to the predictions of QED as computed from the recent work of F.A. Berends and R. Kleiss[24].

Fig. 26 Acollinearity distribution for Bhabha scattering events observed in the JADE detector. The data are compared to the predictions of QED.

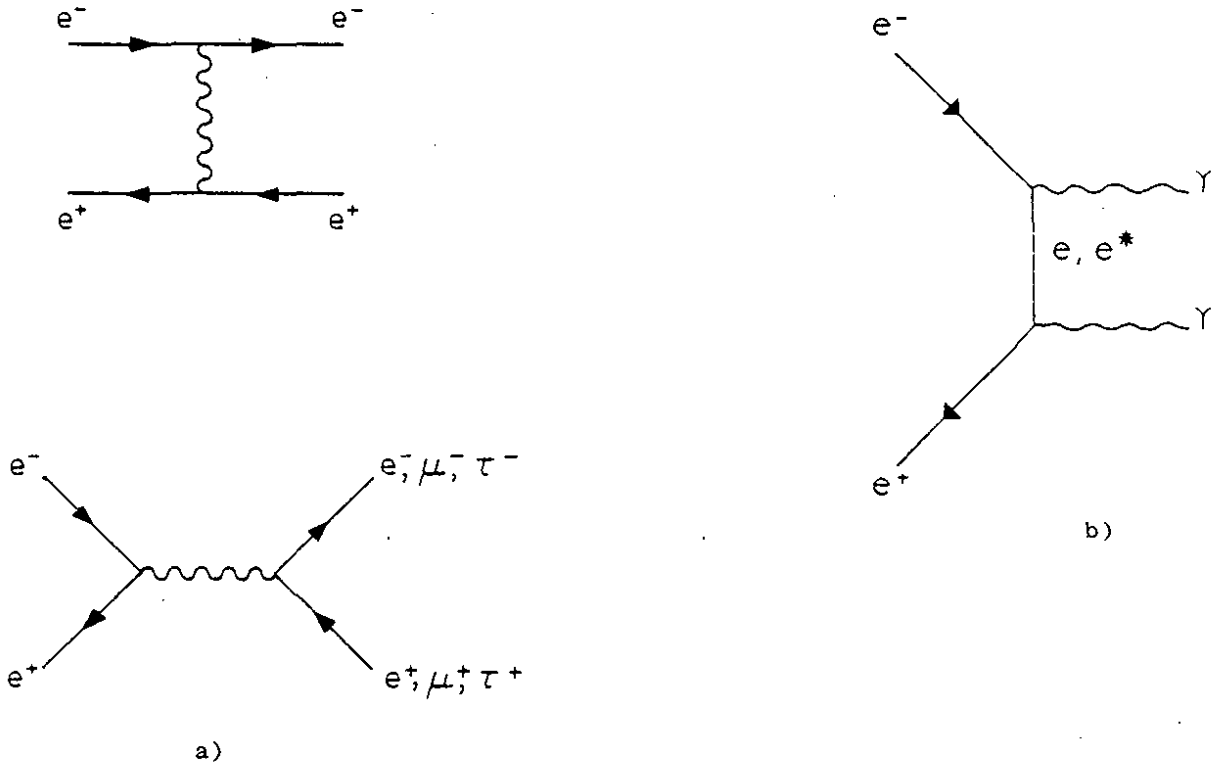

Fig. 5

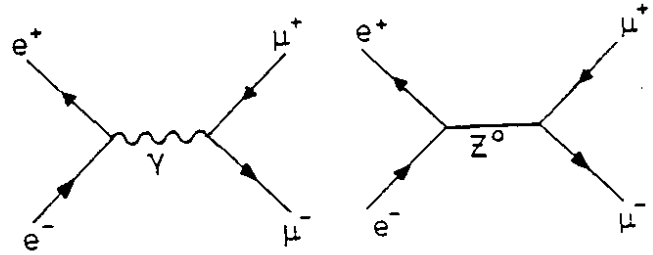

Fig. 6

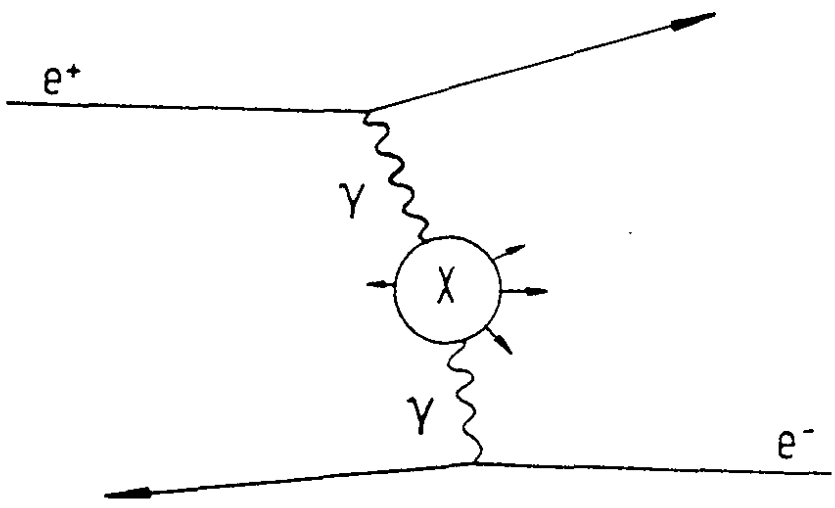

Fig. 7

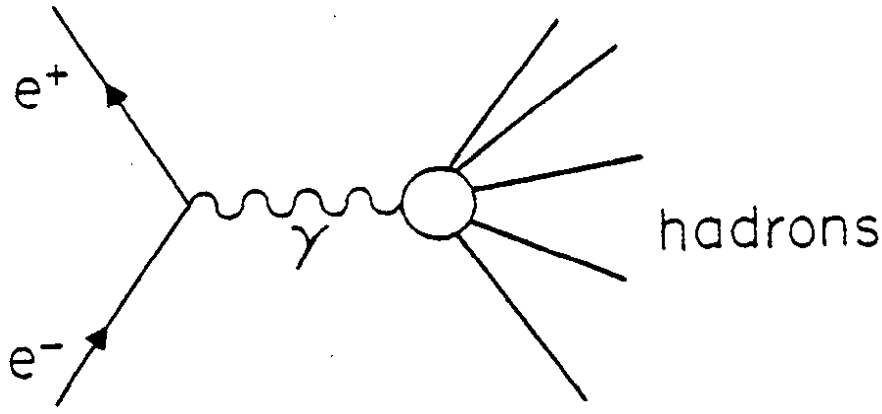

Fig. 8

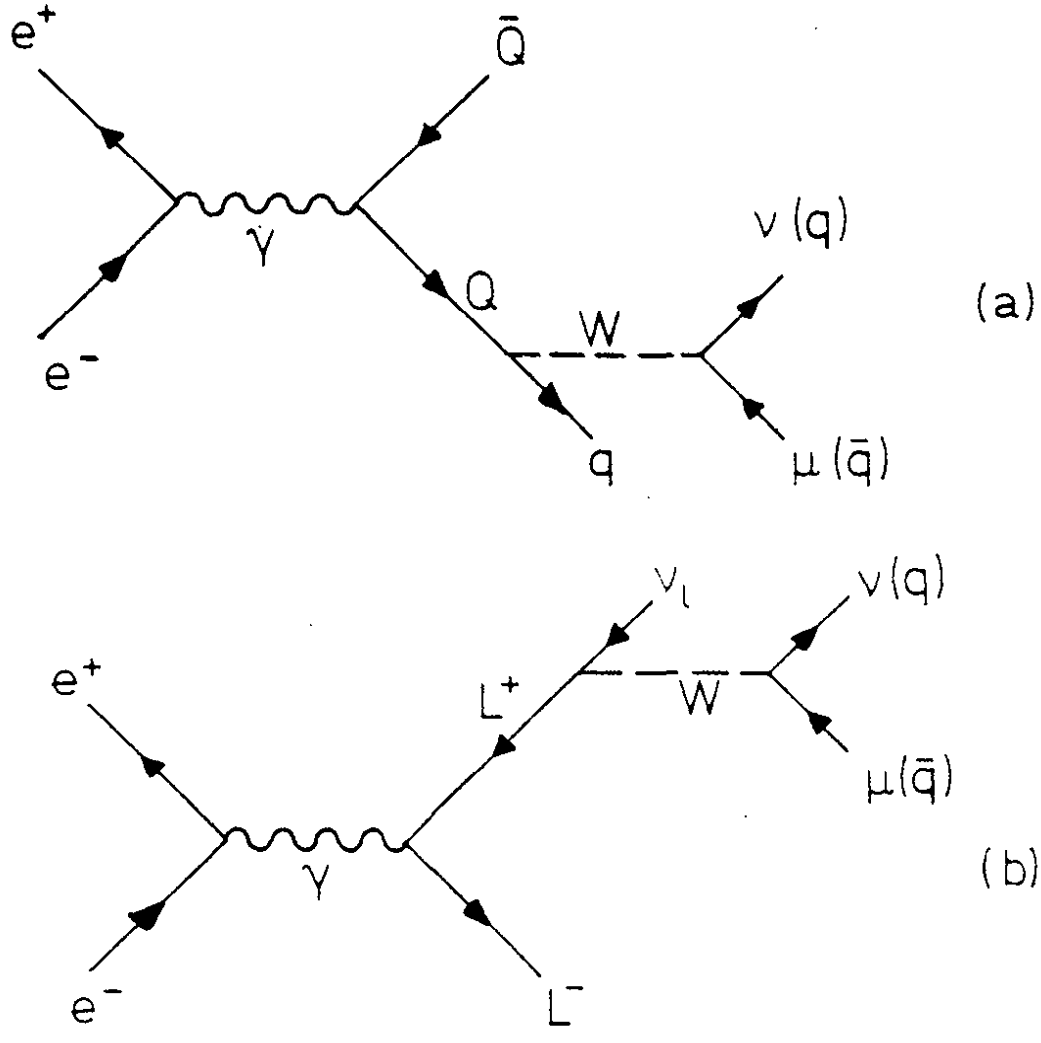

Fig. 9

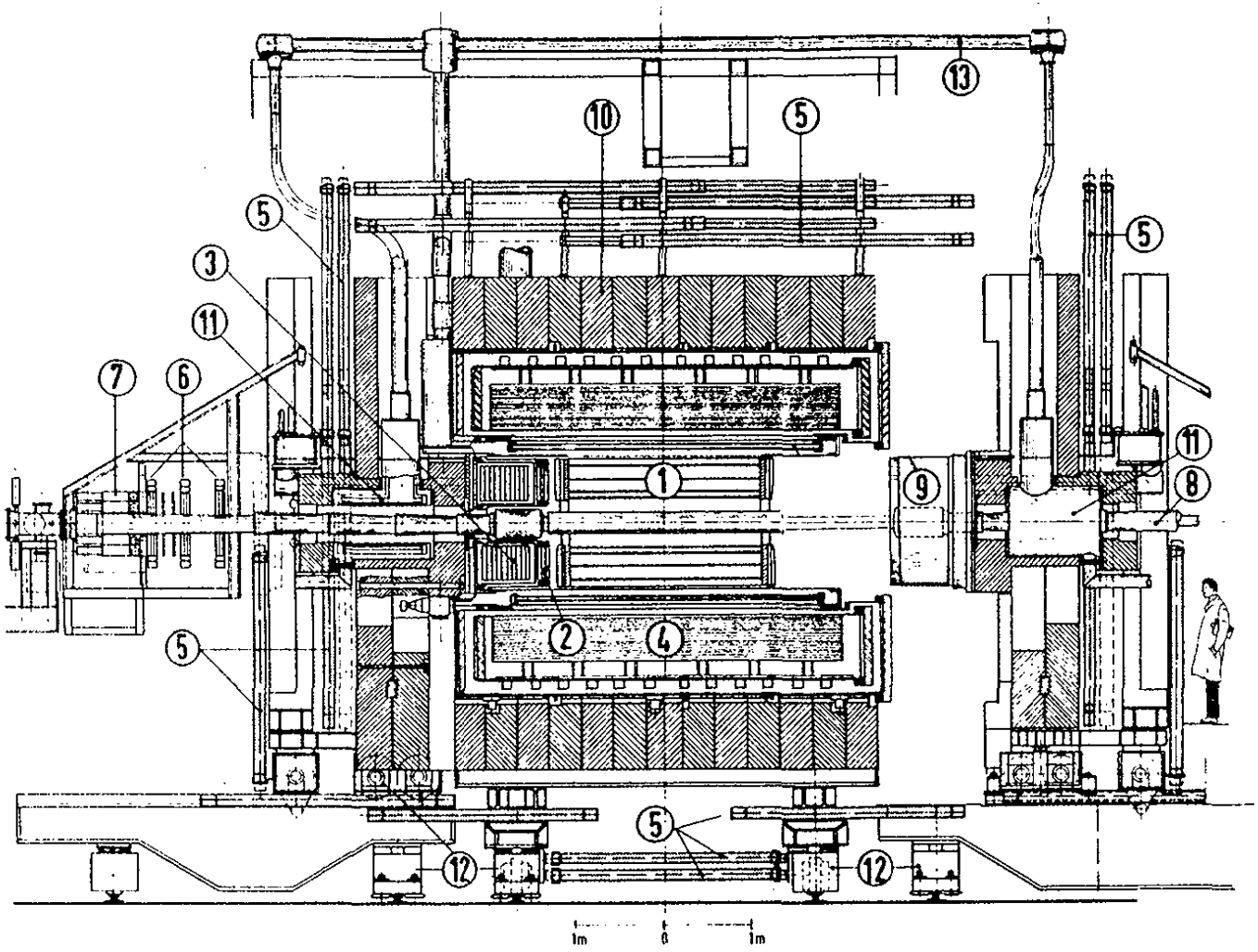

1 Zentrale Drift-u. Proportionalkammern
2 Endkappen-Proportionalkammern
3 Endkappen-Schauerzähler (Flüssig Argon)
4 Zylindrische Schauerzähler (Flüssig Argon)
5 Proportionalkammern für Myon-Nachweis
6 Driftkammern für Vorwärtsdetektor
7 Schauerzähler für Vorwärtsdetektor (Bleiglas)
8 Vakuum-Strahlrohr
9 Supraleitende Spule des Detektors
10 Eisenjoch
11 Kompensationsspulen
12 Fahrwerke
13 Versorgungsleitungen für flüssiges Helium

DETEKTOR CELLO
Gewicht: ~1400 t
Magnetfeld: 15 kΓ

Fig. 10

MAGNETDETEKTOR JADE
MAGNET DETECTOR

1 **Strahlrohrzähler** BEAM PIPE COUNTERS
2 **Endseitige Bleiglaszähler** END PLUG LEAD GLASS COUNTERS
3 **Drucktank** PRESSURE TANK
4 **Myon-Kammern** MUON CHAMBERS
5 **Jet-Kammern** JET CHAMBERS
6 **Flugzeit-Zähler** TIME OF FLIGHT COUNTERS
7 **Spule** COIL
8 **Zentrale Bleiglaszähler** CENTRAL LEAD GLASS COUNTERS
9 **Magnetjoch** MAGNET YOKE
10 **Myon-Filter** MUON FILTERS
11 **Beweglicher Endstopfen** REMOVABLE END PLUG
12 **Strahlrohr** BEAM PIPE
13 **Vorwärts-Detektor** TAGGING COUNTER
14 **Kompensationsmagnet** COMENSATING COIL
15 **Fahrwerk** MOVING DEVICES

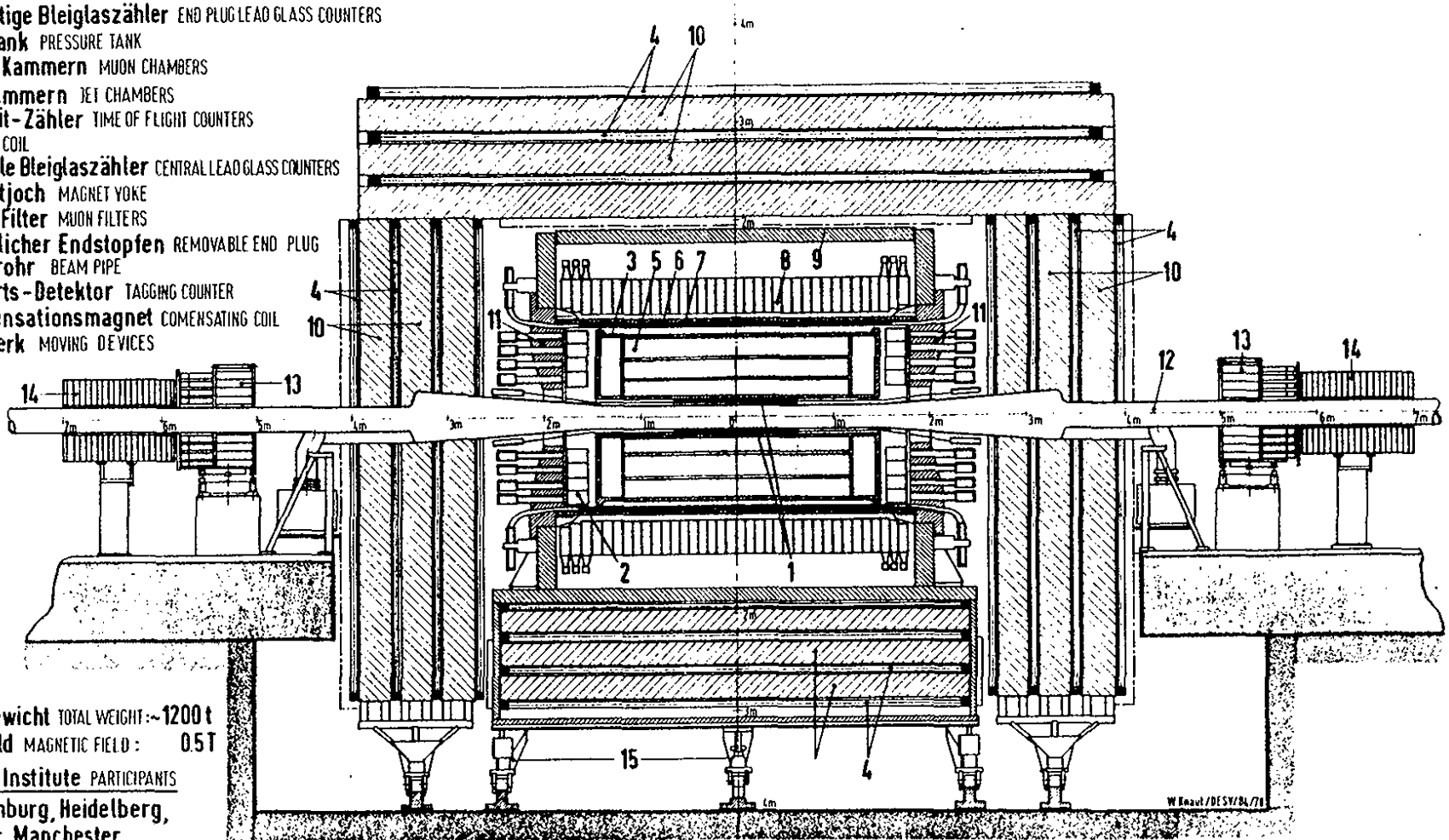

Gesamtgewicht TOTAL WEIGHT: ~1200 t
Magnetfeld MAGNETIC FIELD: 0.5 T

Beteiligte Institute PARTICIPANTS
DESY, Hamburg, Heidelberg,
Lancaster, Manchester,
Rutherford Lab., Tokio

Fig. 11

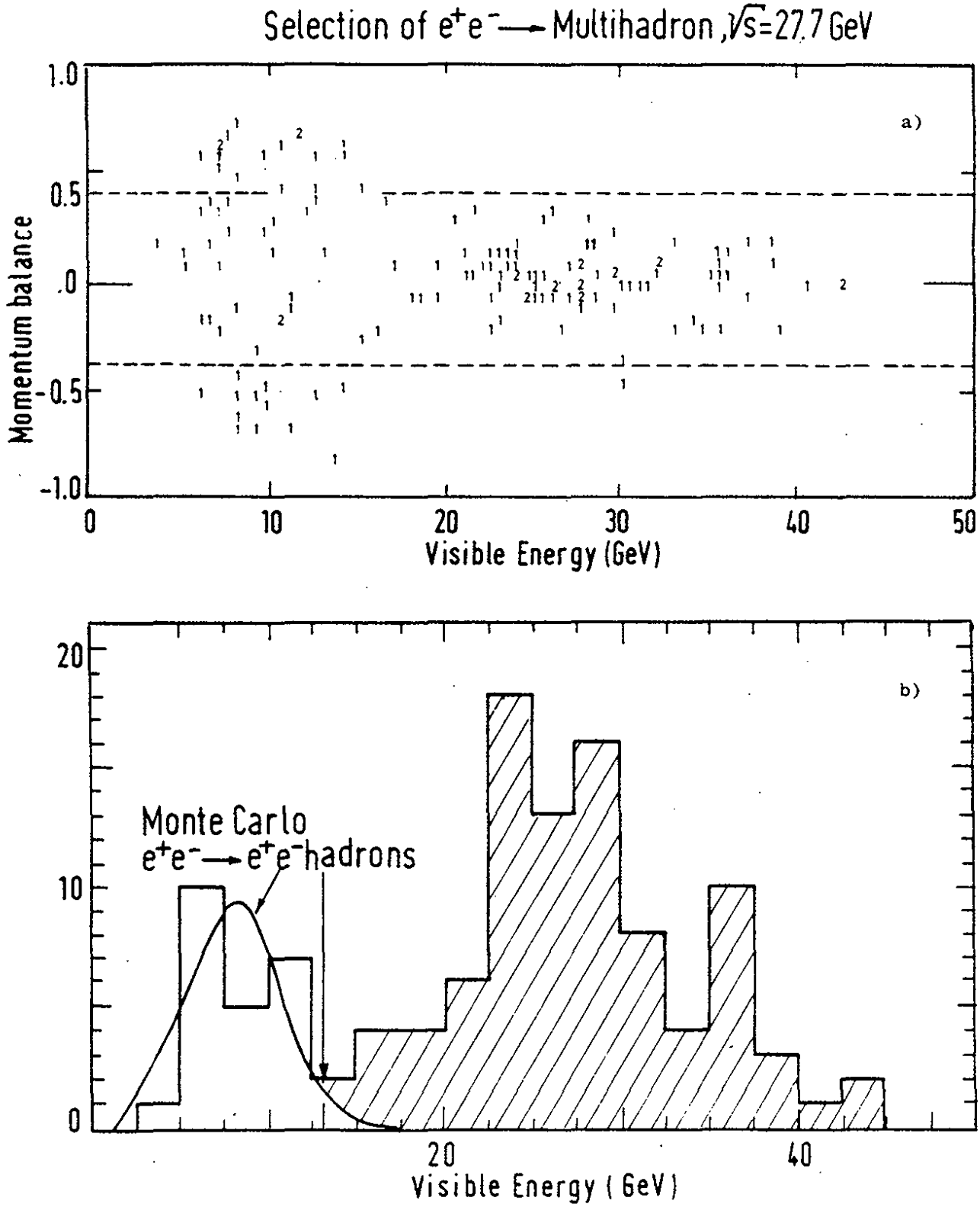
Selection of $e^+e^- \rightarrow$ Multihadron, $\sqrt{s}$=27.7 GeV
a)
Momentum balance
1.0
0.5
.0
-0.5
-1.0
0
10
20
30
40
50
Visible Energy (GeV)
b)
Monte Carlo
$e^+e^- \rightarrow e^+e^-$hadrons
20
10
0
20
40
Visible Energy (GeV)

Fig. 12

PLUTO bei PETRA

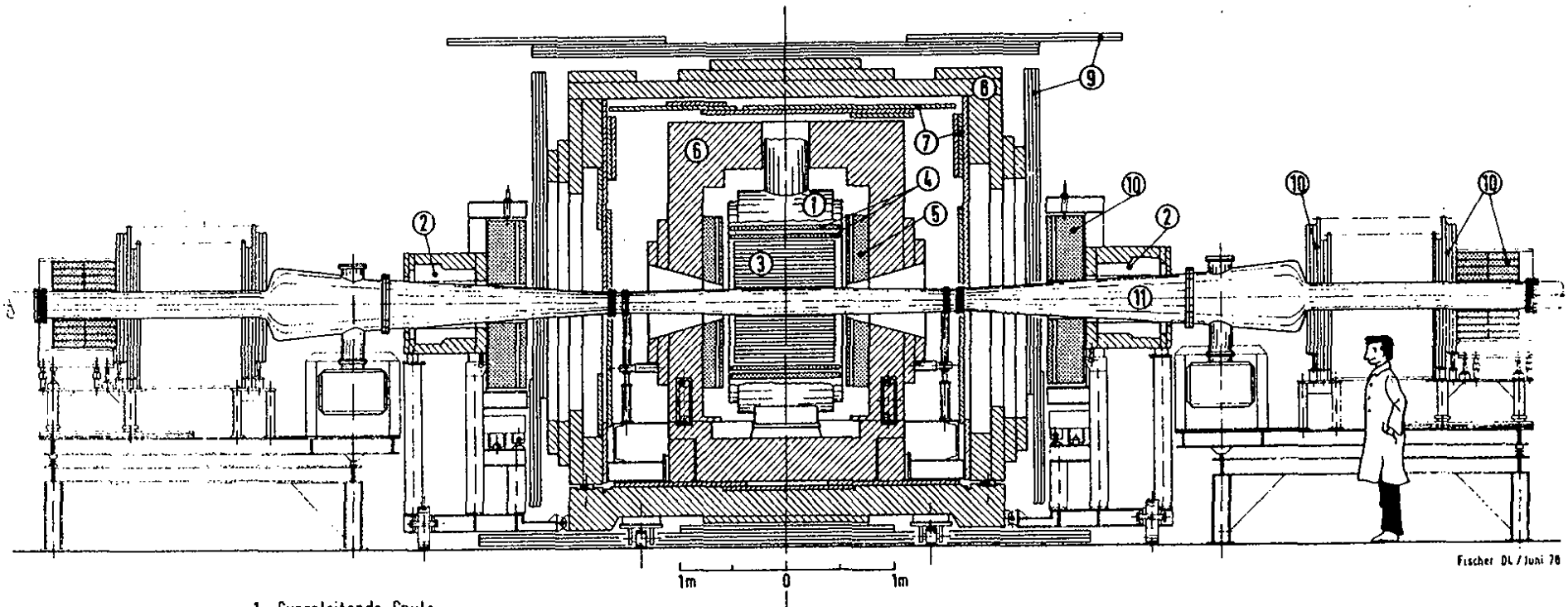

1 Supraleitende Spule
2 Kompensationsspulen
3 Zylindrische Proportionalkammern
4 Zylindrische Schauerzähler
5 Endkappen-Schauerzähler
6 Eisenjoch
7 Myon-Kammern
8 Hadron-Absorber
9 Driftkammern
10 Vorwärts-Spektrometer
11 Vakuumkammern

Beteiligte Institute:

RWTH Aachen
Univ. Bergen (N)
DESY, Hamburg
Univ. Hamburg
Univ. Maryland (USA)
GMS Siegen
GMS Wuppertal

Fig. 13

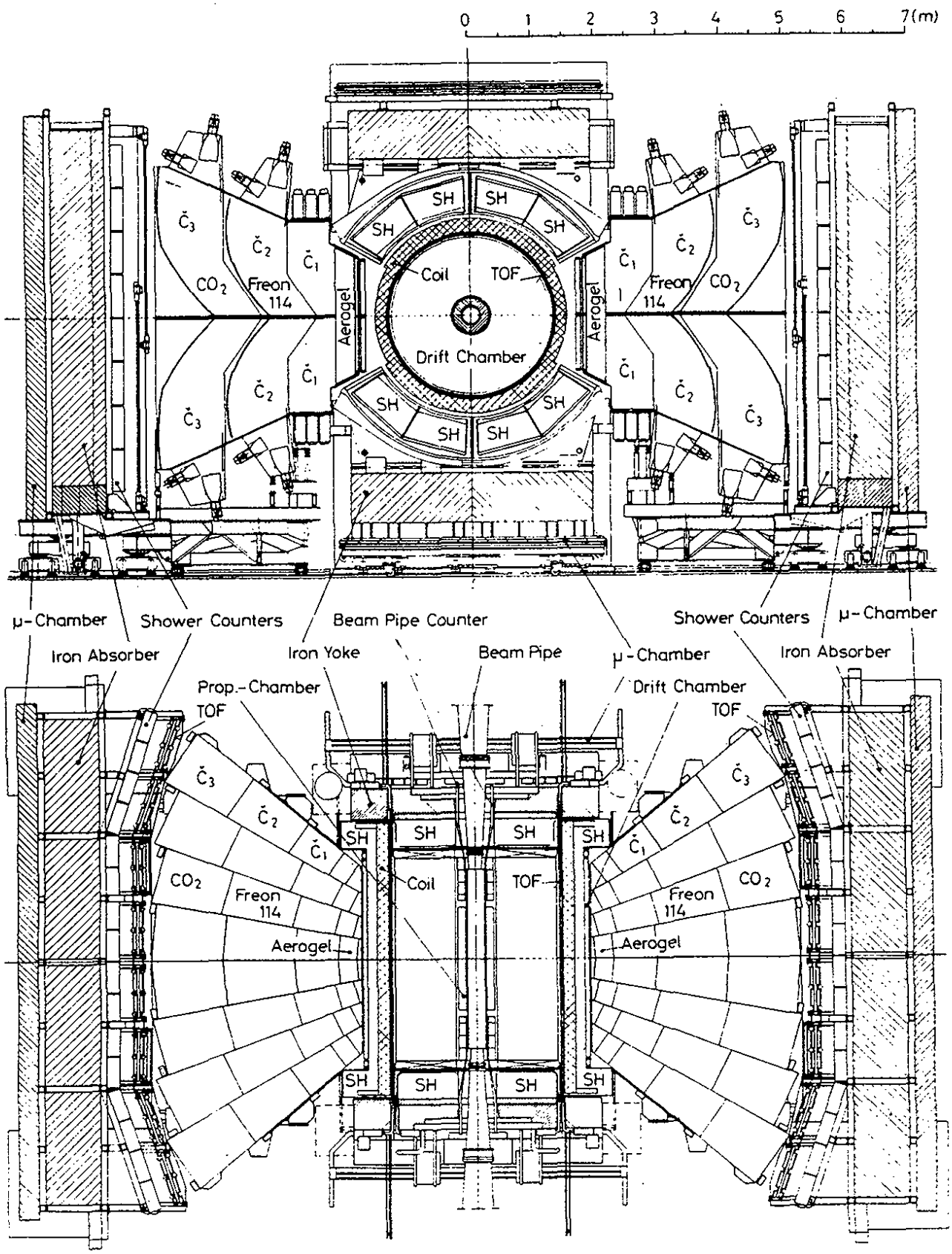
0 1 2 3 4 5 6 7(m)
SH
Coil
TOF
Drift Chamber
Aerogel
Freon 114
CO2
μ-Chamber
Shower Counters
Beam Pipe Counter
Iron Absorber
Iron Yoke
Beam Pipe
Prop.-Chamber
Drift Chamber
TASSO
20.8.80

Fig. 14

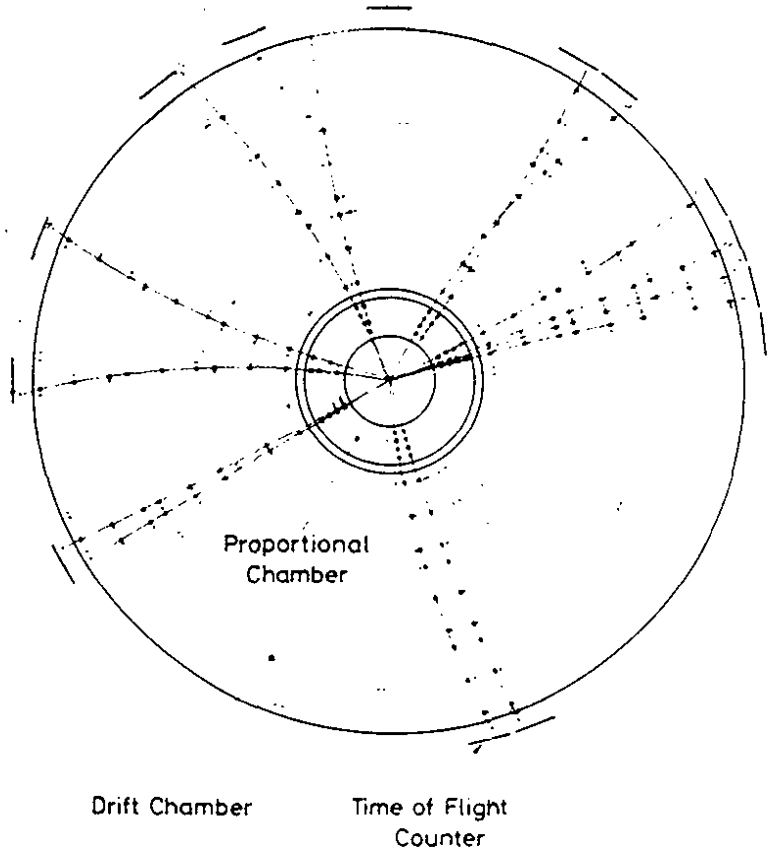
Proportional
Chamber
Drift Chamber
Time of Flight
Counter

Fig. 15

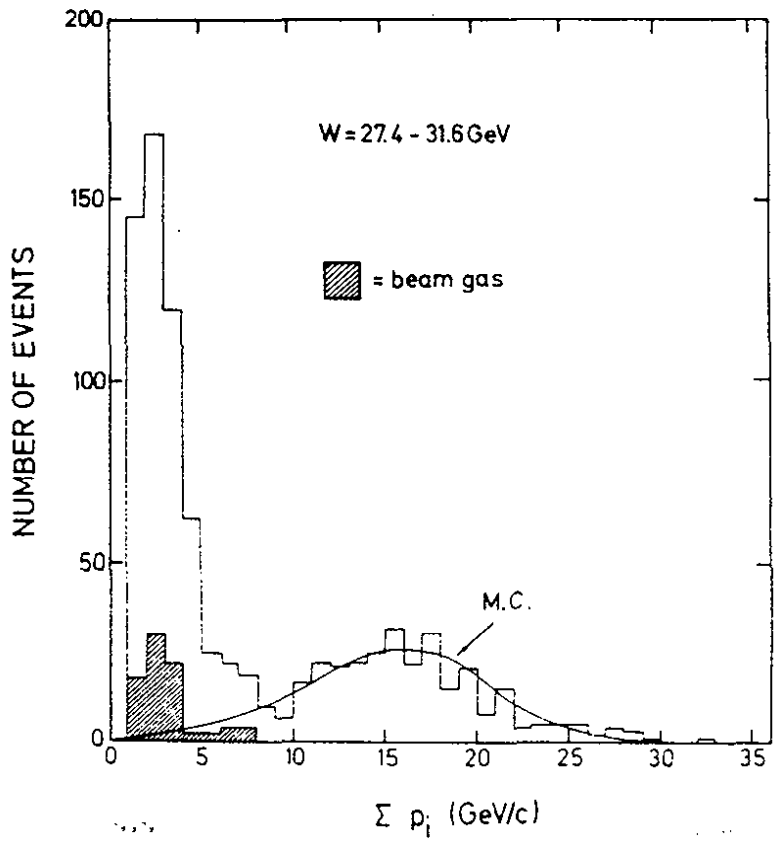
W = 27.4 - 31.6 GeV
= beam gas
M.C.
NUMBER OF EVENTS
Σ p_i (GeV/c)
0
50
100
150
200
0
5
10
15
20
25
30
35

Fig. 16

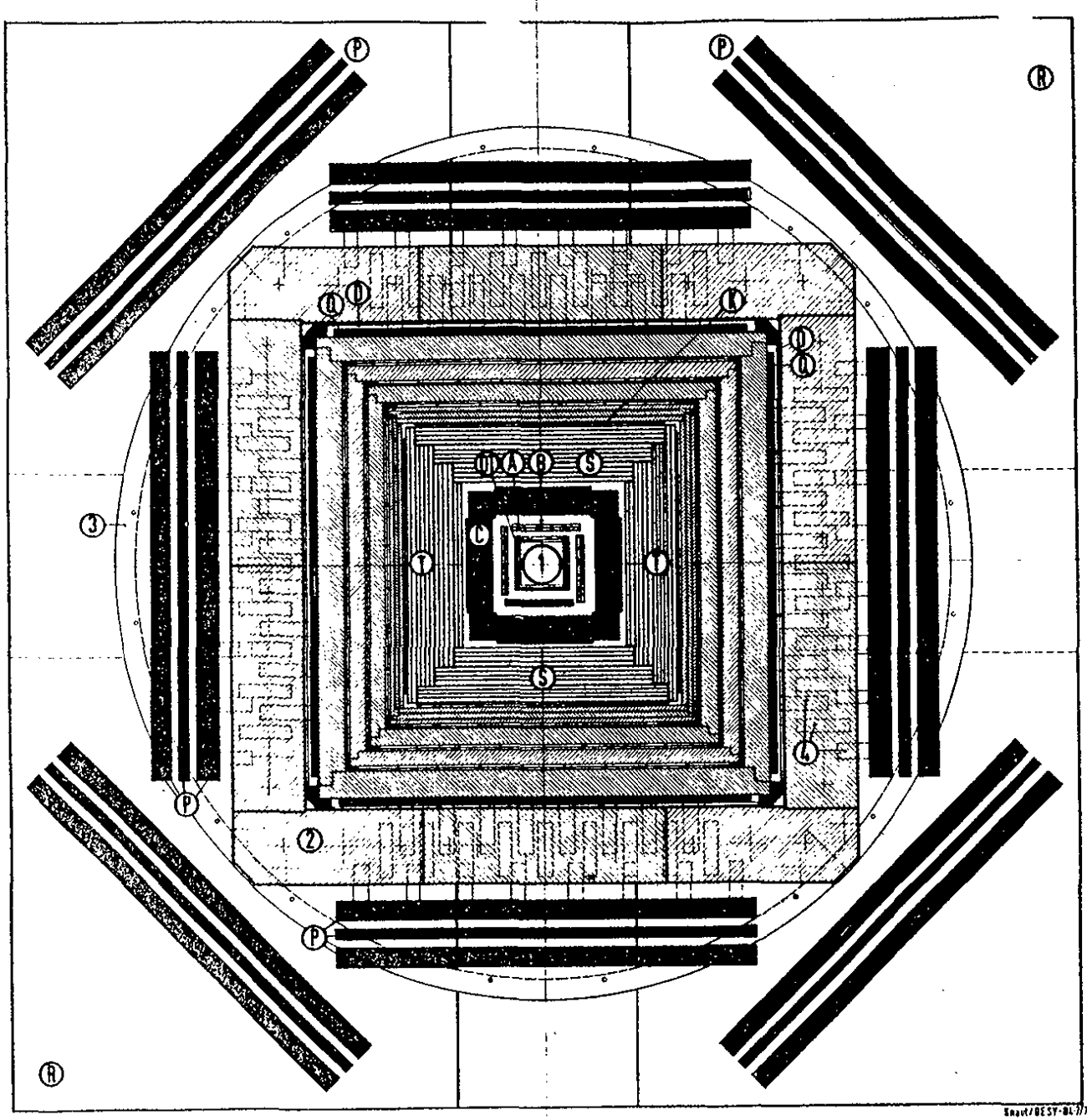

MARK J-DETECTOR

(Cross Section)

A B C	SHOWER COUNTERS
D	TRIGGER COUNTERS
K	DRIFT TUBES
Q	DRIFT CHAMBERS, MEDIAN
P R	DRIFT CHAMBERS, OUTER
S T	DRIFT CHAMBERS, INNER

1	BEAM PIPE
2	MAGNET IRON
3	Al - RING
4	MULTIPLIERS

WEIGHT (total) : ~ 400 t
MAGNETIC FIELD: 1.8 T

PARTICIPANTS:

RWTH - Aachen
DESY - Hamburg
MIT - Cambridge
NIKHEF - Amsterdam
HEPI - Peking

Fig. 17

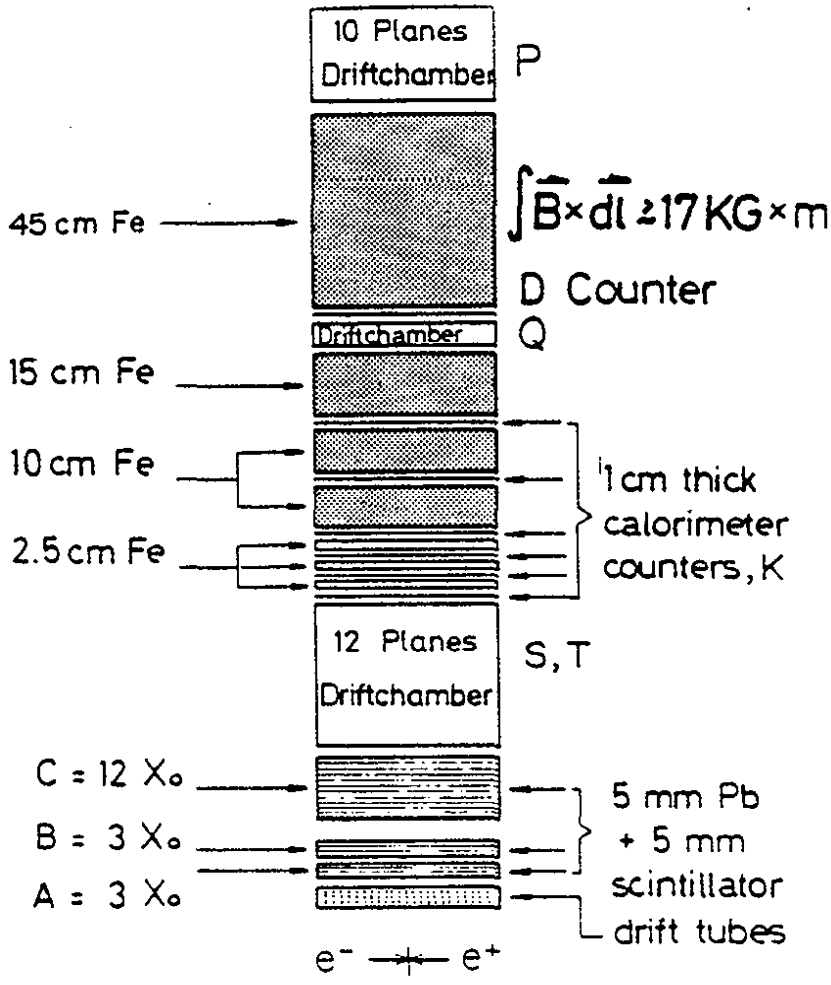
10 Planes
Driftchamber
P
45 cm Fe
$\int \vec{B} \times d\vec{l} \geq 17\,KG \times m$
D Counter
Driftchamber
Q
15 cm Fe
10 cm Fe
2.5 cm Fe
1 cm thick
calorimeter
counters, K
12 Planes
Driftchamber
S, T
C = 12 X₀
B = 3 X₀
A = 3 X₀
5 mm Pb
+ 5 mm
scintillator
drift tubes
e⁻
e⁺

Fig. 18

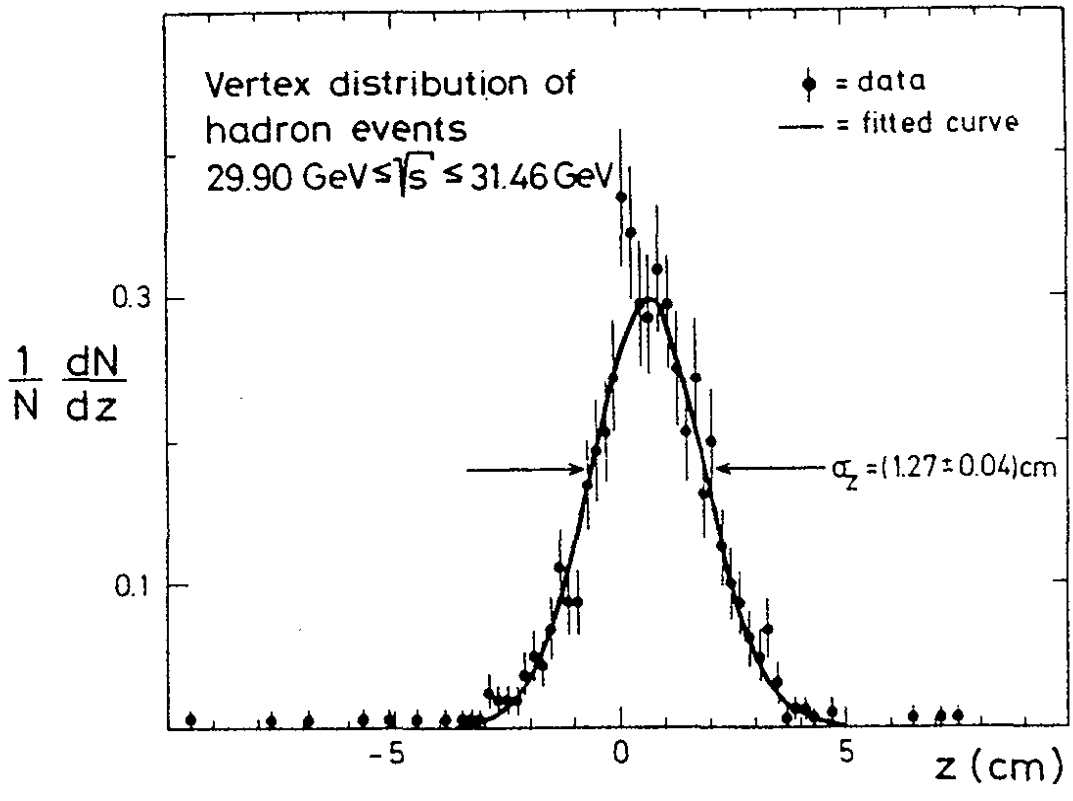
Vertex distribution of
hadron events
29.90 GeV ≤ √s ≤ 31.46 GeV
= data
= fitted curve
$\frac{1}{N}\frac{dN}{dz}$
0.3
0.1
$\sigma_z = (1.27 \pm 0.04)$ cm
-5
0
5
z (cm)

Fig. 19

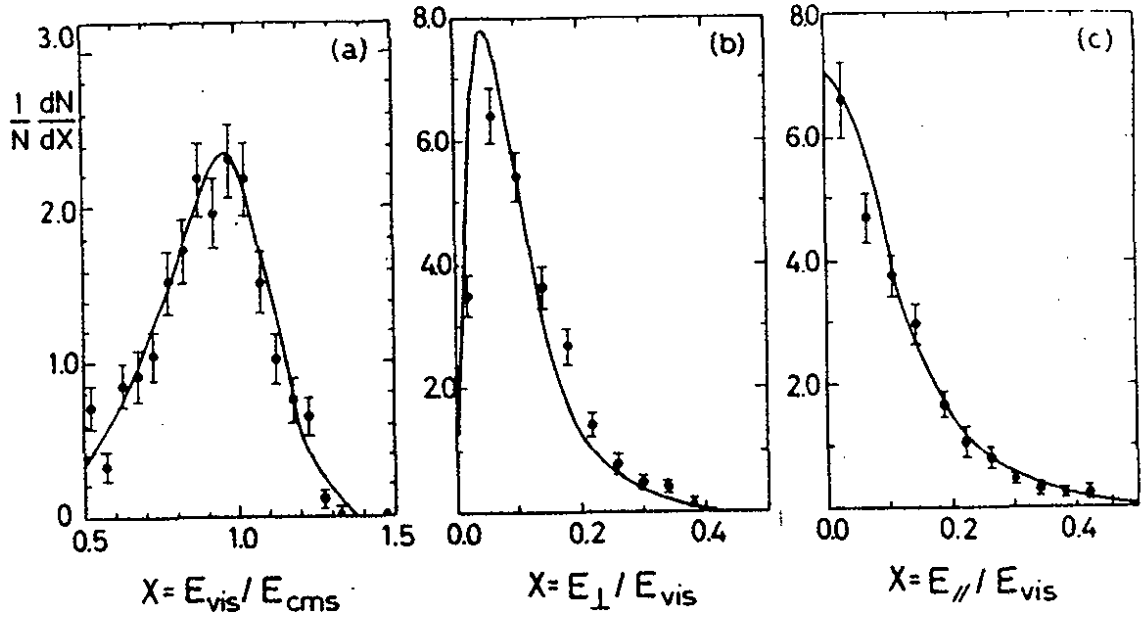

Fig. 20

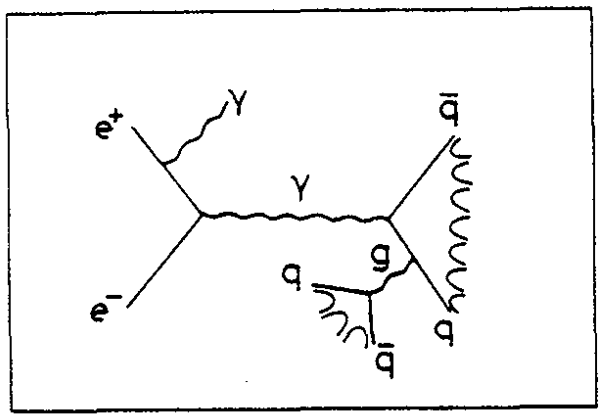

Fig. 21

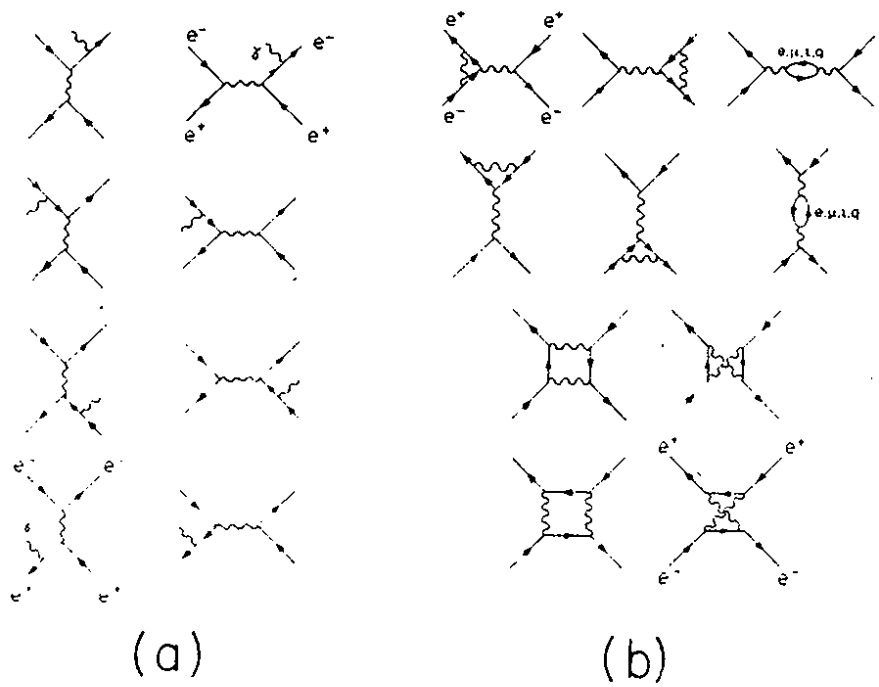

Fig. 22

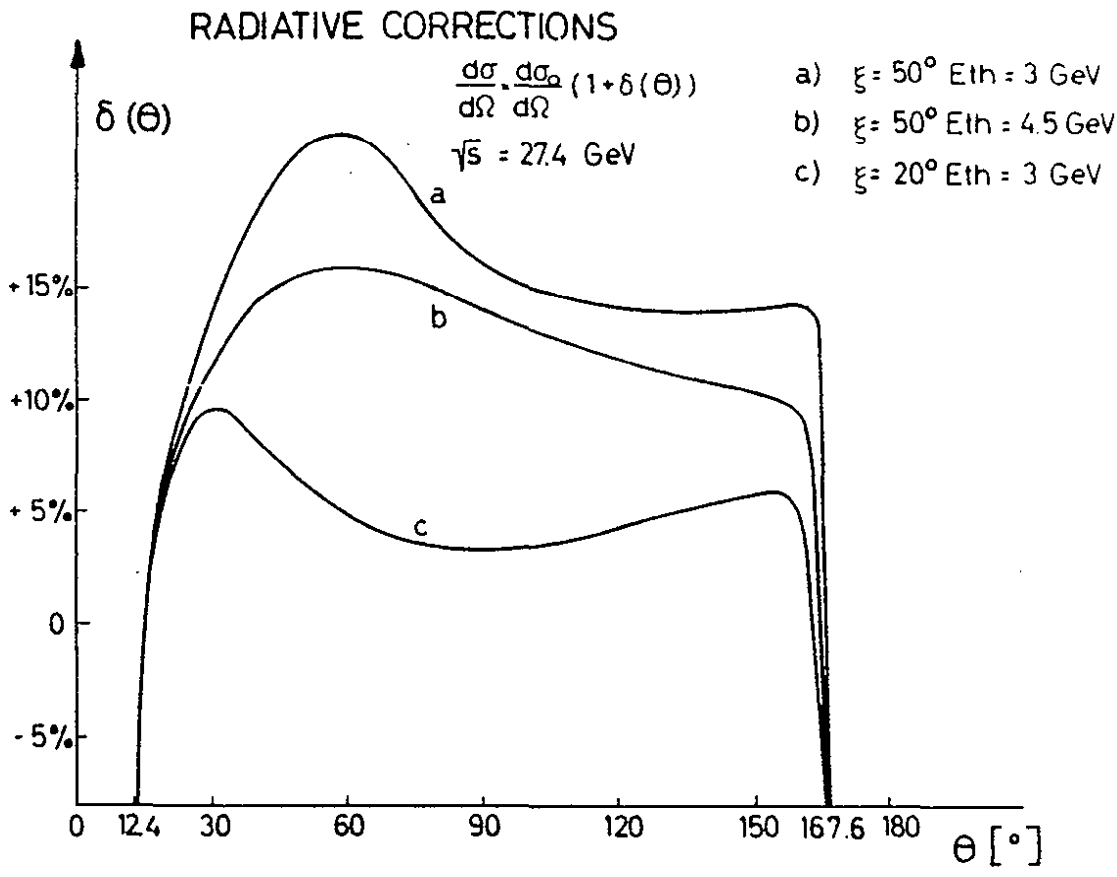

Fig. 23

Relative difference of integrated luminosities measured with central detector (C) and luminosity monitor (G) during energy scan.

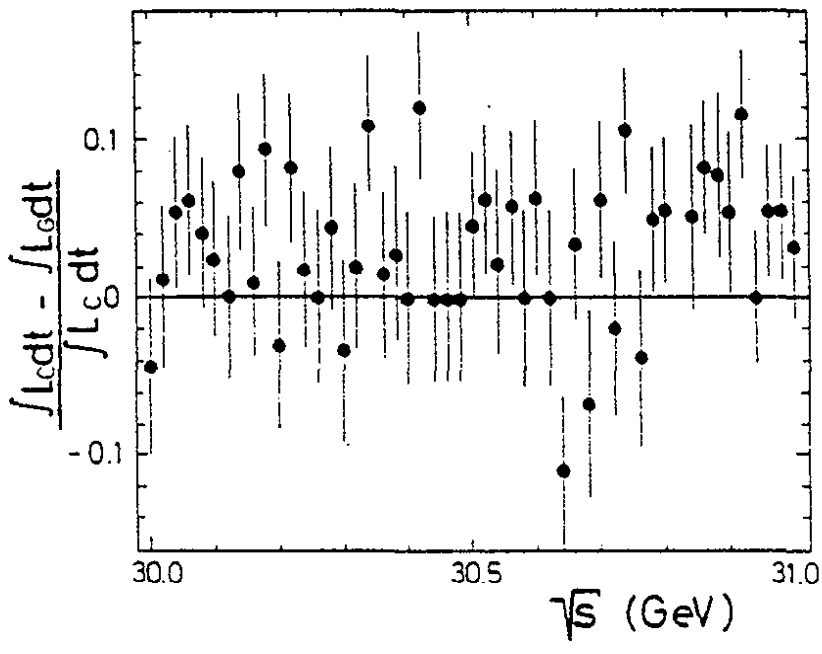

Fig. 24

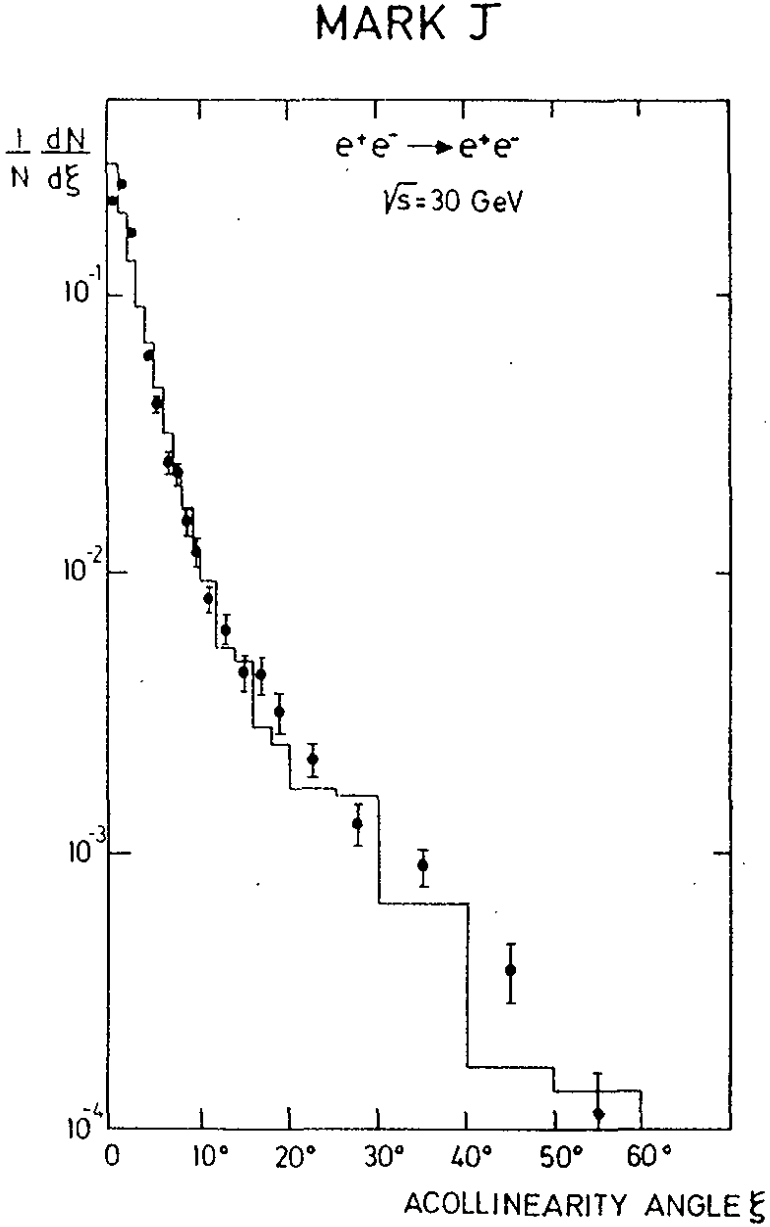
MARK J
$\frac{1}{N}\frac{dN}{d\xi}$
$e^+e^- \rightarrow e^+e^-$
$\sqrt{s}$=30 GeV
10^{-1}
10^{-2}
10^{-3}
10^{-4}
0
10°
20°
30°
40°
50°
60°
ACOLLINEARITY ANGLE ξ

Fig. 25

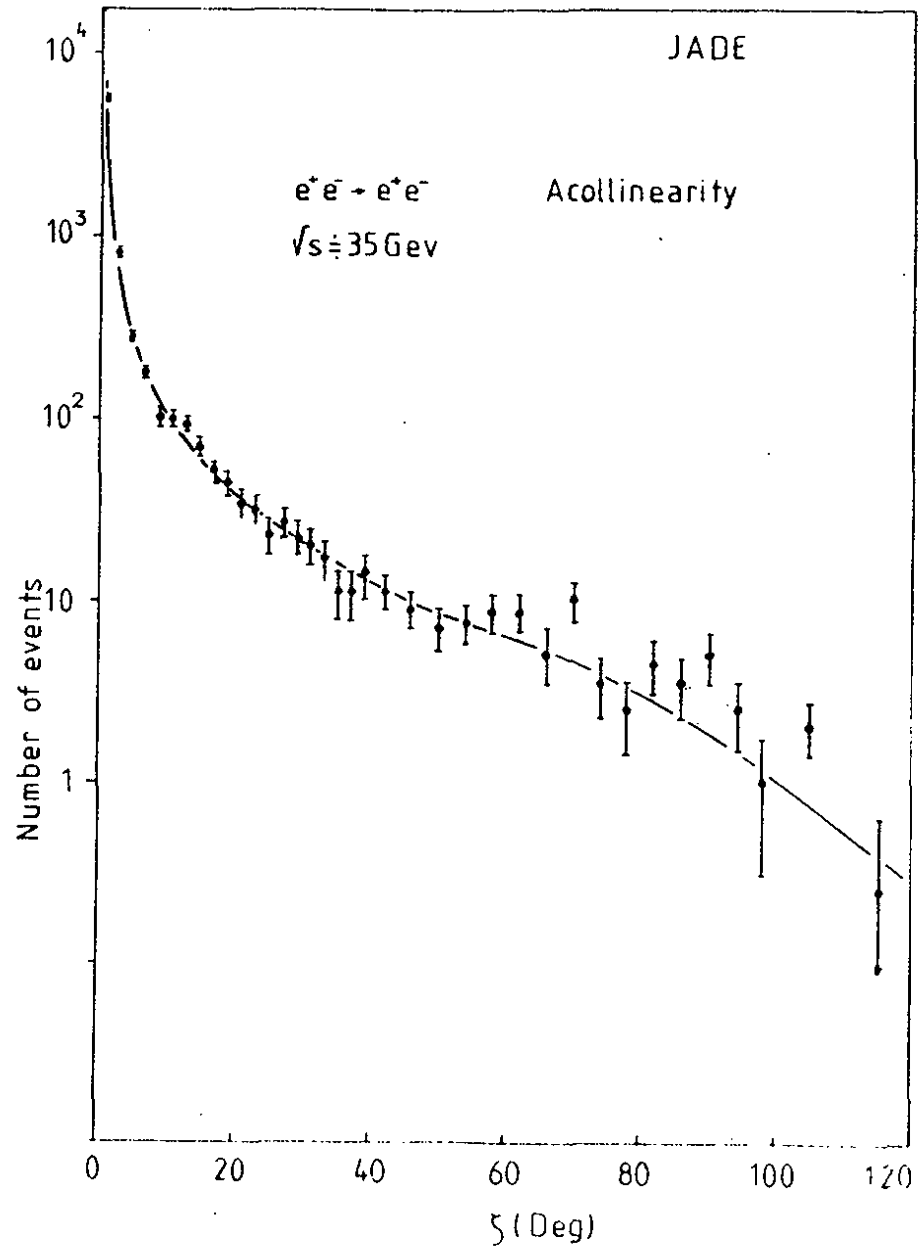
JADE
$e^+e^- \rightarrow e^+e^-$
Acollinearity
$\sqrt{s} \doteq 35$ Gev
10^4
10^3
10^2
10
1
Number of events
0
20
40
60
80
100
120
ξ (Deg)

Fig. 26

4. TESTS OF QUANTUM ELECTRODYNAMICS, UNIVERSALITY FOR CHARGED LEPTONS AND MODELS OF THE ELECTRO-WEAK INTERACTION

4.1 Introduction

There have been many experiments testing quantum-electrodynamics (QED) with electrons, muons and photons at electron-positron storage rings. Notable experiments[25] were done by Alles-Borelli et al., Newman et al., Augustin et al., O'Neill et al. For a comprehensive review of QED work, see Brodsky and Drell[26]. Much has been learned about the properties of the heavy lepton tau since the original search began at ADONE on $e^+ + e^- \to \mu e + \ldots\ldots$[27]. The discovery of the tau lepton at SLAC[28] and it's subsequent confirmation at DESY[29] has inspired further studies. We know it is a spin 1/2 particle which decays weakly[30] and whose properties are very similar to the muon.

With the PETRA experiments the rections $e^+ + e^- \to \ell^+\ell^-$ for all the known charged leptons (ℓ= e,μ,τ) are studied by measuring the dependence of the cross section on center of mass energy of scattering angle over a wide range of PETRA energies. These measurements enable one to compare the data with predictions of quantum electrodynamics, to test the universality of these leptons at very small distances, and to set a limit on the charge radius of these particles. Up to present time the reactions:

$$e^+e^- \to e^+e^- \quad \text{(Bhabha scattering)} \tag{2}$$

$$e^+e^- \to \mu^+\mu^- \tag{3}$$

$$e^+e^- \to \tau^+\tau^- \tag{4}$$

have been measured at the center of mass energies range of $\sqrt{s}$ = 12 to 36.6 GeV.

In particular by combining results from the MARK-J at PETRA on Bhabha scattering, $\mu^+\mu^-$ and $\tau^+\tau^-$ production with recent world data from neutrino-electron scattering experiments, unique values for the leptonic weak neutral coupling constants g_V and g_A in the

framework of electroweak models containing a single Z^o can be determined. In contrast to previous analysis, data from purely leptonic interactions are used, and therefore one avoids the inherent uncertainties resulting from the use of hadronic targets. In the context of the standarf SU(2) x U(1) model of Glashow, Weinberg and Salam a value for $\sin^2\theta_w$ is obtained.

Furthermore, the data are also compared with extended gauge models containing more than one neutral weak boson. Stringent lower limits can be placed on the masses of such bosons.

The results described in this section were also presented by A. Böhm at the High Energy Physics (Wisconsin) Conference[31].

4.2 Test of Quantum Electrodynamics and of Universality of Leptons

The momentum, energy and angular resolution for the QED processes

$$e^+e^- \to e^+e^- \quad (2)$$
$$e^+e^- \to \mu^+\mu^- \quad (3)$$
$$e^+e^- \to \tau^+\tau^- \quad (4)$$
$$e^+e^- \to \gamma\gamma \quad (5)$$

are shown in Table II for the various experiments.

(a) The first order QED photon propagator produces an s^{-1} dependence in the $e^+e^- \to e^+e^-$ cross section. Thus when radiative corrections have been taken into account in the data, the quantity

$$s \frac{d\sigma}{d\Omega}$$

should be independent of s. This distribution is plotted for the TASSO data at $\sqrt{s}$ = 12, 30.7 and 35.2 GeV in Figure 27. Preliminary data for the Bhabha events at $\sqrt{s}$ = 36.5 GeV from the CELLO group are shown in Figure 28. Excellent agreement with the QED predictions is seen in both figures.

To express this agreement analytically, the data are compared with the QED cross section in the following form[32]:

$$\frac{d\sigma}{d\Omega} = \frac{\alpha^2}{s}\left(\frac{q'^4+s^2}{q^4}|F_s|^2 + \frac{2q'^4}{q^2 s} R_e(F_s F_T^*) + \frac{q'^4+q^4}{s^2}|F_T|^2\right)\left(1+C(\theta)\right) \quad (6)$$

where

$$F_s = 1 \mp q^2 / (q^2 - \Lambda^2_{\pm}) \quad (7)$$

is the form factor of the space like photon,

$$F_T = 1 \mp s / (s - \Lambda^2_{\pm}) \quad (8)$$

is the form of the timelike photon, $q^2 = -s\cos^2(\theta/2)$, $q'^2 = -s\sin^2(\theta/2)$, Λ is the cut-off parameter in the modified photon-propagator model[33] and $C(\theta)$ is the radiative correction term as a function of θ. The lower limits of Λ at 95% confidence level for the Bhabha events are shown in Table III for various PETRA groups[34]. One can conclude from this table that QED is valid for the reaction (2) down to small distances.

(b) The two photon annihilation $e^+e^- \to \gamma\gamma$ (Figure 29) is well suited for testing the validity of quantum electrodynamics at high energies since the contributions from electro-weak interference effects are expected to be absent in first order perturbation theory[35]. Two possible modifications of the standard QED cross section can be used:

(i) A vertex modification[36] which modifies the differential cross section as follows:

$$\frac{d\sigma}{d\Omega} = \frac{\alpha^2}{2s}\left(\frac{q'^2}{q^2}|F(q^2)|^2 + \frac{q^2}{q'^2}|F(q'^2)|^2\right)\left(1 + C(\theta)\right) \quad (9)$$

where

$$F(q^2) = 1 \pm q^4/\Lambda^4, \quad F(q'^2) = 1 \pm q'^4/\Lambda^4$$

and q^2 and q'^2 are defined as above. The $C(\theta)$ is the radiative correction as function of the scatter angle θ.

(ii) To test exchange of a hypothetical heavy electron the differential cross section can be written as[37]

$$\frac{d\sigma_{e^*}}{d\Omega} = \frac{\alpha^2}{2s}\left(\frac{q'^2}{q^2} + \frac{q^2}{q'^2} \pm \frac{2s^2 - 4q^2q'^2}{\Lambda_{e^*_\pm}^4}\right)\left(1 + C(\theta)\right) \qquad (10)$$

The value of $\Lambda_{e^*_\pm}$ can be interpreted as the mass of a heavy electron assuming its coupling strength is the same as that of the electron (see Figure 29).

Figure 30 shows the differential cross section for $e^+e^- \to \gamma\gamma$ obtained by JADE and PLUTO in the energy range $12 \leq \sqrt{} \leq 31.6$ GeV. The solid curve is the QED prediction and the dashed curves the prediction including a cut-off parameter effect of $\Lambda = 40$ GeV. The integrated cross section over the measured angular range of the PLUTO detector is shown in Figure 31 as function of the c.m. energy E_{CM} in order to check the 1/s behaviour of the $e^+e^- \to \gamma\gamma$ reaction. The agreement between the data and the QED predictions is good.

The data of the MARK-J[31] and PLUTO[31],[38] groups were fitted to the differential cross section of expression (9) and (10) and the data of the JADE[31],[39], and TASSO[31],[40] groups to expression (10). The results of these fits for the cut-off parameters obtained by the groups are collected in Table III. In both parametrizations the lower limits for the cut-off parameters are about 40 GeV (95% CL). At the highest PETRA energies the lower bounds are raised by a factor 4 to 5 over the values obtained with the lower energy e^+e^- colliding beam machines[41].

(c) Muon and Tau Pair Production and Tests of the Universality of the Leptons[31],[42]

The PETRA detectors are able to distinguish muons from electrons and hadrons and to eliminate cosmic ray muons as a source of background for the back-to-back muon pairs.

I will describe in detail the criteria used by the MARK-J collaboration for the muon and tau pair production identification. Single muons are identified as particles which:

(i) are reconstructed in the inner drift chambers to come from the interaction region;

(ii) leave minimum ionizing pulse heights in the seven layers of counters of the calorimeter;

(iii) leave a track in the outer drift chambers (P) and thus fall into an angular range $45^{o} \leq \theta_{\mu} \leq 135^{o}$.

In addition back-to-back muon pairs from reaction (3) are distinguished from cosmic rays by the requirement that:

(i) the D counter timing signals are coincident with one another (and not relatively off time as in the case for cosmic rays traversing the detector),

(ii) the muons should be collinear and coplanar, and they should pass through the intersection region.

A Monte Carlo study shows that $\mu^{+}\mu^{-}$ acceptance, which is dominated by the geometrical acceptance of the outer drift chambers, is 41% ± 3% independent of beam energy. Tau leptons from reaction (4) are identified by detecting μ-hadron and μ-electron final states. The cross section is determined using the known branching ratio of $\tau \rightarrow \mu\, \nu\nu$ (16%) and $\tau \rightarrow$ (e, hadron or multihadrons) + ν (84%)[30]. The measured muon momentum and hadron energy for the $\tau^{+}\tau^{-}$ candidates is in agreement with calculations based on the known decay properties of the τ lepton.

The acceptance is calculated using a Monte Carlo method to generate $\tau^{+}\tau^{-}$ production from reaction (4) including radiative corrections. A detection efficiency of ~ 10% for τ pairs at various energies, when requiring one decay muon to be detected in association with a single electron, or one or more hadrons, is obtained with the MARK-J detector.

The selection criteria for the tau leptons for the PLUTO[43] and TASSO[44] groups are different from the ones mentioned above. PLUTO identifies one charged particle and neutrals for the decay of the tau, and TASSO requires at least three charged and neutral

particles, recoiling against one charged particle.

The resultant $e^+e^- \to \mu^+\mu^-$ and $\tau^+\tau^-$ cross sections as a function of s are plotted in Figures 32 and 33. We see that from $q^2 = s = 169$ to $q^2 = 1225\ GeV^2$ the data agree well with the predictions of QED for the production of a pair of point-like particles. In particular, Figure 33 represents the evidence that the τ lepton is a point-like particle over a large range of q^2, and demonstrates that it belongs in the same family as the electron and muon. To parametrize the maximum permissible size (radius) of the particles, one uses the form factor:

$$F(s) = 1 \mp s/(s - \Lambda^2_{\pm})$$

By comparing the data with the cross sections including this form factor, lower limits on the cut-off parameters, at the 95% confidence level are calculated and they are summarized in Table III.

Thus, from Heisenberg's Uncertainty Principle, all the known charged leptons are point-like particles in their electromagnetic interactions, with characteristic radii $\leq 10^{-16}$ cm.

4.3 Measurements of the Asymmetry in the Production of $\mu^+\mu^-$ Pairs

Weak interaction effects within the standard GWS model are small. The change in cross section for lepton production in e^+e^- interactions at PETRA energies is in first order

$$\Delta\sigma \simeq g_v^2$$

where $g_v^2 = (1-4\ \sin^2\theta_w)^2$ is the vector coupling constant squared. For the value of $\sin^2\theta_w = 0.23$ one finds that $\Delta\sigma/\sigma \simeq 0.5\%$, an effect that is experimentally not noticeable at PETRA. However, by testing the shape of the angular distributions information on the axial coupling constant of the weak interaction can be extracted. Figure 34 shows the angular distribution for muon pair production as measured by the PETRA groups.

Defining θ as the angle between the incident e^- and the outgoing muon in the forward hemisphere, the asymmetry is:

$$A_{\mu\mu} = \frac{N_- - N_+}{N_- + N_+}$$

where $N_-(N_+)$ is the corrected number of events with the negatively (positively) charged muon in the forward hemisphere, integrated over the accessable angular range. The measured values for $A_{\mu\mu}$ are summarized in Table IV. In first order $A_{\mu\mu}$ is directly related to g_A^2 according to

$$A_{\mu\mu} \simeq 6 g_A^2 \chi^2 \qquad (11)$$

where

$$\chi^2 = g \cdot \frac{s\, m_z^2}{s - m_z^2} \qquad \text{and} \qquad g = G_F/8\pi\alpha\sqrt{2} = 4.49\ 10^{-15}\ \text{GeV}^2$$

s is the total energy squared and m_z the mass of the neutral boson in the standard GWS model ($\sim$ 90 GeV). The energies at PETRA are such that one can work in the low energy approximation which makes χ^2 independent of m_z^2. Thus (11) can be written as:

$$A_{\mu\mu} \simeq -6 g g_A^2 s$$

The combined data of the PETRA groups gives a value of the asymmetry:

$$(-0.09 \pm 4.9)\%$$

while the expected value is -5.7%.

4.4 Tests of Electroweak Interaction Models with one Neutral Boson

Since the first experimental observation of the weak neutral current interaction[45] in $\nu_\mu + e^- \to \nu_\mu + e^-$ several neutrino-electron scattering experiments[46] have obtained important constraints on the structure of the weak neutral currents. A unique determination of the leptonic coupling constants g_V and g_A, however, was only possible in a more general framework incorporating lepton-lepton and lepton- quark neutral current interactions,

as defined by Sehgal[47] or by Hung and Sakurai[48]. The analysis involved the use of data from neutrino-nucleon scattering[49] and the scattering of polarized electrons on deuterium[50], as well as the neutrino-electron scattering results, and depended on factorization relations[48] to relate the lepton-quark to the purely leptonic couplings.

By combining the recent results on e^+e^- elastic scattering, $\mu^+\mu^-$ and $\tau^+\tau^-$ production obtained by the MARK-J experiment over the center of mass energy range $12 \leq \sqrt{s} \leq 36$ GeV with the neutrino-electron scattering data, one is able to determine g_V and g_A uniquely without the complications which arise from the use of hadronic targets. In the general framework of SU(2) x U(1), with a single Z^0 mediating the weak neutral current the sole assumptions required for this determination are:

(1) e, μ, τ universality,

(2) an effective interaction Hamiltonian which is a sum of products of vector and axial-vector currents, and

(3) the point-like nature of leptons.

The MARK-J data which is used to test electroweak theories consists of measurements of the angular distribution of Bhabha scattering, of the muon pair and tau pair production cross section as a function of $\sqrt{s}$, and of the $\mu^+\mu^-$ forward-backward asymmetry[51]. The details of the apparatus and event selection procedures are discussed in section 3.2 and reference 52.

In comparing the data on $e^+e^- \rightarrow \ell^+\ell^-$ (ℓ= e, μ, τ) with the predictions of electroweak theories, the order α^3 radiative corrections as well as the contribution from hadronic vacuum polarization are subtracted[53]. The resulting cross sections are defined as σ^{exp} and $d\sigma^{exp}/d\Omega$. Both weak-electromagnetic interference and pure weak effects are included by using the Hamiltonian[48],[54]:

$$H_t = -4\alpha\bar{e}\gamma_\lambda e\bar{\ell}\gamma^\lambda\ell - 2\frac{G_F}{\sqrt{2}}\left\{\bar{e}\gamma_\lambda(g_V + g_A\gamma_5)e\frac{m_Z^2}{m_Z^2 - s}\ \bar{\ell}\gamma^\lambda(g_V + g_Z\gamma^5)\ell\right\}$$

and for $\ell = \mu,\tau$

$$H = H_t + 4\pi\alpha\bar{\ell}\gamma_\lambda e\frac{1}{q^2}\ \bar{e}\gamma^\lambda\ell + \frac{2G_F}{\sqrt{2}}\left\{\bar{\ell}\gamma_\lambda(g_V + g_A\gamma_5)e\ \frac{m_Z^2}{m_Z^2 - q^2}\ \bar{e}\gamma^\lambda(g_V + g_A\gamma_5)\ell\right\}$$

for $\ell = e$.

In the above formula, g_V and g_A are the coupling constants of the weak neutral current to leptons and $G_F = 1.02 \times 10^{-5}/m_p^2$.

The cross section for $e^+e^- \to e^+e^-$ has been calculated to second order in the weak interaction coupling strengths by Budny[55]. The modification of the Bhabha scattering angle angular distribution by weak effects is not immediately apparent in the distributions of $d\sigma(e^+e^- \to e^+e^-)/d\Omega$ commonly used in tests of pure QED. This is shown in Figure 35, where the measured and corrected distributions $sd\sigma^{EXP}(e^+e^- \to e^+e^-)/d(\cos\theta)$ are compared to the predictions of lowest order QED ($g_A = g_V = 0$) at $\sqrt{s}$ = 12, 30 and 35 GeV. The sensitivity to weak effects is, however, demonstrated in Figure 36, which shows the deviation δ of the combined 30 and 35 GeV data from the lowest order QED predictions as a function of $\cos\theta$[56], where

$$\delta(\cos\theta) \equiv (d\sigma^{EXP}/d\Omega - d\sigma^{QED}/d\Omega)/(d\sigma^{QED}/d\Omega)$$

Also shown in Figure 36 are the predictions of the standard SU(2) x U(1) electroweak theory[7], where $g_A = -1/2$ and $g_V = 1/2(1 - 4\sin^2\theta_w)$, with $\sin^2\theta_w = 0.25, 0.49, 0.55$. While the deviation from QED for $\sin^2\theta_w \simeq 1/4$ depends only on the axial coupling, and amounts to $\leq 2\%$, effects as large as 5% are expected for $\sin^2\theta_w = 0.55$ ($g_V = 0.60$). The latter case can be excluded by the data at the 95% confidence level so that Bhabha scattering data alone imposes stringent limits on the vector coupling constant of the electron.

The cross sections σ^{EXP} for $e^+e^- \to \mu^+\mu^-$ and $e^+e^- \to \tau^+\tau^-$ are

shown in Figure 37 for $12 \leq \sqrt{s} \leq 36$ GeV. As in the case of Bhabha scattering, the data have been corrected for order α^3 QED effects and hadronic vacuum polarization. Curves representing the predictions of lowest order QED and of the standard electroweak theory with $\sin^2\theta_w = 0.55$ are shown for comparison.

As mentioned before in Section 4.3 the forward-backward asymmetry $A_{\mu\mu}$ in $e^+e^- \to \mu^+\mu^-$ provides the principal constraint on g_A. The measured values for A are:

$$A(\sqrt{s} = 30 \text{ GeV}) = -0.03 \pm 0.10$$
$$A(\sqrt{s} = 35 \text{ GeV}) = +0.08 \pm 0.16$$

The corresponding predictions of the standard model are $A = -0.053$ at $\sqrt{s} = 30$ GeV and $A = -0.076$ at $\sqrt{s} = 35$ GeV.

Stringent overall constraints on g_V and g_A from the data are obtained by fitting the e^+e^-, $\mu^+\mu^-$, and $\tau^+\tau^-$ data[57] shown in Figures 35-37, along with the $\mu^+\mu^-$ asymmetry. Including the 3% luminosity error in the fit, one finds $\sin^2\theta_w = 0.24 \pm 0.11$, or $0.07 \leq \sin^2\theta_w \leq 0.42$ at the 95% confidence level.

Also fitted are g_V^2 and g_A^2 in the more general context of single Z^o models, and the result is $g_V^2 = -0.10 \pm 0.11$ and $g_A^2 = 0.11 \pm 0.29$ with $\chi^2=26$ for 31 degrees of freedom. These results including correlations can be converted into an allowed region in the g_V-g_A plane. Since the predicted effects do not depend on the sign of g_V and g_A, the allowed region is four fold symmetric, as shown in Figure 38 for the 95% confidence level contour(which corresponds to an increase in χ^2 of 6 from the minimum value). This contour corresponds to the choice $m_z = \infty$, which of all possible m_z values, gives the weakest overall constraints in the g_V-g_A plane. Also shown in Figure 38 are the standard deviation limits deduced from the purely leptonic processes[58]

$$\nu_\mu e^- \to \nu_\mu e^-,\ \bar{\nu}_\mu e^- \to \bar{\nu}_\mu e^-,\ \bar{\nu}_e e^- \to \bar{\nu}_e e^-$$

Neutrino electron scattering data alone limits the possible values of g_V and g_A to two regions in the g_V - g_A plane around (g_V=0, g_A = -1/2) and (g_V = -1/2, g_A=0). Combining these data with the results on purely leptonic interactions obtained in the MARK-J experiment rules out the second solution with more than 95% confidence. This confirms the conclusion drawn on the basis of deep inelastic neutrino nucleon scattering and polarized electron deuterium scattering data, without recourse to models of hadron production by the weak neutral current.

The leptonic vector and axial vector coupling constants of the weak neutral current are thus determined to be in agreement with the predictions of the standard SU(2) x U(1) theory.

4.5 Tests of Models of the Electro-Weak Interactions with more than one Neutral Boson

There has been the suggestion[59], that the standard model can be naturally extended to models based on an enlarged symmetry group SU(2) x U(1) x G, where G stands for a general symmetry group, without changing any of the predictions which have been made for the low q^2 range covered by lepton-nucleon scattering data. The generalized models differ from the SU(2) x U(1) model in the high q^2 region because they have more than one neutral weak boson. The lowest mass neutral boson in these models has a mass smaller than the Z^o mass in the standard model.

To first order in s/m_z^2 the deviation of the multiple Z^o models from the standard model can be described by an additional term $C\ j_{em}^2$ to the effective Hamiltonian of the standard model. The effective Hamiltonian contains three parameters[48] h_{VV}, h_{VA} and h_{AA}, where the parameter C only modifies h_{VV}.

$$h_{VV} = 1/4\ (1 - 4\sin^2\theta_W)^2 + 4\ C, \qquad C \geq 0$$

$$h_{VA} = 1/4\ (1 - 4\sin^2\theta_W) = g_V \cdot g_A$$

while the terms containing the axial vector current remain the same as in the standard model,

$$h_{AA} = g_A^2 = 1/4$$

where g_V and g_A are the vector and axial vector coupling constants in the standard model respectively. In the case where C vanishes, h_{VV} reduces to g_V^2 as expected in the standard model. This term appears not only in the gauge models of the type of SU(2) x U(1) x G but also in the general electroweak mixing schemes proposed by Bjorken[59]. The parameter C can therefore be used as a universal quantity independent of the details of the models. Since this term is proportional to the electro-magnetic currents which couple to charge and is parity conserving, it contributes neither to the neutrino scattering processes, nor to polarized e-D scattering. On the other hand the reactions $e^+e^- \to \ell^+\ell^-$ (ℓ = e, μ, τ) at present PETRA energies $\sqrt{s}$ = 35 GeV begin to be sensitive to the effects of an additional Z^o with a mass below that of the standard model Z^o and provide an opportunity to set stringent limits on C. The corrections due to the Z^o propagator are incorporated in the calculation of the cross sections.

From the limit of C, limits on the masses of Z^o's in specific models can be obtained. As an illustration, we consider the case of two Z^o's with masses m_1 and m_2. In models based on SU(2) x U(1) x U(1), with one doublet of charged and two neutral gauge bosons, we have the relation[60]

$$C = \cos^4\theta_W \left(\frac{m_Z^2}{m_1^2} - 1\right)\left(1 - \frac{m_Z^2}{m_2^2}\right)$$

while the models based on SU(2) x U(1) x SU(2), with two doublets of charged and neutral gauge bosons, we have[61],

$$C = \sin^4\theta_W \left(\frac{m_Z^2}{m_1^2} - 1\right)\left(1 - \frac{m_Z^2}{m_2^2}\right)$$

With $\sin^2\theta_w = 0.23$, for the same mass m_1 and m_2, C in the SU(1) x U(1) x U(1) model is about eleven times greater than the C in SU (2) x U(1) x SU(2) model. These two models thus represent approximately the extreme cases of the strength of coupling constants of these type of models. In comparing the data on $e^+e^- \to \ell^+\ell^-$ (ℓ=e,μ,τ) with the predictions of electroweak theories, the radiative corrections[53] are subtracted. The weak-electromagnetic interference and pure weak effects are included.

The cross sections for $e^+e^- \to \ell^+\ell^-$ (ℓ=e,μ,τ) have been calculated in terms of $\sin^2\theta_w$ and the parameter C. Using the measured values of $\sin^2\theta_w = 0.23$, the MARK-J group makes a one parameter fit to all of the ee, $\mu\mu$, and $\tau\tau$ data while the normalization is allowed to vary within ±3% due to the uncertainty in the luminosity[31]. They find $-0.04 \leq C \leq 0.027$, at the 95% confidence level. A similar result was obtained by the JADE Collaboration and their value of C was found to be $C \leq 0.033$ at 95% confidence level[62].

The upper limit on C can be converted in a limit in the m_1-m_2 plane for the two models, as shown in Fig. 39. In all these models there is a constraint that $m_1 \leq m_z \leq m_2$. Therefore, the two lines $m_1 = m_z$ and $m_2 = m_z$ are the natural boundaries of the allowed region. The data put severe limits on the SU(2) x U(1) x U(1) model, constraining the masses of the two Z's in a small region. The limits on the SU(2) x U(1) x SU(2) are less stringent but significant.

TABLE CAPTIONS

Table II Resolution and detector type employed by the experiments for various QED processes.

Table III Lower limits of cut-off parameters Λ (in GeV) at 95% confidence limit for various QED processes.

Table IV The measured and predicted values of $A_{\mu\mu}$.

TABLE II

Resolution and Detector Type employed by the Experiment for various QED Processes

	$e^+e^- \to e^+e^-$, $e^+e^- \to \gamma\gamma$					$e^+e^- \to \mu^+\mu^-$		
	SHOWER-DETECTOR							
	$\Delta p/p$	$\Delta E/E$	L_R	MATERIAL	$\Delta\theta/\theta$	$\Delta p/p$	MAGNET	ABSORBER
JADE	60%	3.8%	12.5	Pb-glass	0.6^o	50%	solenoid 0.5T	concrete $L_A = 6$
MARK-J	-	10%	18	Pb/scint.	3^o	26%	Fe-toroid	Fe(magn) $\geq$ 87cm
PLUTO	90%	5-9%	10.6 - 8.6	Pb/scint.	$1-1.4^o$	45%	solenoid 1.7T	Fe 105cm
TASSO	30%	14-18%	9	Pb/scint.	$\sim 15^o$	30%	solenoid 0.5T	Fe 50-87cm

RESOLUTION AT $E_{beam} = 15$ GeV.

TABLE III

Lower Limits of Cut-Off Parameters Λ (in GeV)
at 95% Confidence Limit for Various QED Processes

$ee \to ee$ $\qquad F(s) = 1 \mp \frac{s}{s - \Lambda^2_{\mp}} \quad (\Lambda_S = \Lambda_T)$

	JADE	MARKJ	PLUTO	TASSO
Λ_+	112	106	80	150
Λ_-	106	193	234	136
$ee \to \mu\mu$				
Λ_+	137	192	116	80
Λ_-	96	129	101	118
$ee \to \tau\tau$				
Λ_+	--	100	74	115
Λ_-	--	127	65	76
$ee \to \gamma\gamma$		$F(q^2) = 1 \pm q^4/\Lambda^4_{\pm}$		
Λ_+	48	44	46	34
Λ_-	45	34	36	42
heavy electron e^*		$\Lambda^2_+ \ (e^*) = (M_{e^*}{}^2/\Lambda)$		
$\Lambda_+ \ (e^*)$	45	55	46	34
$\Lambda_- \ (e^*)$	38	38	--	42

TABLE IV

The Measured and Predicted Values of $A_{\mu\mu}$.

	JADE	MARK J	PLUTO	TASSO
Aμμ in %	-8±9	0±9	7±10	-1±12
expected	-6	-5	-5.8	-6

FIGURE CAPTIONS

Fig. 27 The differential cross section s $d\sigma/d\cos\theta$ for $e^+e^- \to e^+e^-$ at $\sqrt{s}$ = 12, 30.7, and 35.2 GeV obtained by the TASSO collaboration.

Fig. 28 The differential cross section $d\sigma/d\Omega$ for $e^+e^- \to e^+e^-$ at $\sqrt{s}$ = 36.5 GeV obtained by the CELLO collaboration.

Fig. 29 Diagram for the process $e^+e^- \to \gamma\gamma$. The e^* indicates the diagram for the exchange of a heavy electron.

Fig. 30 The differential cross section $s.d\sigma/d\Omega$ of the reaction $e^+e^- \to \gamma\gamma$ in the energy range $12 \leq \sqrt{s} \leq 31.6$ GeV. The solid curve is the QED prediction, the dashed curves include the effect of a cut-off parameter of Λ = 40 GeV.

Fig. 31 The cross section for reaction $e^+e^- \to \gamma\gamma$ for $|\cos\theta| \leq 0.75$. The curve is the QED prediction including the effects of radiation and angular resolution.

Fig. 32 Observed cross section for the reaction $e^+e^- \to \mu^+\mu^-$ compared to the predictions of QED (solid curve). The dotted curves are the QED cross sections modified by cut-off parameter $\Lambda\pm$ = 100 GeV.

Fig. 33 Observed cross section for the reaction $e^+e^- \to \tau^+\tau^-$ compared to the predictions of QED (solid curve).

Fig. 34 The differential cross section $s.d\sigma/d\Omega$ for the reaction $e^+e^- \to \mu^+\mu^-$. The solid curve is the QED prediction.

Fig. 35 The differential cross section $s.d\sigma^{exp}/d\cos\theta$ for $e^+e^- \to e^+e^-$ at $\sqrt{s}$ of 12, 30 and 35 GeV obtained by the MARK-J group.

Fig. 36 The deviation δ of the combined 30 and 35 GeV data from the lowest order QED predictions is plotted as a function of $\cos\theta$. The solid, dashed-dotted and dashed curves represent the predictions of the standard electroweak theory with $\sin^2\theta_W = 0.25$, 0.49 and 0.55 respectively.

Fig. 37 The experimental cross sections as a function of $\sqrt{s}$ for the reactions $e^+e^- \to \mu^+\mu^-$ and $e^+e^- \to \tau^+\tau^-$ compared to the predictions of QED (solid curves).

Fig. 38 Results obtained from neutrino experiments and the MARK-J experiment expressed in terms of limits on g_V and g_A. The regions in between the concentric ellipses correspond to 1σ limits from the neutrino-electron scattering experiments. The two black areas indicate the two allowed regions for g_V and g_A from the combined neutrino data. The shaded area represents the 95% confidence limit contour from the MARK-J experiment. The solid line indicated with "A_μ only" give the contour when the asymmetry measurement is used alone in the fit.

Fig. 39 The 95% confidence level contours for fits to the two gauge boson models of de Groot et al. and Barger et al. by the MARK-J and JADE Collaborations.

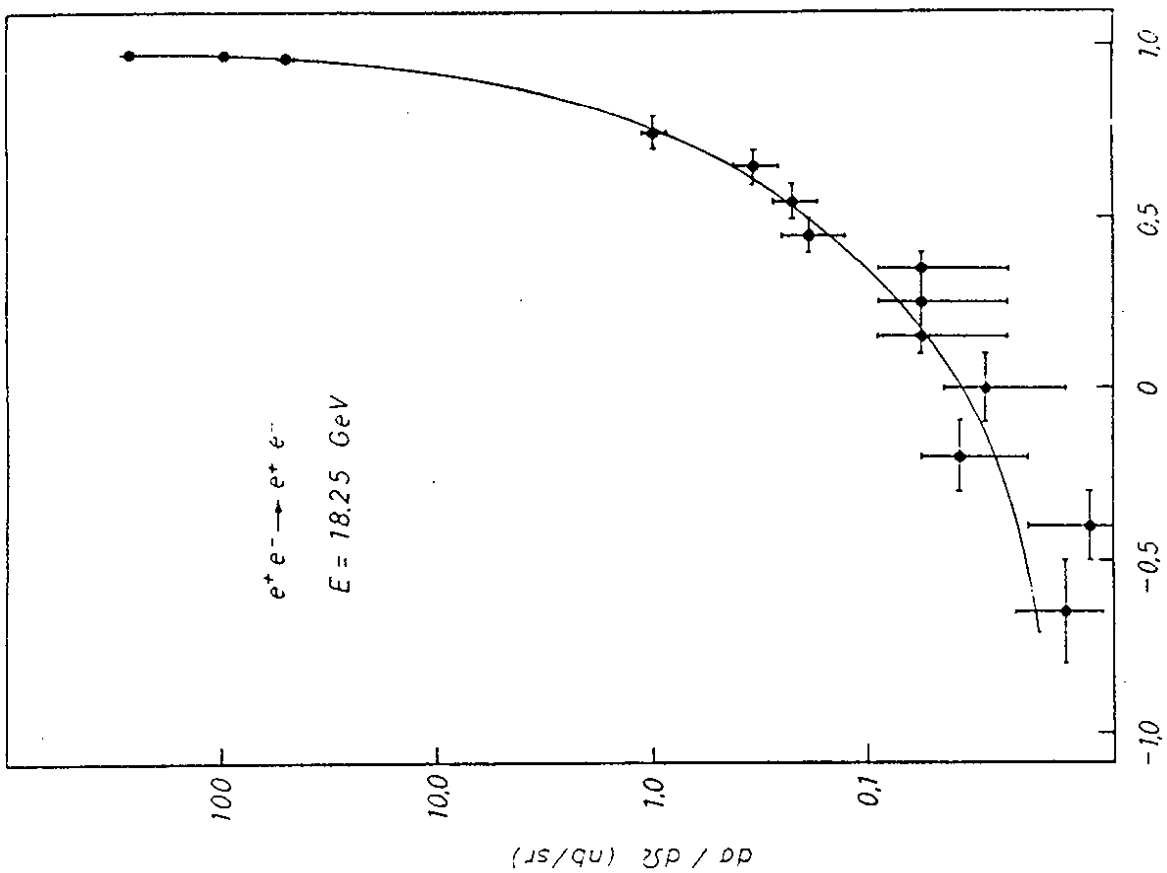
$e^+e^- \to e^+e^-$
$E = 18.25$ GeV
$d\sigma / d\Omega$ (nb/sr)
100
10,0
1,0
0,1
-1,0
-0,5
0
0,5
1,0
cos θ

Fig. 28

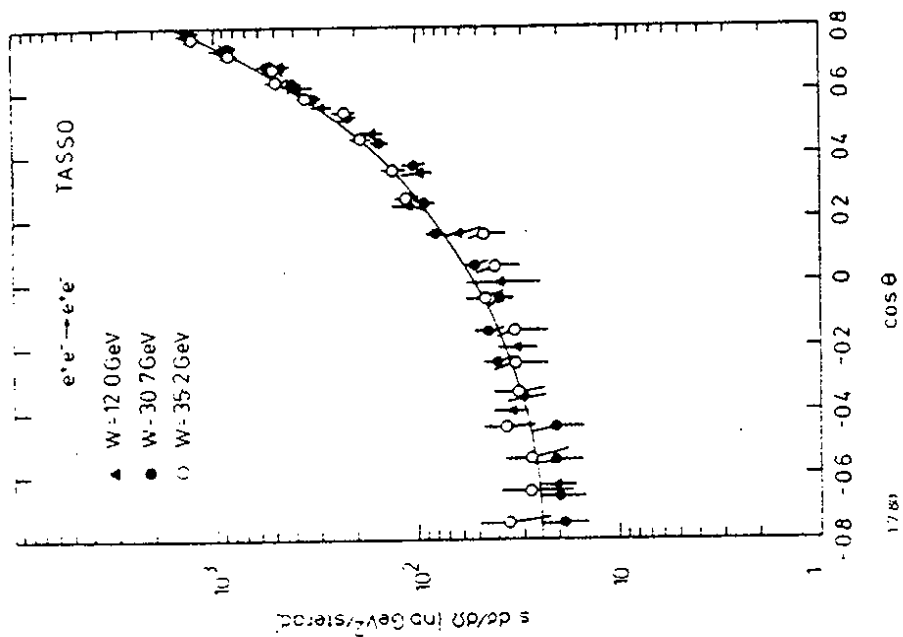
TASSO
$e^+e^- \to e^+e^-$
W = 12.0 GeV
W = 30.7 GeV
W = 35.2 GeV
s dσ/dΩ (nb GeV²/steradian)
10^3
10^2
10
1
-.08 -.06 -.04 -.02 0 .02 .04 .06 .08
cos θ

Fig. 27

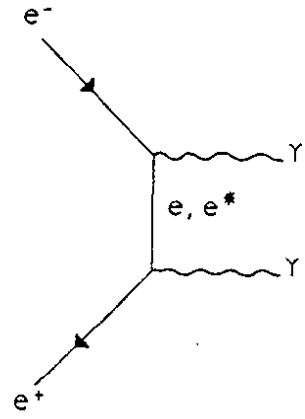

Fig. 29

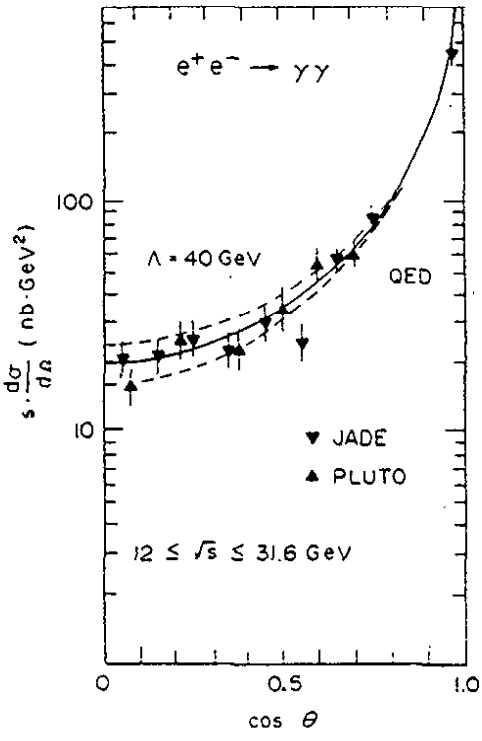

Fig. 30

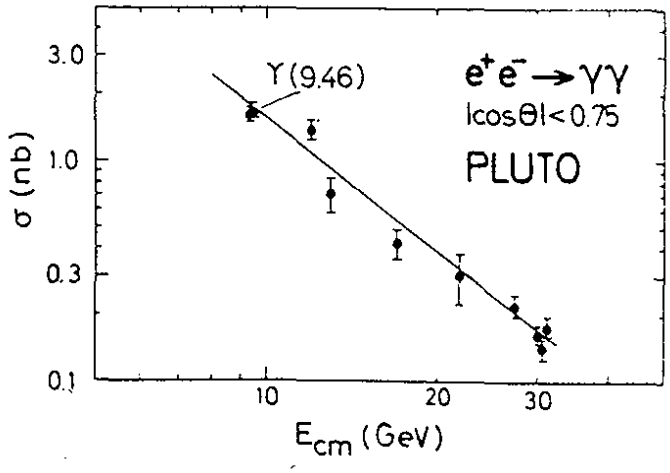

Fig. 31

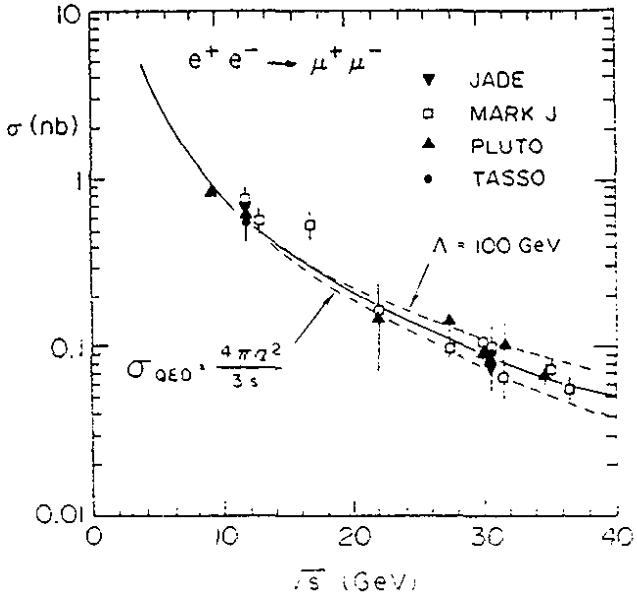

Fig. 32

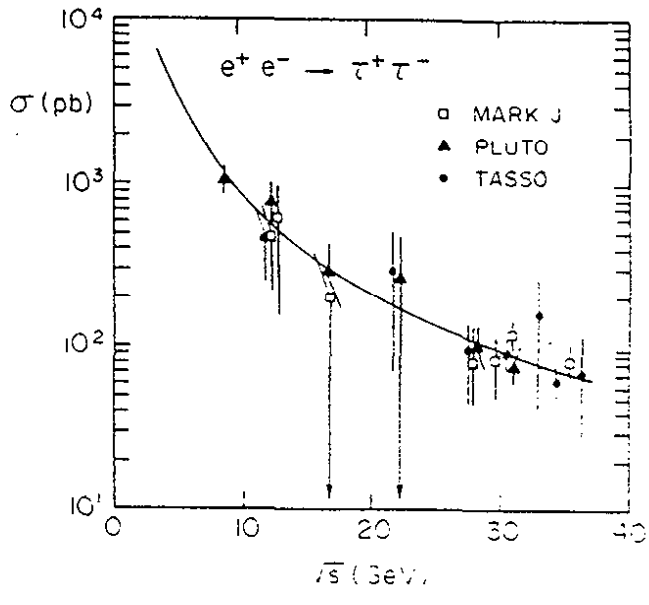

Fig. 33

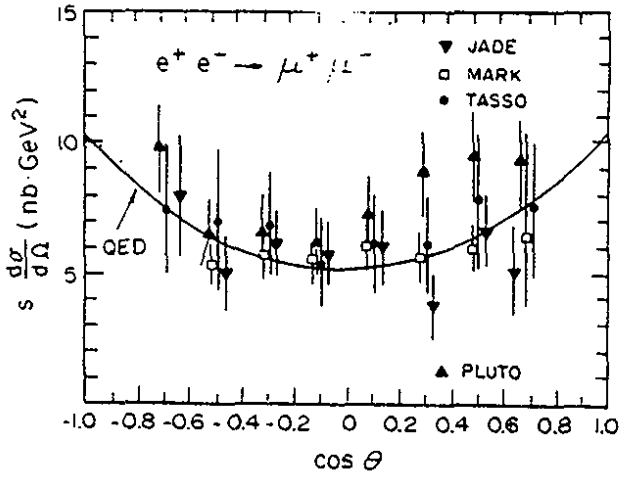
$e^+ e^- \to \mu^+ \mu^-$
JADE
MARK
TASSO
PLUTO
QED
$s \frac{d\sigma}{d\Omega}$ (nb·GeV²)
cos θ

Fig. 34

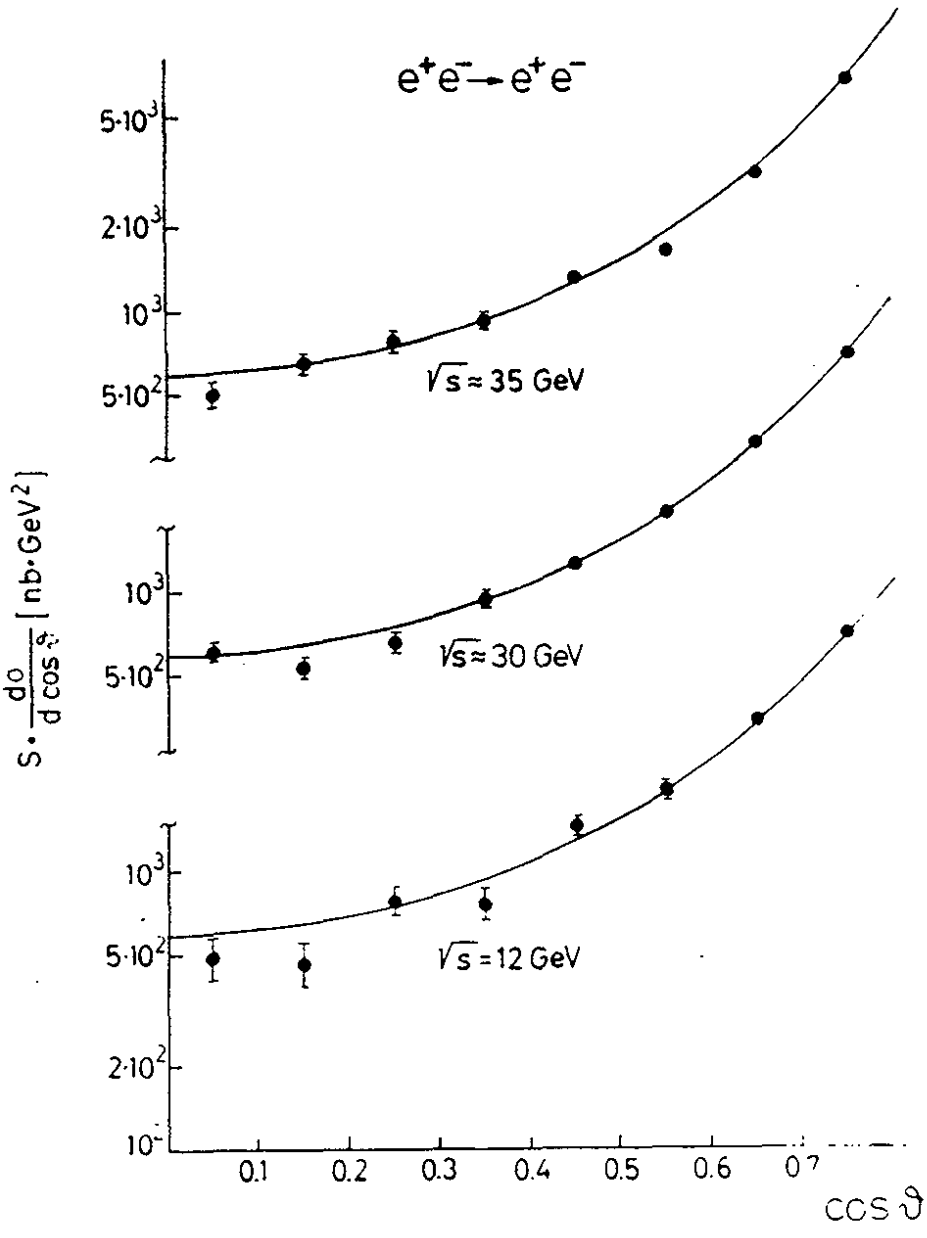
$e^+e^- \to e^+e^-$
$\sqrt{s} \approx 35$ GeV
$\sqrt{s} \approx 30$ GeV
$\sqrt{s} = 12$ GeV
$S \cdot \frac{d\sigma}{d\cos\vartheta}$ [nb·GeV²]
cos ϑ

Fig. 35

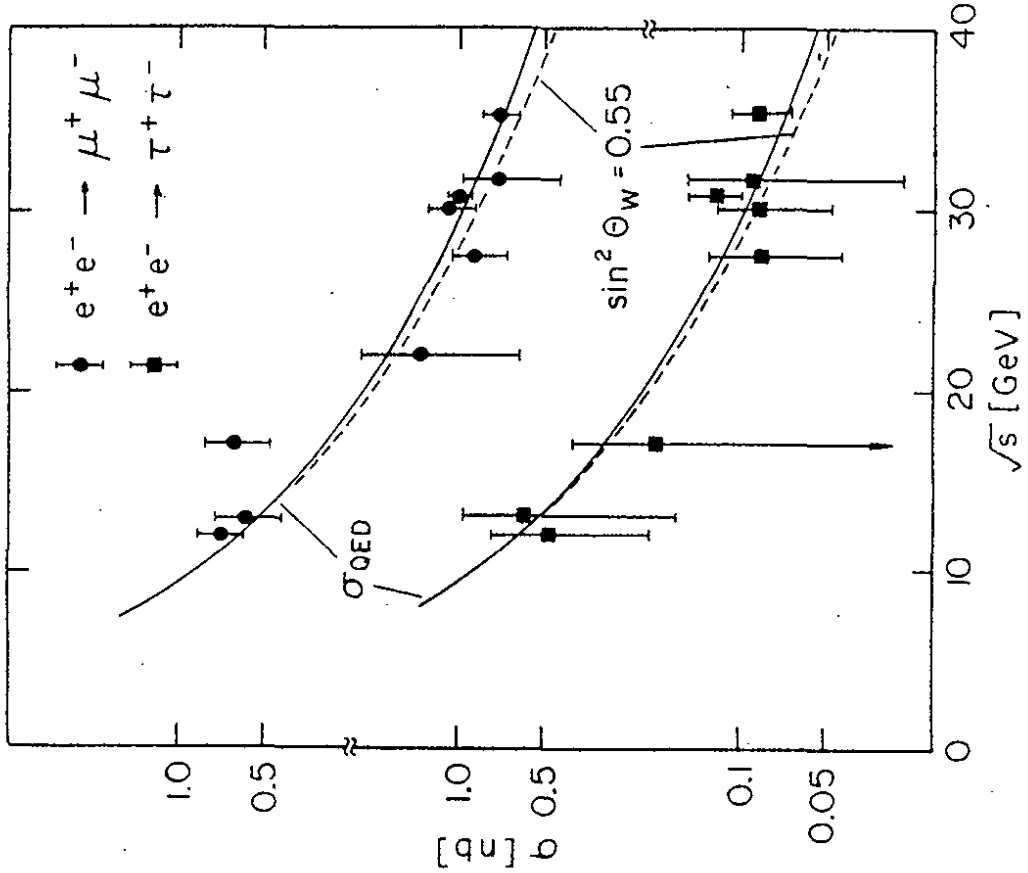
e⁺e⁻ → μ⁺μ⁻
e⁺e⁻ → τ⁺τ⁻
σ_QED
sin² Θ_W = 0.55
σ [nb]
√s [GeV]

Fig. 37

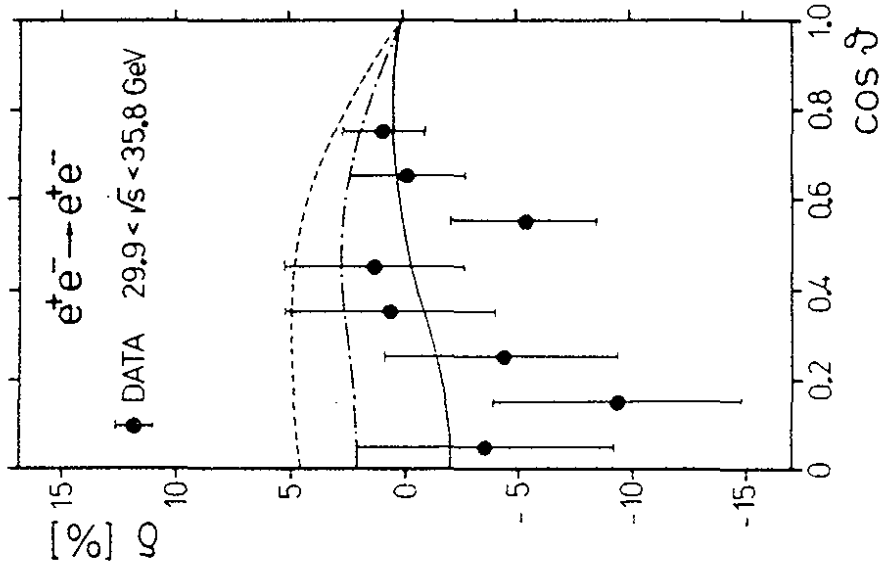
e⁺e⁻→e⁺e⁻
DATA 29,9 < √s < 35,8 GeV
σ [%]
cos ϑ

Fig. 36

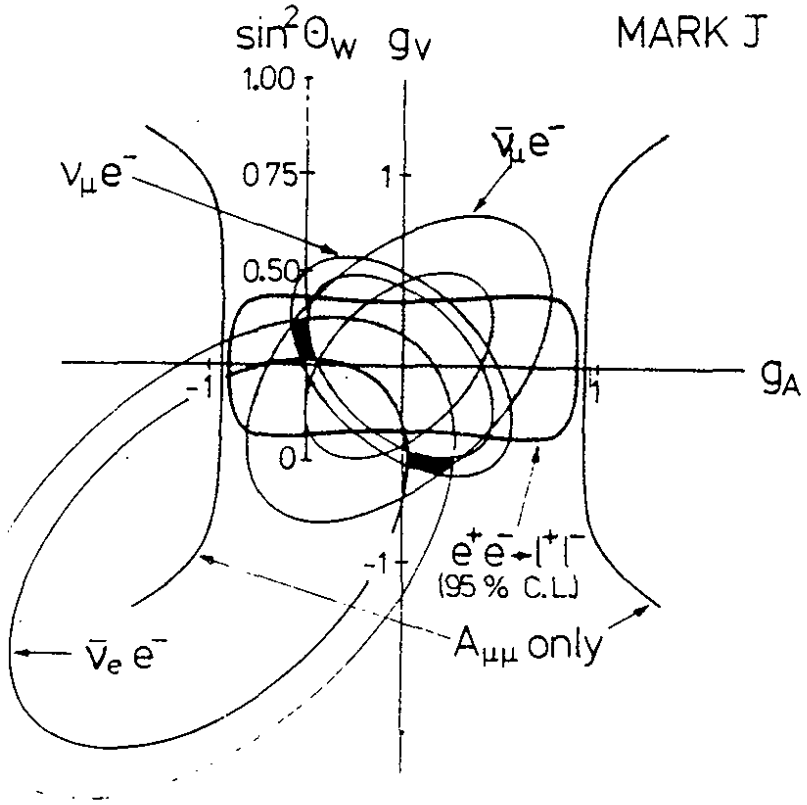
sin²Θw gv
MARK J
1.00
0.75
0.50
1
-1
0
-1
gA
νμe⁻
ν̄μe⁻
e⁺e⁻→l⁺l⁻
(95% C.L.)
ν̄e e⁻
Aμμ only

Fig. 38

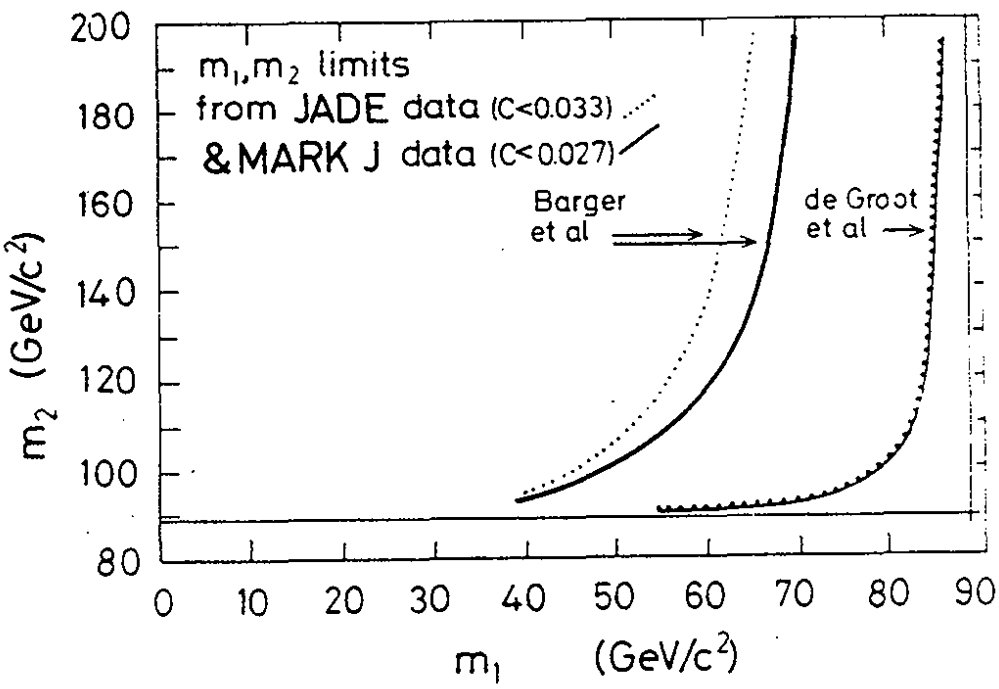
m1,m2 limits
from JADE data (C<0.033)
& MARK J data (C<0.027)
Barger
et al
de Groot
et al
m2 (GeV/c²)
m1 (GeV/c²)
200
180
160
140
120
100
80
0
10
20
30
40
50
60
70
80
90

Fig. 39

5. TWO PHOTON RESULTS FROM PETRA

5.1 Introduction

A high energy e^+e^- storage ring like PETRA offers the possibility to study the two photon exchange reactions in a detailed and systematic way. The reaction under study is:

$$e^+e^- \rightarrow e^+e^- X \qquad (12)$$

where X can be a lepton-antilepton pair or hadrons.

Several of the PETRA detectors have built measuring devices in the forward direction to determine the angle and energy of the scattered electron or positron emerging at small angles from reaction (12). One of these tagging systems, the one belonging to the PLUTO detector, has been described in some detail in Section 3.2.

When the system X of reaction (12) is a lepton-antilepton pair tests of QED can be performed. In the case that system X consists of hadrons several interesting studies on resonance production in the two-photon exchange reaction have been carried out. Total cross section measurements have been performed and results on comparisons between a $q\bar{q}$ production model with the Vector Dominance Model (VDM) for events with high transverse momentum jets have been made.

A structure function for the photon has been extracted by the PLUTO collaboration from the deep inelastic electron-photon scattering events.

Review talks by C.L. Berger[63] and W. Wagner[64] of the PLUTO collaboration and by E. Hilger of the TASSO collaboration[65] cover the topics of the two-photon physics in detail.

Figure 40 shows a schematic view of a two-photon exchange reaction producing hadrons in the final state. Defining $(E, \vec{k})$ as the four momentum of the incoming electron and $(E', \vec{k}')$ as the four momentum of the outgoing electron the momentum transfer squared to the virtual photon γ, is given by

$$-q^2 = \{ (E - E', \vec{k} - \vec{k}') \}^2 \equiv Q_1^2$$

When both the outgoing electron and positron are detected in the tagging systems one speaks of a double tagged event. These events are rare owing to the very limited solid angle and no results have been obtained so far for this type of configuration. In the case that only the electron or positron is detected (a single tagged event) one of the virtual photons will have a very small Q^2. Events of this type can be pictured as the scattering of an electron on a quasi real photon. For the no-tag events only lepton-antilepton pairs or hadrons are measured in the central detectors and none of the scattered electrons and positrons.

A common feature of all the two-photon events is the limited energy for the lepton-antilepton pairs or the hadronic system. The total visible energy in the central detectors is small because of the small amount of energy transferred to the virtual photons from the incoming electron and positron beams. The separation of the two-photon exchange events and the one-photon annihilation events is therefore straightforward and can be readily made by cuts on the visible energy and the sum of the transverse momenta of the particles in the central detector.

5.2 Tests of Quantum Electrodynamics in Two-Photon Processes

The relevant diagrams for tests of QED in the two-photon exchange channels are shown in Figure 41a. The following reactions are studied:

$$e^+e^- \rightarrow e^+e^- \; e^+e^- \qquad (13)$$

$$e^+e^- \rightarrow e^+e^- \; \mu^+\mu^- \qquad (14)$$

Higher order corrections in the single photon annihilation channel due to the conversion of a radiated photon in a lepton-antilepton pair (shown in Fig. 41b) give rise to the same final states as processes (13) and (14).

The results obtained by the JADE collaboration for $e^+e^- \to e^+e^-\mu^+\mu^-$ are shown in Figure 42. The comparison with QED was performed by using a Monte Carlo program written by J. Vermaseren[66]. The prediction of QED includes an exact calculation of the diagrams of Fig. 41a plus their interference with the bremsstrahlung terms of Fig. 41b. The agreement between data and predictions is good.

The calculated cross section in the MARK-J detector for reaction(14), when the observed particles are:

(a) two μ's only,
(b) only one μ and one e,
(c) two μ's and one e,

are shown in Fig. 43.

The cross sections for each of these configurations were computed by using the same Monte Carlo program as above. The measured cross sections, also shown in Fig. 43 agree well with the calculations in all cases.

5.3 The Exclusive Reactions $\gamma\gamma \to f^o$ and $\gamma\gamma \to \rho^o\rho^o$

5.3.1 The Reaction $\gamma\gamma \to f^o$

The PLUTO and TASSO collaborations have measured the final state

$$e^+e^- \to e^+e^- + \text{two charged particles}$$

without tagging the forward electron and positron. By studying only those events with low visible energy in the central detector and demanding that the two tracks reconstruct the crossing point of the colliding beams, the processes $e^+e^- \to e^+e^-e^+e^-$, $e^+e^- \to e^+e^-\mu^+\mu^-$ and $e^+e^- \to e^+e^-\pi^+\pi^-$ are selected with little background from beam gas interactions. The background is reduced even further by selecting the events for which the two charged tracks are coplanar but acollinear, The dominant part of the final event sample contains lepton-antilepton pairs from reactions(13) and (14). The

$\gamma\gamma \to \pi^+\pi^-$ final state was calculated[67] to contribute ~ 16% to the events.

The invariant mass distribution of the two prong events for average beam energies of 15.5 GeV obtained in the PLUTO detector[68] is shown in Fig. 44. The agreement with the QED calculation below 1 GeV and above 1.5 GeV is good, however, a clear excess of events is seen in the region between 1 and 1.5 GeV. The insert in Fig. 44 shows the difference between the data and the QED precition: a resonant behaviour is seen at the mass of the f^o resonance. In order to extract the decay width of $f^o \to \gamma\gamma$ a helicity amplitude of $\lambda = 2$ is assumed and a value for the width $\Gamma(f^o \to \gamma\gamma) = 2.3 \pm 0.5$ KeV with an additional systematic error of ± 15% is obtained.

The distribution of the difference between the measured invariant mass of the two charged particles and the QED background of the TASSO collaboration[65] is shown in Fig. 45. A very clear f^o signal is observed. The curve shown in the figure is the result for the f^o contribution using the model of reference[67]. A preliminary value for $\Gamma(f^o \to \gamma\gamma) = 4.1 \pm 0.4$ KeV with a systematic uncertainty of 15% has been derived.

The results for the width $\Gamma(f^o \to \gamma\gamma)$ of the two groups is compared with the theoretical predictions in Fig. 46. The calculations with the non-relativistic quark model are in reasonable agreement with the data, the predictions of the other models, however, clearly disagree[69].

5.3.2 The Reaction $\gamma\gamma \to \rho^o\rho^o$

The first observation of the reaction

$$\gamma\gamma \to \rho^o\rho^o \qquad (15)$$

has been reported by the TASSO collaboration[70]. Events with two negative and two positive tracks in the central detector originating from the interaction point are the candidates for reaction(15).

Additional requirements are that the energy of the two photon system is in the region $1.5 \leq W_{\gamma\gamma} \leq 2.3$ GeV and that the P_T, defined as the sum of the transverse momenta of the four charged particles is smaller than 0.15 GeV/c. Applying the above criteria leave an event sample of 89 events for further study. Assuming these events to be

$$e^+e^- \rightarrow e^+e^- \pi^+\pi^-\pi^+\pi^-$$

the invariant mass distribution of the $\pi^+\pi^-$ combination can be calculated. Fig. 47a shows the two-dimensional mass distribution of one such a combination versus the opposite one for $1.5 \leq W_{\gamma\gamma} \leq 2.0$ GeV. The pronounced enhancement when both mass values are near the ρ mass is evidence for the $\rho^o\rho^o$ final state. Fig. 47b gives the projection onto the $\pi^+\pi^-$ mass axis.

The curves in Fig. 47b are the results of a fit including photon flux calculations and contributions from non-interfering $\rho^o\rho^o$ production, ρ^o + non-resonant $\pi^+\pi^-$ production and contributions from phase space. The result of this fit indicates that the four charged pion state results mainly from the production of $\rho^o\rho^o$ at low $W_{\gamma\gamma}$.

The cross sections for $\rho^o\rho^o$ production are determined using the results of the above mentioned fit by calculating the acceptance for the events. The results are shown in Fig. 48 together with the prediction of a VDM model calculation. At large $W_{\gamma\gamma}$ this model could be correct but the disagreement for $W_{\gamma\gamma} \leq 2$ GeV indicates the presence of a threshold enhancement in the process $\gamma\gamma \rightarrow \rho^o\rho^o$.

5.4 Total Cross Section Measurements for Multi-Hadron Production

The total cross section for the two-photon exchange reactions producing hadrons

$$\gamma\gamma \rightarrow \text{hadrons} \qquad (16)$$

has been measured by the PLUTO[71] and TASSO Collaborations[65]

using the single tagged events.

The measurement is a difficult one because several assumptions and approximations have to be made in order to extract from the data the relevant quantities.

I will describe the procedure followed by the TASSO group[65] in some detail. The luminosity for the photon-photon collisions is calculated by this group using the functions of Field[72]. According to the TASSO group the photon-photon luminosity at low total photon-photon energy $W_{\gamma\gamma}$ is considerably higher than the one obtained when using the Weizsäcker-Williams approach[73]. To derive values for the $\gamma\gamma$ cross section for real photons the measurements at finite Q_1^2 values are extrapolated to $Q^2 = 0$. The functional form for this extrapolation is in the spirit of the Vector Dominance Model (VDM). Form factors for the virtual photons are included and the cross section is written as:

$$\sigma_{tot}\ (W_{\gamma\gamma}, Q_1^2,\ Q_2^2) = A + \frac{B}{W_{\gamma\gamma}} \left(\frac{1}{1 + \frac{Q_1^2}{m_\rho^2}} \right) \left(\frac{1}{1 + \frac{Q_2^2}{m_\rho^2}} \right) \qquad (17)$$

where A and B are parameters to be determined and the last two expressions in brackets are the form factors. The other assumptions put into a model to describe the hadron events are:

(a) The hadronic system is generated according to a phase-space model with limited transverse momentum with respect to the photon-photon axis.

$$< P_T^{\gamma\gamma} > = C$$

(b) The ratio between charged to neutral particles is 2:1.

(c) The mean charged multiplicity is a function of $\ell n\ W_{\gamma\gamma}$,

$$< n_{ch} > = D + E\ \ell n\ W_{\gamma\gamma}$$

The Monte Carlo events thus generated are compared to the data. The measured distributions of Q_1^2, the charged multiplicity, and

the visible energy in the central detector are used to fit the five parameters A to E. The results of the fit are:

$$< P_T^{\gamma\gamma} > = 0.298 \text{ GeV/c}$$

$$< n_{ch} > = 2.1 + 1.5 \ln W_{\gamma\gamma}$$

and $$\sigma_{\gamma\gamma \to \text{hadr}} = (380 + 520/W_{\gamma\gamma})\text{nb}$$

Figure 49 shows the result of the total cross section measurements of the TASSO-group.

The above expression for $\sigma_{\gamma\gamma \to \text{hadrons}}$ corresponds to the central line in the figure. An overall systematic error of ~ 25% has to be taken into account.

The cross section for $W_{\gamma\gamma} \geq 3$ GeV are, as far as the shape is concerned in agreement with the VDM prediction, the absolute scale disagrees with the measurements. This effect, however, can only be resolved if the systematic errors become less than the 25% at present.

The PLUTO results[71] are shown in Figure 50. Figure 50a) and b) show the Q^2 behaviour for two visible invariant mass bins W_{vis}. The solid lines in these graphs are the prediction from a ρ meson dominance model calculation.

To extract the total cross section an additional term is introduced in expression(17) and the ansatz for the fit to the data is:

$$\sigma_{tot}(W_{\gamma\gamma}) = A\sigma^{VDM}(W_{\gamma\gamma}) + B/W_{\gamma\gamma}^2 \qquad (18)$$

where

$$\sigma^{VDM}(W_{\gamma\gamma}) = (240 + 270/W_{\gamma\gamma})\text{nb}$$

The best fit to the invariant mass distribution is achieved for $A = 0.97 \pm 0.16$ and $B = 2250 \pm 500\text{nbGeV}^2$. The result is shown in Fig. 50c. The dramatic rise at low $W_{\gamma\gamma}$ can only be described

by the fit if a $B/W_{\gamma\gamma}^2$ term is introduced. This term is expected if there are contributions of quark-antiquark production in the two-photon exchange channel.

The discrepancy between the results at low $W_{\gamma\gamma}$ between the PLUTO and TASSO groups is unresolved at the moment. The PLUTO group notes in reference (71) that one should take into account the following:

(1) The triggering efficiency of an hadronic event is about 25%, quite in contrast to the events from single photon annihilation, where the efficiency is 80 to 90%.

(2) Due to the limited solid angle in the central regions the visible invariant mass is always smaller than $W_{\gamma\gamma}$ due to losses of particles. The correction $W_{vis} \rightarrow W_{\gamma\gamma}$ is done in both cases by unfolding procudures.

(3) There are two major differences in the analysis of the two experiments, a) PLUTO uses single tagged events only but TASSO includes the double tagged events, and b) TASSO uses the charged particles only but PLUTO includes the neutrals, leading to a smaller correction $W_{vis} \rightarrow W_{\gamma\gamma}$.

Preliminary results were reported on hard scattering processes and deep inelastic $e\gamma$ scattering, they can be found in references (63) and (64).

FIGURE CAPTIONS

Fig. 40 Schematic view of a two-photon annihilation event $e^+e^- \rightarrow e^+e^- +$ hadrons.

Fig. 41 Feynman diagrams for pair production via the two-photon exchange process (a) and the bremsstrahlungsprocess (b) ($\ell^- = e^-, \mu^-$).

Fig. 42 The distribution of the $\mu^+\mu^-$ effective mass from the events $e^+e^- \rightarrow e^+e^-\mu^+\mu^-$ as measured by the JADE detector. The solid line is the QED prediction.

Fig. 43 The observed cross section of $e^+e^- \to e^+e^-\mu^+\mu^-$ in the MARK-J detector as functions of $\sqrt{s}$ when the observed particles are: (a) two μ's, (b) one μ and one e, (c) two μ's and one e. The solid lines are Monte Carlo calculations of the yield from two-photon diagrams and the points are the measurement.

Fig. 44 The effective mass spectrum of the two opposite charged particles from the reaction $e^+e^- \to e^+e^-$ + 2 charged particles at $\sqrt{s}$ = 31 GeV for events where the outgoing e^+ and e^- go undetected. The solid curve is the expectation for the QED processes $e^+e^- \to e^+e^-e^+e^-$ and $e^+e^- \to e^+e^-\mu^+\mu^-$. The insert shows the difference between the measured histograms and the solid curve.

Fig. 45 The f^o signal of the TASSO collaboration together with the fit of the model[67].

Fig. 46 Data and predictions for the radiative width $\Gamma(f^o \to \gamma\gamma)$.

Fig. 47 Mass distributions of $\pi^+\pi^-$ pairs for events with $1.5 \leq W_{\gamma\gamma} \leq 2.0$ GeV. (a) Two-dimensional mass distribution of a $\pi^+\pi^-$ combination versus the opposite one, and (b) distribution of the $\pi^+\pi^-$. The curves are the result of a fit[70].

Fig. 48 Cross section for the reaction $\gamma\gamma \to \rho^o\rho^o$. The curve is the prediction of the VDM model[70].

Fig. 49 The hadronic cross section for scattering of two real photons vs. the c.m. energy of the two-photon system as obtained from the fit to the data under the assumption stated in the text. The hatched area indicates the range of the statistical error.

Fig. 50 The total cross section $\sigma_t + \varepsilon\sigma$, as function of Q^2 for $W_{vis} \leq 3.5$ GeV (a) and for $W_{vis} \geq 3.5$ GeV (b). The solid line is the prediction from ρ meson dominance. (c) The total photon-photon cross section extrapolated to $Q^2 = 0$ versus the true invariant mass W. The hatched band represents the 1σ limits as obtained from the fit. The VDM prediction is given by the dashed line.

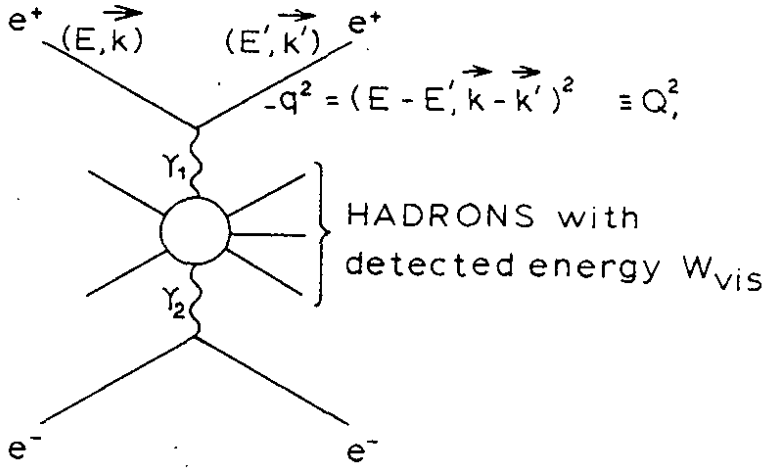
e+
(E, k)
(E', k')
e+
-q² = (E - E', k - k')² ≡ Q²
γ1
HADRONS with
detected energy Wvis
γ2
e-
e-

Fig. 40

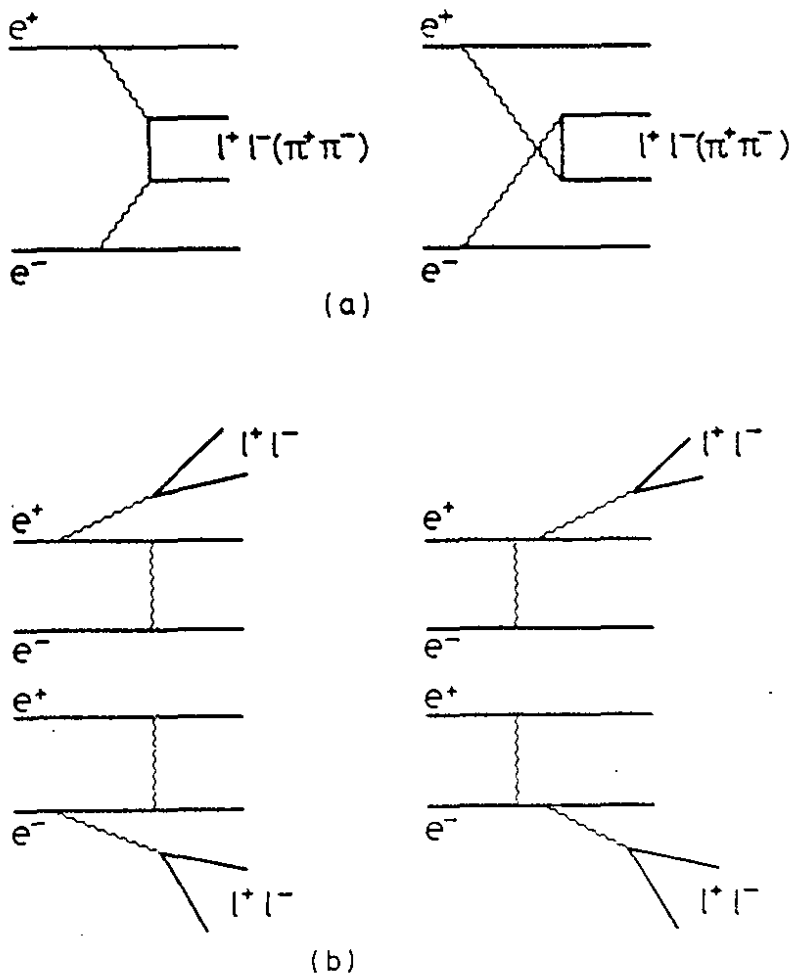
e+
l+ l-(π+ π-)
e-
e+
l+ l-(π+ π-)
e-
(a)
l+ l-
e+
e-
e+
e-
l+ l-
l+ l-
e+
e-
e+
e-
l+ l-
(b)

Fig. 41

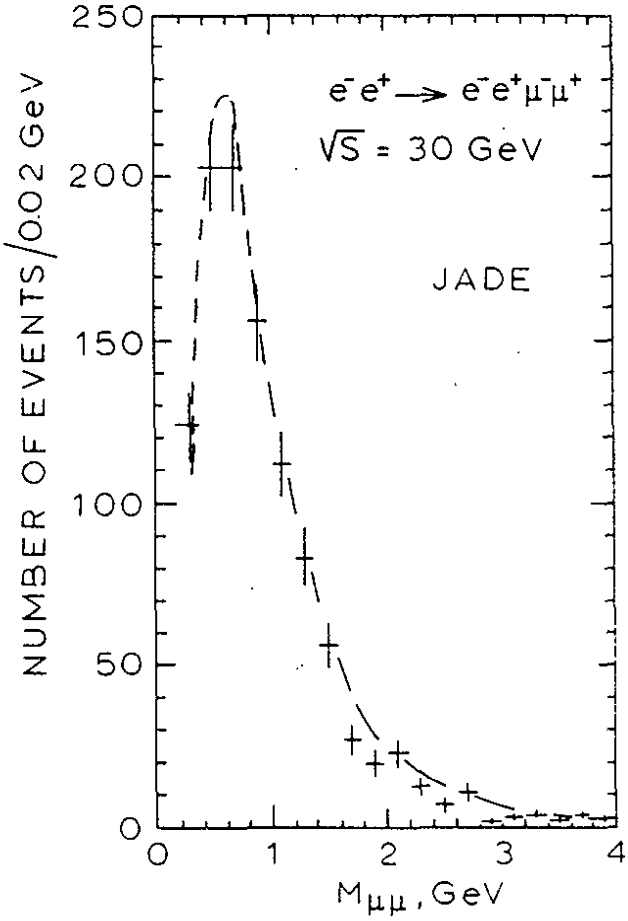

Fig. 42

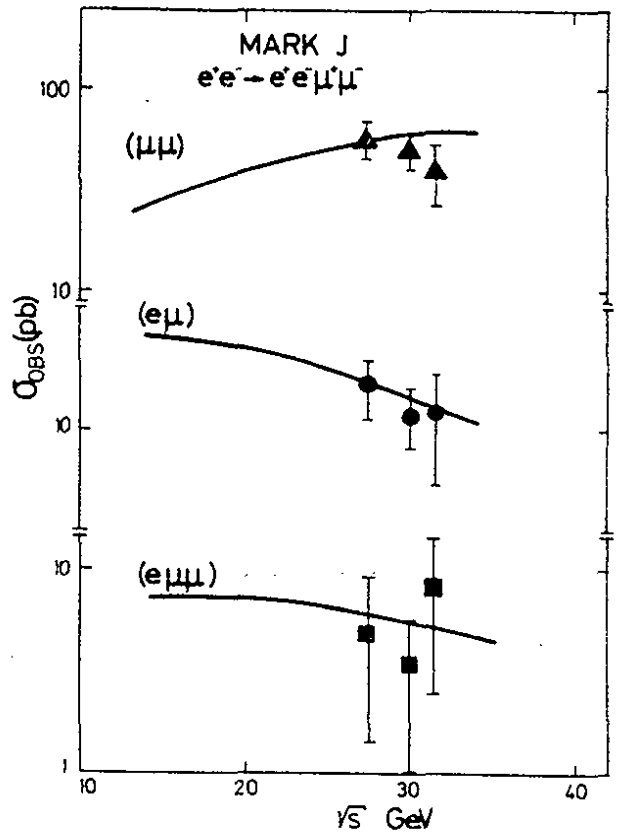

Fig. 43

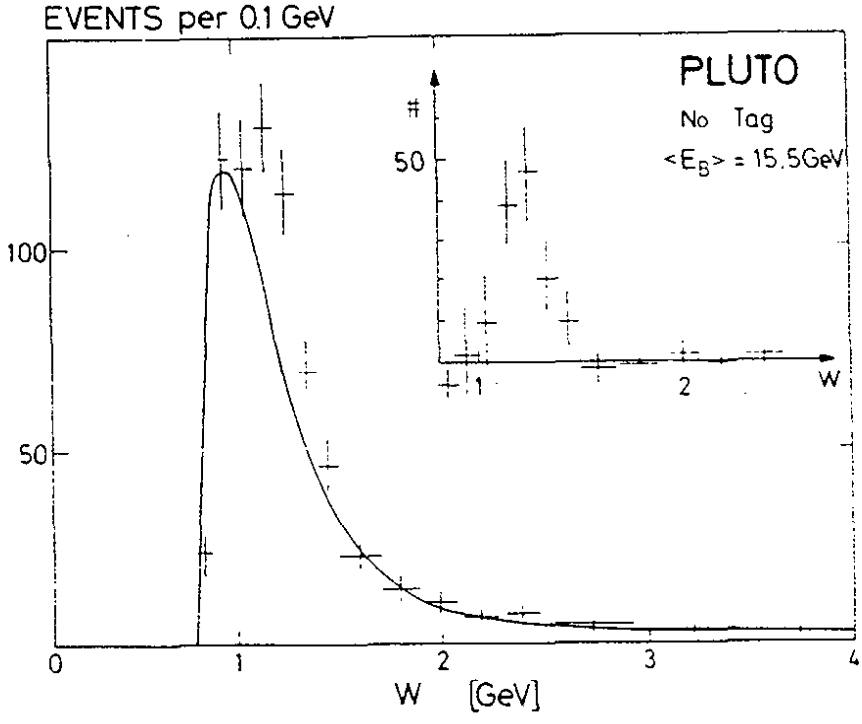

Fig. 44

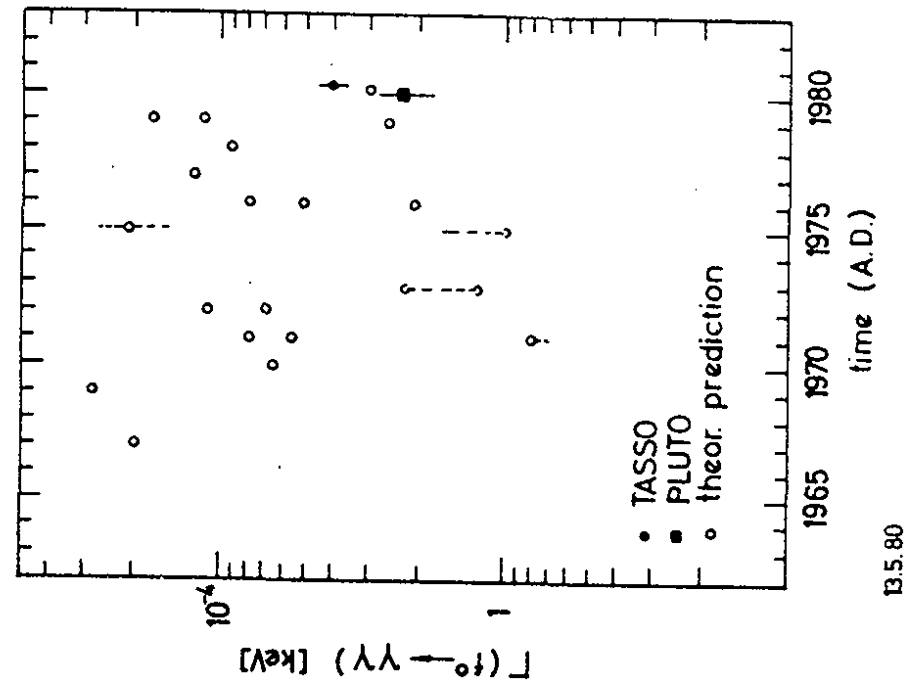
Γ (π⁰ → γγ) [keV]
10⁻⁴
1
1965
1970
1975
1980
time (A.D.)
TASSO
PLUTO
theor. prediction
13.5.80

Fig. 46

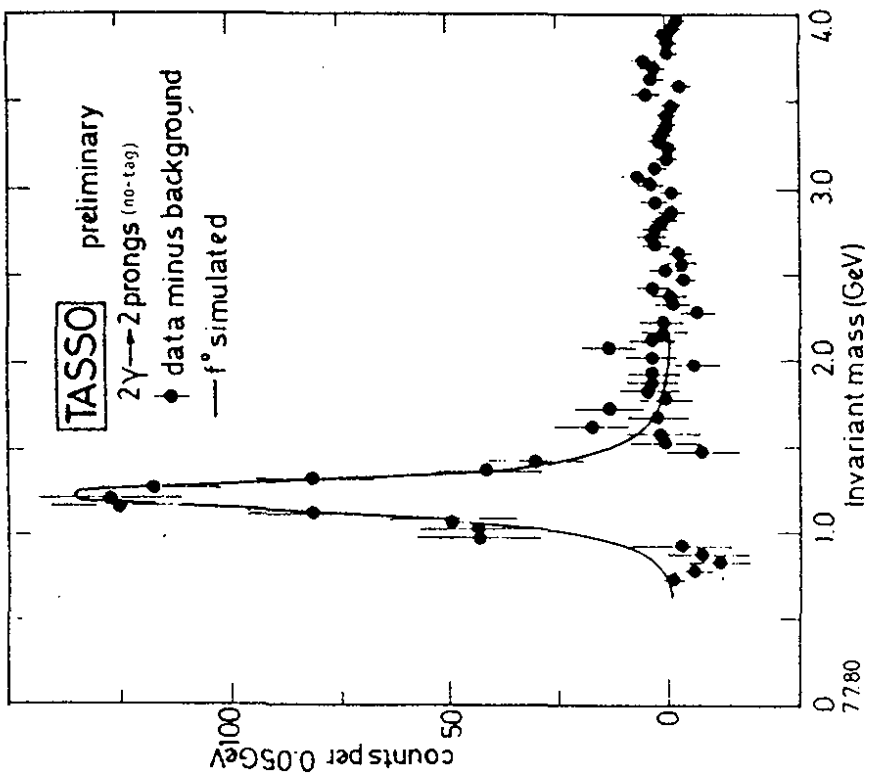
TASSO
preliminary
2γ → 2 prongs (no-tag)
data minus background
f° simulated
counts per 0.05GeV
100
50
0
0
7.80
1.0
2.0
3.0
4.0
Invariant mass (GeV)

Fig. 45

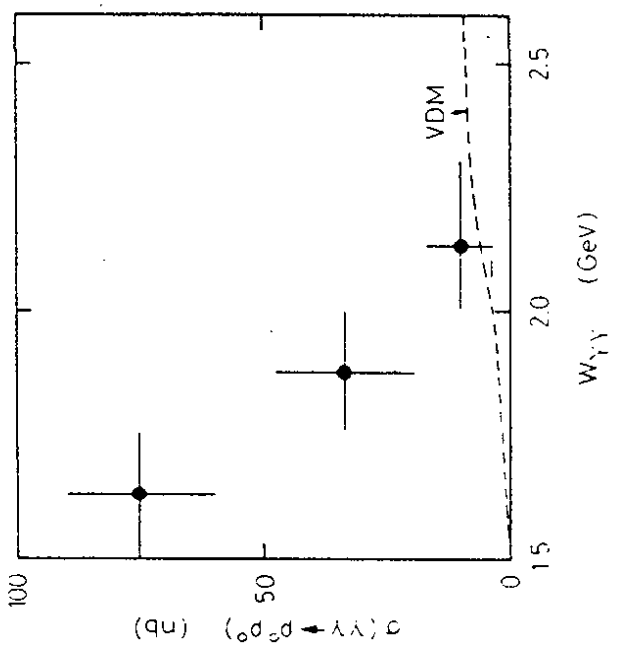
σ(γγ → ρ⁰ρ⁰) (nb)
100
50
0
1.5
2.0
2.5
VDM
$W_{\gamma\gamma}$ (GeV)

Fig. 48

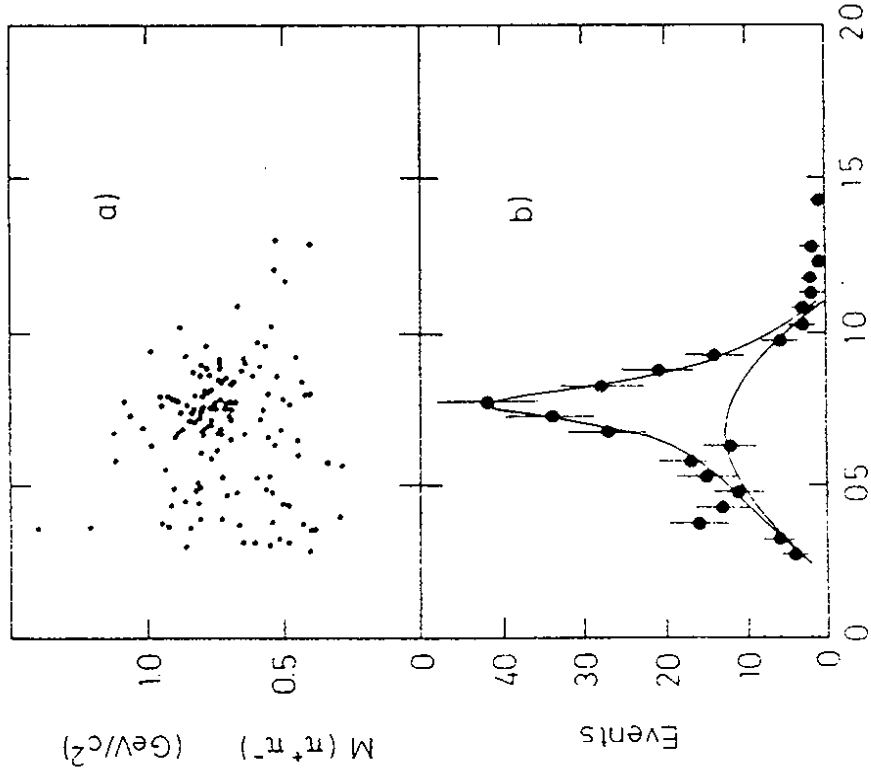
a)
b)
M (π⁺π⁻) (GeV/c²)
Events
0
0.5
1.0
10
20
30
40
0
5
10
15
20
M(π⁺π⁻) (GeV/c²)

Fig. 47

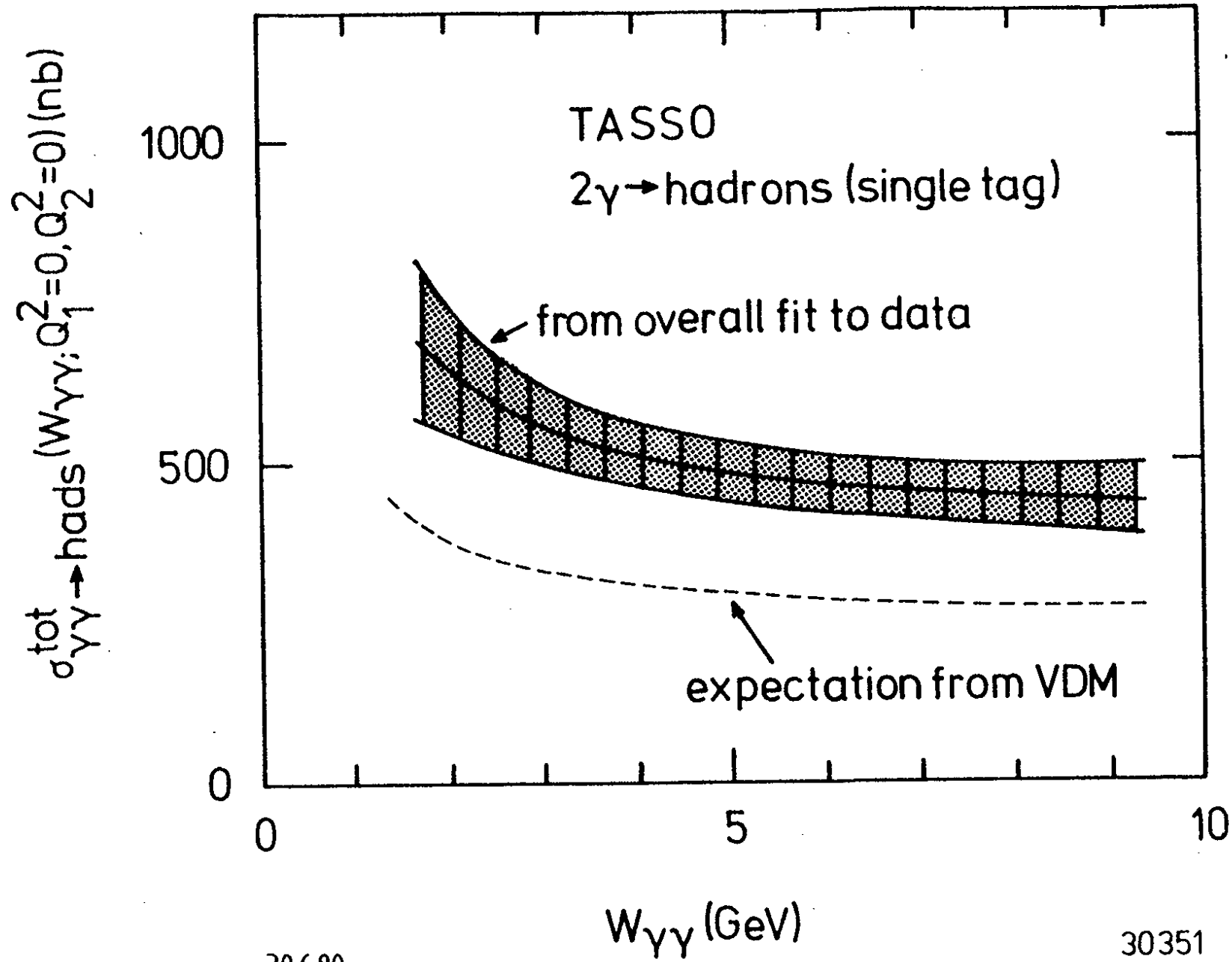
TASSO
2γ→hadrons (single tag)
from overall fit to data
expectation from VDM
$\sigma^{tot}_{\gamma\gamma\to hads}(W_{\gamma\gamma};Q_1^2=0,Q_2^2=0)$(nb)
1000
500
0
0
5
10
$W_{\gamma\gamma}$ (GeV)
30.6.80
30351

Fig. 49

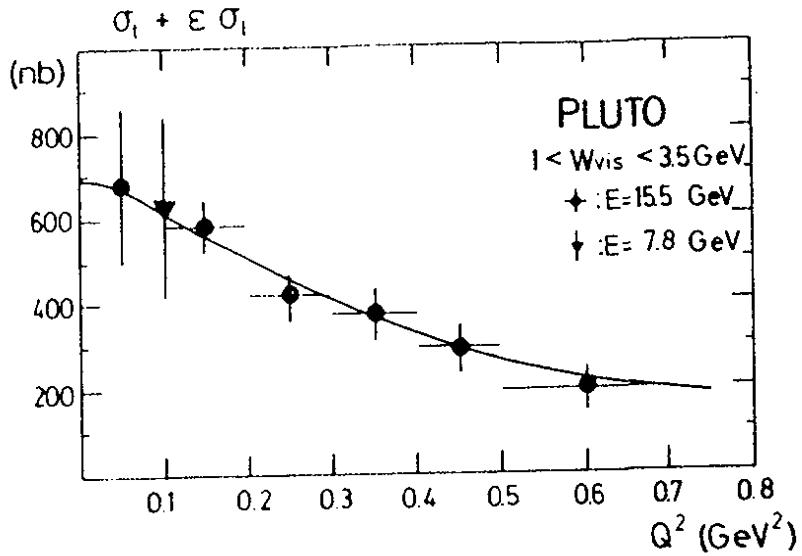
$\sigma_t + \varepsilon \sigma_l$
(nb)
PLUTO
1 < Wvis < 3.5 GeV
: E=15.5 GeV
: E= 7.8 GeV
800
600
400
200
0.1
0.2
0.3
0.4
0.5
0.6
0.7
0.8
Q^2 (GeV^2)

a)

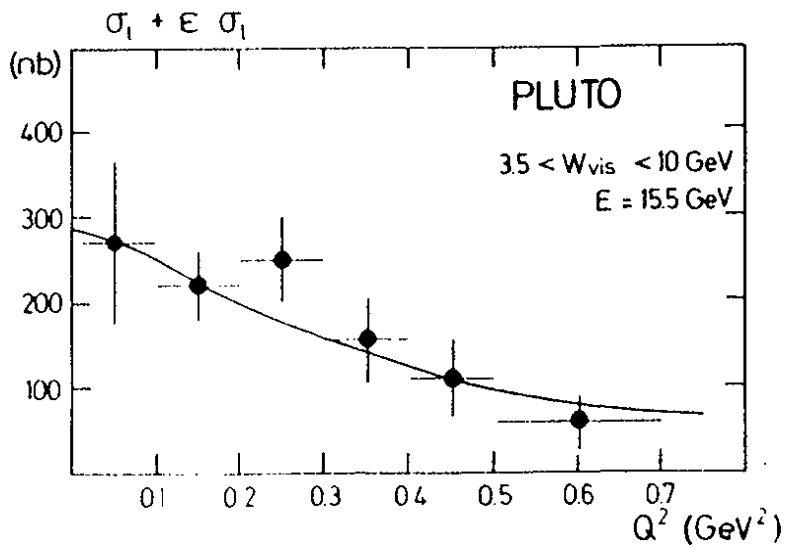
$\sigma_t + \varepsilon \sigma_l$
(nb)
PLUTO
3.5 < Wvis < 10 GeV
E = 15.5 GeV
400
300
200
100
0.1
0.2
0.3
0.4
0.5
0.6
0.7
Q^2 (GeV^2)

b)

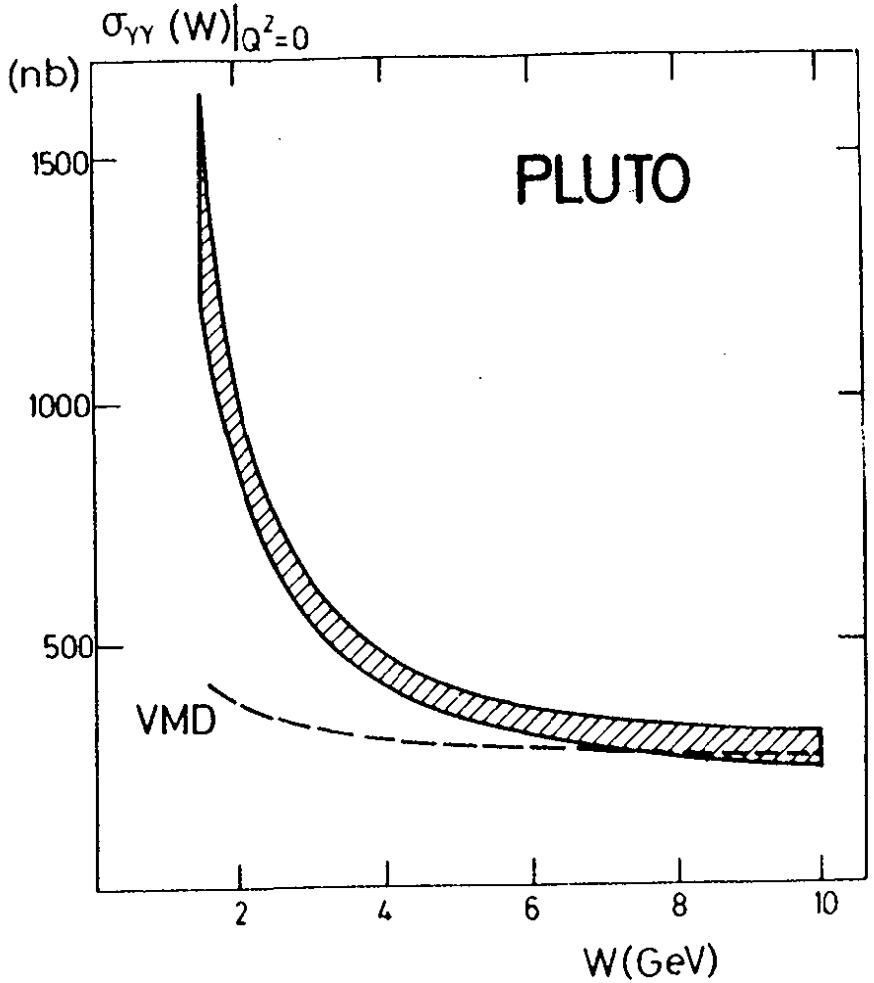
$\sigma_{\gamma\gamma}$ (W)$|_{Q^2=0}$
(nb)
PLUTO
1500
1000
500
VMD
2
4
6
8
10
W(GeV)

c)

Fig. 50

6. GENERAL CHARACTERISTICS OF HADRON EVENTS

6.1 Hadron Identification

The final selection of the hadronic events from the single photon annihilation process

$$e^+e^- \rightarrow \text{hadrons}$$

is made by scanning the events on an interactive graphics display system after a preselection which includes cuts in the charged multiplicity, visible energy and momentum balance cuts. Beam gas events not coming from the interaction region are recognized by reconstructing the event vertex[74].

The energy spectrum measured with the MARK-J detector at $\sqrt{s}$ = 30 GeV is shown in Figure 51. The energy cut employed by this group for the analysis of hadronic final states used for the determination of the total hadronic cross section, most of the thrust (section 6.3) analysis and the study of inclusive muons in hadron events (section 6.4) is $E_{vis} \geq 0.5\sqrt{s}$. For reasons discussed in section 7.3 an even more restrictive cut is used by the MARK-J group of $E_{vis} \geq 0.7\sqrt{s}$ for 3jet events and the determination of the strong coupling constant α_s. Both of these cuts are indicated by arrows in Figure 51.

6.2 Total Hadronic Cross Section [74, 75, 76, 77]

The total cross section for $e^+e^- \rightarrow$ hadrons was measured over a wide range of center of mass energies from 12 to 36.6 GeV, including results obtained by extended periods of running at a fixed beam energy and by fine energy scans covering the ranges of 29.92 to 31.46 GeV and 33.00 to 35.56 GeV. The results are expressed in terms of R:

$$R = \sigma(e^+e^- \rightarrow \text{hadrons}) / \sigma(e^+e^- \rightarrow \mu^+\mu^-)$$

In the naive quark-parton model, the cross section for the

hadron production process is simply given by the sum over flavours of the point-like $q\bar{q}$ pair cross sections. Using this picture with spin 1/2 massless quarks, and with three colours gives

$$R_o = 3\Sigma\, e_q^2 \qquad (19)$$

where e_q is the charge of the quark with flavour q. Considering the five known quarks (u,d,s,c, and b), and correcting the naive model for gluon emission as predicted by QCD, one expects $R \tilde{\sim} 4$, over the entire PETRA energy range, with only a slight decrease in R with increasing beam energy.

The experimental R-values have to be corrected for initial-state radiative corrections, for contamination of the sample by hadronic events produced by the two-photon process $e^+e^- \rightarrow e^+e^-$ + hadrons, and for the contribution of $e^+e^- \rightarrow \tau^+\tau^- \rightarrow$ hadrons + leptons. In addition to the statistical errors, there is an additional systematic uncertainty due to the model dependence of the acceptance calculations of 10% for the four groups. The measurements of $R^{(74)}$, from the four groups are averaged and plotted in Figure 52. Including the region below $\sqrt{s}$ = 20 GeV one sees that there is a large range up to 36 GeV where the R-values vary only very little. The error weighted average of the combined data above $\sqrt{s}$ = 20 GeV yields a value R = 4.03 ± 0.06. The two solid lines in the figure are the predictions of QCD with the five known quark flavours for two different values of α_s, the running coupling constant of the strong interaction related to Λ, a free parameter in QCD, in the following way:

$$\alpha_s = \frac{12\pi}{\{\,(33 - 2N_f)\ln q^2/\Lambda^2\,\}}$$

where N_f is the number of quark flavours and q^2 is put equal to s, the square of the C.M. energy. The prediction of R by QCD to first order is than:

$$R = R_o\,(1 + \alpha_s/\pi)$$

where R_o is defined in expression (19). The error in the average value of $R = 4.03 \pm 0.06$ is not small enough to measure Λ or α_s with any precision, the value varies only 2.6% between the limits of Λ of 0.2 to 1.0 GeV. The combined data of course also excludes the production of a new quark with charge 2/3, however, a 1/3 charged quark cannot be excluded by these measurements. The ΔR in the latter case would only be 0.26 and the systematic errors do not allow to draw a negative conclusion.

In addition to the $t\bar{t}$ contribution to the hadronic continuum, the toponium system should form one or more bound states, with the number of such states depending on the shape of the binding potential[77]. Interpretation of the vector mesons ρ, ω, ϕ, J, ψ', Υ, Υ', and Υ'', as non-relativistic $q\bar{q}$ bound states, or"quarkonia" leads to the prediction that the gap between the lowest bound state and the continuum is probably ~ 1 GeV, and very likely $\leq$ 2 GeV.

In order to check for the existence of $t\bar{t}$ bound states lying below 36.6 GeV, the energy scans mentioned earlier were performed in 20 MeV center of mass energy steps (matching the r.m.s. energy spread of PETRA), with an average of ~ 25 nb^{-1} to 50 nb^{-1} per point and per experiment. The combined results of the scans are shown in Figure 53. The figure shows that the data are entirely consistent with the predictions of QCD for u,d,s,c, and b quarks, that is, with constant values of R over the regions of the scans. There is no indication of an upward slope with increasing energy signaling the onset of a new contribution to the continuum. The value of R averaged over the energy ranges of the scans of 3.96 ± 0.28 and 4.17 ± 0.44 respectively.

In order to set a quantitative upper bound on the possible production of a narrow resonance, the data in Figure 53 were fitted by a constant plus a gaussian. Using the relation between the resonance strength, the width into e^+e^- (Γ_{ee}), the hadronic width (Γ_h), the total width (Γ) and the hadronic branching ratio ($B_h \equiv \Gamma_h/\Gamma$) one obtains as an upper limit for

$$B_h \Gamma_{ee} \leq 0.6 \text{ KeV (90\% C.L.)}$$

This upper limit excludes the production of a vector particle consisting of a $q\bar{q}$ bound state where the quark has charge 2/3. This fact is also illustrated by the Gaussian curve drawn in Fig. 53b, where the curve is the expectation for the production of a $t\bar{t}$ bound state. On the basis of the experimental fact that Γ_{ee}/e_q^2 is approximately constant for the vector meson ground states ρ, ω, ϕ, J, and Υ, as is predicted by duality arguments[77], one expects $\Gamma_{ee} \tilde{>} 5$ KeV for the lowest mass meson in the toponium family. Effects due to radiative corrections and the energy spread of the machine which influence the shape of the cross section have been taken into account in this analysis.

6.3 Jet Analysis

6.3.1. Thrust and Sphericity Distributions

Data at lower energies from SPEAR[78] have shown that the final state hadrons from the process $e^+e^- \rightarrow$ hadrons are predominantly collimated into two back-to-back "jets" in agreement with the expectations of simple models in which the time-like photon materializes inititally into a quark-antiquark pair. It is thus necessary to develop kinematic quantities which describe the jet-like nature of the hadronic events.

A jet analysis has been devised using the spatial distribution of the measured momenta of charged and neutral particles for the track detectors and the distribution of the deposited energy in the case of a calorimetric detector. A schematic view of a two jet event is drawn in Figure 54. The vectors drawn stand for either the measured momenta p_i of individual particles or the vector energy flow E_i for one or more particles emitted closely together. The aim of the jet analysis is to determine the jet-axis and the related quantities like momentum p_T or transverse energy flow E_T and the longitudinal momentum $p_{//}$ or longitudinal energy flow $E_{//}$.

Other parameters describing the general shape of the individual events are the sphericity (S) and thrust (T) defined[79] as:

$$S = 3/2 \min \Sigma p_T^{i\,2} / \Sigma p^{i\,2}$$

where p_T^i is the transverse component of p^i along a given axis and the minimum is found by varying the direction of this axis. The resultant direction is thus the direction along which the p_T^2 is minimized. The parameter thrust (T) is defined[80] as

$$T = \max \left(\Sigma p_{//}^{\,i} / \Sigma |p^i| \right)$$

for the track detectors and

$$T = \max \left(\Sigma E_{//}^{\,i} / \Sigma |E^i| \right)$$

for the MARK-J detector[81]. The resultant direction found in this case is the direction along which the sum of the longitudinal momenta or projected energy flow is maximized. Both quantities S and T simultaneously define the jet axis and it has been found that by applying these two methods to the same event sample the axis coincides within a few degrees for both methods.

The $\cos\theta$ distribution of the MARK-J data shown in Fig. 55, where θ is the angle between the beam and jet axis, is compared with the expectation from QCD. The agreement with the essentially $1 + \cos^2\theta$ distribution multiplied by the angular acceptance of the detector is very good, supporting the idea of the underlying e^+e^- annihilation process proceeds via the production of two spin 1/2 particles, the quark and antiquark. Spin 0 particles would give a $\sin^2\theta$ distribution, which is clearly excluded by the data.

The mean longitudinal $\langle p_{//} \rangle$ and transverse momentum $\langle p_T \rangle$ of charged particles with respect to the thrust axis (measured by the PLUTO and TASSO detectors[81] is shown in Figure 56 as function of the c.m. energy. Both the increase of $\langle p_{//} \rangle$ and the constancy of

$\langle p_T \rangle$ indicate that the jet structure is getting more and more pronounced, most of the particles are emitted in narrower back to back cones as expected in the naive quark model. The behaviour of $\langle p_T^2 \rangle$, a higher moment of the p_T distribution is, however, in disagreement with the expectations of this model. The $\langle p_T^2 \rangle$ rises with increasing energy by almost a factor two over the energy range while the quark model predicts a constant energy dependence.

For events in which the spatial momentum or energy distribution is isotropic, S and T are expected to approach 1 and 0.5 respectively. This would be the situation if, for example, the virtual photon matererializes into two very heavy quarks, each with a mass close to the beam energy. Such quarks would be produced almost at rest. On the other hand, pairs of light quarks would move at high speed and the Lorenz boost of their hadronic fragmentation products would result in the hadrons being produced in narrow jets collimated around the initial quark directions. Higher beam energies would result in narrower jets, so that S and T should approach the value 0 and 1 respectively. Thus, sphericity and thrust measurements can be used as sensitive methods to detect the presence of a new threshold due to new heavy quarks. Production of a new heavy quark would also result in raising respectively lowering the average S respectively T as the energy is raised and the threshold is passed.

The normalized thrust distributions of the MARK-J group $1/N\ (dN/dT)$ for 13, 17, 22, and the combination of 27.4 and 27.7 GeV data (labelled 27 GeV combined) are shown in Figures 57a-d) along with the Monte Carlo predictions of a quark-parton model with u,d,s,c, and b quarks and no gluon emission[82].

As expected for production of final states with two jets of particles, the distributions become narrower and shift towards high thrust with increasing energy.

Figure 58 shows the normalized thrust distributions (MARK-J) for combined data $27 \leq \sqrt{s} \leq 33$ GeV and $33 \leq \sqrt{s} \leq 37$ GeV. The

curves show the Monte Carlo predictions with inclusion of gluons and also calculations which include charge 2/3 and 1/3 quarks produced as described previously. The QCD model without top quark describe the data very well. One can also conclude that there is no evidence for production of a new heavy quark with charge $q = 2/3$ e.

Figure 59 shows the average thrust <T> plotted at nine PETRA energies. The solid curves are from Monte Carlo calculations which include u,d,s,c, and b quarks with gluon emission. The energy dependence of the data is smooth and shows none of the steps which would have appeared at new quark thresholds. The sphericity measurements of the TASSO Collaboration in the energy range $\sqrt{s}$ = 13-31.2 GeV are shown in Figure 60. A top quark contribution (dashed-dotted curve in the figure) is clearly ruled out and the data are well described by thw quark model with u,d,s,c, and b quarks plus gluon corrections. The average sphericity <S> measured at DORIS and PETRA by PLUTO and at PETRA by the JADE and TASSO groups is shown in Figure 61 as function of $\sqrt{s}$. The quantity S is related with the jet cone half opening angle δ by $S \simeq 3/2 \langle\delta^2\rangle$. The solid line is the expectation from the naive model with five quarks. The dotted curve shows the expected threshold behaviour after the appearance of the $t\bar{t}$ continuum and the data clearly once again rules out their production.

At the highest PETRA energies the combined thrust distributions of the JADE, MARK-J and TASSO groups give evidence against the existence of a t-quark with mass of 17.5 GeV and charge 2/3 of 12σ at $\sqrt{s}$ = 35-35.8 GeV and 5σ at $\sqrt{s}$=36.5 GeV for the events with thrust ≤ 0.8. The existence of a quark with charge 1/3 is unlikely at the highest energy but cannot be excluded with absolute certainty[76].

6.3.2. Inclusive Muons in Hadronic Events

In the framework of the six quark model for the weak decays of heavy quarks, (c,b and t) copious muon production is expected from the cascade decays $t \to b \to c$[18],[19]. The onset of the production of a new heavy lepton would also lead to an increase in muon production. Thus, in addition to indications based on thrust and R measurements, a measurement of inclusive muon production in hadronic final states should provide a clear indication of the formation of top quarks or new leptons. All the hadron data for $\sqrt{s}$ from 12 to 36.5 GeV have therefore been analyzed and scanned in a search for muons.

The main sources of muons in the hadron sample are decay products of bottom and charm quarks. Background contributions to the muon signal, arising from hadron punch through and decays in flight of pions and kaons have been calculated using the Monte Carlo simulation to be ~ 2% at these energies. The contribution of $\tau^+\tau^-$ events to the μ + hadron sample becomes negligible when the total energy cuts and energy balance cuts are applied. Figure 62 summarizes the results from the JADE, MARK-J and PLUTO groups for the relative production rate of hadronic events containing muons as a function of the c.m. energy[76]. The figure demonstrates once again the absence of new heavy mesons containing t-quarks up to 36.5 GeV. The observed rate agrees with the Monte Carlo predictions for five quark flavours but is approximately 5 standard deviations away from the prediction which includes the top quark. Figure 63 shows the thrust distribution of the hadronic events containing muons compared with all the hadronic events from the MARK-J group. The scarcity of events at low thrust in the figure also rules out the existence of the top quark. The agreement between the data and the Monte Carlo containing five quarks is good.

6.3.3 Searches for New Particles

(i) Heavy Leptons[76],[83]

Following the initial searches[27] for the τ-lepton, the discovery[28] and the further study of its properties[29],[30], there has been great interest in searching for a new heavy lepton, which would extend the series e, μ, τ. Analogous to the τ-lepton one assumes that a new heavy lepton HL couples universally to leptons and quarks according to the standard V-A weak interaction theory and has the following decay modes: (in %), $\tau^- \bar{\nu}_\tau \nu_{HL}$ (9.2), $\mu^- \bar{\nu}_\mu \nu_{HL}$ (10.6), $e^- \bar{\nu}_e \nu_{HL}$ (10.6) and hadrons + ν_{HL} (69.6). The branching ratios[84], which are mass dependent, are given here for a heavy lepton mass of 14 GeV. Owing to their large mass and low velocity, the decay products would be expected to have large angles with respect to the HL line of flight. This contrasts to the decay products of the τ at PETRA energies which are tightly collimated.

Heavy lepton production is recognized in the MARK-J detector for events in which one lepton decays into a muon and neutrinos and the other lepton decays into hadrons and neutrinos. Hadrons are detected by their energy deposit, E_{vis}, in the calorimeter[83].

Heavy lepton candidates with masses greater than 6 GeV are selected by applying the following criteria:

1) $0.2\ E_{beam} < E_{vis} < E_{beam}$,

2) Acoplanarity $> 30^\circ$,

3) $E_K > 0.1\ E_{vis}$,

4) Charged multiplicity of events > 2,

5) $30^\circ < \theta_H < 150^\circ$.

The "acoplanarity" is defined as the absolute value of $|180^\circ - \delta\phi|$, where $\delta\phi$ is the angle between the muon momentum vector and the total energy flow of the hadrons E_H projected on a plane perpendicular to the beamline. E_K is the energy deposited in the iron plate which form the outer part of the calorimeter and θ_H is

the polar angle between E_H and the beamline. Cut 1 reduces the background from $e^+e^- \to$ hadron, cut 2 suppresses the contribution from $e^+e^- \to \tau^+\tau^-$, and cut 3 helps to select hadronic as opposed to electromagnetic showers. Cuts 1-5 are also effective in eliminating background from the "2-photon" process, $e^+e^- \to e^+e^- \mu^+\mu^-$, and from $e^+e^- \to \mu^+\mu^-\gamma$ where a high energy photon is radiated at large angles.

No event was observed in the data with $33 \lhd \sqrt{s} < 36.7$ GeV, corresponding to a time integrated luminosity of 6.9 pb^{-1}. The number of events predicted by a Monte Carlo calculation as a function of the heavy lepton mass M_{HL} is shown in Figure 64 along with the 95% confidence level upper limit from the data. Figure 64 demonstrates that the existence of a sequential heavy lepton with a mass between 6 and 16 GeV is excluded.

Heavy leptons with $M_{HL} < 6$ GeV would decay into final states similar in appearance to those from τ decay, and would tend to be included in the sample of $e^+e^- \to \tau^+\tau^-$ events. The inset in Fig.64 shows the Monte Carlo prediction for the total number of events in the τ sample from $e^+e^- \to \tau^+\tau^-$ [52] and from heavy lepton production, as a function of M_{HL}. The inset demonstrates that the predicted number of heavy lepton events exceeds by more than 2σ the number of observed τ events. Therefore, with more than 95% confidence they exclude the existence of the heavy lepton with mass $M_{HL} < 6$ GeV. One is thus able to rule out the existence of a new heavy lepton for a $M_{HL} <$ 16 GeV.

The criteria employed by the PLUTO group for finding heavy leptons is very similar to the ones mentioned above and they find a limit for M_{HL} of 14.5 GeV. The TASSO group searches for a single charged particle recoiling against many hadrons and obtains as a limit $M_{HL} < 15.5$ GeV. The JADE group concentrates on the possible hadronic decays of the heavy leptons. They calculate the thrust of the two hadron jets and demand that the jets are very acoplanar, excluding by such criteria the events produced by quark-antiquark

pairs which give rise to two back-to-back jets. They expect for a 17 GeV heavy lepton ~ 10 events, and they find none[76].

(ii) Scalar Electrons and Muons

In the framework of supersymmetric theories[85], spin zero partners of the electron and the muon are expected to decay only according to the reactions

$$s^- \rightarrow e^- (\mu^-) + \text{photino (goldstino)} \qquad (20)$$

$$t^- \rightarrow e^- (\mu^-) + \text{antiphotino (antigoldstino)} \qquad (21)$$

where s and t are the spin zero partners of the electron (muon) associated with the left and right handed parts of the electron (muon) field respectively, and the photino and goldstino are the spin 1/2 partners of the photon and the goldstone boson. Since s and t carry unit electric charge they may be produced in pairs in e^+e^- annihilation according to the cross section:

$$\frac{d(e^+e^- \rightarrow s^-s^+ \text{ or } t^-t^+)}{d(\cos\theta)} = \frac{\pi\alpha^2\beta^3\sin^2\theta}{4s} \; ; \; \beta = \{ 1 - (\frac{m}{E})^2 \}^{1/2}$$

which is characteristic of spin zero particle production. m is the mass of s or t, E is the beam energy, and θ is the scattering angle.

Because of the uniqueness of the decay reactions (20) and (21), the extremely short lifetime of s and t and the prediction that the interaction cross section of photino and goldstino are expected to be very small[85], only electron and muon pairs are observed in the final state. Near threshold production of s and t, the two residual electrons or muons would be produced isotropically in space. Data from SPEAR place a lower limit of 3.5 GeV[86] on the mass of s and t. Thus, over the PETRA energy range of 12 and 36.7 GeV an increase in the production of acoplanar electron-positron or muon pairs should be observed if a new threshold is passed.

The event selection criteria used by the PLUTO and JADE

groups[76] to obtain an upper limit for the production of these particles are based on the considerations mentioned above. The electron-positron pair must have an energy greater than 20% (30%) and the acoplanarity angle must be greater than 15° (10°) for the PLUTO (JADE) group. No events are observed and the 95% confidence upper limit is found at 13 and 16 GeV by the PLUTO and JADE groups respectively.

A set of criteria for selection of muon pairs from reactions (20) and (21) has been established by the MARK-J[83] group which eliminates events from the processes:

$$e^+e^- \rightarrow \mu^+\mu^-, \quad \mu^+\mu^-\gamma$$

$$e^+e^- \rightarrow \tau^+\tau^-, \quad \tau^+\tau^-\gamma$$

$$e^+e^- \rightarrow e^+e^-\mu^+\mu^-$$

which are the main sources of background. To reject this background they select events with the following criteria:

1) acoplanarity $\geq 20^{\circ}$,

2) electromagnetic energy $\leq 20\%\ E_{Beam}$,

3) muon momenta $\geq 20\%\ E_{Beam}$.

No event was observed in the energy range 33 GeV $\leq \sqrt{s} \leq$ 36.7 GeV.

Figure 65 shows the expected number of events predicted by a Monte Carlo calculation for the production of s or t pairs. Also indicated are the number of events corresponding to the 95% confidence level.

Thus, the MARK-J data show that no s or t type particle is produced with a mass between 3 GeV and 15 GeV. If s and t particles have the same mass and are both produced, the number of expected events is twice as large. In this case they can both be excluded with more than 99% confidence.

iii) Searches for Free Quarks and Heavy Long Living Particles[87]

The JADE group, using their jet chamber[34], a cylindrical drift chamber filled with an argon, methane, isobuthane mixture at a pressure of 4 atm., is able to identify particles by a simultaneous measurement of the mean energy loss dE/dX and the apparent momentum p/Q. Two cases are studied: 1) the exclusive production of quark-antiquark pairs, giving rise to two nearly collinerar tracks and 2) the inclusive production of quarks, in which case a quark within a hadron jet is searched for.

In case 1) the sample of events contains mainly Bhabha events and $\mu^+\mu^-$ pairs. The mean energy loss of the tracks is investigated for a candidate with charge q = 2/3. None of such tracks were found.

Case 2) is studied by plotting (Figure 66) the energy loss of positive and negative tracks of the multi-hadron events as a function of the apparent momentum p/Q. The 65 tracks which were found to be more than 2.5σ away from the known stable particles (solid lines in the figure) were examined in detail. They could be explained by deuterons and tritium produced by secondary interactions in the beam pipe, by overlapping tracks giving an apparent dE/dX of twice the minimum, and by statistical fluctuations. The conclusion of this search was also negative.

From the observation (Fig. 66) that no heavy long living meson of 5 GeV has been detected within the 80 cm of the jet chamber an upper limit for the life time of such a meson containing a b-quark can be derived. Assuming an exponential momentum distribution, an upper limit of $2 \cdot 10^{-9}$ sec has been obtained which is a factor 25 less than the previous limit. This upper limit could even be improved[88] by searching for secondary decay vertices with more than 3 outgoing charged particles at least 5 cm away from the interaction point. Decays with protons, identified by the dE/dX measurements, and vertices in the beam pipe or other

layers of material were rejected. The 90% confidence limits on the life time with this method was found to be $\tau_B \leq 10^{-10}$ sec for an exponential momentum distribution and $\tau_B \leq 3.10^{-11}$ sec for a constant one.

6.4 Multiplicity Distributions, Inclusive Particle Spectra and Particle Yields

6.4.1. Multiplicity Distributions[75],[89]

At low energy the charged multiplicity distributions for the hadronic events produced in e^+e^- interactions have been measured at ADONE[90], SPEAR[91] and DORIS[92]. The mean charged multiplicity was found to behave in agreement with the Feynman scaling hypothesis[93] and increase logarithmically according to:

$$\langle n_{ch} \rangle = a + b \ln s \qquad (22)$$

in the energy range 1.4 GeV $\leq \sqrt{s} \leq$ 7 GeV.

The first evidence from the TASSO group[94] indicated that the quantity $\langle n_{ch} \rangle$ was rising much faster in the PETRA energy range than expression (22) could describe. An increase of ~ 4 charged particles more than the extrapolation of the low energy fit to the data with expression (22) could account for was observed. The drastic change could not be due to $b\bar{b}$ production above threshold, a change of only ~ 0.2 is expected from the additional production of these quarks.

The data for $\langle n_{ch} \rangle$ at the lower energies combined with the measurements of the JADE, PLUTO and TASSO[89] groups is shown in Figure 67. Included in the data points are the charged pions from K_s^o decay, a contribution of ~ 0.7 units in $\langle n_{ch} \rangle$. A possible explanation for the fast rise are the gluon effects which are observed at the highest PETRA energies (see section 7). In QCD the multiplicity is expected[95] to behave as

$$\langle n_{ch} \rangle = a + b \exp\left(c\sqrt{\ln s/\Lambda^2}\right)$$

A fit to all the data (solid line in the figure) with Λ=0.5 GeV yields: a = 2.38±0.09; b = 0.04±0.01; and c = 1.92±0.07. Due to relatively large error bars other simple functions like $a(\ln s)^2$ or an exponential as^b fit the trend of the data equally well[75]. The question which sort of particles, of low or intermediate momentum, cause the rise in average multiplicity will be answered in the next paragraph.

6.4.2 Single Particle Spectra and Particle Yields[89]

The TASSO Collaboration investigated the energy behaviour of the scaling cross section $s \cdot d\sigma/dx$ as function of the Feynman variable $x = p/p_{beam}$, where p is the momentum of the produced hadron. If scale invariance holds $s \cdot d\sigma/dx$ should be independent of the c.m. energy. The data measured at 12, 27.4 - 31.6 and 35.0 - 36.6 GeV by this group is shown in Figure 68. For $x \geq 0.2$ the data are the same within errors and agree with those measured at low energy by DASP[96] and SLAC - LBL[97] within 30%. However, at low x values a dramatic rise for increasing c.m. energy is seen. As the only energy dependent quantity in the integrated function $\int s \cdot d\sigma/dx$ is the quantity $\langle n_{ch} \rangle$, this rise is related to the one seen in the average multiplicity. This scale breaking when interpreted in terms of QCD can be explained by the emission of gluons, namely the primary momentum is now shared at low x values. This effect should become more pronounced as the energy becomes larger and at 30 GeV one expects[98] for x = 0.2 the data to be 10% higher than at 5 GeV. At x = 0.7 the data should be 20% lower compared with the low energy data. The data at present are not precise enough to test these predictions.

With the JADE and TASSO detectors one is able to distinguish $\pi^{\pm}$ from $K^{\pm}$, proton and antiprotons. The x-spectra for the different particle types have been measured over a wide x-range. In Figure 69 a,b, and c the preliminary scaling cross sections $(s/\beta) \cdot d\sigma/dx$ are shown, where x = 2E/W, for $\pi^{\pm}$, $K^{\pm}$ and $(p, \bar{p})$. The pion and kaon

data are compared to low energy data. For $x \geq 0.2$ the 5.2 GeV pion spectra are above the high energy ones by $\tilde{}$ 30% which is the expected outcome from scale breaking. The statistical error for the high energy data however, is still large so this conclusion is only tentative. In Figure 69b, the kaon spectra are shown. The solid line represents the high energy $\pi^+ + \pi^-$ data. The yield of kaons is a factor 2 to 4 lower than the $\pi^\pm$ yield, at higher x values, however, the difference becomes smaller.

The particle fraction is shown in Figure 70 as function of the particle momentum p. The data from JADE and TASSO are combined in this graph. Results in the momentum range where the dE/dX measurements of JADE are in the "relativistic rise" region are shown around 3-5 GeV. The latest results from the TASSO Cerenkov counters are also included. At low momentum, below 1 GeV the pions completely dominate, however, at around 3 to 5 GeV the pions are reduced to ~ 50%, the kaons are ~ 35% and $(p, \bar{p})$ are ~ 15%. The solid line is the prediction of QCD from the Monte Carlo program by Ali et al.[16]. An average event of $\sqrt{s}$ = 30 GeV has approximately 11 $\pi^\pm$, 1.4 $K^o, \bar{K}^o$, 1.4 $K^\pm$ and 0.4 $p, \bar{p}$ in the final state.

FIGURE CAPTIONS

Fig. 51 Energy distribution of hadron events as measured by the MARK-J detector.

Fig. 52 The total relative hadronic cross section R as function of W the c.m. energy. The lines indicate the prediction by QCD for two values of the parameter α_s (see text).

Fig. 53a) Average R values as measured by the PETRA experiments during the energy scan between 29.90-31.46 GeV.
b) As a) for energy scan between 35.00-35.8 GeV.

Fig. 54 Schematic drawing of a 2-jet event.

Fig. 55 Angular distribution of the jet axis. The angle θ is defined as the angle between the beam axis and the jet axis. The solid curve is the expectation from QCD multiplied by the angular dependent acceptance of the MARK-J detector.

Fig. 56 The mean transverse and longitudinal momentum components $\langle p_t \rangle$ and $\langle p_{//} \rangle$ and $\langle p_T^2 \rangle$ for charged particles produced in hadronic events plotted as function of the c.m. energy W.

Fig, 57 Thrust distribution observed by the MARK-J group at $\sqrt{s}$ = a) 13, b) 17, c) 22, d) 27 GeV (see text). The solid line is the quark model prediction for u,d,s,c and b quarks with no gluon emission.

Fig. 58 The thrust distributions with a 70% energy cut for $\sqrt{s} \sim 30$ GeV and $\sqrt{s} \simeq 35$ GeV. The curves are predictions for various models as described in the text.

Fig. 59 Average value of thrust as a function of $\sqrt{s}$ together with the QCD prediction (solid line). The values expected from a QCD model with a top quark are also shown.

Fig. 60 Sphericity distributions for the energies $\sqrt{s}$ = 13 to 31.2 GeV. The solid line is the prediction of the QCD model with u,d,s,c,b quarks. The dashed-dotted curve includes a heavy charge 2/3 quark.

Fig. 61 Average sphericity <S> as function of the total c.m. energy W. The dashed line shows the expected <S> behaviour when the threshold for the production of heavy t-quarks is passed.

Fig. 62 Relative production rate of hadronic events containing muons as a function of the c.m. energy E_{CM}. The hatched areas are the predictions or models containing five and six quarks.

Fig. 63 Thrust distributions of inclusive muon events compared with all hadronic events from MARK-J.

Fig. 64 Number of events expected for the production of a new (sequential) heavy lepton as a function of mass. The inset shows the number of events expected in the τ sample from tau and heavy lepton production. A total of 52 τ events is observed. The dashed line corresponds to the 95% confidence upper limits for τ events.

Fig. 65 Number of events expected for the production of a spin zero partner s_μ or t_μ of the muon as a function of mass. The upper limit of events (95% confidence) and the mass range excluded is also indicated.

Fig. 66 Energy loss of positive and negative tracks in multi-hadron events as a function of apparent momentum p/Q. The solid lines are the expectations for the particles e, π, K, p, d, t. The dashed line is the expectation for a heavy particle (M = 5 GeV) with charge q = 2/3.

Fig. 67 Measurements of the mean charged multiplicity $\langle n_{ch} \rangle$ as a function of the c.m. energy $\sqrt{s}$.

Fig. 68 The $sd\sigma/dx$ distribution as function of $x = p/p_{beam}$ for charged particles in the c.m. energy range of 5 to 36.6 GeV.

Fig. 69a) The $(s/\beta)\, d\sigma/dx$ distribution as function of $x = 2E/W$ for the pion data at several c.m. energy values.

b) As a) but for charged and neutral kaons. The solid line is the trend of the charged pion data.

c) As a) but for protons and antiprotons.

Fig. 70 The particle fraction at $\sqrt{s} = 30$ GeV for $\pi^{\pm}$, $K^{\pm}$ and $p + \bar{p}$ as function of particle momentum. The solid line is the prediction by QCD.

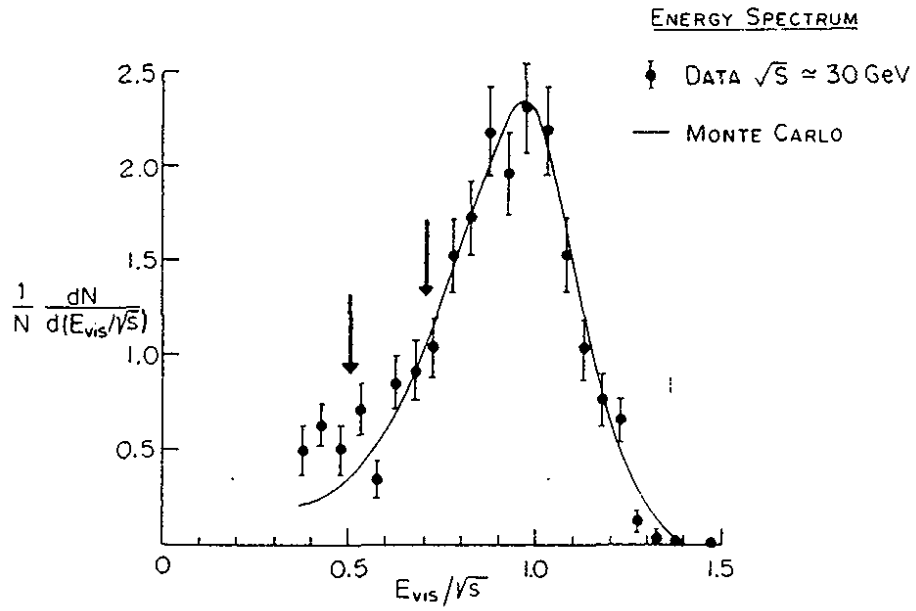
ENERGY SPECTRUM
DATA √S ≃ 30 GeV
MONTE CARLO
2.5
2.0
1.5
1.0
0.5
0
0.5
1.0
1.5
1/N dN/d(E_vis/√S)
E_vis/√S

Fig. 51

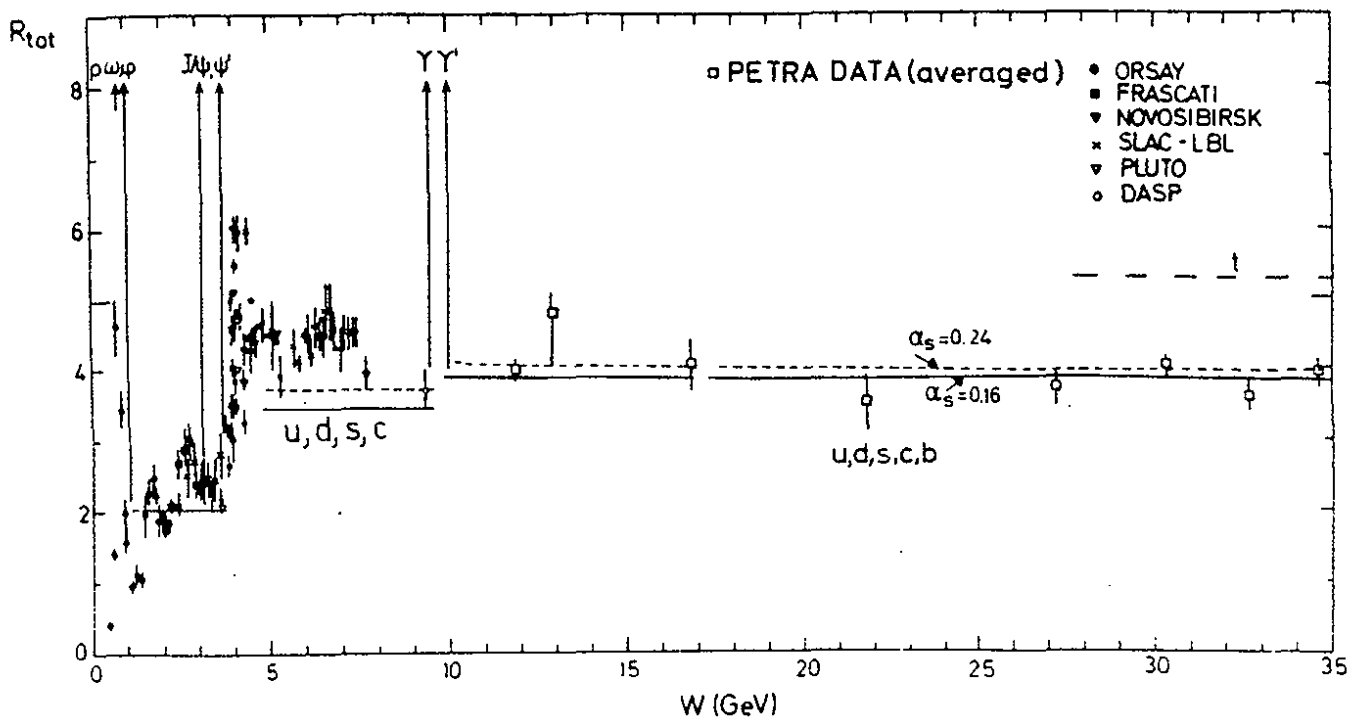
R_tot
ρωφ
JΛψ,ψ'
ΥΥ'
PETRA DATA (averaged)
ORSAY
FRASCATI
NOVOSIBIRSK
SLAC - LBL
PLUTO
DASP
α_s=0.24
α_s=0.16
u,d,s,c
u,d,s,c,b
W (GeV)

Fig. 52

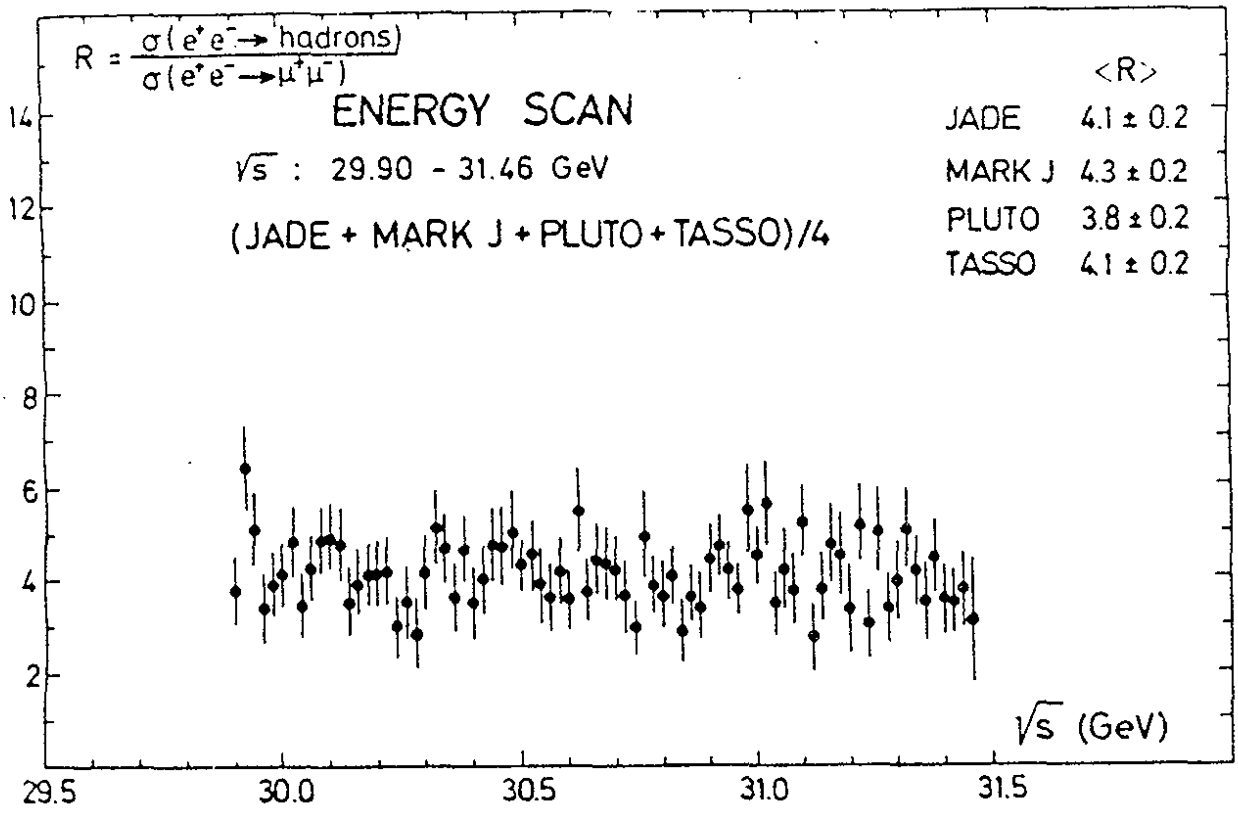
R = σ(e⁺e⁻ → hadrons) / σ(e⁺e⁻ → μ⁺μ⁻)
ENERGY SCAN
√s : 29.90 - 31.46 GeV
(JADE + MARK J + PLUTO + TASSO)/4
<R>
JADE 4.1 ± 0.2
MARK J 4.3 ± 0.2
PLUTO 3.8 ± 0.2
TASSO 4.1 ± 0.2
√s (GeV)

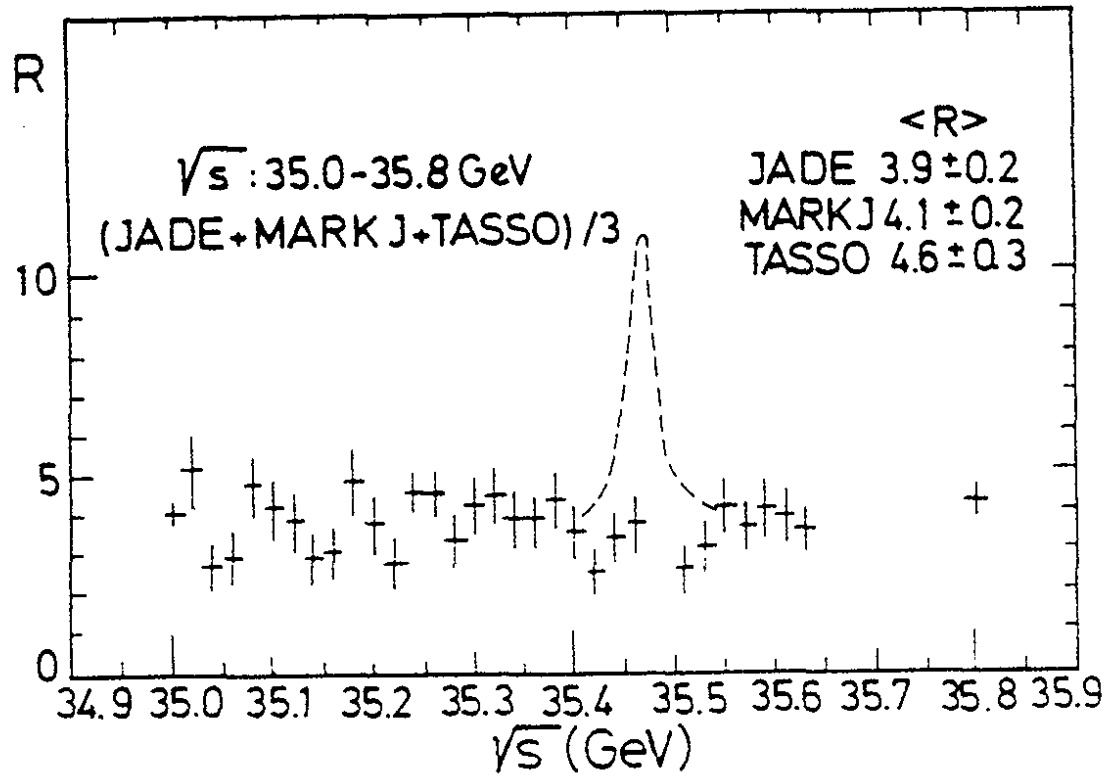
R
√s : 35.0-35.8 GeV
(JADE+MARK J+TASSO)/3
<R>
JADE 3.9±0.2
MARKJ 4.1±0.2
TASSO 4.6±0.3
√s (GeV)

Fig. 53

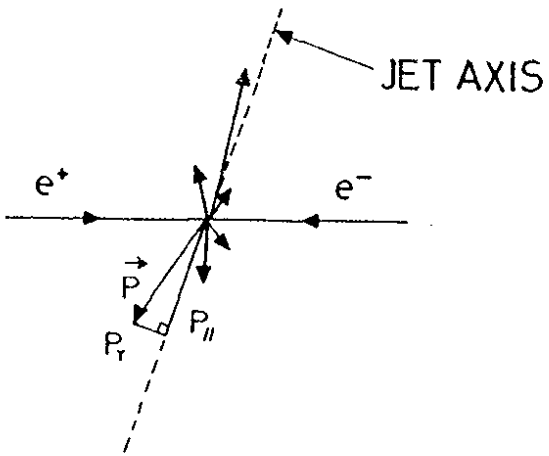

JET QUANTITIES

Fig. 54

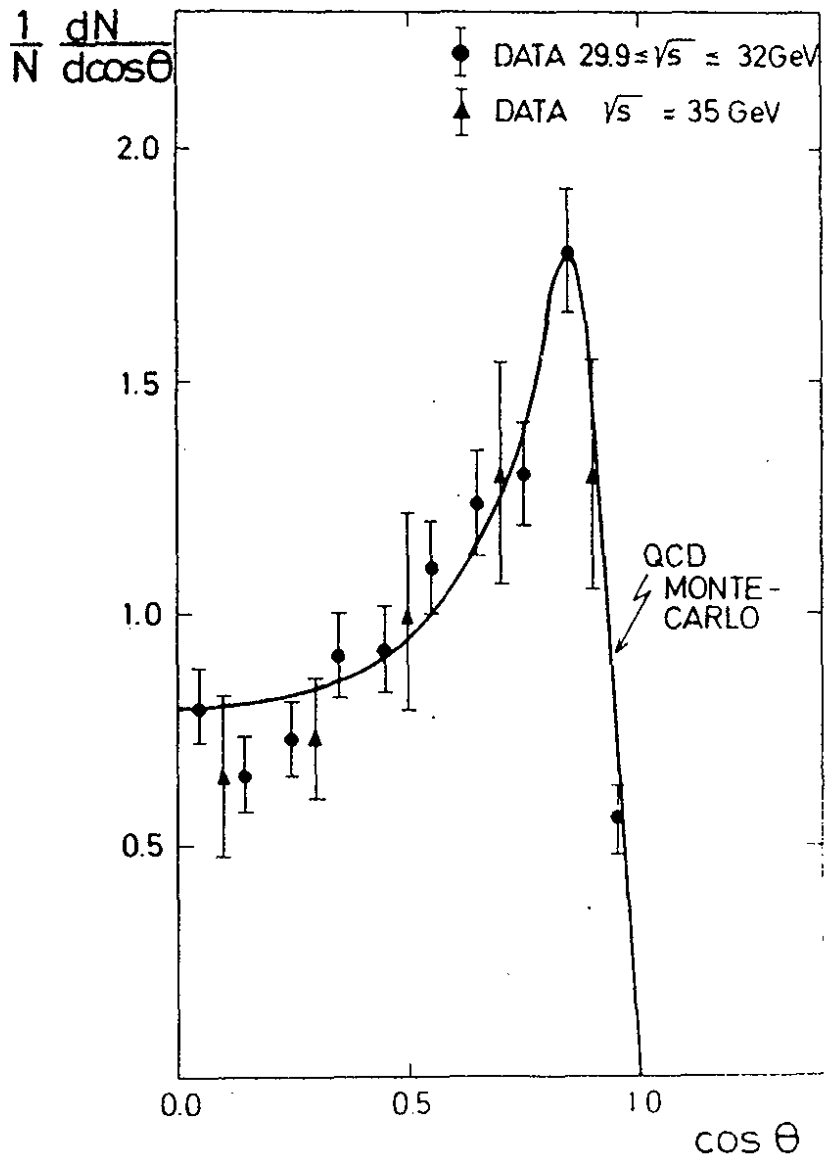

Fig. 55

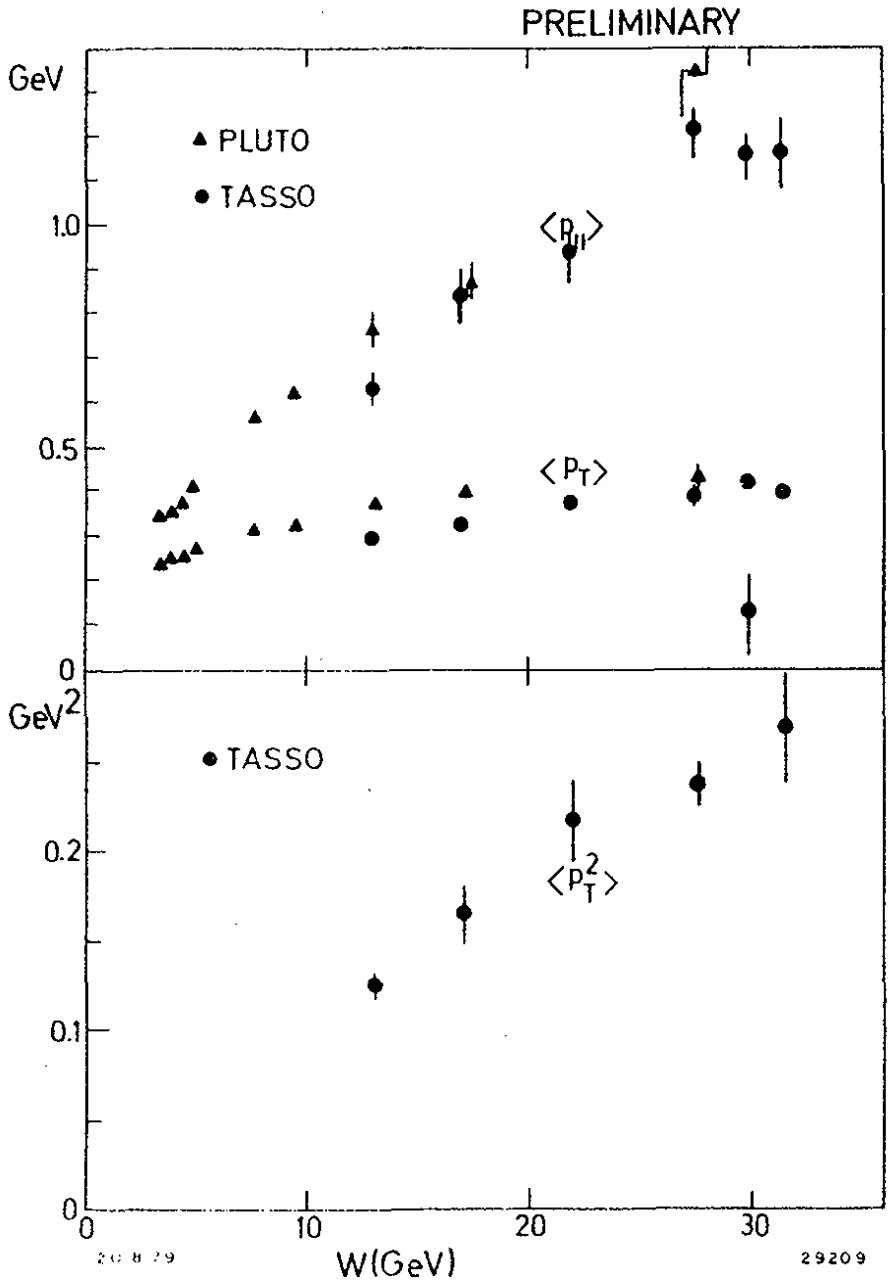
PRELIMINARY
GeV
PLUTO
TASSO
$\langle p_{II} \rangle$
$\langle p_T \rangle$
1.0
0.5
0
GeV^2
TASSO
$\langle p_T^2 \rangle$
0.2
0.1
0
0
10
20
30
W(GeV)
29209

Fig. 56

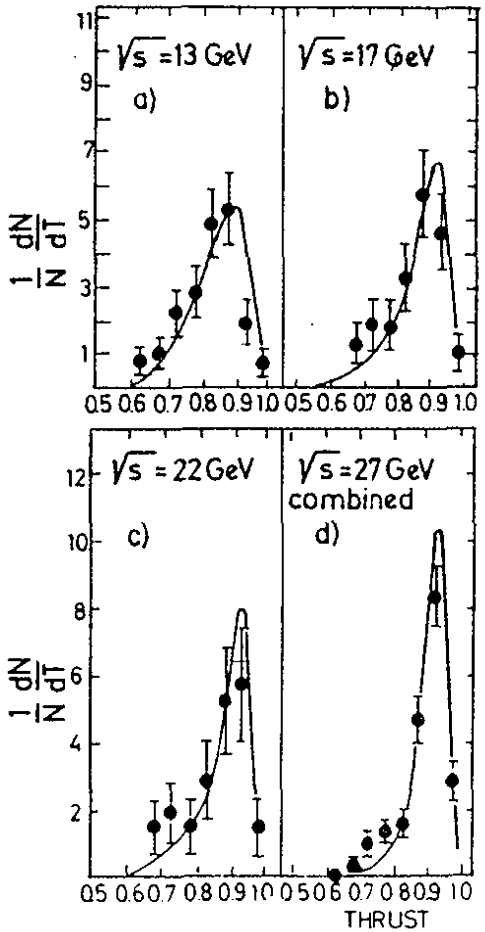
$\sqrt{s}$ =13 GeV
a)
$\sqrt{s}$ =17 GeV
b)
$\sqrt{s}$ = 22 GeV
c)
$\sqrt{s}$ =27 GeV
combined
d)
$\frac{1}{N}\frac{dN}{dT}$
THRUST

Fig. 57

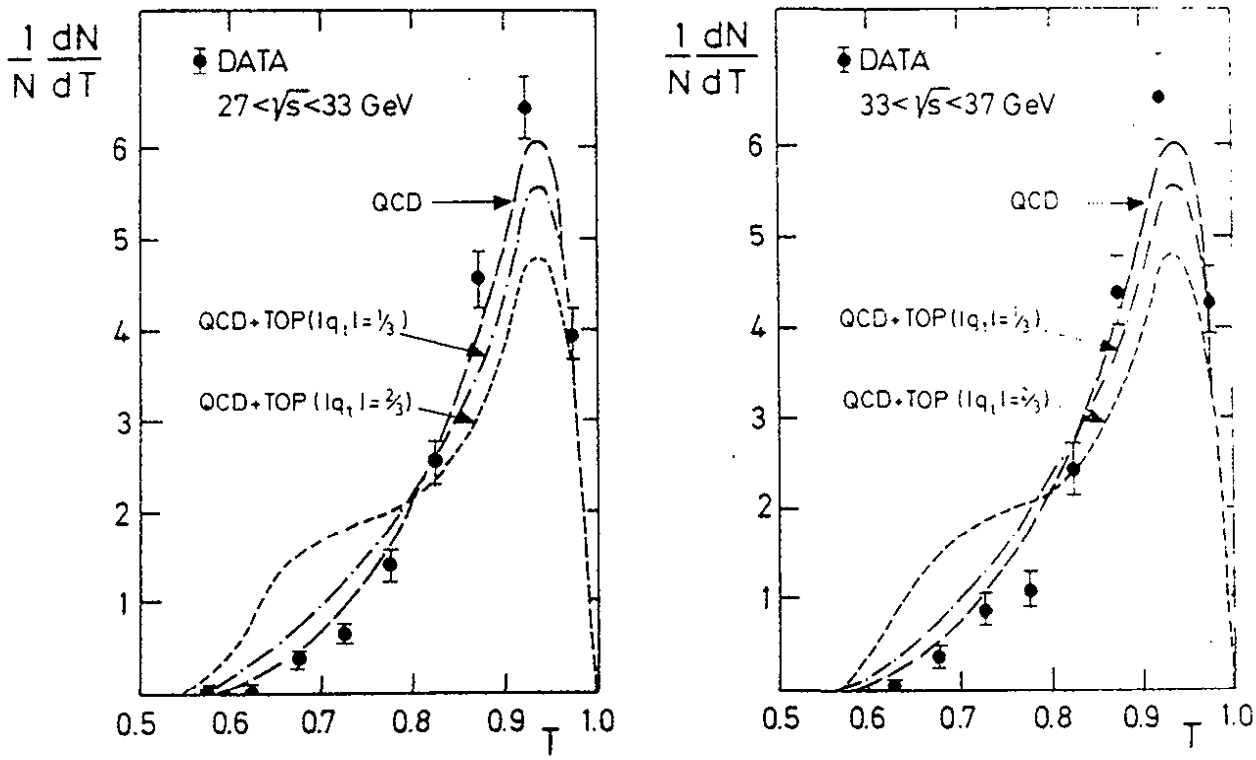
1/N dN/dT
DATA
27<√s<33 GeV
QCD
QCD+TOP(|q_t|=1/3)
QCD+TOP(|q_t|=2/3)
T
1/N dN/dT
DATA
33<√s<37 GeV
QCD
QCD+TOP(|q_t|=1/3)
QCD+TOP(|q_t|=2/3)
T

Fig. 58

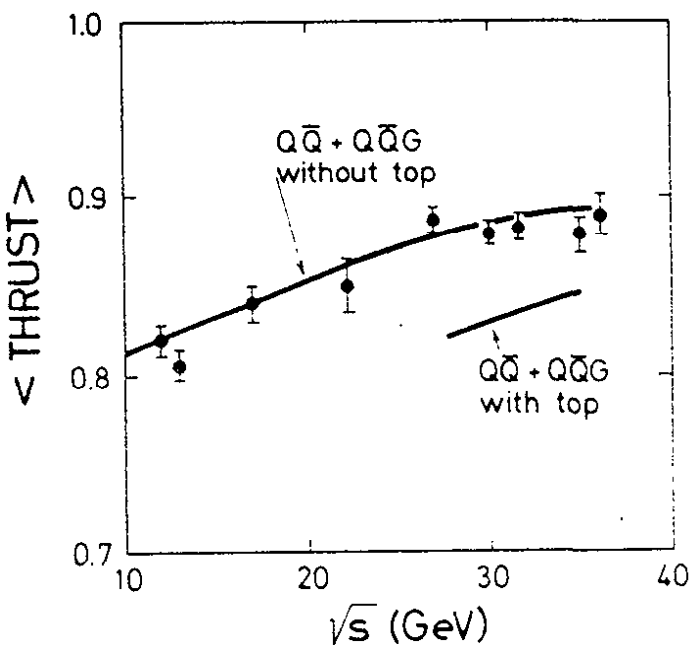
<THRUST>
QQ̄ + QQ̄G
without top
QQ̄ + QQ̄G
with top
√s (GeV)

Fig. 59

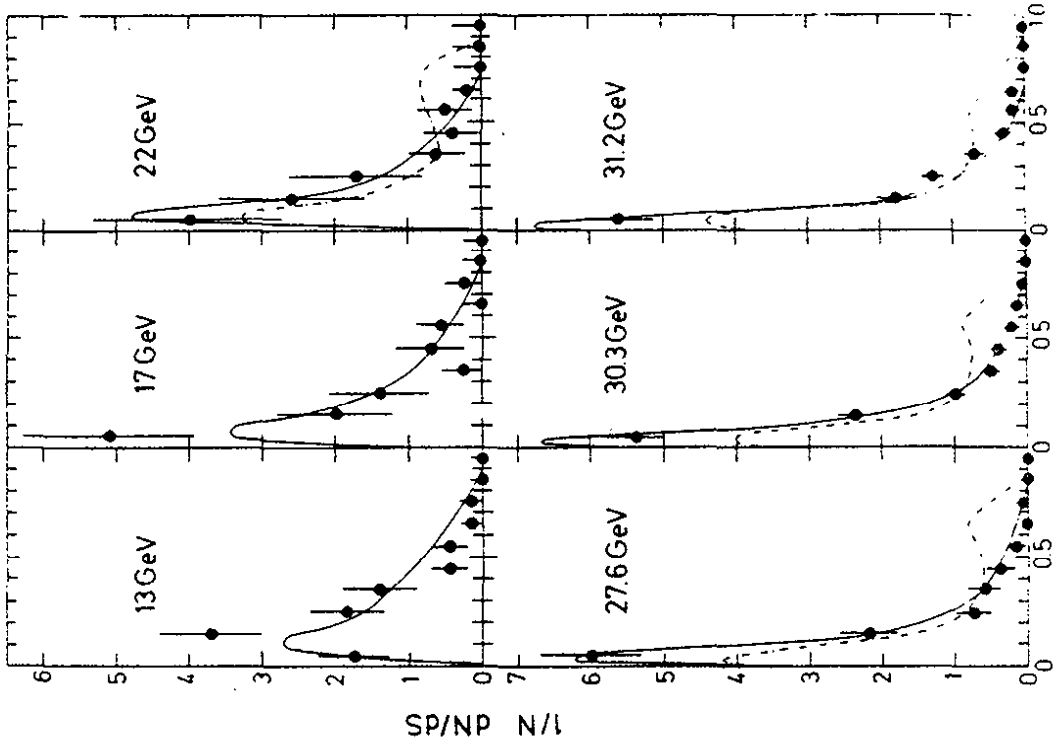
1/N dN/dS
13GeV
17GeV
22GeV
27.6GeV
30.3GeV
31.2GeV
SPHERICITY

Fig. 60

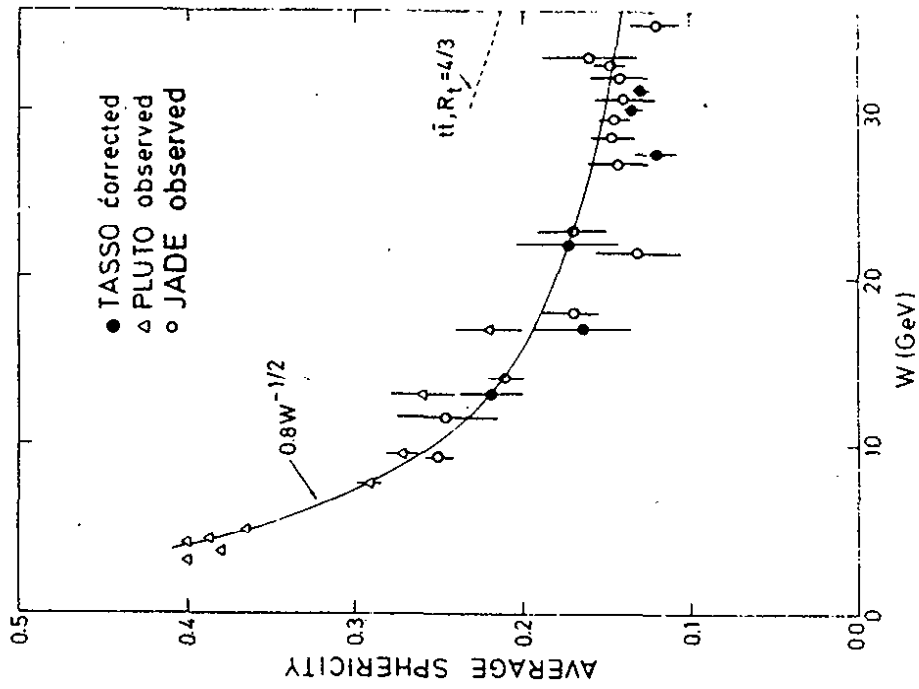
AVERAGE SPHERICITY
W (GeV)
● TASSO corrected
△ PLUTO observed
○ JADE observed
$0.8W^{-1/2}$
$t\bar{t}, R_t=4/3$

Fig. 61

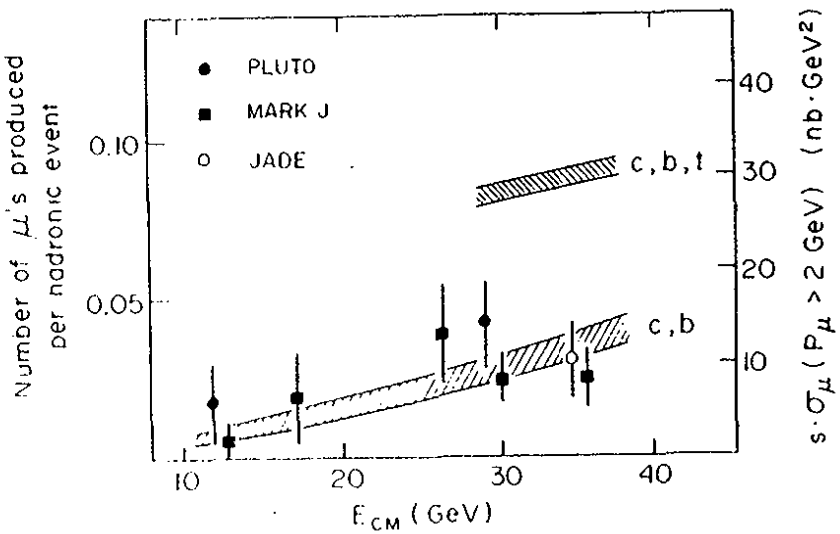

Fig. 62

MARK J

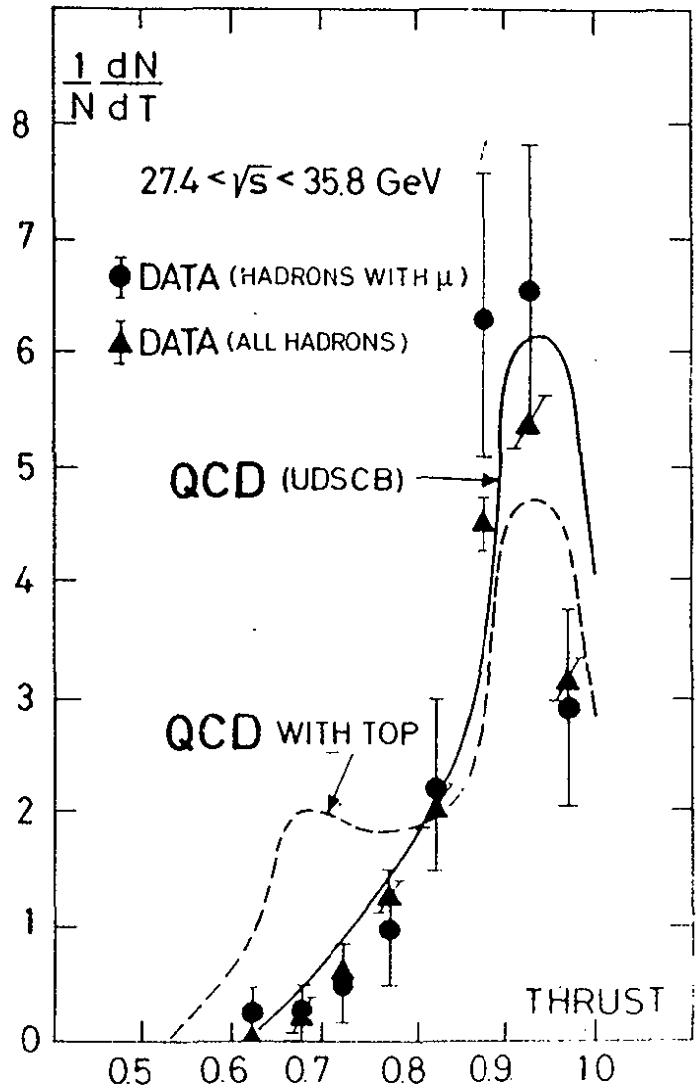

Fig. 63

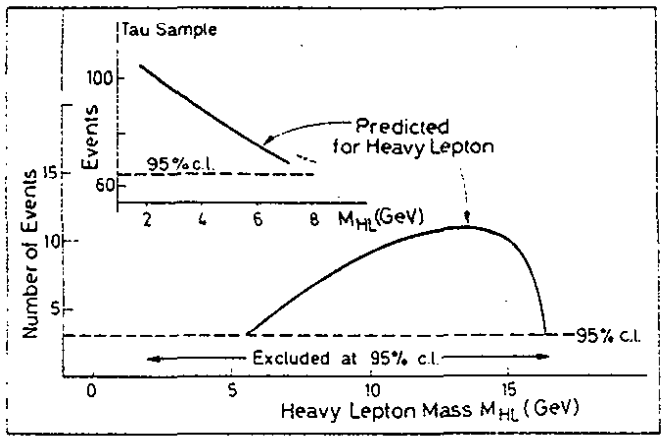

Fig. 64

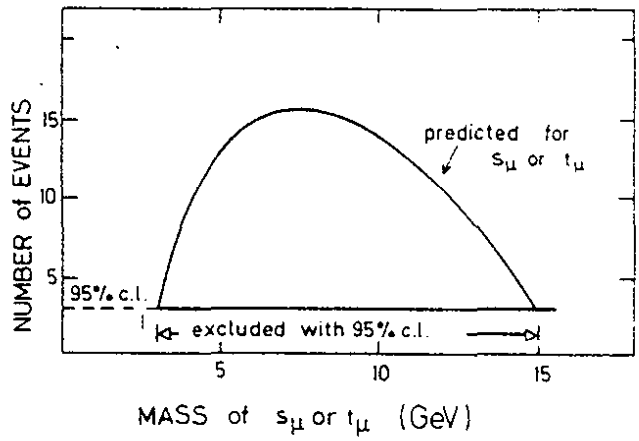

Fig. 65

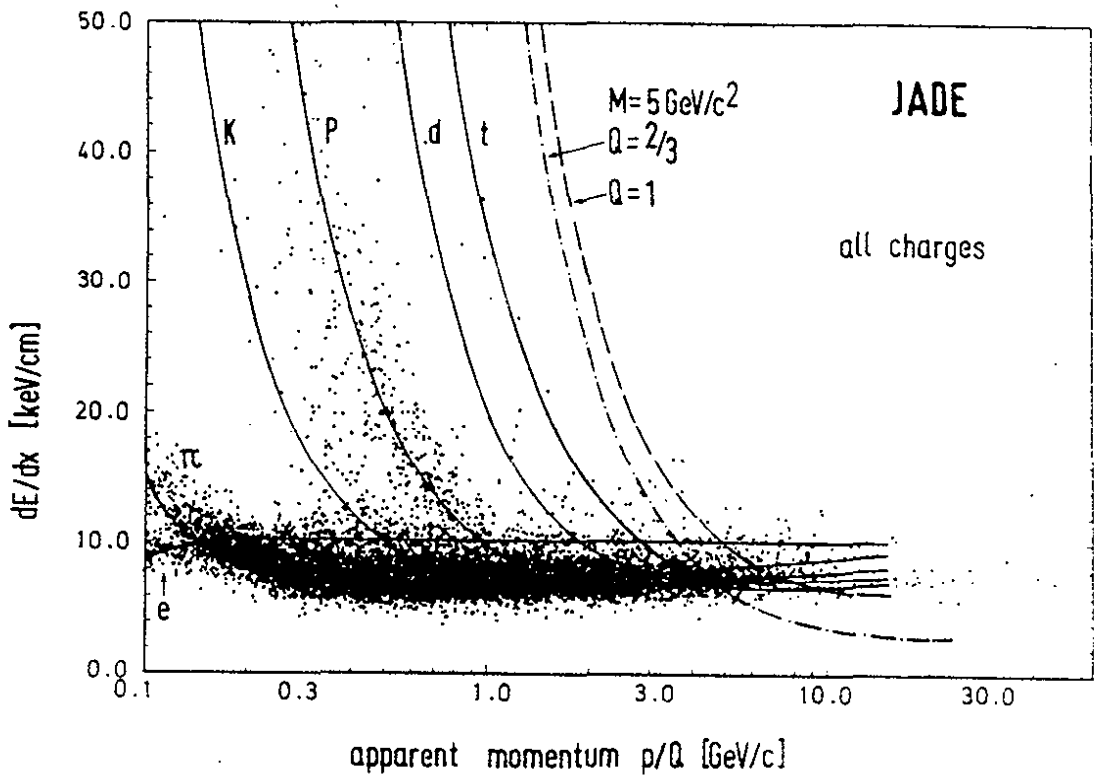

Fig. 66

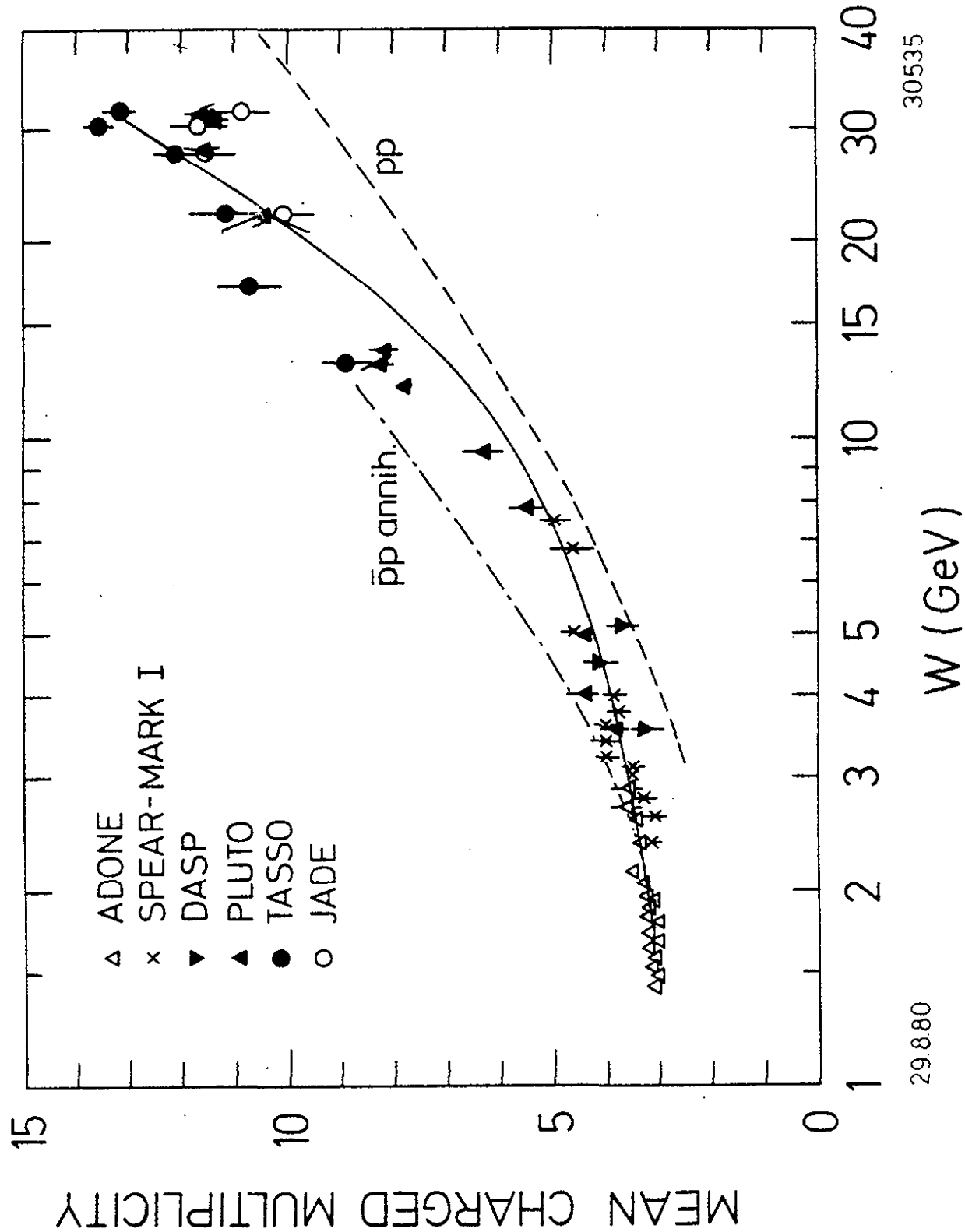
MEAN CHARGED MULTIPLICITY
W (GeV)
ADONE
SPEAR-MARK I
DASP
PLUTO
TASSO
JADE
pp
p̄p annih.
29.8.80
30535

Fig. 67

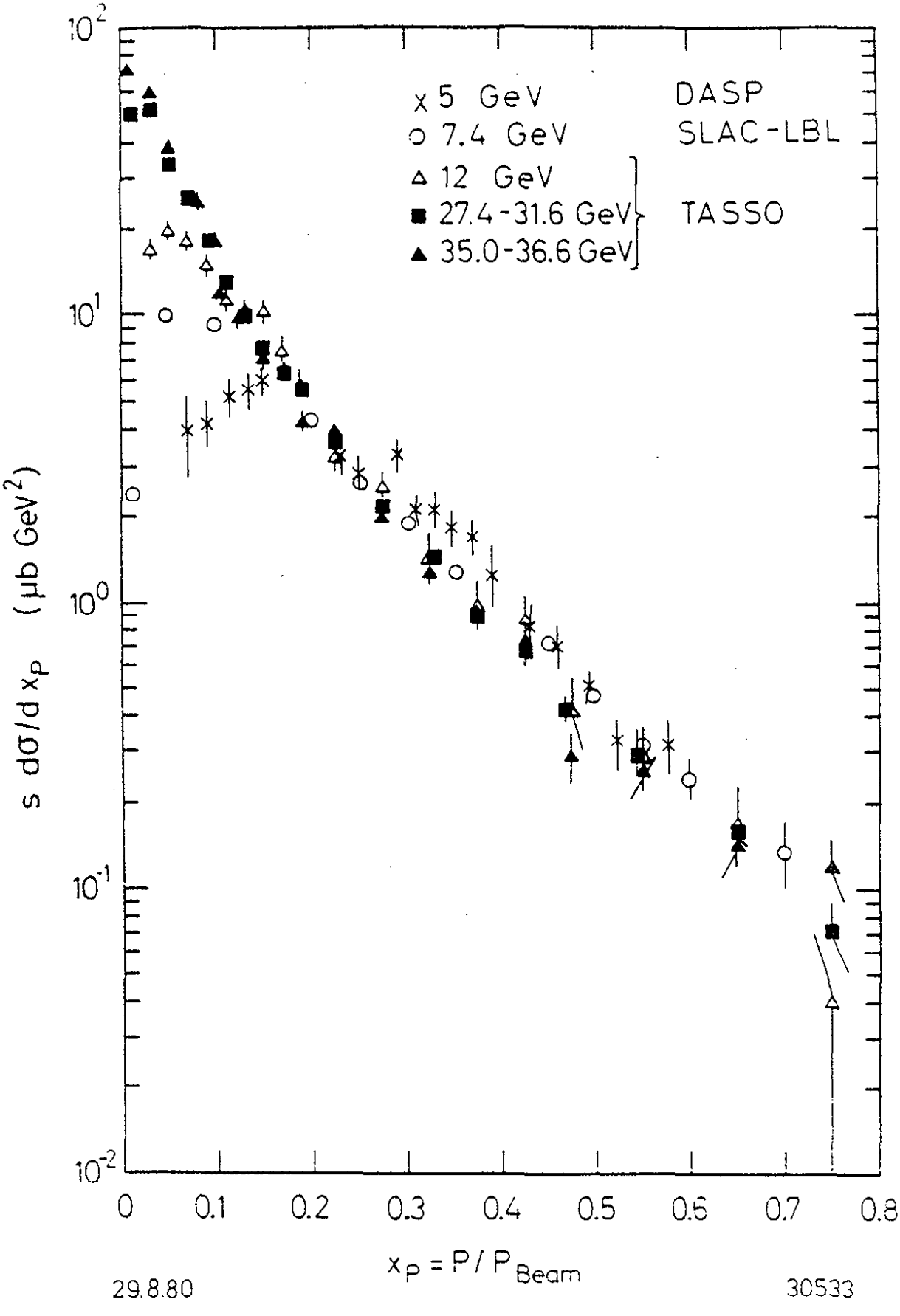
x 5 GeV
○ 7.4 GeV
△ 12 GeV
■ 27.4-31.6 GeV
▲ 35.0-36.6 GeV
DASP
SLAC-LBL
TASSO
s dσ/d x_P (μb GeV²)
x_P = P / P_Beam
29.8.80
30533

Fig. 68

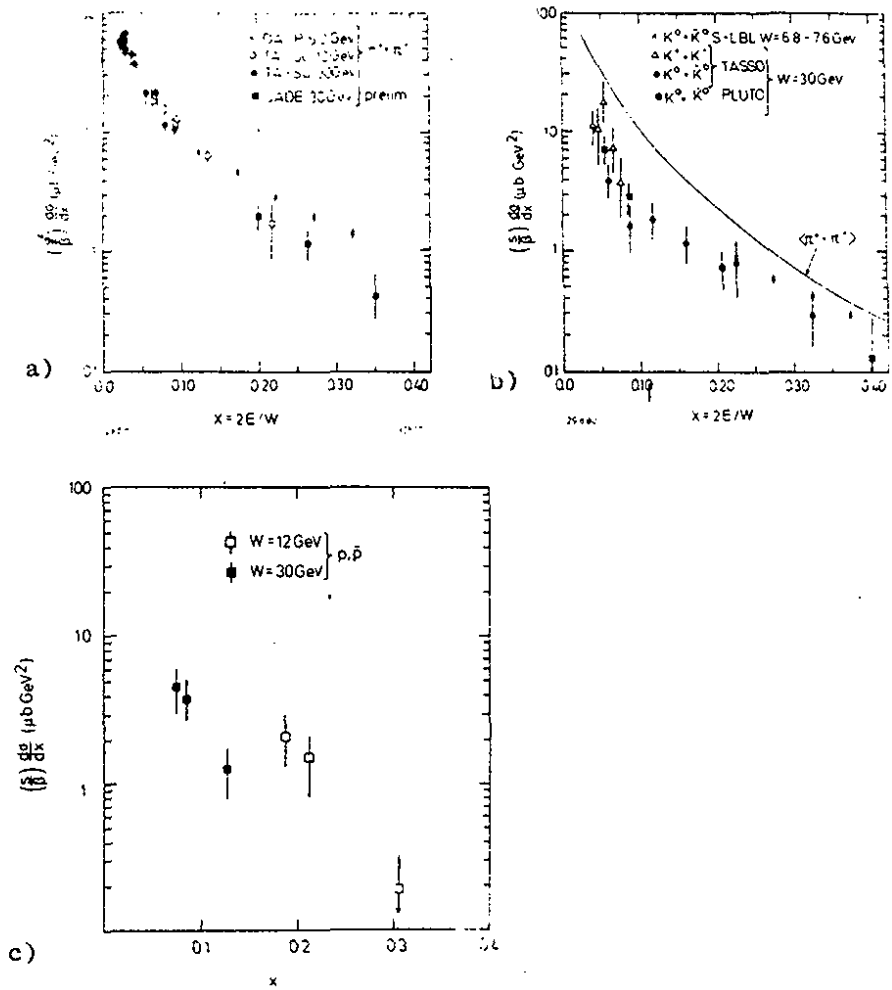
a)
b)
c)
X = 2E/W
W = 12GeV
W = 30GeV
p,p̄
W = 30GeV
TASSO
PLUTO
x

Fig. 69

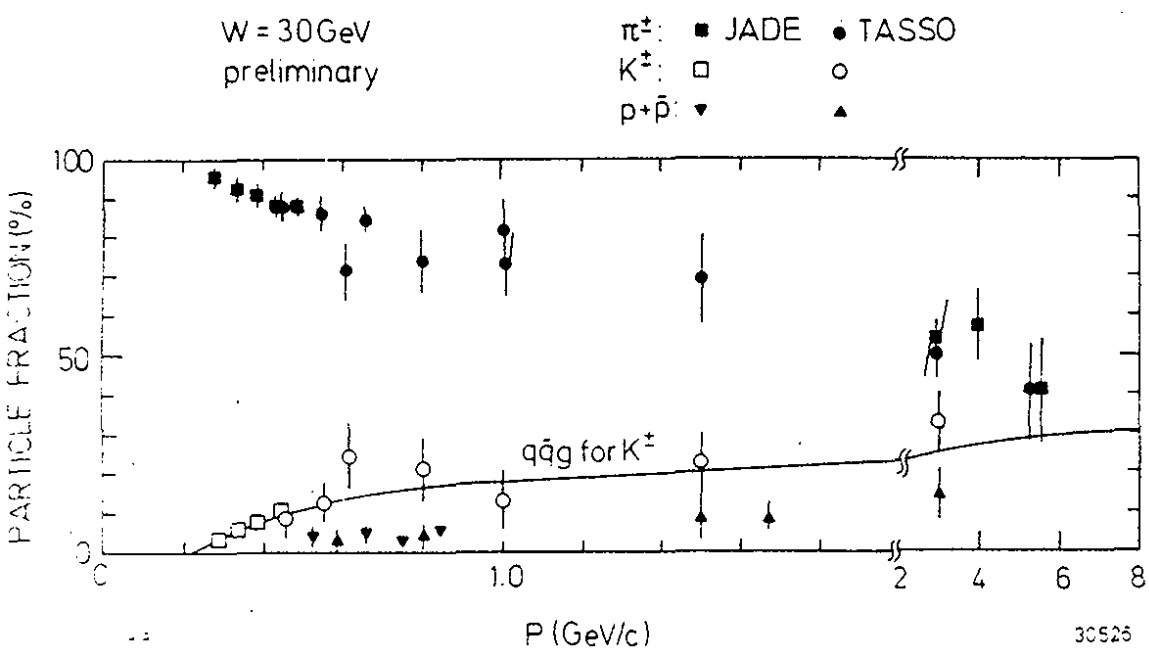
W = 30GeV
preliminary
π±: JADE TASSO
K±:
p+p̄:
PARTICLE FRACTION (%)
qq̄g for K±
P (GeV/c)
30526

Fig. 70

7. TEST OF QUANTUM CHROMODYNAMICS

7.1 Introduction

In the framework of QCD, the process $e^+e^- \rightarrow$ hadrons proceeds through the production of a quark-antiquark pair, which is sometimes accompanied by one or more gluons.

The consequences of gluon radiation in e^+e^- physics were seen before the advent of PETRA by the experiments at DORIS[99] which observed the decay of the upsilon. In particular the PLUTO collaboration[100] demonstrated that a variety of topological features of the events were in excellent agreement with Monte Carlo model predictions based on the direct decay of the upsilon via three gluons into three broad jets. In Figures 71 a and b the triplicity (see section 7.2.3) and the angular distribution between two of the three broad jets are plotted and compared with model predictions of a phase-space like, a quark-antiquark and a three-gluon decay of the upsilon. The three-gluon decay is clearly the one which is the most favoured of the three alternatives. The jet axis angular distributions (Fig. 71c) indicates that the gluons are vector particles.

This analysis, however was not able to prove unambiguously the existence of gluon jets. The upsilon mass is not high enough to produce three well-collimated jets which can be clearly distinguished from other resonant decay channels, so that a statistical model including clusters or resonances could not be ruled out.

The PETRA results on tests of QCD with data obtained up to the summer of 1980 will be reviewed in the next sections for each of the groups. In reference (101) a brief sketch of the chronological sequence of mounting evidence leading to the establishment of gluon effects in e^+e^- interactions can be found.

Some of the main features established by the summer of 1979 can be summarized as follows: The naive two-jet picture at the then highest PETRA energy of $\sqrt{s} \approx 30$ GeV could no longer be maintained as

is demonstrated in the p_T^2 distribution of the TASSO group in Fig. 72. The low energy data $\sqrt{s}$ = 17 GeV can be described by the two-jet model with an average p_T of the produced hadrons with respect to the jet axis of ~ 300 MeV. The 30 GeV data, however cannot be described in this way and the $\langle p_T \rangle$ has to be raised to 450 MeV to get agreement with the measured distribution. To study the structure of the events, each event can be divided into two hemispheres using the plane perpendicular to the thrust axis. Each hemisphere can then be separately analyzed, as if it were a single jet. The jet having the smaller p_T with respect to the thrust axis is defined as the 'narrow' or 'slim' jet and the other as a 'broad' or 'fat' jet. Fig. 73 shows the data from the PLUTO group for the $\langle p_T \rangle$ of a 'slim' and 'fat' jet as a function of $x = p_i/p_{beam}$ for the low and high energy data. For both energies the 'slim' jet can be described by a normal quark jet, the 'fat' jet, however is too broad and can be described by either an increase in $\langle p_T \rangle$ on the fat side alone or by QCD.

It was also noted that the above mentioned effects were due to an excess of so-called planar or oblate events and that some of these showed a three-jet structure. An example of such an event is given in Fig. 74 which shows an event from the JADE group projected onto the event plane.

The first statistically relevant results, establishing the 3-jet pattern from $q\bar{q}g$ of a sample of hadronic events are shown in Fig. 75 of the MARK-J group in which a sample of the events with low thrust and high oblateness, where the gluon-emission effect is expected to be relatively large, is selected for detailed examination. The key feature of this figure is that it consists of the superposition of an entire event sample, and thus displays the average behavior of the energy flow for planar events at high energy. The event sample is composed of 40 events with $T < 0.8$ and $O_b > 0.1$ out of 446 hadronic events.

The calculated Monte Carlo predictions based on QCD in both the rate and shape of three-jet events in the figure were compatible with the data with $\chi^2 = 67$ for 70 degrees of freedom. The accumulated energy distribution in the lower part of the figure, showing the view in the plane perpendicular to the event plane, exhibits a flat distribution consistent with the model predictions.

These results can be contrasted to those obtained with a simple phase space model. Using a χ^2 fit of the phase-space energy distribution to the data one found that $\chi^2 = 222$ for 70 degrees of freedom. Therefore, phase-space is inconsistent with the data. From the oblateness or flatness distribution it could be established that the $q\bar{q}$ contribution is negligible.

7.2 QCD Tests with the MARK-J Detector

7.2.1 Energy Flow Method

In this section the detailed topological analysis is reviewed which was used by the MARK-J to test QCD and to isolate the 3-jet events arising from the emission of hard non-collinear gluons[102].

In order to exclude events where leading particles have escaped down the beam pipe, or where part of a broad jet is missed, only those events are selected for which the visibly energy, $E_{vis} \geq 0.7\sqrt{s}$. This cut also eliminates two-photon events and events where a hard photon is emitted in the initial state. The drift tubes surrounding the beam pipe enables this group to separate more distinctly the distribution of charged particles from neutrals. Since neutral particles carry away a large portion of the total energy, they will not only affect the axes of the jets, but will also affect the identification of individual jets. The characteristic features of hard non-collinear gluon emission in $e^+e^- \rightarrow q\bar{q}g$ are illustrated in Fig. 76. Because of momentum conservation the momenta of the three particles have to be coplanar.

For events where the gluon is sufficiently energetic, and at large angles with respect to both the quark and antiquark, the observed hadron jets also tend to be in a recognizable plane. This is shown in the upper part of the figure where a view down onto the event plane shows three distinct jets; distinct because the fragmentation products of the quark and gluons have limited P_t with respect to the original directions of the partons. The lower part of the figure shows a view looking towards the edge of the event plane, which results in an apparent 2-jet structure. Fig. 76 thus demonstrated that hard non-collinear gluon emission is characterized by planar events which may be used to reveal a 3-jet structure once the event plane is determined.

The spatial energy distribution is described in terms of three orthogonal axes called thrust, major and minor axes. The axes and the projected energy flow along each axis T_{thrust}, F_{major} and F_{minor} are determinted as follows:

(1) The thrust axis, $\vec{e}_1$, is defined as the direction along which the projected energy flow is maximized. The thrust, T_{thrust} and $\vec{e}_1$ are given by

$$T_{thrust} = \max \frac{\Sigma_i \, | \vec{E}^i \cdot \vec{e}_1 |}{\Sigma_i \, |\vec{E}^i|}$$

where $\vec{E}^i$ is the energy flow detected by a counter as described above and $\Sigma_i \, | \vec{E}^i |$ is the total visible energy of the event (E_{vis}).

(2) To investigate the energy distribution in the plane perpendicular to the thrust axis, a second direction, $\vec{e}_2$, is defined perpendicular to $\vec{e}_1$. It is the direction along which the projected energy flow in that plane is maximized. The quantity F_{major} and $\vec{e}_2$ are given by

$$F_{major} = \max \frac{\Sigma_i \, |\vec{E}^i \cdot \vec{e}_2|}{E_{vis}}, \quad \vec{e}_2 \perp \vec{e}_1$$

(3) The third axis, $\vec{e}_3$ is orthogonal to both the thrust and the major axes. It is found that the absolute sum of the projected energy flow along this direction, called F_{minor}, is very close to the minimum of the projected energy flow along any axis, i.e.,

$$F_{minor} = \frac{\Sigma_i |\vec{E}^i \cdot \vec{e}_3|}{E_{vis}} \simeq \min \frac{\Sigma_i |\vec{E}^i \cdot \vec{e}|}{E_{vis}}$$

If hadrons were produced according to phase-space or a $q\bar{q}$ two-jet distribution, then the energy distribution in the plane as defined by the major and minor axes would be isotropic, and the difference between F_{major} and F_{minor} would be small. Alternatively, if hadrons were produced via three-body intermediate states such as $q\bar{q}g$, and if each of the three bodies fragments into a jet of particles with $\langle P_t \rangle \sim 325$ MeV, the energy distribution of these events would be oblate(P_t refers to the quarks). Following the suggestion of H. Georgi, the quantity oblateness, O, is defined as

$$O = F_{major} - F_{minor}.$$

The oblateness is $\sim 2\, P_t\text{gluon}/\sqrt{s}$ for three-jet final states and is approximately zero for final states coming from a two-jet distribution.

As mentioned in section 7.1 for the study of the detailed structure of the events each event is divided into two hemispheres using the plane defined by the major and minor axes, and separately analyzed the energy distribution in each hemisphere as if it were a single jet. The jet having the smaller P_t with respect to the thrust axis is defined as the 'narrow' jet (n) and the other as a 'broad' jet (b). In each hemisphere we calculate the oblateness, $O_n = 2(F^n_{major} - F^n_{minor})$, and $O_b = 2(F^b_{major} - F^b_{minor})$, and thrusts T_n and T_b.

One approach to analyze the flat events for a possible 3-jet structure is illustrated by Fig. 77. The figure shows the energy flow diagram for each of two high energy hadronic events, viewed in the event plane determined by the major and thrust axes. The energy flow diagram is a polar coordinate plot in which the energy vectors $\vec{E}^i$ are summed in 10^o intervals. Each point in the plot represents the summed energy in an angular interval, with the radius given by the magnitude, and the azimuth given by the center of the angular interval in the event plane. The two events in the figure both show an apparent 3-jet structure.

However, the examination of individual event appearances cannot be used to establish the underlying 3-jet structure characteristic of $q\bar{q}g$ final states. This is demonstrated by Fig. 78, which shows two low thrust, planar events at 12 GeV center of mass energy. The events also show a distinct multi-jet structure. It should be noted that all the measured distributions at low energies (thrust, oblateness, etc.) are well described by a simple $q\bar{q}$ model (see Fig. 79), so that the suggestive event appearances are unrelated to gluon emission, but are dominated by fluctuations in the quark fragmentation process. The views of the events in the minor-thrust plane (looking at the edge of the event plane in Fig. 78), also show that the events are planar.

In the analysis discussed below, the Monte Carlo of Ali et al. [16] was adopted. As discussed in Section 3.3, this model incorporates higher order QCD effects, the q^2 evolution of the quark and gluon fragmentation functions and the weak decays of heavy quarks.

Figs. 80a and 80b show the event distribution as a function of O_n and O_b, compared to the predictions of the QCD model and of two quark-parton models with quark $\langle P_t \rangle$ = 300 MeV and 500 MeV, respectively. Fig. 80a shows that the narrow jet distribution agrees with the various models indicating that it comes from a single quark jet. Fig. 80b, however, shows that the quark-parton models severely

underestimate the number of events with $O_b \geq 0.3$ while the QCD model correctly predicts the observed distribution.

The T_n and T_b thrust distributions of the flat events in the region $O_b \geq 0.3$ are shown in Figs. 80c and 80d along with the QCD and high P_t $q\bar{q}$ models. The observed distribution is also compared to the 'flattened' $q\bar{q}$ model in which the quarks have $\langle P_t \rangle$ = 500 MeV in the thrust-major plane and $\langle P_t \rangle$ = 300 MeV in the thrust-minor plane. The T_n distribution in Fig. 80c is in good agreement with the QCD model predictions and has the same general shape as the thrust distribution for high energy $e^+e^- \to q\bar{q}$ reactions shown in Fig. 57 and 58. As expected the T_b distribution, however, is much broader than that of T_n and agrees only with the QCD predictions.

The distributions in Figs. 80c and 80d demonstrate that the relative yield of flat events, and the shape of these events as measured by T_n and T_b, can only be explained by the QCD model. The distributions T_n and T_b further exclude phase-space (which peaks at lower thrust values) as well as $q\bar{q}$ models as possible explanations of the energy flow plots.

The development of the 3-jet structure with decreasing thrust and increasing oblateness, as predicted by QCD[1o3], is shown in a series of energy flow diagrams in Fig. 81a - c.

As seen in Fig. 81a the events at high thrust values are dominated by a 2-jet structure characteristic of $e^+e^- \to q\bar{q}$. In Fig. 81b, where the thrust is lower, we begin to see the appearance of the gluon jet; and in Fig. 81c the 3-jet events are predominant. It is important to note that in all three cases the data agree with the QCD model prediction, showing the increased incidence of hard non-collinear gluon emission with decreasing thrust and increasing oblateness. The energy flow in the minor-thrust plane contains only two nearly identical lobes similar to the narrow jet in Fig. 81a, in good agreement with QCD predictions. In Fig. 82 we unfold the energy flow diagram of Fig. 81c to see more clearly the compa-

rison of the data with the predictions of QCD, $q\bar{q}(\langle P_t \rangle = 500$ MeV), and a 'mixed model' consisting of a combination of $q\bar{q}$ and phase-space contributions. All models in Fig. 82 are normalized to have the same areas (as the data) before the individual cuts are imposed. The normalization for the mixed model was determined by adjusting the $q\bar{q}(\langle P_t \rangle = 300$ MeV) and phase-space contributions to agree with the measured thrust distribution. As seen in Fig. 82, only QCD can describe the observed 3-jet structure.

Including the highest PETRA data the same picture emerges as the one described above. The event sample consists of 3600 hadronic events over the range $12 \leq \sqrt{s} \leq 36.6$ GeV.

Fig. 83 shows the event distribution as a function of the broad jet oblateness O_b, compared to the predictions of the QCD model and of a quark-parton $q\bar{q}$ model without gluon emission. The data agree with the QCD predictions, but the $q\bar{q}$ model severely underestimates the rate of production of flat events, particularly for $O_b \geq 0.3$. The small contribution of $q\bar{q}$ above $O_b \geq 0.3$ consists mainly of events containing a photon radiated at large angles from the initial state.

In Fig. 84a the energy flow pattern of the planar event samples with $O_b \geq 0.3$ in the high energy ($\sqrt{s} \geq 27.4$ GeV) and the low energy ($\sqrt{s} \leq 22$ GeV) regions is compared to the predictions of QCD, and to the predictions for the simple production of hadrons according to phase space. The pattern shown by the high energy data agrees with the QCD predictions but is quite distinct from the pattern given by phase space. The low energy data, on the other hand, gives a pattern much closer to phase space, as the jets at lower energy indicates.

To study the properties of the individual jets, the event plane is divided into three subregions bounded by the angles corresponding to the minima in the energy flow diagram. The thrusts distribution of the individual jets shown in Fig. 84a are in excellent agreement with the QCD predictions, corresponding to the appearance of well

collimated jets. The phase space model predicts distributions which are much broader in all three regions.

In Fig. 84b we unfold the energy flow diagram of Fig. 84a to see more clearly the comparison between the high energy planar events and the predictions of the QCD, $q\bar{q}$, and phase space models. All models in the figure are normalized to have equal area. Fig. 84b demonstrates that at high energy, only QCD can explain the shape of the energy flow pattern of planar events.

Fig. 84c shows the two dimensional distribution $d^2\sigma/d\theta_{12}d\theta_{23}$ for the planar events at high energy where θ_{12} is the angle between the first and second jet and θ_{23} is the angle between the second and the third jets. The three jets in this analysis are ordered according to the energy projected along the major axis. The data are compared to the expectations of the QCD model, absolutely normalized. This figure demonstrates that the three jet kinematics seen in the data (which would be completely determined by θ_{12} and θ_{23} if the jets originated from massless constituents) agrees well with QCD predictions over the full range of θ_{12} and θ_{23}. The planar events in this sample show three well defined jets with $\langle\theta_{23}\rangle \simeq 70^{\circ}$ and $\langle\theta_{12}\rangle \simeq 145^{\circ}$. From Fig. 84a we find more than 90 % of the energy of each jet is within $\pm 20^{\circ}$. Therefore, all the jets are well separated.

The structure of three jet events viewed on edge to the event plane is shown in Fig. 85. The energy flow pattern of events with $O_b \geq 0.3$ viewed in the thrust-minor plane is given in Fig. 85a, compared to the QCD and $q\bar{q}$ predictions. The individual jets, two of which overlap in this view, are shown separately. As seen in the figure, all three jets have approximately the same thickness, indicating that the P_t distributions relative to the axis of each jet are similar. This is seen more clearly in Fig. 85b, where the energy flow diagram of Fig. 85a is unfolded, and where the data are compared to the three afore-mentioned models. Fig. 85b demon-

strates that the individual jets are thinner than the expectations of the phase space model, and thicker than the $q\bar{q}$ model would predict. The data agrees well in all cases with the QCD predictions.

In Fig. 85c the distribution is shown of the fraction of the visible energy projected along the minor axis for the entire event (defined as F_{minor}), compared to the model predictions. Fig. 85c shows that if the source of low thrust oblate events were simply phase space production of hadrons, then the events would be thicker. The figure also shows that if the underlying process were $q\bar{q}$ production, then the events would be even flatter than what is actually observed. In this case the main contribution would be the result of hard non-collinear photon emission (see Fig. 84b) where the photon contribution to F_{minor} is ~ 0. Therefore, $q\bar{q}$ can at most be a small fraction of the three jet sample. The QCD model once again provides an excellent description.

Thus, the MARK-J group used an analysis of energy flow to show that the planar hadronic events produced at high energies consists of three jet events where the individual jets are strongly collimated around the jet axis and are separated by large angles. These general topological features are not model-dependent. The rate of production and the detailed shape of the events agree with the predictions of QCD.

7.2.2 Determination of the Strong Coupling Constant α_s [102]

Recent experiments on scaling violations in lepton inelastic scattering[104], on high P_t events in dilepton production by hadrons and multi-jet events in e^+e^- annihilations all indicate that the results are explained naturally in the Quantum Chromodynamics (QCD) theory of the strong interactions of quarks and gluons[14]. The strong coupling constant $\alpha_s(q^2)$ between quarks and gluons has been measured indirectly in quarkonium bound states[105], and in deep inelastic experiments[104]. At PETRA, where the q^2 is much larger,

computations are expected to be more reliable. In addition, high energy e^+e^- annihilations offer a more direct way of measuring α_s and testing perturbative QCD because it is expected to give rise to multi-jets which can be systematically identified.

The 3-jet events discussed in the previous section, which consist of $q\bar{q}g$ fragmentation products with relatively small backgrounds from fluctuations of phase-space-like processes, or quark-antiquark intermediate states, allows one to make further comparisons of the event properties with the predictions of QCD. In particular the relative yield of 3-jet events and the shape distribution gives a way to measure directly α_s.

Several methods were used by the MARK-J group in determining the strong coupling constant α_s, including

(1) the average oblateness $\langle O_b \rangle$,
(2) the fraction of events with $O_b \geq 0.3$,
(3) the relative yield of events with $O_b - O_n \geq 0.3$ where O_n is constrained to be greater than zero.

For each quantity α_s was allowed to vary in the QCD model, and then the range of α_s values for which the QCD model predictions agree with the data within errors was determined. In particular, the samples obtained using criteria (2) and (3) consist predominantly of 3-jet events from $e^+e^- \rightarrow q\bar{q}g$, in which the gluon emitted is both very energetic and at a large angle with respect to both the quark and antiquark. This leads to an event sample where the number of events in the sample is a quasi-linear function of α_s, and in which the influence of non-perturbative effects which are not calculable in QCD is minimal. For criterion (2), for example, a value of $\alpha_s = 0.19 \pm 0.02$ was obtained matching the QCD model. The predominance of $q\bar{q}g$ in a sample with $O_b \geq 0.3$ is maintained even if $\langle P_t \rangle$ is allowed to vary from 200 MeV to 400 MeV in the model.

The methods described above yield a self-consistent set of α_s values, as illustrated in Fig. 86. On the basis of the results of the three methods they obtained

$$\alpha_s = 0.19 \pm 0.02 \quad \text{(statistical error)}$$
$$0.04 \quad \text{(systematic error)}$$

The large systematic error was mostly due to uncertainties in QCD calculations[16]. For method (2) the range of α_s due to variation in $\langle P_t \rangle$ from 200 to 400 MeV is ± 0.01 and the change in α_s due to different cuts in O_b from $O_b \geq 0.3$ to $O_b \geq 0.2$ or cuts in O_n from no cuts to $|O_n| \leq 0.1$, is -0.01. For method (2), changing the fragmentation function zD(z) to 1-z for u, d, and s quarks and zD(z) to z for c and b quarks does not change the α_s value noticeably.

7.2.3 Triplicity Analysis

The triplicity method has been used by the PLUTO Collaboration[106] analyzing the hadron events from the decay of the T as already mentioned in section 7.1. This method has been specially derived for the treatment of 3-jet events and has been adapted to the particular MARK-J requirements. The energy flow is split for each event into three continuous non-overlapping subregions, adding up to 4π. In each subregion a unit vector $\vec{n}_i$ (i = 1,3) is constructed in the direction of the energy flow vector sum $\Sigma\vec{e}_i$, giving the jet direction. The split into regions is then varied until the 3-jet analog to thrust, the triplicity T_3 is maximized

$$T_3 = (t_1 + t_2 + t_3) \; / \; E_{vis}$$

where t_j is the thrust in subregion j, $t_j = \Sigma_k \vec{e}_k \cdot \vec{n}_j$.

After this procedure, the total energies and directions of the three jets $\vec{E}_i$ and $\vec{n}_i$ (i = 1,3) are submitted to a kinematical

fit balancing the four momenta such that energy momentum conservation is respected under the assumption that all jets are massless. Monte Carlo studies show that the jet momenta reconstructed by this method reproduce the momenta of partons with good accuracy when fragmentation is described by the Feynman & Field model. In the following analysis the jets will be ordered according to their energy, jet 1 being the most energetic and jet 3 the least energetic one.

For events in which the jets are well separated from each other, the energy flow inside jets can be studied. This condition is fulfilled for jet 1 in all events at energies above 12 GeV, while jet 2 and 3 can only be reliably separated in clear 3-jet events ($O_B \geq 03.$) at high energies ($\sqrt{s} \geq 27$ GeV, see below).

Fig. 87 shows the longitudinal energy flow $1/E_j \frac{dE_j}{d\ \cos\varepsilon}$ for the jet 1 and 3 at $\sqrt{s} \approx 30$ and 35 GeV, where ε denotes the angle with respect to the corresponding jet axis $\vec{n}_j$. At these high energies even the least energetic third jets ($\langle E_3 \rangle$ = 6.4, 7.1 GeV, respectively) show an exponentially falling distribution indicating their high degree of collimation around the jet axis. The longitudinal energy flow of jet 3 in the flat events at 30 GeV is compared to that of jet 1 of all the events at 12 GeV $\leq \sqrt{s} \leq$ 17 GeV, which has the same average energy. The two distributions agree with each other within errors, indicating that the fragmentation of gluons, forming ~ 40 % of the least energetic jets at high energies, is not substantially different from that of quarks.

The data in Fig. 87 shows that about 90 % of the jet energy is contained inside a cone of halfangle ~ 20° for a high energy jet and ~ 40° for a low energy jet. For a reliable separation of jet 2 and 3 in the high energy data it is necessary therefore that they be more than about 60° apart. This requirement is naturally met by selecting events with high oblateness in the 'broad' hemisphere, $O_B \geq 0.3$. Fig. 88 shows the double differential distribution $N^{-1} d^2N/dx_3 d\Theta_3$ for the whole hadron sample at high energies $27 \leq \sqrt{s} \leq 37$ GeV, which is dominated by 2-jet events up to an

energy fraction $x_3 = E_3/\sqrt{s} \lesssim 25$ % contained in the third 'jet'. Consequently, since the split up of one jet into 'jet 2' and 'jet 3' is artificial, the average opening angle between these 'jets', $\langle\Theta_{23}\rangle$ decreases with increasing energy fraction x_3, from about 65° at $x_3 \approx 0$ to 55° at $x_3 \approx 10$ %. In contrast to this, genuine 3-jet events ($O_B \gtrsim 0.3$, Fig. 87b) show an opposite behaviour. While events with low x_3 or Θ_{23} are cut out ($O_B \simeq 2x_3 \sin\Theta_{13}$), the average opening angle $\langle\Theta_{23}\rangle$ increases with increasing x_3, being ~ 70° at $x_3 = 10$ % and ~ 90° at $x_3 = 30$ %. The 3-jet events with $O_B \gtrsim 0.3$ thus represent a sample where the two less energetic jets can be reliably separated and their properties can be studied.

Also shown in Fig. 88 as solid curves are the double differential distributions obtained from the QCD model, in remarkable agreement with the data especially for the 3-jet sample in Fig. 88b.

As a further consistency check, the methods of dividing up each event according to the energy flow diagram and triplicity have been compared, particularly the determination of the inter-jet angles Θ_{12} and Θ_{23} for events with $O_b \gtrsim 0.3$, and the results are in good agreement.

The definition of broad jet oblateness O_b is such that for events with the second and third jet well separated, $O_b \approx 2P_t\text{gluon}/\sqrt{s}$, where $P_t$gluon is the gluon transverse momentum with respect to the thrust axis. In the context of the triplicity analyis, an analogous quantity

$$O \equiv 2x_3 \sin\Theta_{13} \simeq 2P_t\text{gluon}/\sqrt{s}$$

has also been used to select a clean sample of three-jet events. The distribution of O is shown in Fig. 89 for the high energy data. The solid curve is the QCD prediction and the dashed and dashed-dotted curves are the contributions of the different parton processes composing the solid curve. By making a cut $O \gtrsim 0.25$, the strong coupling constant α_s was determined and as for the case in

which O_B was used (section 7.2.2) a value of $\alpha_s = 0.19$ with a statistical error of 0.02 was found.

The conclusions obtained by the MARK-J Collaboration from their tests of quantum chromodynamics can be summarized as follows:

a) The rate and the shape of the three jet events can only be explained by QCD and not by any of the other models they have tried.

b) No deviations from QCD have been seen.

c) Correlations of the energy fractions x_1, x_2, x_3, and the angles between the jets have been studied and found to be in agreement with QCD.

d) The strong coupling constant is determined to be $\alpha_s = 0.19 \pm 0.02$ (stat.), ± 0.04 (syst.).

e) Parton energies and directions can be reconstructed using a triplicity method and a kinematic fitting procedure.

7.3 Tests of QCD by the PLUTO Collaboration[107]

The PLUTO Collaboration has analyzed their hadronic events obtained at DORIS and PETRA in the c.m. energy range $9.4 \leq \sqrt{s} \leq 31.05$ GeV with three different methods. QCD predictions for hard gluon emission and soft gluon-quark cascades, the so called QCD leading log approximation[108], denoted in the following paragraphs as QCD-LLA are tested and values for the strong coupling constant α_s are derived using various methods. Two of these methods, transverse momenta in jets and a cluster analysis of the hadron events will be discussed.

7.3.1 Transverse Jet Momentum

The aim of this analysis is to find a quantity which is less sensitive to the hadronization effects of the produced quarks than the single particle transverse momentum. The group has chosen the summed transverse momentum $K_\perp$ for the jets as the quantity to

study the effect of hard gluon bremsstrahlung. For every hadron event the thrust axis is determined using the neutral and charged particles. The transverse jet momentum is defined as

$$K_{\perp} = \Sigma_i |P_{\perp i}| \qquad (23)$$

where $P_{\perp i}$ is the transverse momentum of a particle with respect to the thrust axis. The summation in (23) includes only particles on one side of an arbitrary plane through the thrust axis. This plane is varied randomly and the quantity $K_{\perp}$ is determined for every position of the plane. The final value for $K_{\perp}$ is the average $K_{\perp}$ obtained from the various random plane positions in order to reduce fluctuations.

The $K_{\perp}$ distribution at $\sqrt{s}$ = 9.4, 12.0 and 17.0 GeV are shown in Fig. 90. The data are well desribed by the QCD-LLA calculations[109], a model which is essentially a $q\bar{q}$ model, with the addition of the emission of low energetic gluons. The average P_t in this model is able to rise slowly with increasing c.m. energy in contrast with the naive quark model. At higher energy, $\sqrt{s}$ = 17 GeV, there is some evidence that hard gluon emission is necessary to account for the high $K_{\perp}$ part of the spectrum.

The $K_{\perp}$ distributions of the high energy data are shown in Fig. 91. Above 2.5 GeV in $K_{\perp}$ the tail has become very pronounced and this part of the distribution can only be described by first order QCD[14], that is hard-gluon bremsstrahlung. By comparing the low energy part which is very well described by QCD-LLA, with the high energy part of the distributions the rate of the events where hard gluon effects occur can be determined. The fraction of those events can be related directly to the value of the strong coupling constant α_s. This method enables the PLUTO group to determine α_s without recourse to Monte Carlo calculations involving fragmentation parameters or by counting jets. A value for α_s = 0.19 ± 0.02 (stat. error) ± 0.04 (syst. error) is obtained at $\sqrt{s}$ = 30 GeV.

The systematic error is caused by the cut defining the onset of hard gluon effects in the $K_\perp$ distribution.

7.3.2 Cluster Analysis of Hadronic Events[107]

At the higher PETRA energies the hadron events are characterized by jets, a stream of collimated particles, and the PLUTO group has developed a pattern recognition program to identify in their detector clusters of particles. Particles within an angle of 30° are collected into clusters. Two clusters are merged into one if they are wihtin 30° of each other. When the energy, the sum of the energies of the individual particles contributing to a cluster, exceeds 2 GeV, it is called a jet. The experimental number of jets can then be determined for every hadronic event. The experimentally obtained jet frequency distribution can be compared with model calculations. Fig. 92 shows the jet frequency distributions for some of these models where the underlying parton processes are $q\bar{q}$, $q\bar{q}g$, and a phase space like production of hadrons. The $q\bar{q}$ model predicts a cluster distribution with a peak at two. The $q\bar{q}g$ model shows a slightly wider distribution peaking at three and the phase space calculation shows a wide distribution quite distinct from the others.

The data for the frequency distribution can be well described by a mixture of the $q\bar{q}$ and $q\bar{q}g$ distributions, as is shown in Fig. 93. From the class of 2-jet events the transverse momentum of the quarks is determined to be

$$P_t = (290 \pm 30)\ \text{MeV}$$

The fraction of three-jet events is a measure of the strong coupling constant and determined by this method to be $\alpha_s = 0.15 \pm 0.03$ (stat. error) $\pm$ 0.03 (syst. error).

By identifying the jet with one of the underlying partons one

can reconstruct the energy and direction of the quark or gluon. The parton thrust distribution can then be formed and that distribution after subtraction of the $q\bar{q}$ background is displayed in Fig. 94. The solid curve is the abolute prediction from first order QCD[110] for a vector gluon. The dashed curve is the spin = 0 prediction normalized to the number of events. The spin-one solution is clearly favoured.

7.4 Tests of QCD by the TASSO Collaboration[111]

7.4.1 Determination of the strong coupling constant α_s

The TASSO Collaboration uses in the analysis of their hadronic events the sphericity tensor[112]

$$T_{\alpha\beta} = \Sigma_i P_{i\alpha} P_{i\beta} \qquad \alpha, \beta = x,y,z$$

and i = 1, ..., N particles.

The summation is over the charged particles, which have their momenta measured with the central dectector. The tensor $T_{\alpha\beta}$ has eigen-vectors $\vec{n}_1$, $\vec{n}_2$, $\vec{n}_3$ and the normalized eigen-values

$$Q_k = \frac{\Sigma_i (\vec{P}_i \cdot \vec{n}_k)^2}{\Sigma \vec{P}_i}$$

which satisfy $Q_1 + Q_2 + Q_3 = 1$ and $0 \leq Q_1 \leq Q_2 \leq Q_3$.

The quantity sphericity S and aplanarity A can be expressed in the eigenvalues

$$S = 3/2\ (Q_1 + Q_2)$$
$$A = 3/2\ Q_1$$

and a third quantity Y is defined as

$$Y = \sqrt{3/2}\ (Q_2 - Q_1).$$

The event plane is defined by the eigen-vectors $\vec{n}_2$ and $\vec{n}_3$, the sphericity axis is given by $\vec{n}_1$. As discussed in section 3.3

the QCD model of Ali et al.[16] has several parameters to describe the fragmentation of the quarks into hadrons. They are

i) The average transverse momentum of the quarks, P_t. The distribution for the transverse momentum $k_\perp$ is assumed to be exponential and of the form $\exp(-k_\perp^2 / 2P_t^2)$.

ii) The ratio of the pseudoscalar (P) to vector mesons (V) produced in the fragmentation process $P/(P + V)$.

iii) The function D(z) describing the fragmentation of a quark into a hadron in the Feynman-Field model for u,d, and s quarks depends on a parameter a_F according to

$$D(z) = 1 - a_F + 3a_F (1 - z)^2$$

where $z = (E + P)h / (E + P)q$.

The data at $\sqrt{s}$ = 30 GeV was used by the TASSO group for the determination of α_s. The background from hard photon bremsstrahlung was removed with an angular cut. The angle between $\vec{n}_1$ and the beam direction, Θ_N, was required to be smaller than 80°. A total number of 777 hadronic events remained which are plotted in the triangular plot of Fig. 95 with axes S and A. The events populating the corner with small S and small A are the 2-jet events, the planar events are spread out in the region of large S and small A. The region of $S \geq 0.25$ was used to determine α_s, a region dominated by the planar events due to the effects of hard gluon bremsstrahlung. The parameters α_s and P_t were fitted for various values of the parameters P/P + V and a_F. It was found that the α_s value is relatively independent of the fragmentation parameters. The average result for $\alpha_s = 0.16 \pm 0.04$. All the hadronic events were then fitted using this α_s value obtained in thr restricted area of $S \geq 0.25$ in order to determine the fragmentation parameters in a way which includes the two-jet events. The single particle distribution is most sensitive to the a_F, the P_t of the quarks is most sensitive to the average squared momentum out of the event plane and the multiplicity distribution is sensi-

tive to P/P + V. The parameters obtained in this way are:

$a_F = 0.57 \pm 0.20$, $P_t = 0.32 \pm 0.04$ GeV/c and $P/(P + V) = 0.56 \pm 0.15$. A more precise value of α_s was then obtained by using the above values and fit α_s again in the region of $S \geq 0.25$.

As a final result they obtain $\alpha_s = 0.17 \pm 0.02$ with a systematic error of 0.03 due to uncertanties of the QCD model.

7.4.2 Comparion of the Data with QCD

Having obtained the fragmentation parameters the gross features of the data at $\sqrt{s}$ = 12 and 30 GeV can be compared with the QCD model predictions. The value of α_s at $\sqrt{s}$ = 12 GeV is given by:

$$\alpha_s = \frac{12}{(33 - 2N_f)\ \ell n^s/\Lambda^2}$$

where N_f is the number of flavours taken to be five and Λ is calculated with the α_s value obtained at $\sqrt{s}$ = 30 GeV. Fig. 96a-c display the sphericity, aplanarity and $x = P/P_{beam}$ distribution at $\sqrt{s}$ = 12 GeV and Fig. 96d-f the data at $\sqrt{s}$ = 30 GeV. The agreement between the measurements and the QCD calculations is in all cases excellent.

7.4.3 Study of Details of Three-Jet events

The 77 events with $S \geq 0.25$ and $A \leq 0.08$, the so called planar events, are studied in detail with regard to their shape in order to investigate the detailed properties of the individual jets. The method of generalized sphericity[113] was used to analyze the 3-jet structure. Instead of maximizing the triplicity as discussed in section 7.2.3, an optimal separation on an event by event basis is obtained by minimizing the sum of the sphericities of the individual jets ($S_1 + S_2 + S_3$). Having assigned with this method every charged particle to one of three jets the average momentum

squared, P_t^2, with respect to the individual jet axis can be calculated. The P_t^2 distribution of the 3 x 77 jets at high energy is compared with the distribution obtained for the 2-jet events at low energy. At $\sqrt{s}$ = 12 GeV the P_t^2 is calculated with respect to the two axes found for these events. The behaviour of the P_t^2 is found to be the same in both cases and also the QCD model for $\sqrt{s}$ = 30 GeV compares well with the data as can be seen in Fig. 97. The shape of the three jet events is expressed by the TASSO group in a quantity called the 'trijettiness'[111] defined as:

$$J_3 = \frac{1}{N-3} \sum_{i=1}^{N} \frac{q_{\perp i}^2}{\frac{1}{2} P_t^2}$$

where P_t, the average quark transverse momentum was taken to be 0.33 GeV/c and where $q_{\perp i}$ is the transverse momentum in the event plane with respect to associated jet axis. For a genuine 3-jet event, J_3 is expected to peak near 1 while for a disk like distribution J_3 is larger than 1. The J_3 distribution for the planar 3-jet events is shown in Fig. 97b. The QCD model is in good agreement with the data, but the disk like model (dashed curve) is unable to explain the distribution. The multiplicity distributions for the individual jets is shown in Fig. 97c. The jets are ordered by their energies ($E_i \geq E_2 \geq E_3$) and the data compare again well with the QCD predictions.

The energies of the jets were calculated from the angles between the jets, assuming the underlying partons to have zero mass. The minimum and maximum opening angles between the jets are plotted in Fig. 97d (Θ_{min} and Θ_{max}) for the total hadron sample at $\sqrt{s}$ = 30 GeV. The Θ_{min} distribution is small for 2-jet events and larger for the 3-jet events. Both distributions are well described by the QCD model.

From the detailed comparisons made by the TASSO group of their data with the QCD model the conclusions are that

1) $\alpha_s = 0.17 \pm 0.02$ (statistical error), ± 0.03 (systematic errors). 2) The shape and the detailed properties like P_t^2, multiplicity and angular distributions of the 3-jet events are well described by QCD.

7.4.4 Evidence for a Spin 1 Gluon in Three Jet Events[114]

As discussed in the previous section the TASSO group determines the axes of the three-jet events in the event plane with the generalized sphericity method. Having obtained the angle between the jets and knowing the total c.m. energy, the energy of the individual jets can be easily calculated. The fractional energy for each jet is defined as $x_i = E_i/E_b$ where E_i is the energy of jet i, and E_b is the beam energy. The jet can now be equated with the primordial parton, the quark or gluon. The energies of the partons is ordered such that $x_3 \leq x_2 \leq x_1$ and the relation $x_1 + x_2 + x_3 = 2$ follows from the definition of x_1. In addition, the quantity x_1 is equal to the thrust of the $q\bar{q}g$ system. When the masses of the quarks and gluons are neglected the x_i are determined by the angles Θ_i

$$x_i = \frac{2 \sin\Theta_i}{\sin\Theta_1 + \sin\Theta_2 + \sin\Theta_3}$$

(see Fig. 98a).

Ellis and Karlinar[115] have suggested the angle $\tilde{\Theta}$ to test the vector gluon hypothesis against the scalar gluon possibility. This angle is obtained by boosting the 3-parton system in such a way that parton 2 and 3 are in their rest frame (see Fig. 98b). Neglecting the masses of quarks and gluons $\cos\tilde{\theta}$ can be written as

$$\cos\tilde{\Theta} = \frac{x_2 - x_3}{x_1} = \frac{\sin\Theta_2 - \sin\Theta_3}{\sin\Theta_1}$$

The double differential distributions for vector and scalar

gluons can be expressed in terms of x_1 and x_2 as follows:

$$\text{VECTOR:}\quad \frac{1}{\sigma_0}\frac{d\sigma}{dx_1 dx_2} = \frac{2\alpha_s}{3\pi}\frac{x_1^2 + x_2^2}{(1-x_1)(1-x_2)} + \ldots \text{ cycl. perm. of } 1,2,3$$

$$\text{SCALAR:}\quad \frac{1}{\sigma_0}\frac{d\sigma}{dx_1 dx_2} = \frac{\tilde{\alpha}_s}{3\pi}\frac{x_3^2}{(1-x_1)(1-x_2)} + \ldots \text{ cycl. perm. of } 1,2,3$$

In order to avoid the infrared divergencies from perturbative QCD which are expressed by the $(1- x_i)$ terms in the denominators, the events used for the determination of the spin have a thrust $x_i < 0.90$. The number of 2-jet events are reduced by this cut to about 18 %.

The $\cos\tilde{\theta}$-distribution for events with $1 - x_1 > 0.10$ are shown in Fig. 99. The predictions for the vector goluon (solid curve) and scalar gluon (dashed curve) are drawn normalized to the number of events. The spin 1 case describes the data very good, with a CL of 79 % and the spin 0 case has only a CL of 0.2 %. Various other checks have made like higher moments of the $\cos\tilde{\theta}$ distribution and testing the thrust distribution itself against the two possibilities. In all these cases the spin 1 hypothesis was favoured.

The results of the TASSO group can be summarized as follows:

i) The fragmentation parameters of the Feynman-Field model are determined to be $a_F = 0.57 \pm 0.20$, $P_t = 0.32 \pm 0.04$ GeV/c and $P/P + V = 0.56 \pm 0.15$.

ii) $\alpha_s = 0.17 \pm 0.02$ (stat.), ± 0.03 (syst.).

iii) A good description of the data at $\sqrt{s} = 12$ and $\sqrt{s} = 30$ GeV is obtained by using these fragmentation parameters and α_s.

iv) The 3-jet data at $\sqrt{s} = 30$ GeV is consistent with the QCD model of vector gluons and exclude a scalar gluon with a confidence of about 10^{-4}.

7.5 QCD Tests with the JADE Detector

7.5.1 Three Jet Events[117]

The JADE group has used a model independent way to test the shape of the three jet events. By forming the sphericity tensor (discussed in section 7.4.1) in a similar way as the TASSO group, they are selecting planar events by making a cut in the quantity planarity $Q_2 - Q_1 < 0.1$ where Q_1 and Q_2 are two of the three eigenvalues of the tensor. The planar events are divied by a plane normal to the thrust axis into a narrow and broad jet (see section 7.2.1). The charged and neutral particles contained in the broad jet are boosted to their combined rest system and the details of the shape are then investigated using the boosted four vectors of the particles to calculate the quantities thrust (T^*), average transverse momentum $\langle P_T^* \rangle$ and charge multiplicity n_{ch}^*. If the broad jet consists of two jets, these jets will appear in the boosted system well separated and they will be collinear. Fig. 100 shows the T^*-distribution of the broad jet in its own rest system. This distribution peaks at high thrust, which is indicative for a two jet structure. For comparison the thrust distribution of all the hadron events at $\sqrt{s}$ = 12 GeV are also plotted. The low energy as has been discussed in section 6.3.1 can be completely understood as the production of quarks-antiquark pairs and as a consequence is completely dominated by two jet events. The similarity of the two distributions means that the broad jet has a two jet structure. In Fig. 101 the quantities $\langle P_T^* \rangle$ and the multiplicity n_{ch}^* of the boosted broad jet are compared with the $\sqrt{s}$ = 12 GeV data. Also here the similarity is striking. In conclusion the data show in a model independent way that the planar events at $\sqrt{s}$ = 30 GeV exhibit a three jet structure expected from hard gluon bremsstrahlung.

7.5.2 Determination of α_s [88]

The JADE group followed essentially the same procedure to obtain α_s as the TASSO group (section 7.4.1) and they find $\alpha_s = 0.18 \pm 0.03 \pm 0.03$. The fragmentation parameters are determined from the $x_i = p_i/p_{beam}$, the sphericity, the planarity, and the $\langle P_T^2 \rangle_{out}$ distribution. This last distribution, the average transverse momentum squared out of the event plane, is shown in Fig. 102 together with the QCD prediction.
The fragmentation parameters as defined in section 7.4.1 are found to be $a_F = 0.5 \pm 0.1$, $P_t = 0.34 \pm 0.03$ and $P/(P + V) = 0.5 \pm 0.1$ in good agreement with the values found by the TASSO collaboration. The observed charge multiplicity distribution is also well reproduced by the above mentioned parameters.

The JADE group has in addition investigated whether the jets from the fragmentation of a quark are different from a gluon. Their preliminary result was presented at the Wisconsin Conference [88] and they found some indication that the gluon jet produces higher yield of low energy particles emitted at large angles to the jet axis in agreement with a prediction of Andersson, Gustafson and co-workers [118].

7.6 Summary QCD Tests

From the studies of the four PETRA groups the following picture emerges:

1. The rate and the shape of the three jet events can only be explained by QCD and not by any other model tried sofar.
2. The running coupling constant of the strong interaction ranges from .15 to 0.19. The values reported by the groups are shown in Fig. 103. It has to be noted that in these determinations the QCD correction to the 2-jet graph is not included. The systematic error reported by the groups is 0.03 to 0.04.

3. Parton energies and directions can be reconstructed.
4. The PLUTO and TASSO groups have reported evidence for the vector nature of the gluon using the reconstructed directions and energies of the partons.

FIGURE CAPTIONS

Fig. 71 Experimental distribution as measured by PLUTO of (a) triplicity T_3 (see section 7.2.3) and (b) reconstructed angle Θ_3 between jets compared to Monte Carlo calculations based on various models. (c) The jet axis angular distribution as measured by PLUTO and the theorectical curves for scalar (dashed) and vector (solid) gluons.

Fig. 72 The P_T^2 distribution for hadron events at $\sqrt{s}$ = 13-17 GeV and $\sqrt{s}$ = 27.4-31.6 GeV. The dashed lines are predictions for the quark-antiquark model with the average $P_T(\sigma_q)$ for the quarks 0.30 GeV/c and σ_q = 0.45 GeV/c.

Fig. 73 The average P_T^2 plotted as function of the normalized momentum x for the hadrons at low c.m. energy ($\sqrt{s}$ = 13-17 GeV) and at high energy ($\sqrt{s}$ = 27-32 GeV) as obtained by the PLUTO group. The solid curves are the QCD predictions. The dashed and dashed-dotted curves are $q\bar{q}$ model calculations with different σ_q for the quarks.

Fig. 74 A flat hadronic event in the JADE detector. The solid lines indicate the trajectories of the charged tracks. The dotted lines from the intersection point are the detected neutral particle directions.

Fig. 75 (a) Energy distribution in the event plane for all events of the MARK-J group with $T \leq 0.8$ and $O_B \geq 0.1$ at $\sqrt{s}$ = 27.4, 30 and 31.6 GeV. The radial distance of the data points is proportional to the energy deposited in a 10° bin. The superimposed dashed line represents the distribution predicted by QCD.

(b) Measured and predicted energy distribution in the plane perpendicular to the event plane, which shows only 2-jets.

Fig. 76 A schematic view of the process $e^+e^- \rightarrow q\bar{q}g$, and the

three resulting hadron jets showing the axes used to describe the event.

Fig. 77 Energy flow diagrams for two high energy hadronic events viewed in the major-thrust plane.

Fig. 78 Energy flow diagram. Two events measured at $\sqrt{s}$ = 12 GeV with the lines showing the direction and magnitude of energy deposited in the calorimeter displayed in two projections. The events appear to have a multi-jet structure in the thrust-major plane. The view in the thrust-minor plane shows the events are flat.

Fig. 79 The broad jet oblateness distribution $1/N\ dN/dO_b$ for all hadron events at $\sqrt{s}$ = 12 GeV. The dotted curve is the prediction of the two-quark-antiquark model with $\langle P_t \rangle$ = 350 MeV.

Fig. 80(a) The narrow jet oblateness distribution $1/N \cdot dN/dO_N$ for all hadron events with measured energy $E_{vis} \geq 0.7\sqrt{s}$. The data are compared to the predictions of the QCD model and to two quark-antiquark models with $\langle P_t \rangle$ = 300 MeV and 500 MeV, respectively.

(b) The broad jet oblateness distribution $1/N \cdot dN/dO_b$ under the same condition as (a).

(c) The thrust distribution of the narrow jets for events with $O_b \geq 0.3$. Also shown are the various model predictions including a flattened $q\bar{q}$ (500, 300) discussed in the text. Note that the narrow jet thrust distribution is consistent with thrust distribution of all the hadron event labelled 'ALL DATA'.

(d) The thrust distribution of the broad jets for events with $O_b \geq 0.3$. The curves are discussed in the text.

Fig. 81(a) Energy flow diagram in the thrust-major plane for high energy data (27-31.6 GeV) with $T \geq 0.9$. The solid line is the prediction of QCD.

(b) The same as (a) for events with $0.8 \leq T \leq 0.9$ and broad

jet oblateness $O_b \geq 0.1$

(c) Same as (a) for events with $T < 0.8$ and $O_b \geq 0.1$

Fig. 82 The unfolded energy flow diagram of Fig. 81c as compared to QCD, the quark model ($<P_t> = 500$ MeV) and a mixed $q\bar{q}$ and phase space model (see text).

Fig. 83 The broad jet oblateness distribution $1/N\ dN/dO_B$. The data are compared to the predictions of the QCD and $q\bar{q}$ models. The cut at $O_B = 0.3$ is also indicated.

Fig. 84(a) Energy flow diagram in the thrust-major plane for events with $O_B \geq 0.3$, for the high energy data ($\sqrt{s}$ = 27.4-36.6 GeV) and the low energy data ($\sqrt{s}$ = 12-22 GeV), compared to the predictions of QCD at high energy and of the phase space model. The thrust distribution $1/N\ dN/dT$ for each individual jet is shown beside the corresponding jet in the energy flow diagram.

(b) The unfolded energy flow diagram of Fig. 84a compared with the QCD and $q\bar{q}$ models.

(c) The two-dimensional distribution in the opening angles between the jets Θ_{12} and Θ_{23}, compared with QCD predictions.

Fig. 85(a) The energy flow diagram in the thrust-minor plane for the high energy events (27.4-36.6 GeV) with $O_B \geq 0.3$, compared with the predictions of the QCD, $q\bar{q}$ and phase space models.

(b) The unfolded energy flow diagram of Fig. 85a. Here the third jet is shown above the second jet at $\sim 180^{\circ}$.

(c) The minor distribution $1/N\ dN/dF_{minor}$ where F_{minor} is defined for the entire event (see text).

Fig. 86 The left graph: the average value of oblateness $<O_b>$ for all events with $E_{vis} \geq 0.7\sqrt{s}$ as a function of α_s in the QCD model. The right graph: the fraction of hadronic events $O_b \geq 0.3$ (σ_{3j}) as a function of α_s com-

puted by varying α_s in the QCD model.

Fig. 87(a) The quantity 1/E dE/dcosε is plotted vs. cosε for jet1 and jet3. ε is the angle between the measured energy flow element and the jet axis. The lowest energy jet from the 30 GeV data is compared to the highest energy jet from the 12 GeV data (histrogram). The solid line is the QCD prediction.

(b) The highest and lowest energy jets from the ≈ 35 GeV data sample are compared to QCD (solid lines).

Fig. 88 The observed double differential cross section for three jets after kinematic fitting is plotted for

(a) all events and

(b) for events with broad jet oblateness greater than 0.3. Since two variables are sufficient to describe three body kinematic with total momentum and energy constrained, this gives a complete description of the events in terms of three jets. The two variables chosen here are Θ_{23}, the angle between the second and third jets, and x_3, the normalized momentum of the third jet. The data (solid points) agree with the predictions of QCD (solid curves).

Fig. 89 The parton oblateness distribution for the hadronic events at high energy. The solid curve is the QCD prediction. The dashed and dashed-dotted curves are the parton processes as indicated.

Fig. 90 The distribution $1/N \cdot dN/dK_\perp$ ($dP/dK_\perp$) at the c.m. energies, $\sqrt{s}$ = 9.4, 12.0, 17.0 GeV. The dashed curves are the predictions from the QCD-LLA calculations. The curves are the predictions of the QCD-LLA plus the first order QCD corrections.

Fig. 91 The $dP/dK_\perp$ distributions at the c.m. energies $\sqrt{s}$ = 27.5, 30.0, 31.05 GeV. The curves are as in Fig. 90.

Fig. 92 The jet frequency distributions for various model calculations as indicated in the figure.

Fig. 93 The measured frequency distribution (closed circles) and the prediction for this distribution of a QCD model with a mixture of $q\bar{q}$ and $q\bar{q}g$ events (open circles).

Fig. 94 The parton thrust distribution for the events with three jets. The solid curve is the absolute prediction for the spin=1 vector gluon, the dashed curve the prediction for spin=0.

Fig. 95 Distribution of the observed events as a function of sphericity S and aplanarity A for the data at c.m. energy W = 30 GeV. The events with $S \geq 0.25$ are projected onto the S and A axes as histograms. The curve is the result of fitting the QCD model to all the events (see text).

Fig. 96 Comparison of the QCD model (curves at W = 12 GeV for a) sphericity, b) aplanarity, c) the single charged particle inclusive x-distriubtion; and at W = 30 GeV for d) S, e) A, and f) x.

Fig. 97(a) Observed transverse momentum distribution of the hadrons from the planar region $S \geq 0.25$ and $A \leq 0.08$ with respect to three axes at W = 30 GeV and the same quantity for all hadron events at W = 12 GeV (open circles) with respect to two axes. The curve is the prediction of the QCD model.

(b) Comparison of the trijettiness distributon for the planar events at W = 30 GeV with the distribution of disk-like events (dashed curve) and the QCD model (solid curve). The curves are normalized to the number of observed events.

(c) Observed charged multiplicity distributions for the jets of highest (E_1), medium (E_2), and lowest (E_3) energy for the events in the planar region at W = 30 GeV.

Fig. 97(d) Distribution of the smallest and largest angle between any of the three jets for all hadron events at W = 30 GeV. The curves are the results of the QCD model.

Fig. 98(a) Momenta and angles of a $q\bar{q}g$ final state in the center-of-momentum frame.

(b) The $q\bar{q}g$ final state transformed to the rest frame of particles 2 and 3.

Fig. 99 Observed distribution of the data in the region $1 - x_1 \geq 0.10$, as a function of the $\cos\tilde{\theta}$ angle. The solid line is the prediction for a vector gluon, the dashed line the prediction for the scalar gluon. Both curves are normalized to the number of events in the histogram.

Fig. 100 The observed distribution of T^* as defined in the text for the broad jet of planar events compared with the two-jet thrust distribution at $\sqrt{s}$ = 12 GeV.

Fig. 101 The observed $\langle P_T \rangle$ and $n_{charged}$ distribution of the broad jet at $\sqrt{s} \simeq 30$ GeV in its rest system compared with the two-jet events at $\sqrt{s}$ = 12 GeV.

Fig. 102 The measured distribution of the $\langle P_T^2 \rangle$ out of the event plane, the histogram is the QCD calculation.

Fig. 103 The α_s values obtained by the four groups.

PLUTO

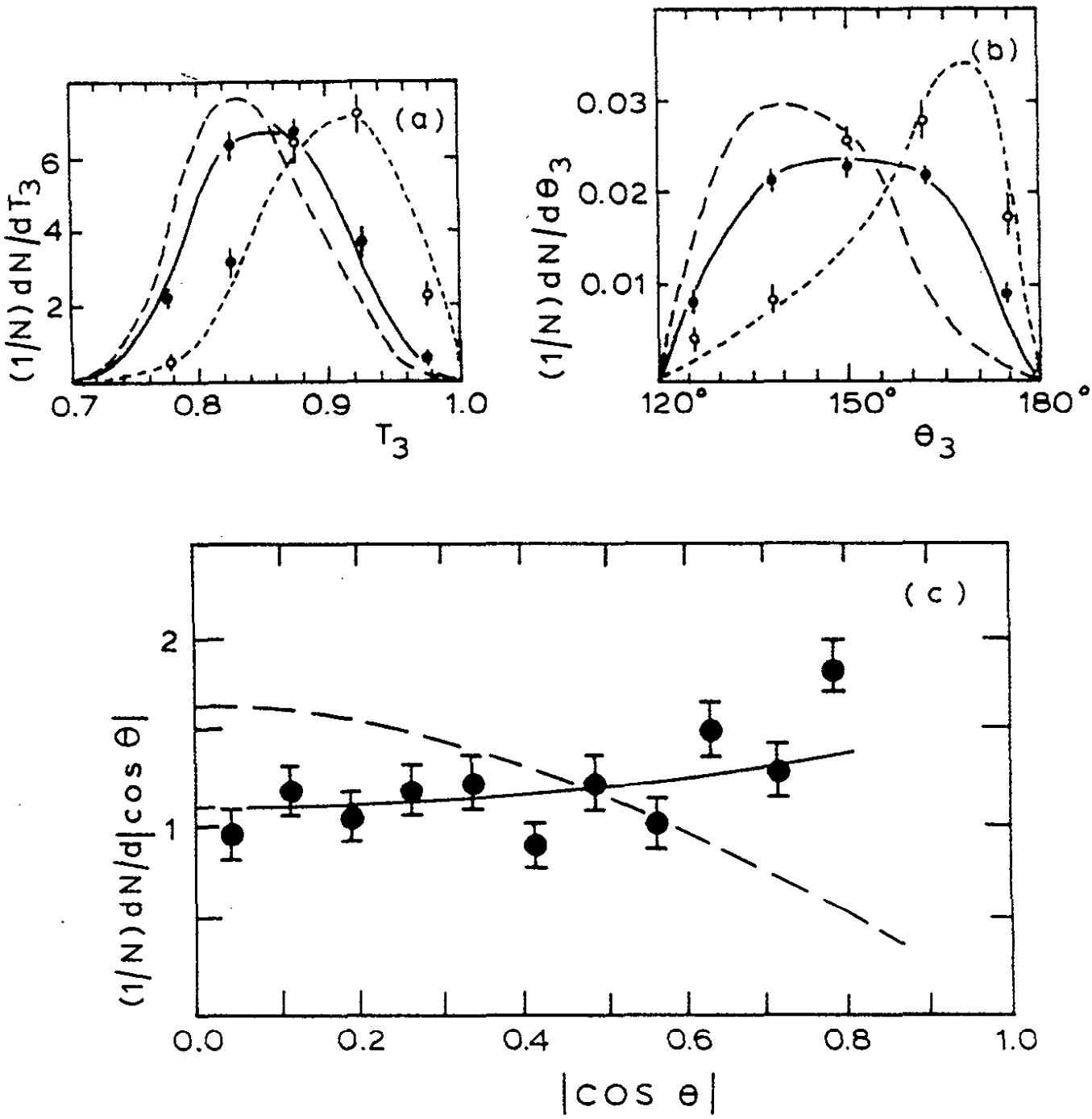
(a)
(1/N) dN/dT3
T3
0.7
0.8
0.9
1.0
2
4
6
(b)
(1/N) dN/dθ3
θ3
120°
150°
180°
0.01
0.02
0.03
(c)
(1/N) dN/d|cos θ|
|cos θ|
0.0
0.2
0.4
0.6
0.8
1.0
1
2

Fig. 71

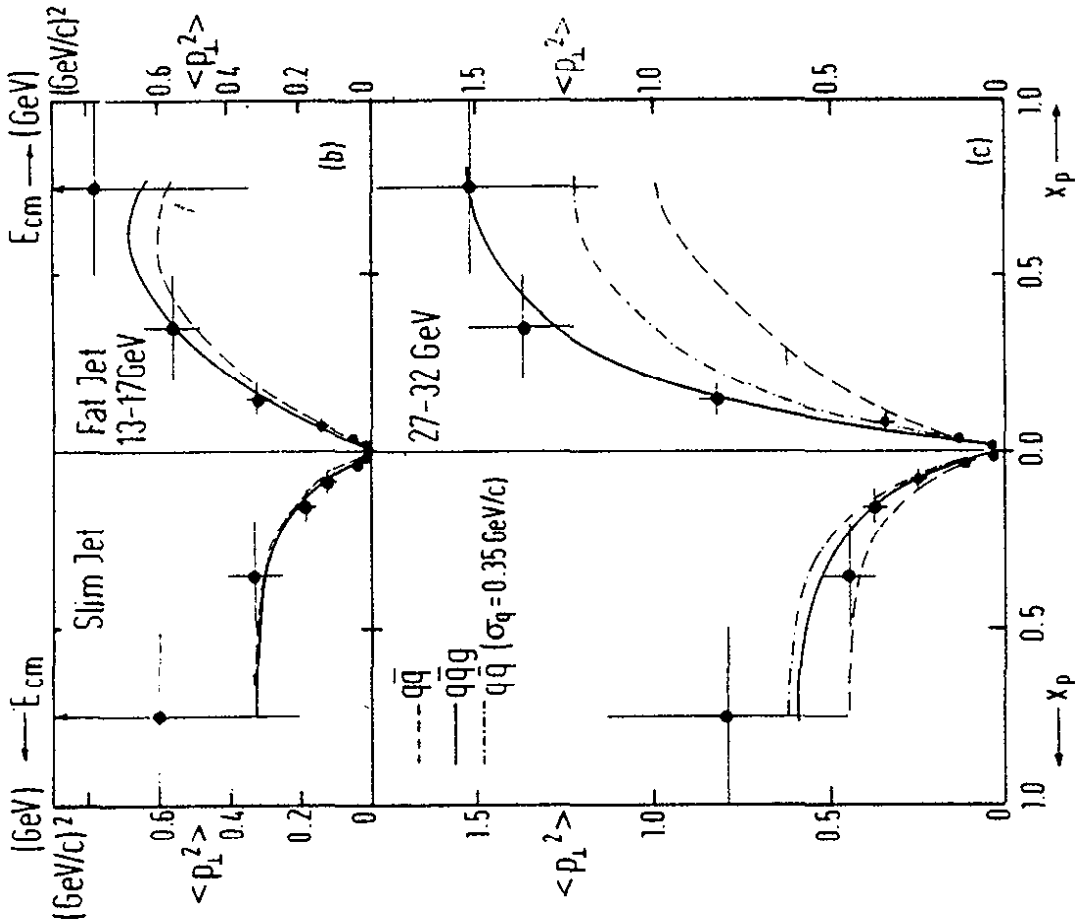
Ecm → (GeV)
(GeV/c)²
Slim Jet
Fat Jet
13-17GeV
27-32 GeV
(b)
(c)
<p_T²>
x_p
qq̄
qq̄g
qq̄ (σ_q = 0.35 GeV/c)

Fig. 73

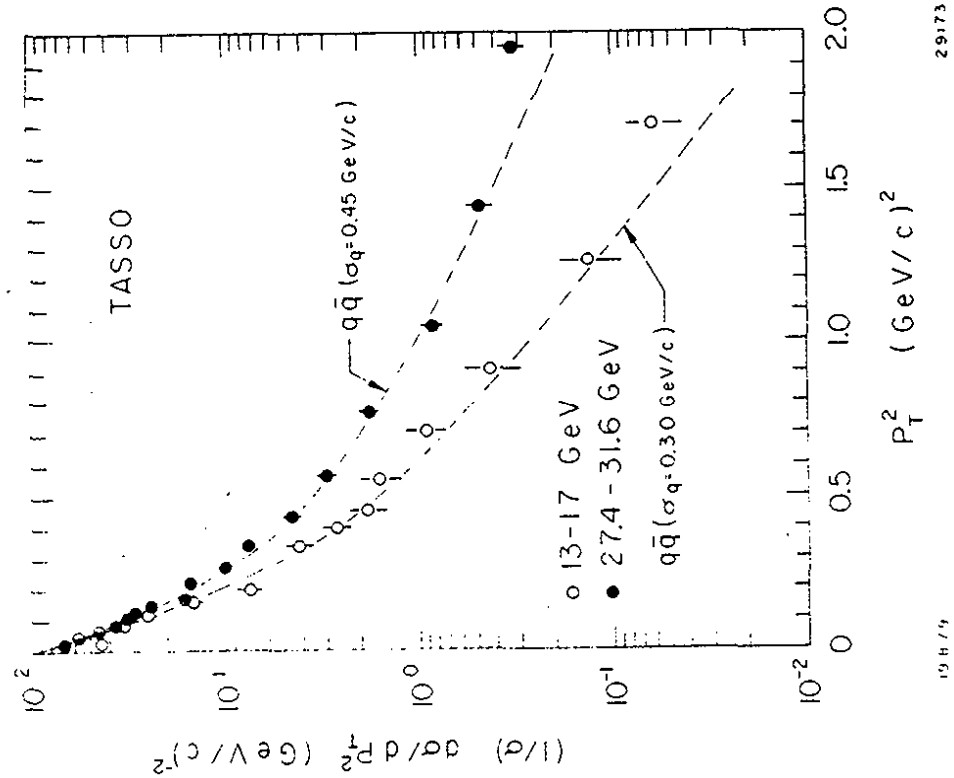
TASSO
qq̄ (σ_q=0.45 GeV/c)
qq̄ (σ_q=0.30 GeV/c)
o 13-17 GeV
• 27.4 - 31.6 GeV
(1/σ) dσ/dP_T² (GeV/c)^-2
P_T² (GeV/c)²
29.73

Fig. 72

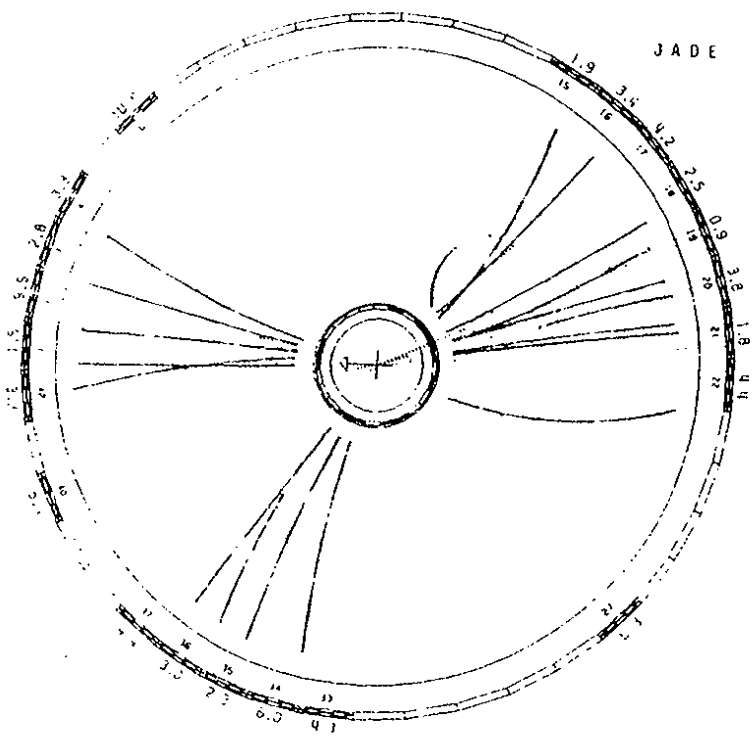

Fig. 74

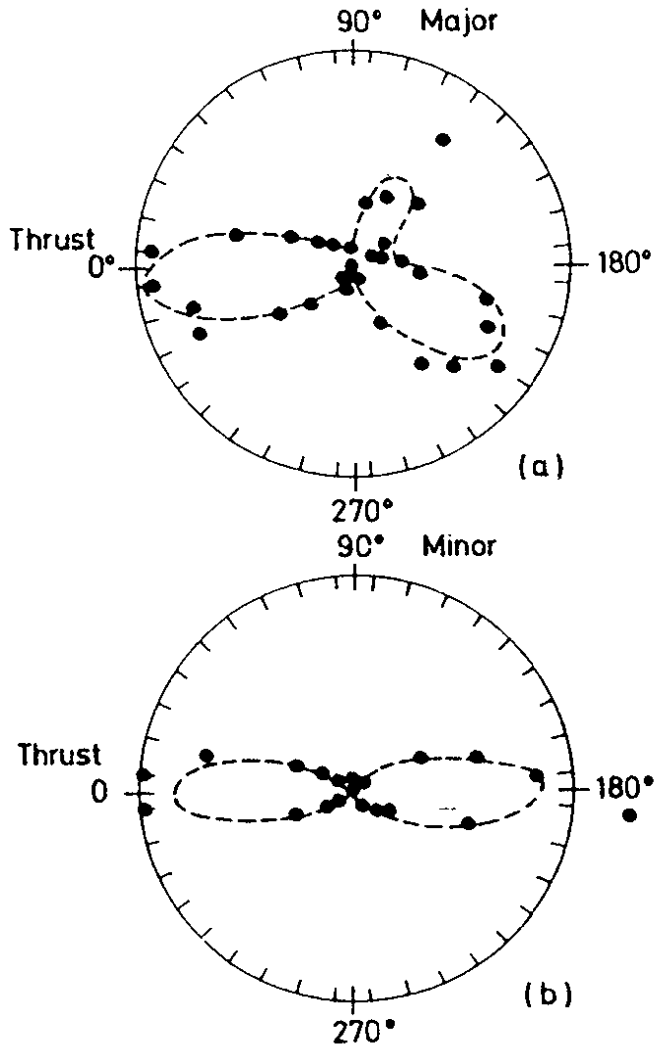

Fig. 75

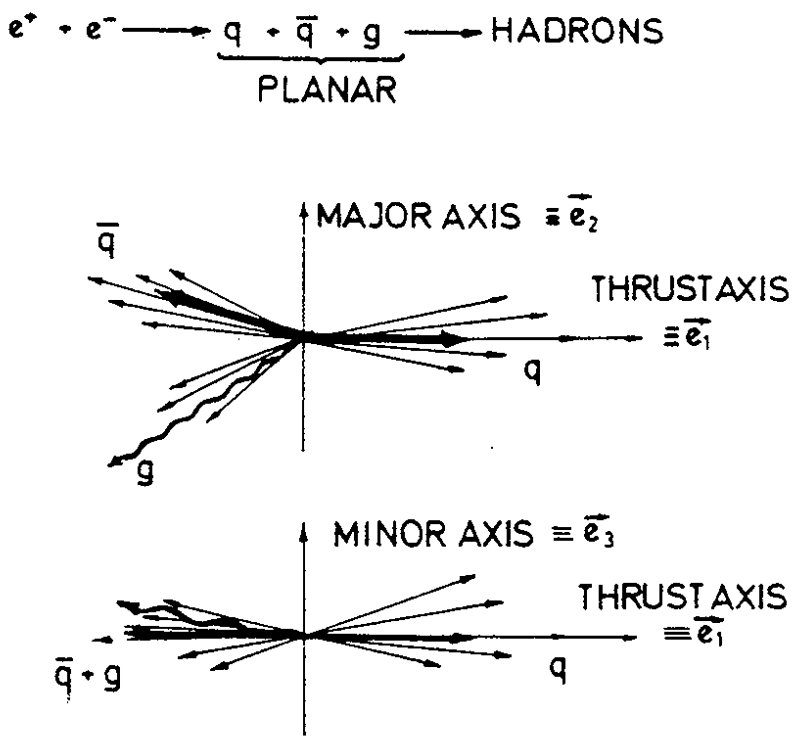
e⁺ + e⁻ → q + q̄ + g → HADRONS
PLANAR
MAJOR AXIS ≡ e₂
q̄
THRUST AXIS
≡ e₁
q
g
MINOR AXIS ≡ e₃
THRUST AXIS
≡ e₁
q̄ + g
q

Fig. 76

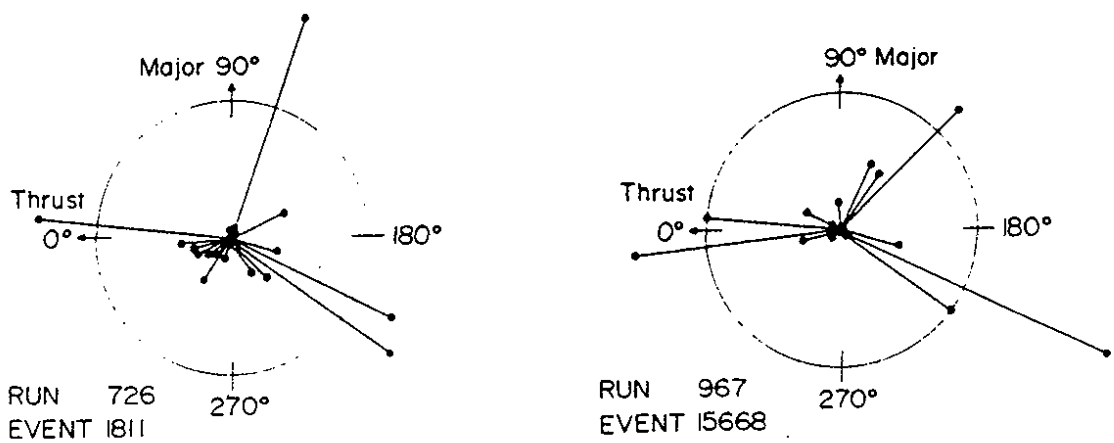
Major 90°
Thrust
0°
180°
270°
RUN 726
EVENT 1811
90° Major
Thrust
0°
180°
270°
RUN 967
EVENT 15668

Fig. 77

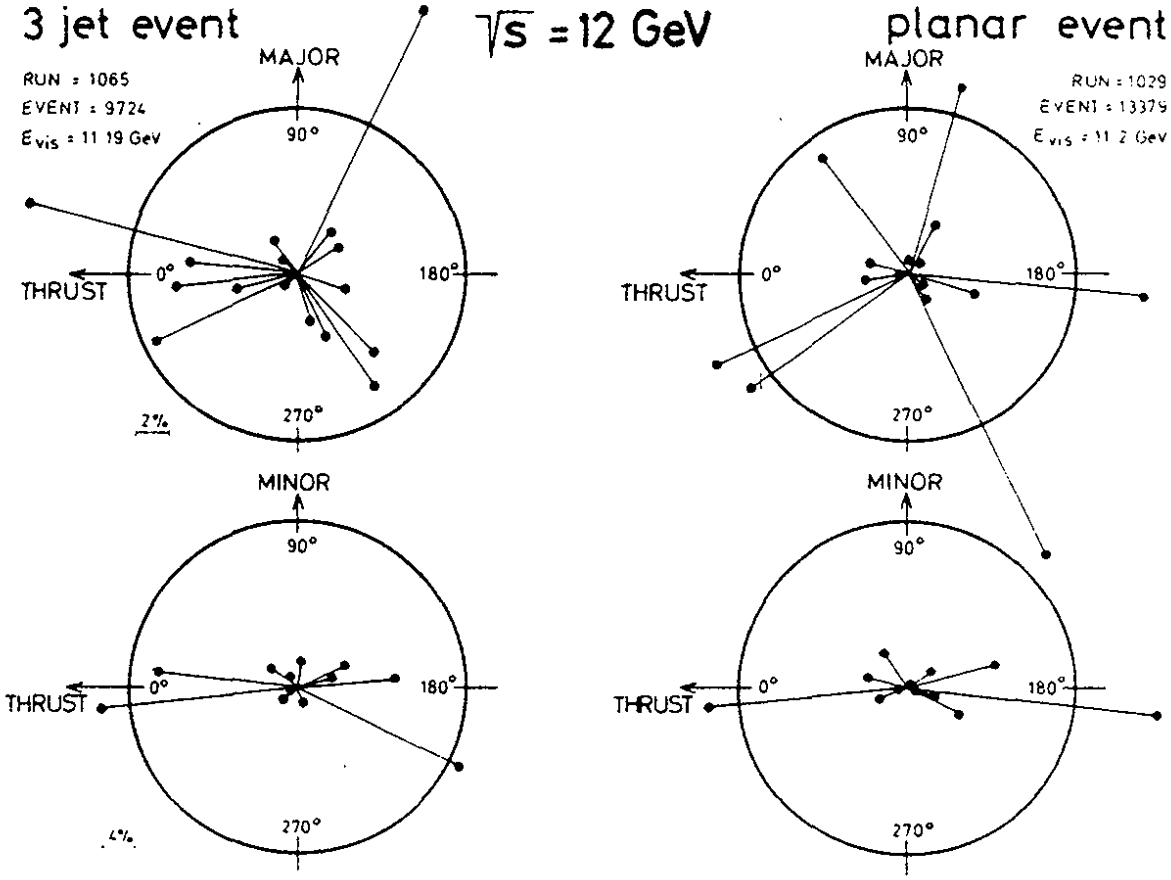
3 jet event
√s = 12 GeV
planar event
RUN = 1065
EVENT = 9724
E_vis = 11.19 GeV
RUN = 1029
EVENT = 13379
E_vis = 11.2 GeV
MAJOR
MINOR
THRUST
0°
90°
180°
270°
2%
4%

Fig. 78

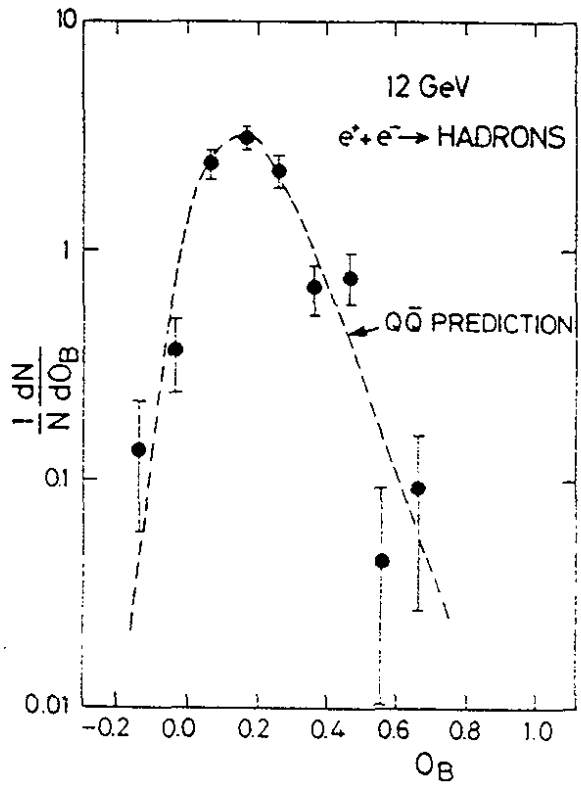
12 GeV
e⁺+e⁻→ HADRONS
QQ̄ PREDICTION
1/N dN/dO_B
O_B
10
1
0.1
0.01
-0.2
0.0
0.2
0.4
0.6
0.8
1.0

Fig. 79

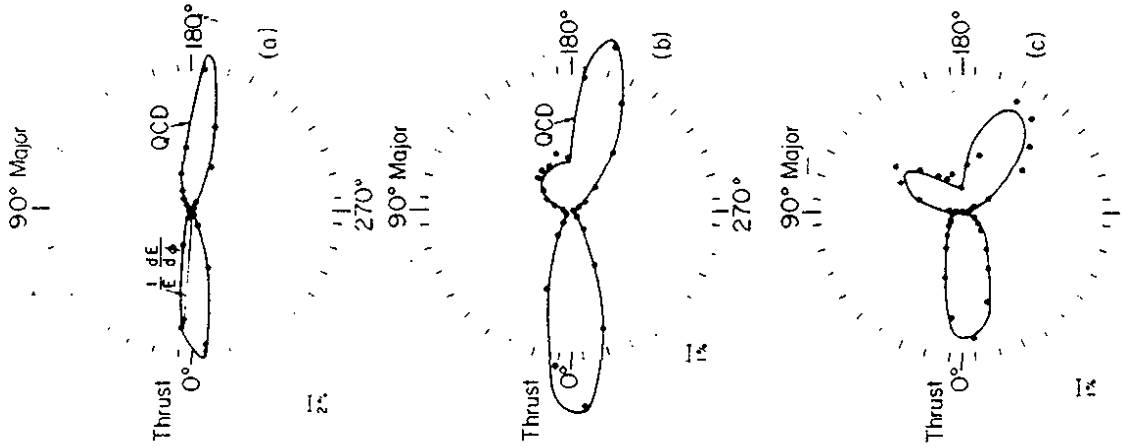
90° Major
Thrust
0°
180°
QCD
(a)
(b)
(c)
270°

Fig. 81

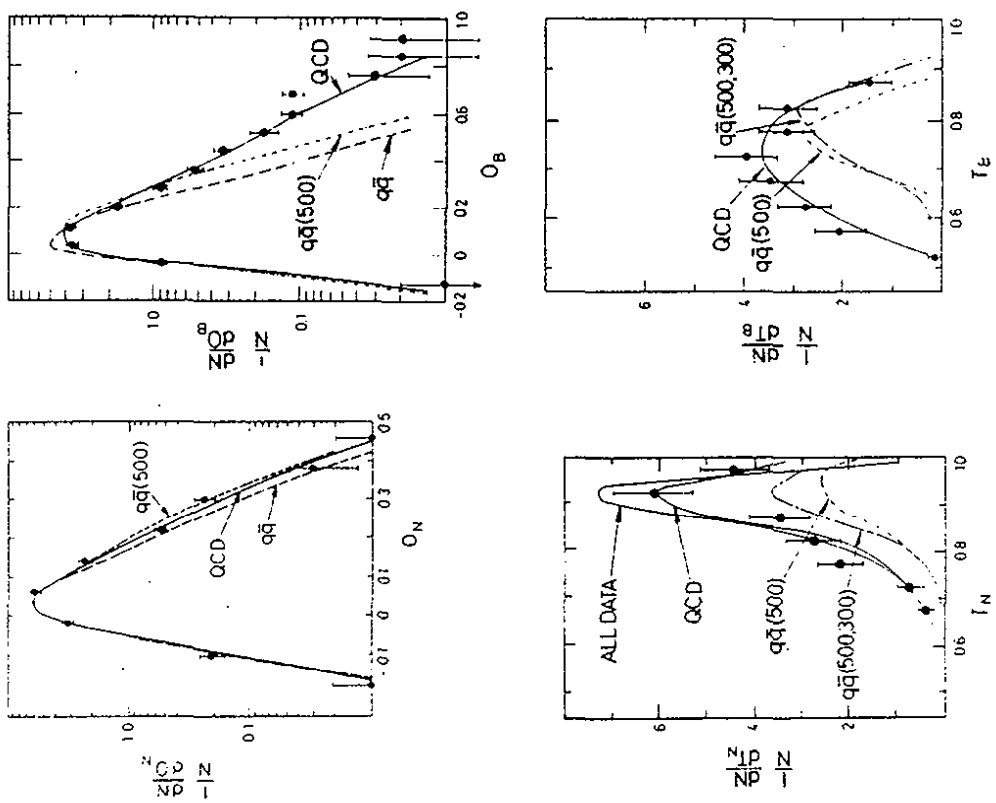
QCD
qq̄(500)
qq̄
qq̄(500,300)
ALL DATA

Fig. 80

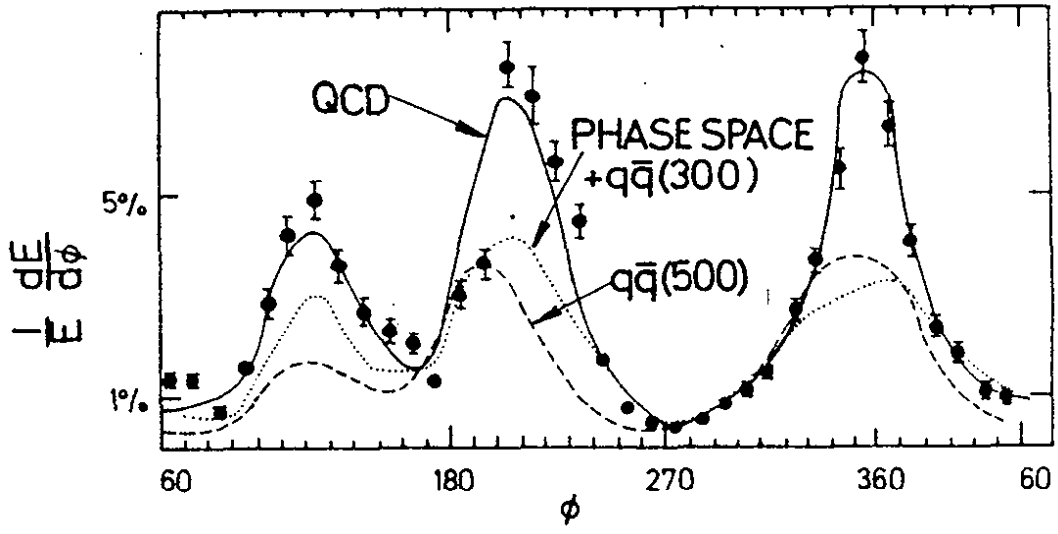
QCD
PHASE SPACE
+qq̄(300)
qq̄(500)
5%
1%
60
180
270
360
60
φ

Fig. 82

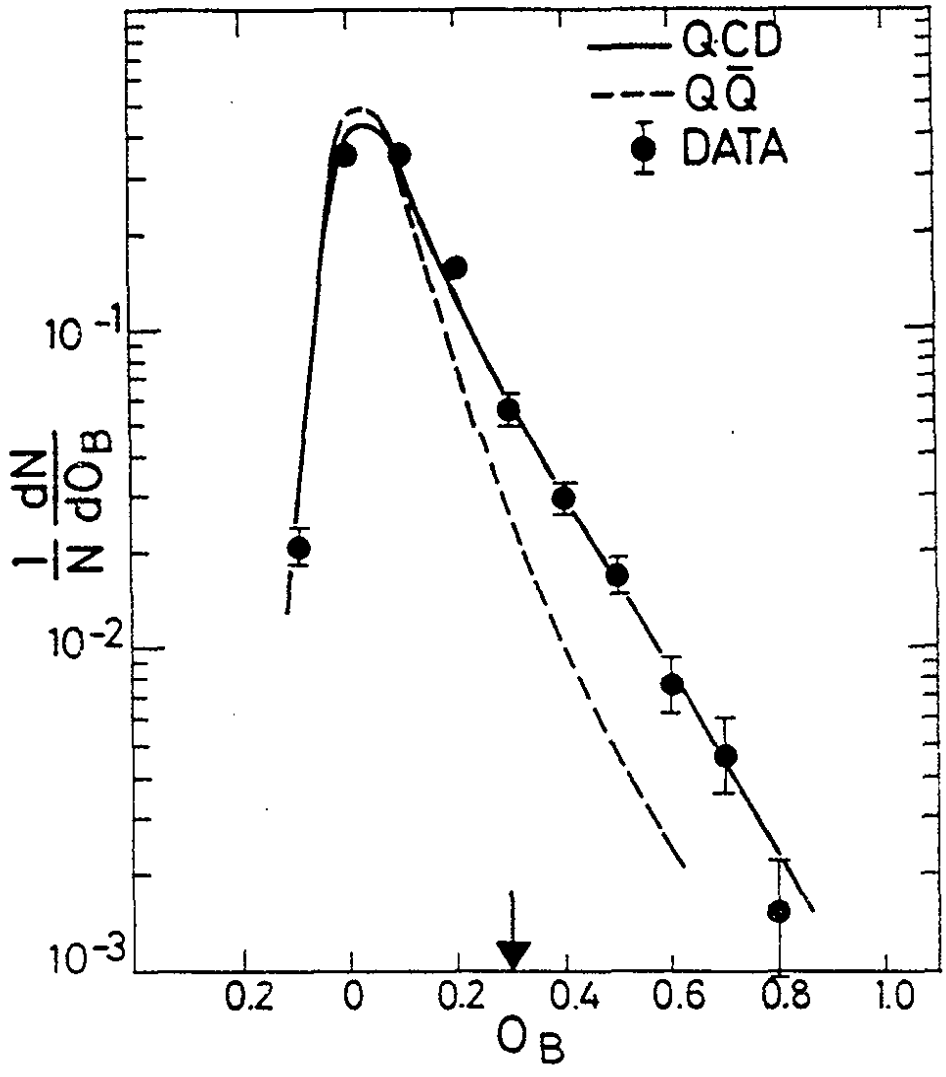
QCD
QQ̄
DATA
10 -1
10-2
10-3
0.2
0
0.2
0.4
0.6
0.8
1.0
O B

Fig. 83

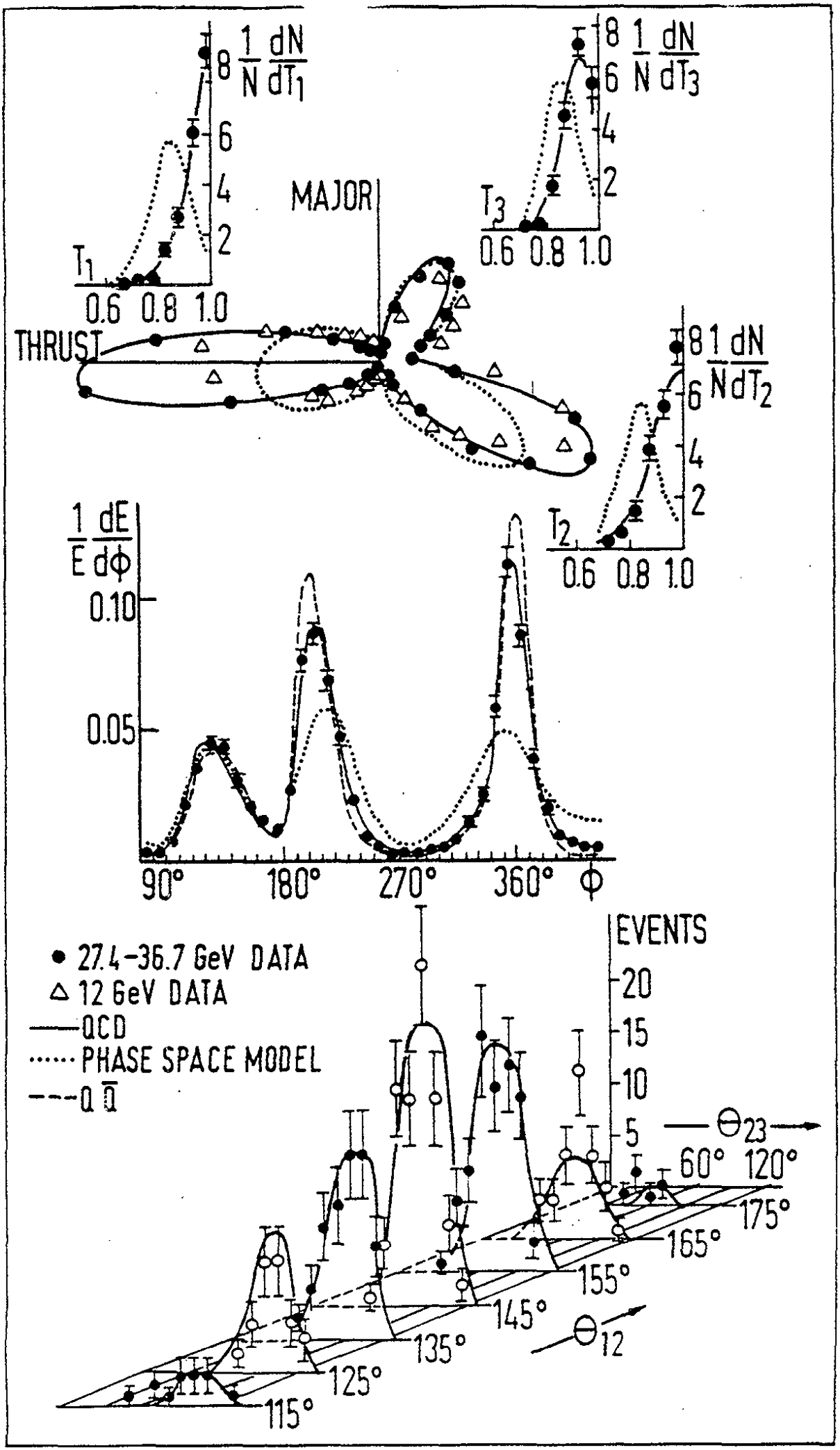
1/N dN/dT1
T1
0.6 0.8 1.0
MAJOR
THRUST
1/N dN/dT3
T3
0.6 0.8 1.0
1/N dN/dT2
T2
0.6 0.8 1.0
1/E dE/dΦ
0.10
0.05
90° 180° 270° 360° Φ
EVENTS
20
15
10
5
• 27.4–36.7 GeV DATA
△ 12 GeV DATA
QCD
PHASE SPACE MODEL
Q Q̄
Θ23
60° 120°
175°
165°
155°
145°
135°
125°
115°
Θ12

Fig. 84

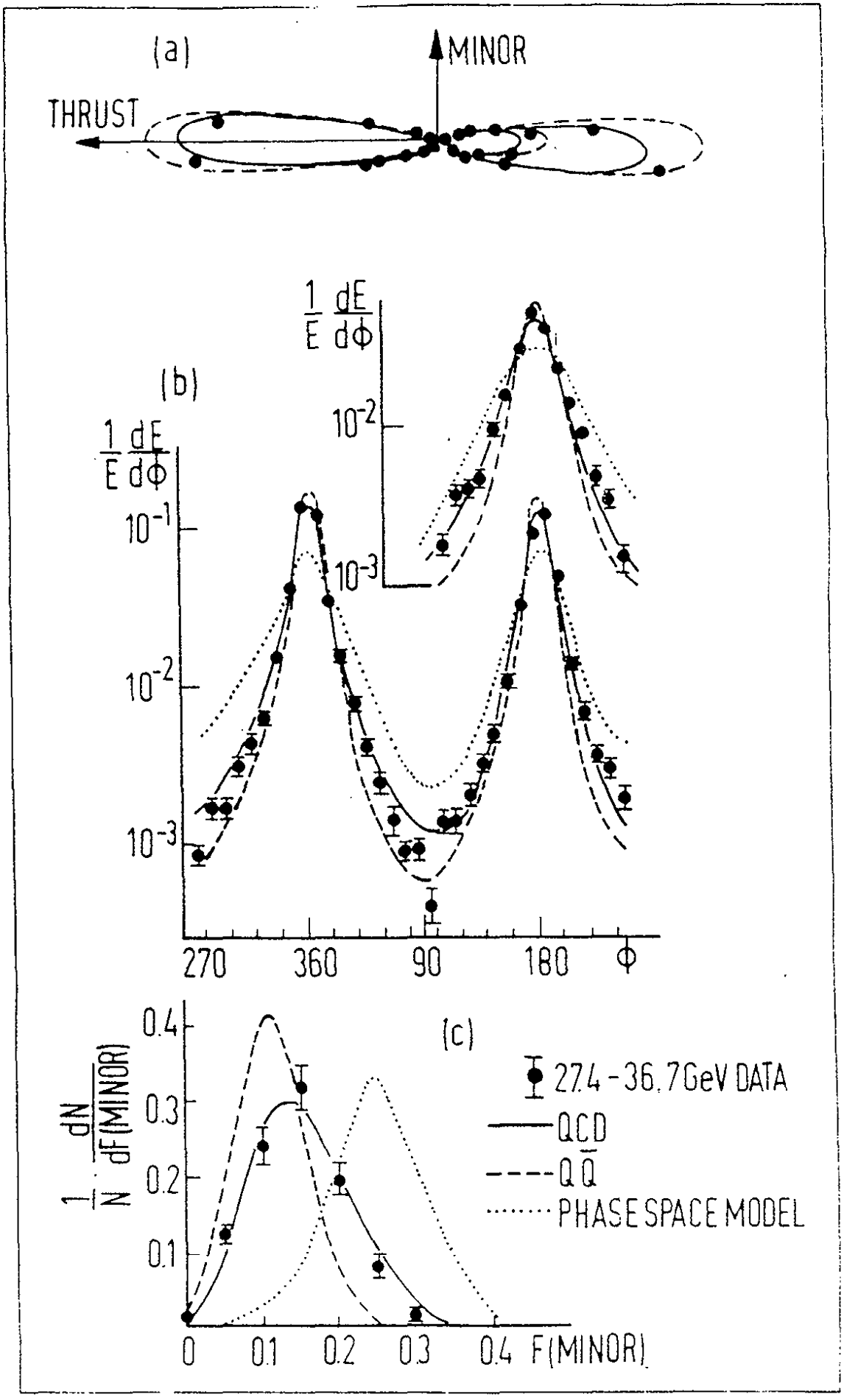
(a)
MINOR
THRUST
(b)
$\frac{1}{E}\frac{dE}{d\Phi}$
10^{-1}
10^{-2}
10^{-3}
270
360
90
180
Φ
(c)
$\frac{1}{N}\frac{dN}{dF(MINOR)}$
0.4
0.3
0.2
0.1
0
0.1
0.2
0.3
0.4
F(MINOR)
27.4 - 36.7 GeV DATA
QCD
Q Q̄
PHASE SPACE MODEL

Fig. 85

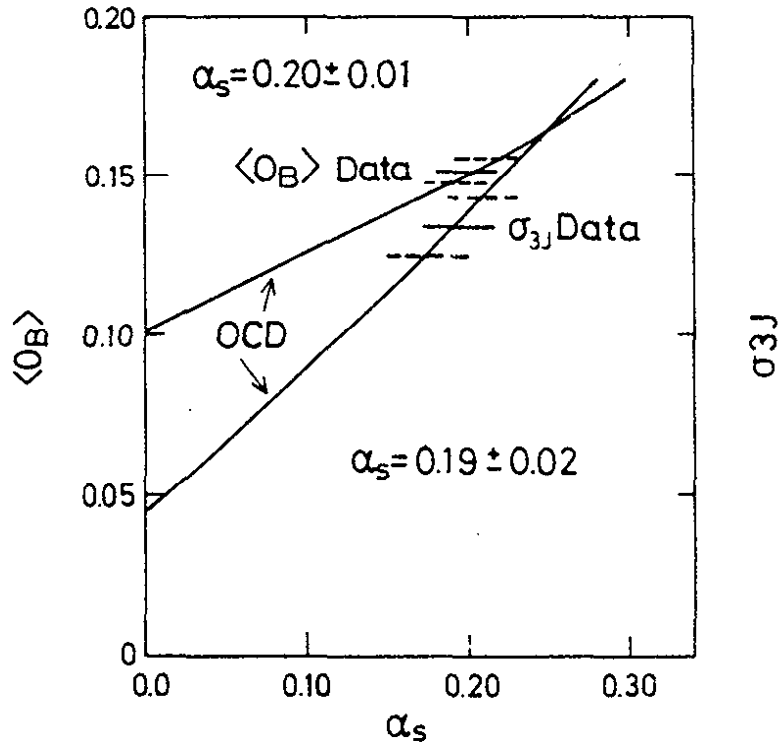
0.20
0.15
0.10
0.05
0
0.0
0.10
0.20
0.30
α_s
$\langle O_B \rangle$
σ_{3J}
$\alpha_s = 0.20 \pm 0.01$
$\langle O_B \rangle$ Data
σ_{3J} Data
QCD
$\alpha_s = 0.19 \pm 0.02$

Fig. 86

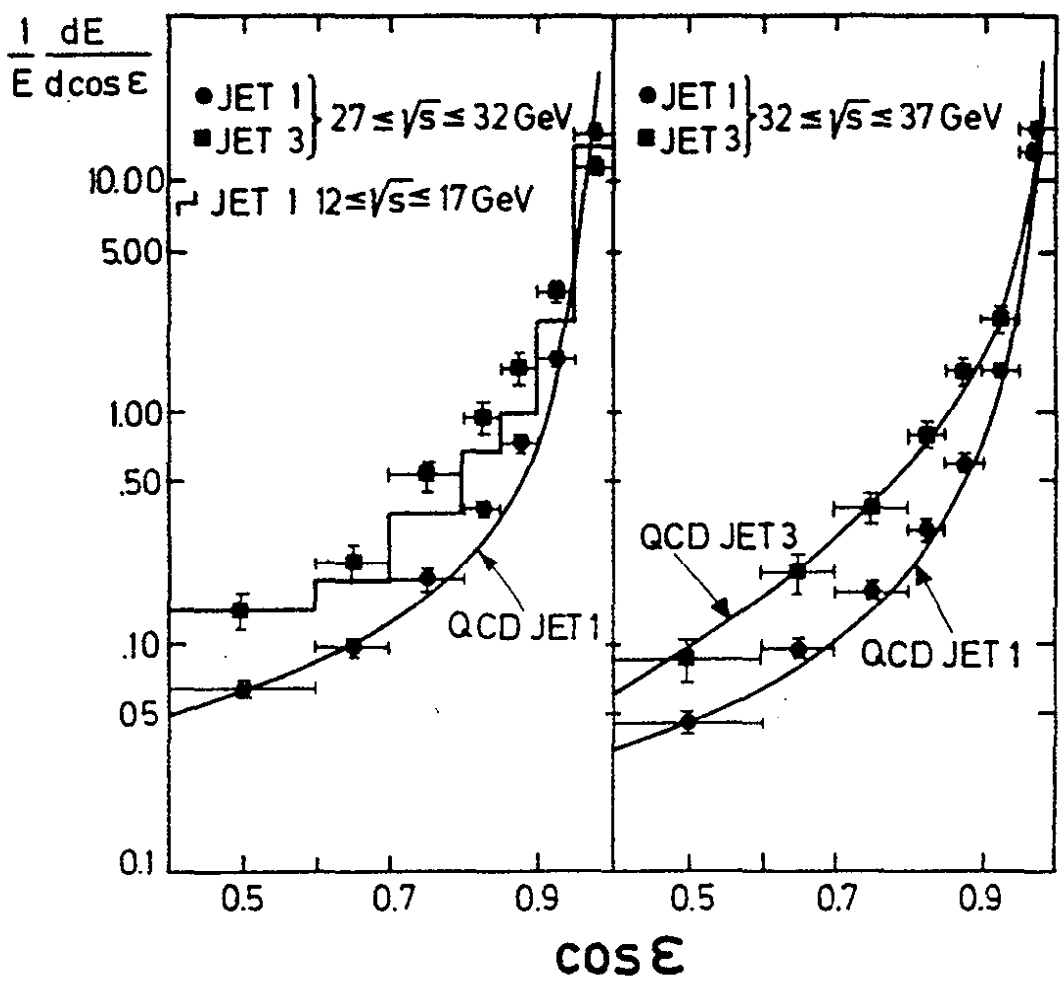
$\frac{1}{E}\frac{dE}{d\cos\varepsilon}$
JET 1
JET 3
$27 \le \sqrt{s} \le 32$ GeV
JET 1 $12 \le \sqrt{s} \le 17$ GeV
$32 \le \sqrt{s} \le 37$ GeV
10.00
5.00
1.00
.50
.10
05
0.1
QCD JET 1
QCD JET 3
0.5
0.7
0.9
$\cos\varepsilon$

Fig. 87

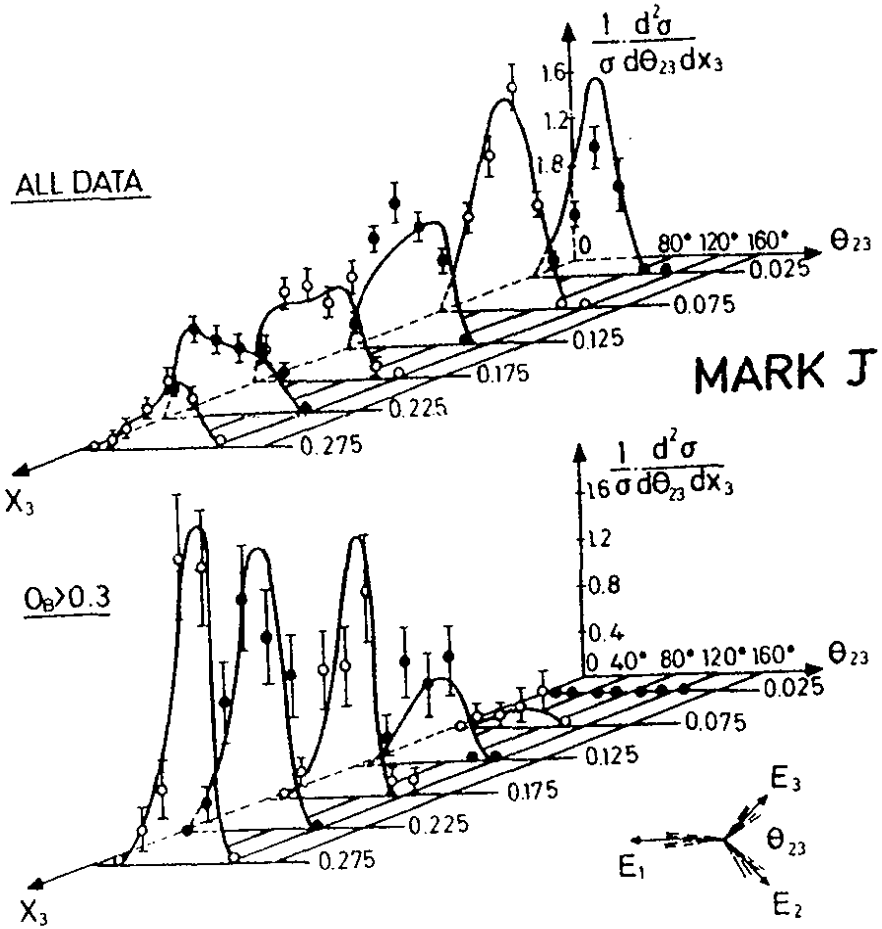
ALL DATA
$\frac{1}{\sigma}\frac{d^2\sigma}{d\theta_{23}dx_3}$
1.6
1.2
0.8
0
80° 120° 160°
θ_{23}
0.025
0.075
0.125
0.175
0.225
0.275
X_3
MARK J
O_B>0.3
0.4
40°
E_3
E_1
E_2

Fig. 88

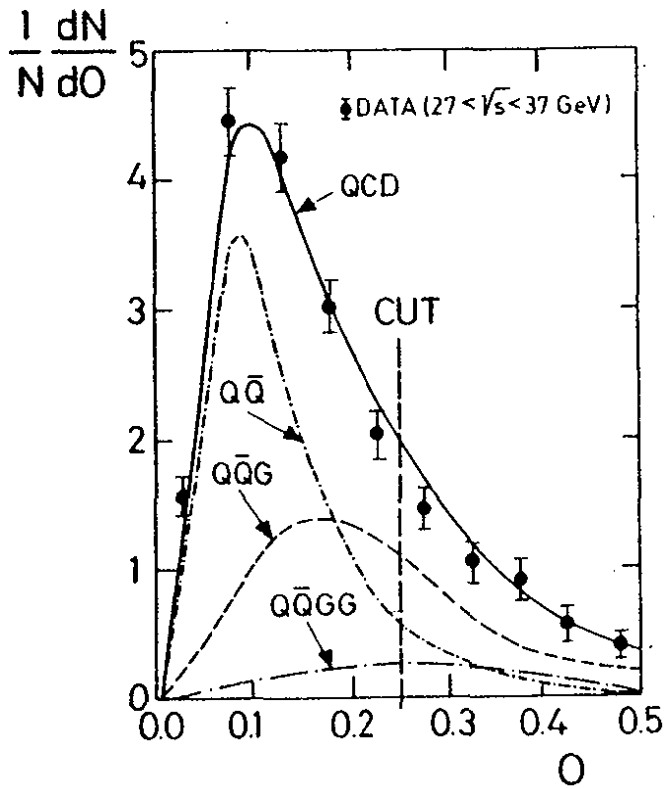
$\frac{1}{N}\frac{dN}{dO}$
DATA (27 < $\sqrt{s}$ < 37 GeV)
QCD
CUT
$Q\bar{Q}$
$Q\bar{Q}G$
$Q\bar{Q}GG$
0.0
0.1
0.2
0.3
0.4
0.5
O

Fig. 89

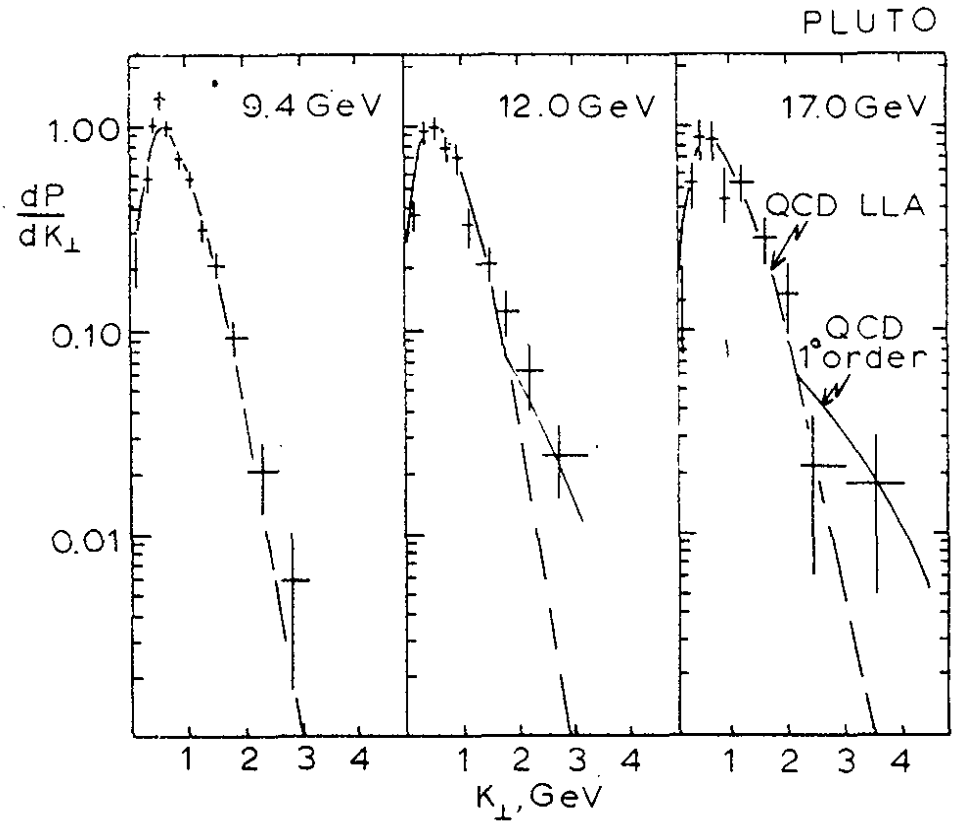
PLUTO
9.4 GeV
12.0 GeV
17.0 GeV
QCD LLA
QCD
1° order
1.00
0.10
0.01
dP/dK⊥
1 2 3 4
K⊥, GeV

Fig. 90

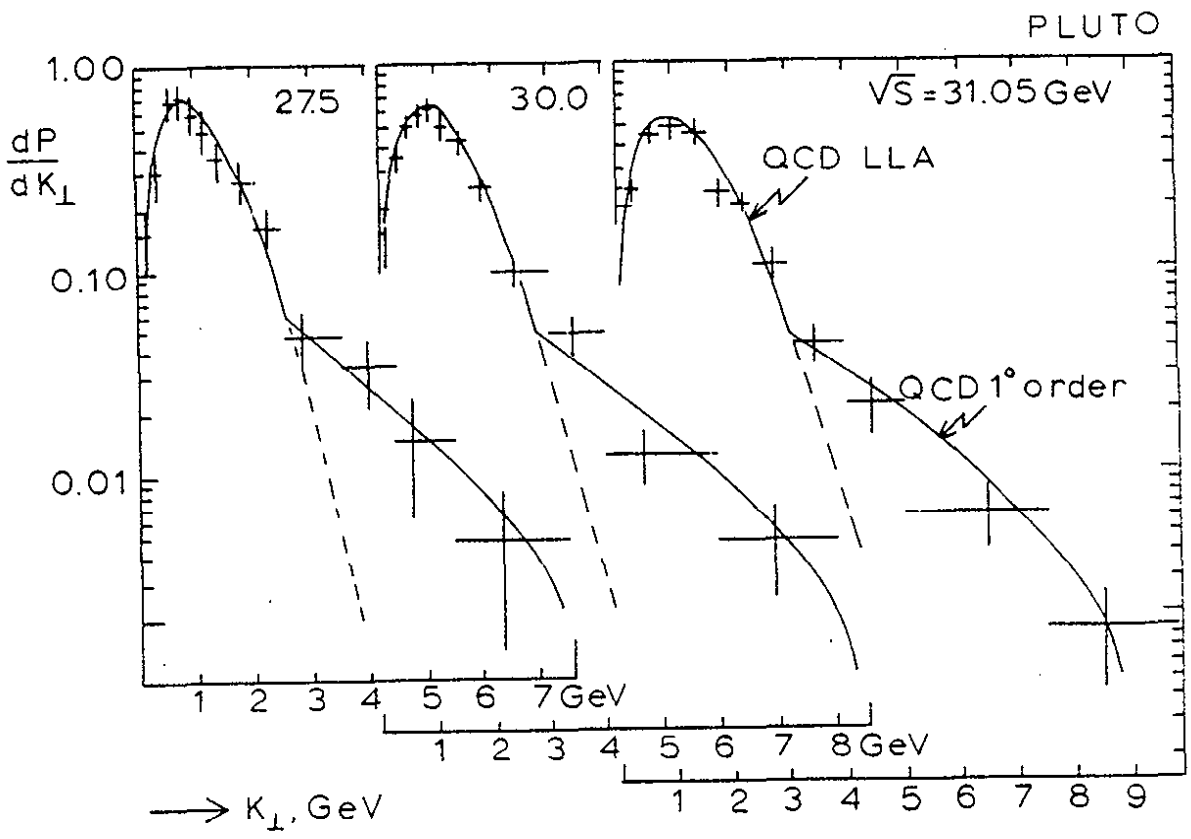
PLUTO
27.5
30.0
√S = 31.05 GeV
QCD LLA
QCD 1° order
1.00
0.10
0.01
dP/dK⊥
1 2 3 4 5 6 7 GeV
1 2 3 4 5 6 7 8 GeV
1 2 3 4 5 6 7 8 9
K⊥, GeV

Fig. 91

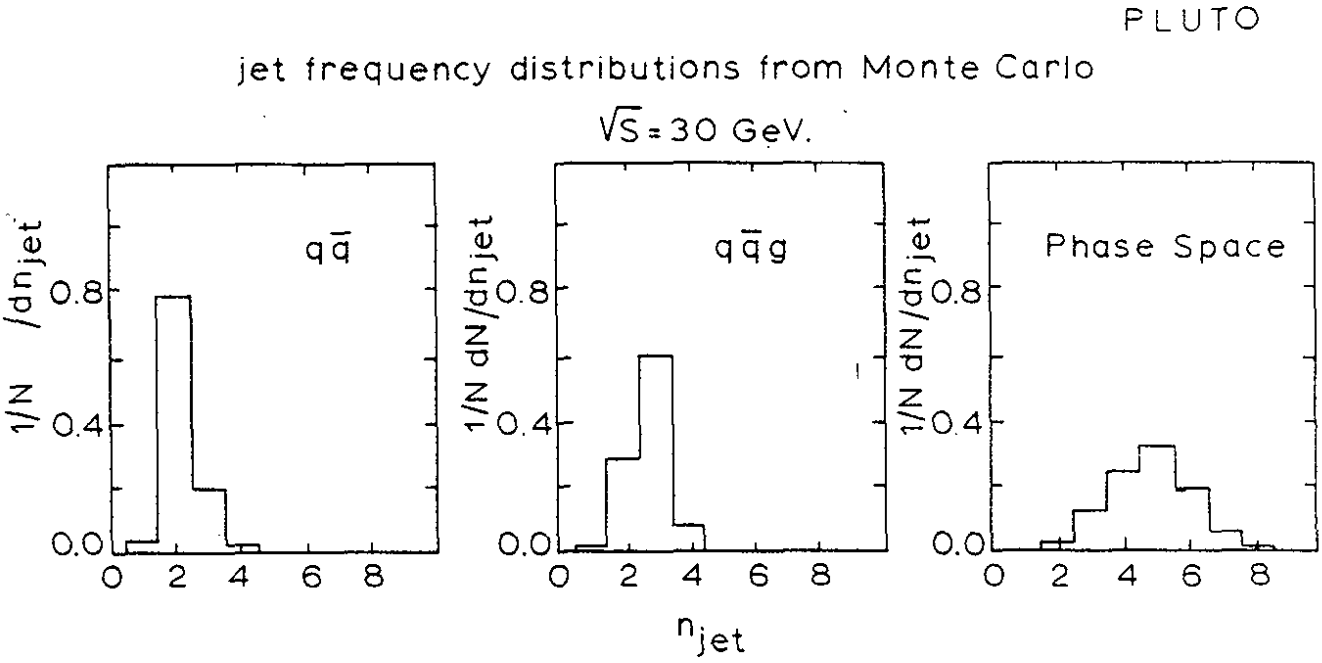
PLUTO
jet frequency distributions from Monte Carlo
√S = 30 GeV.
qq̄
qq̄g
Phase Space
1/N dn_jet/dn_jet
1/N dN/dn_jet
0.0
0.4
0.8
0 2 4 6 8
n_jet

Fig. 92

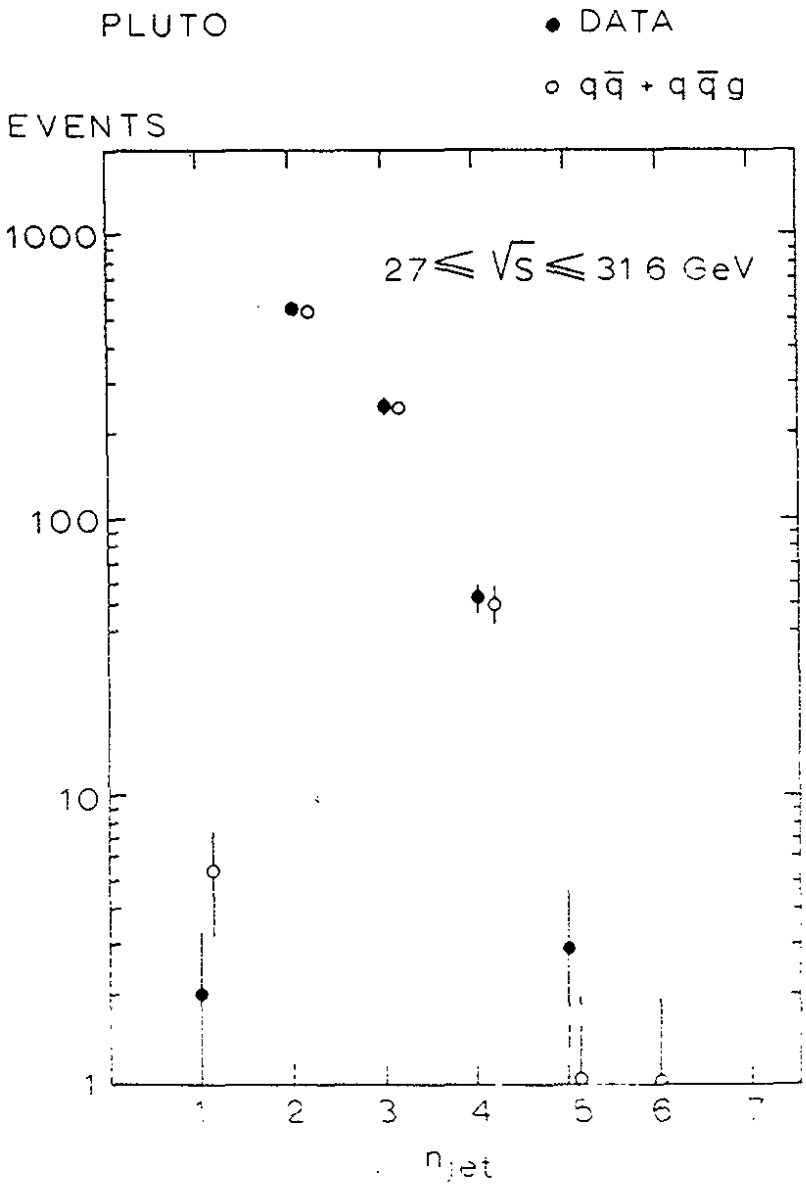
PLUTO
● DATA
○ qq̄ + qq̄g
EVENTS
27 ≤ √S ≤ 31.6 GeV
1000
100
10
1
1 2 3 4 5 6 7
n_jet

Fig. 93

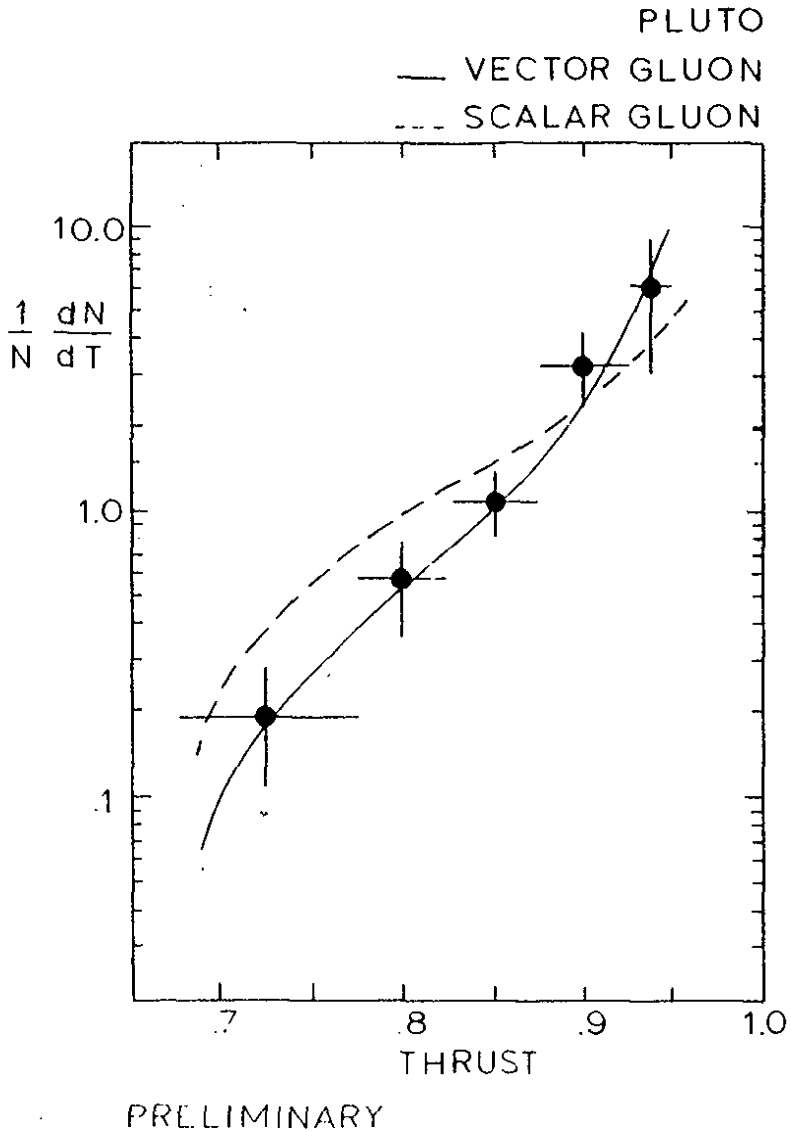
PLUTO
VECTOR GLUON
SCALAR GLUON
10.0
1.0
.1
1/N dN/dT
.7
.8
.9
1.0
THRUST
PRELIMINARY

Fig. 94

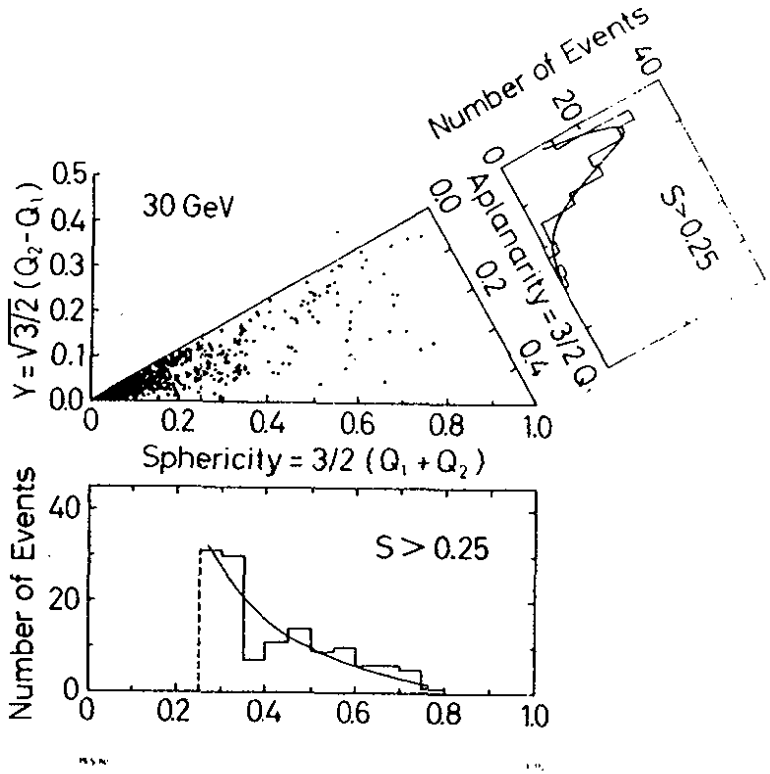
30 GeV
Y = √3/2 (Q2-Q1)
Sphericity = 3/2 (Q1 + Q2)
Number of Events
S > 0.25
Aplanarity = 3/2 Q3
S>0.25

Fig. 95

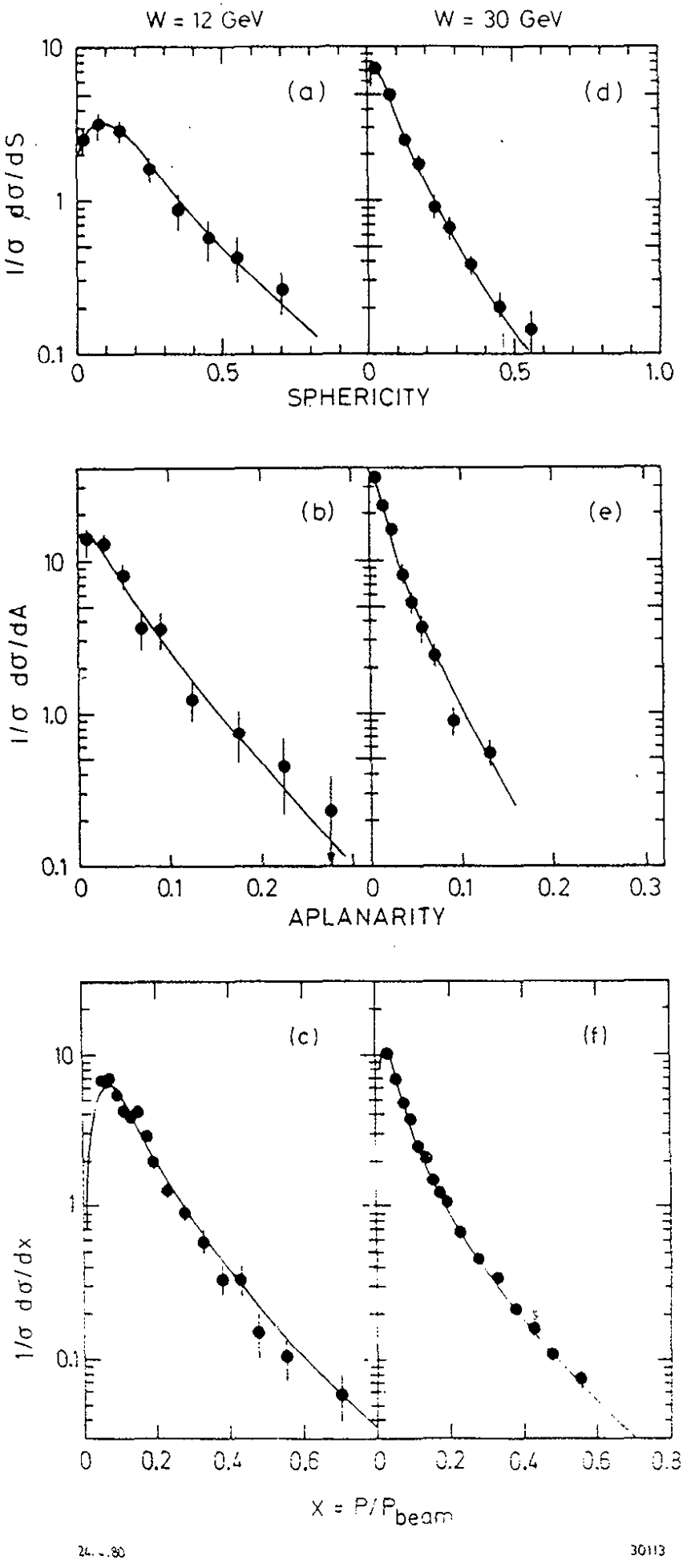
W = 12 GeV
W = 30 GeV
(a)
(d)
1/σ dσ/dS
SPHERICITY
(b)
(e)
1/σ dσ/dA
APLANARITY
(c)
(f)
1/σ dσ/dx
X = P/P beam
24.. .80
30113

Fig. 96

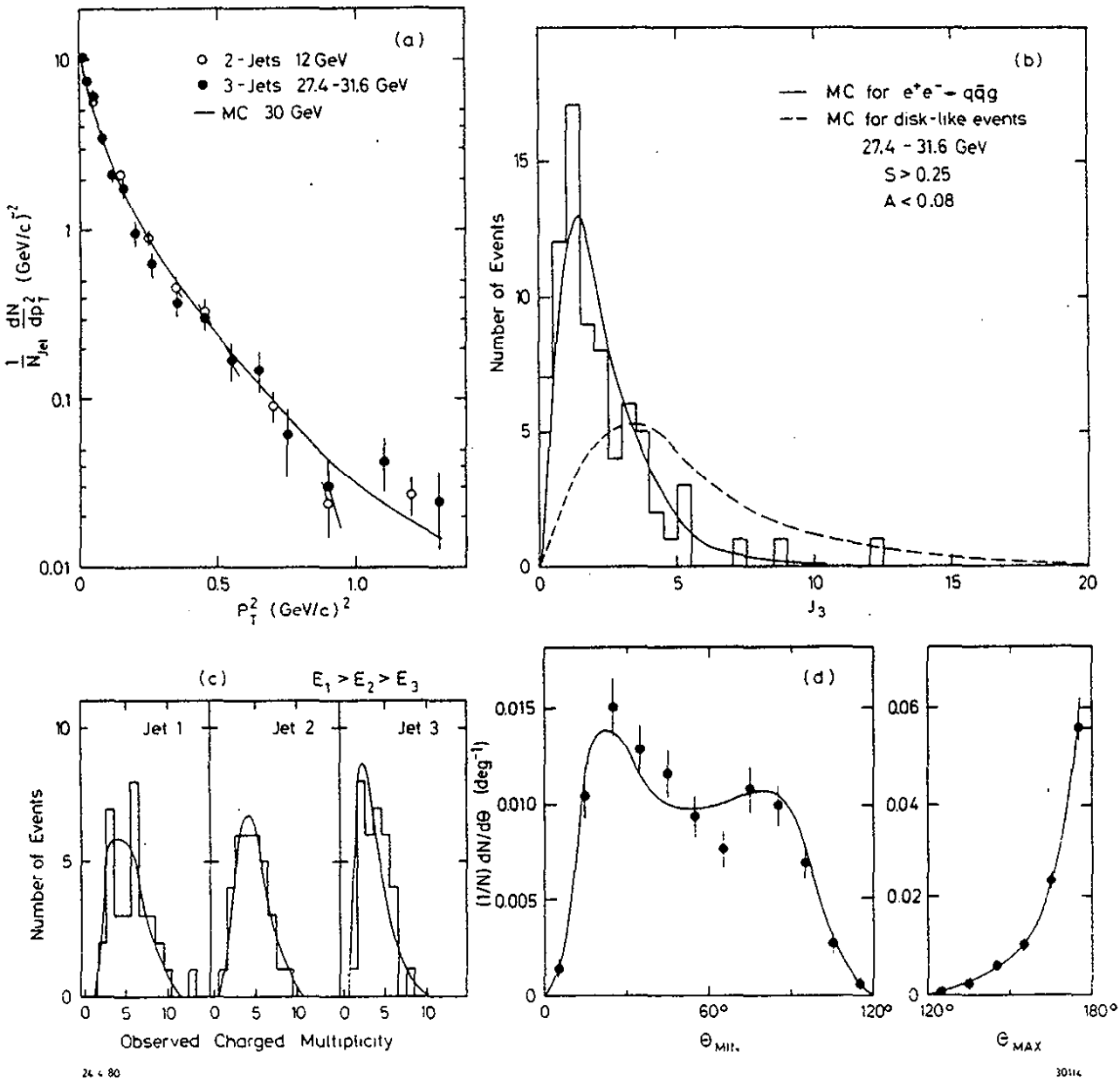
(a)
2-Jets 12 GeV
3-Jets 27.4-31.6 GeV
MC 30 GeV
$\frac{1}{N_{Jet}} \frac{dN}{dp_T^2}$ (GeV/c)$^{-2}$
P_T^2 (GeV/c)^2
(b)
MC for $e^+e^- \to q\bar{q}g$
MC for disk-like events
27.4 - 31.6 GeV
S > 0.25
A < 0.08
Number of Events
J_3
(c)
$E_1 > E_2 > E_3$
Jet 1
Jet 2
Jet 3
Number of Events
Observed Charged Multiplicity
(d)
(1/N) dN/dθ (deg^{-1})
Θ_{MIN}
Θ_{MAX}

Fig. 97

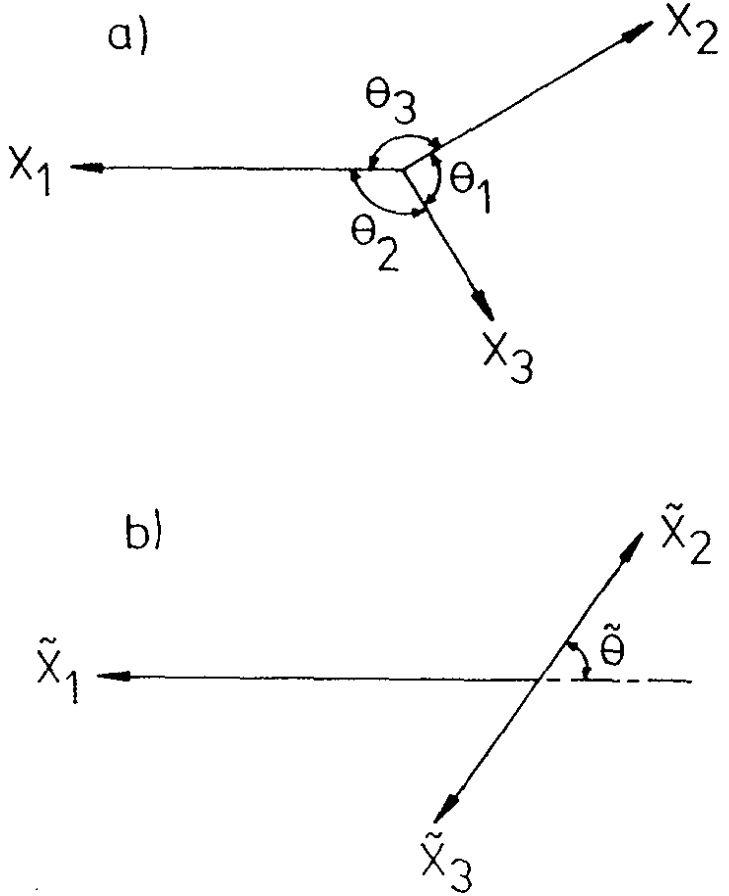
a)
X_1
X_2
X_3
θ_1
θ_2
θ_3
b)
$\tilde{X}_1$
$\tilde{X}_2$
$\tilde{X}_3$
$\tilde{\theta}$
29880

Fig. 98

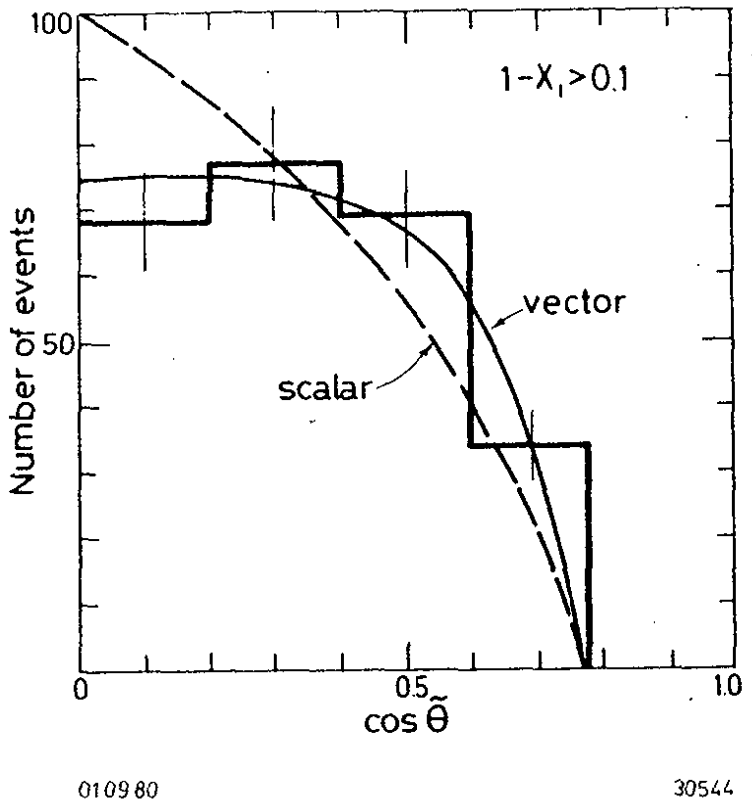
100
50
0
0.5
1.0
Number of events
cos $\tilde{\theta}$
$1-X_1>0.1$
vector
scalar
010980
30544

Fig. 99

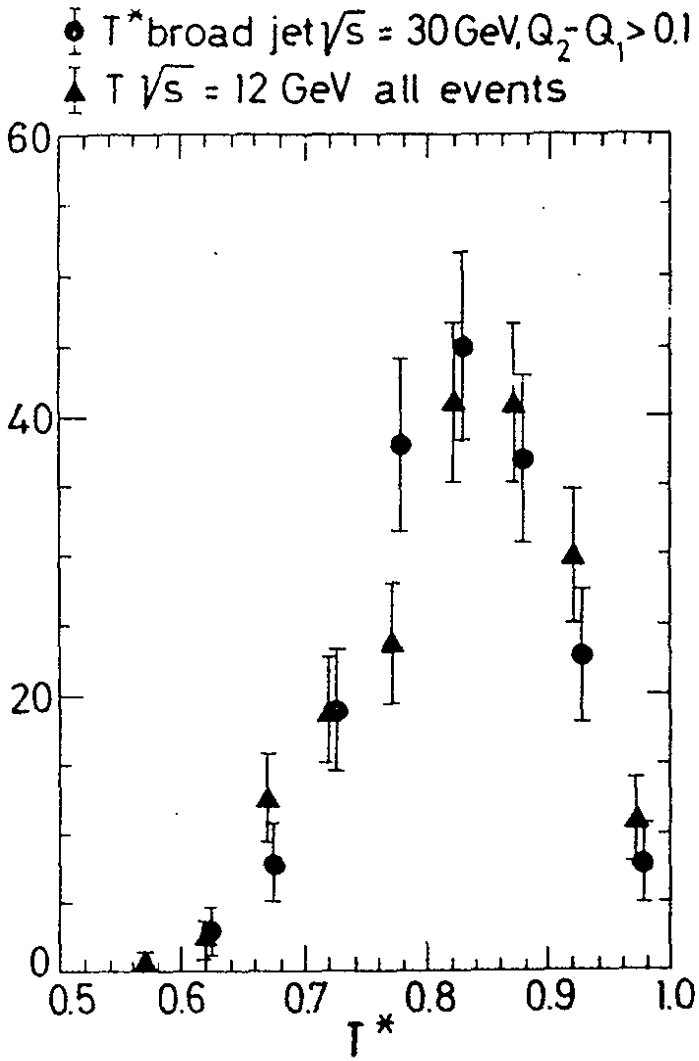

Fig. 100

JADE

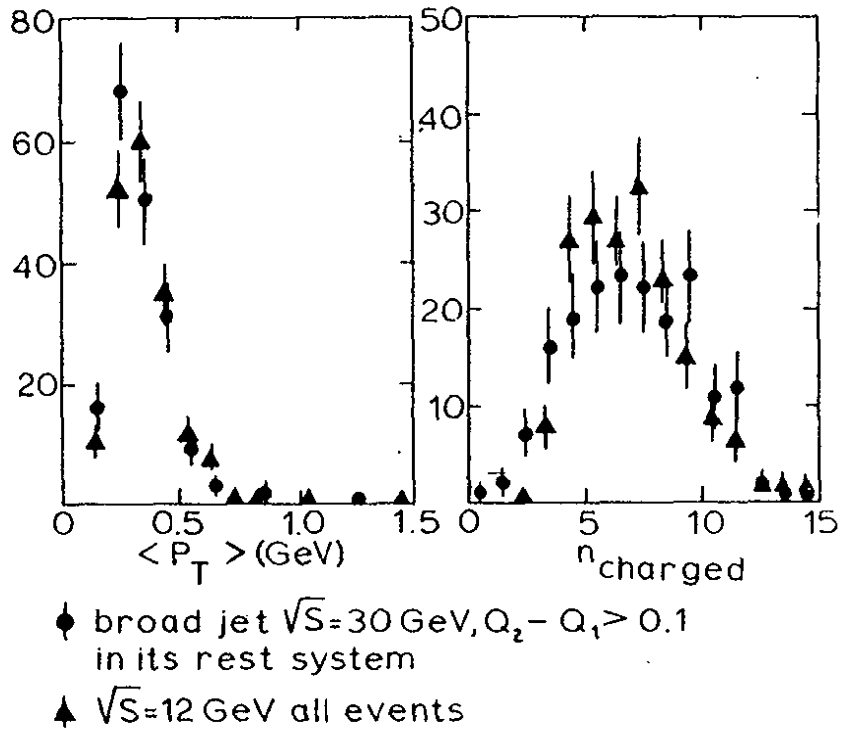

Fig. 101

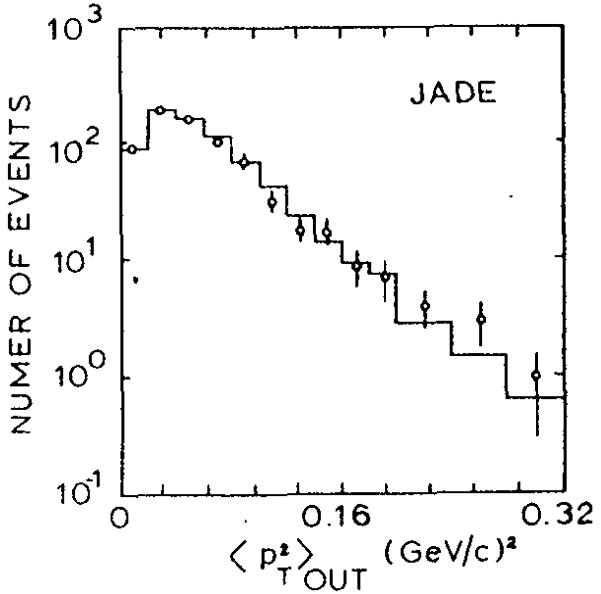

Fig. 102

α_s FROM THE PETRA EXPERIMENTS

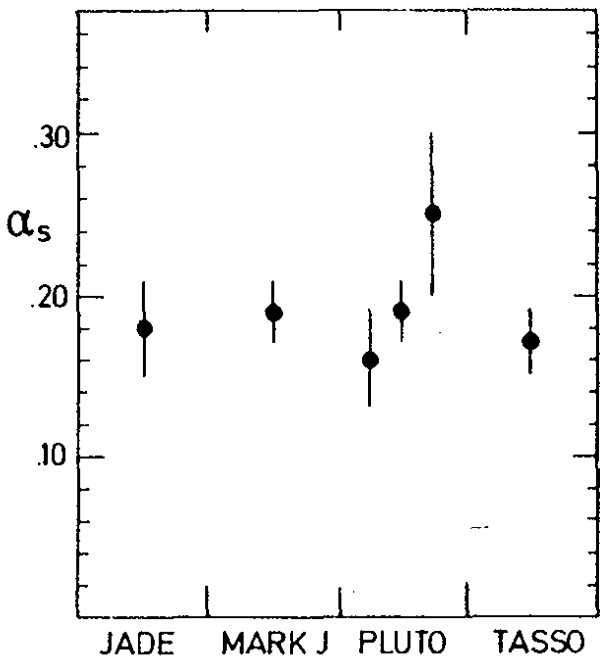

SYSTEMATIC ERROR 0.03 - 0.04

Fig. 103

8. CONCLUSIONS

After two years of experimentation the main physics results obtained at PETRA can be summarized as follows:

1) Quantum Electro Dynamics is valid to a distance $< 10^{-16}$ cm. Electrons, muons and tau leptons are point like with sizes smaller than 10^{-16} cm.
2) The leptonic vector and axial vector coupling constants of the weak neutral current are determined to be in agreement with the predictions of the standard SU(2) x U(1) theory using purely leptonic interactions for the first time.
3) Using models containing two neutral bosons the masses of the two Z's can be tightly restricted.
4) The first results on the measurements of the total cross section of the two photon exchange raction producing hadrons have been reported.
5) The relative cross sections for the single photon annihilation reaction producing hadrons and the event distributions show that there is no new charge 2/3 quark pair production up to $\sqrt{s}$ = 36.6 GeV.
6) No evidence has been found for the production of heavy leptons, spin zero partners of the electron and muon expected in supersymmetric theories, free quarks and heavy long living particles.
7) An average hadronic event at $\sqrt{s}$ = 30 GeV contains approximately $11\pi^{\pm}$, 1.4 K^{o}, $\overline{K}^{o}$, 1.4 $K^{\pm}$ and 0.4 $p,\bar{p}$ in the final state.
8) Tests of Quantum Chromodynamics (QCD) have been performed and no deviations from this model have been observed.
9) Three jet events have been discovered and the rate and the shape of these events can only be explained by the hard non-collinear gluon bremsstrahlung expected in QCD.
10) The running coupling constant α_s has been measured and evidence has been reported for the vector nature of the gluon.

All these results have been made possible by the good performance of PETRA since its beginning.

ACKNOWLEDGEMENTS

I wish to thank my colleagues of the MARK-J Collaboration and acknowledge helpful discussions with W. de Boer, D. Cords, D. Pandoulas and U. Timm. I thank Prof. A. Zichichi for giving me the opportunity to give these lectures and my secretary M. White for her help at Erice.

REFERENCES

(1) PETRA Proposal (updated version), DESY, Hamburg (Febr. 1976).

(2) G. Voss, The 19 GeV e^+e^- Storage Ringe, Internal Report, DESY M/79/16.

(3) S.W. Herb et al., Phys. Rev. Lett. 39,252 (1977).

(4) C.W. Darden et al., Phys. Lett. 76B,246 (1978)
Ch. Berger et al., Phys. Lett. 76B,243 (1978)
J.K. Bienlein et al., Phys. Lett. 78B,360 (1978)
C.W. Darden et al., Phys. Lett. 78B,364 (1978).

(5) A. Febel and G. Hemmie, 'PIA, The Positron Intensity Accumulator for the PETRA Injection', Internatl Report, DESY M/79/13.

(6) H.D. Bremer et al., 'First results from the PETRA-polarimeter', Internal Report, DESY 80/76, July 1980.

(7). S.L. Glashow, Nucl. Phys. 22,579 (1961)
S. Weinberg, Phys. Rev. Lett.19,1264 (1967)
S.Weinberg, Phys. Rev. D5,1412 (1972)
A. Salam, Proc. 8th Nobel Symposium, Aspenäsgaden, 1968 Almqvist and Wiksell, Stockholm 1968, 367.

(8) L.D. Landau, E.M. Liftschitz, Sov. Phys. 6,244 (1934)
H. Euler and B. Kockel, Naturwiss. 23,246 (1953).

(9) F.E. Low, Phys. Rev. 120, 582 (1960);
F. Calogero and C. Zemack, Phys. Rev. 120,1860 (1960)
A. Jaccerini, N. Arteaga-Romero, J. Parisi and P. Kessler, Compt. Rend. 269B,153,1129 (1969), Nuovo Cimento 4,933 (1970).

(10) V.E. Balakin, V.M. Budner and I.F. Ginzburg, Zl. E.T.F. Pis'ma 11 (1970) 559 (JETP Lett. II, 388);
S.Brodsky, T. Kinoshita and H. Terazawa, Phys. Rev. Lett. 25 972 (1970), Phys. Rev. D4,1532 (1971)
H. Terezawa, Rev. Mod. Phys. 45,615 (1973)

(11) L. Paoluzi et al., Lett. al Nuovo Cimento 10,435 (1974)

(12) H.J. Besch et al., Phys. Lett. 81B,79 (1979)

(13) G.S. Abrams et al., Phys. Rev. Lett. 43,477 (1979)

(14) D.J. Gross and F.A. Wilczek, Phys. Rev. Lett. 30,1343 (1973)
H.D. Politzer, Phys. Rev. Lett.30,1346 (1973)
J. Ellis et al., Nucl. Phys. B111,253 (1976)
T. deGrand et al., Phys. Lett. D16,3251 (1976)
G. Kramer et al., Phys. Lett. 79B,249 (1978)
A. DeRujula et al., Nucl. Phys. B138,337 (1978)
P. Hoyer et al., DESY-Reprint 79/21 (unpublished)
A. Ali et al., Phys. Lett. 82B,285 (1979); also DESY-Report 79/54, submitted to Nucl. Phys. B.

(15) CELLO: PETRA-proposal, and W. de Boer et al., MPI-PAE/EXP. EL.84 (1980)
JADE: PETRA-proposal, and D. Drumm et al., DESY 80/38 (1980)
MARK-J: PETRA-proposal, and Physics Reports, Vol. 63, No. 7, (1980), 337-391
PLUTO: PETRA-proposal, and L. Criegee et al., Proc. of the 1973 Inernational Conference on Instrumentation for High Energy Physics, pg. 707 (1973)
TASSO: PETRA-proposal, H. Boerner et al., DESY 80/27 (1980, and H. Burkhardt et al., DESY 80/100 (1980).

(16) A. Ali, E. Pietarinen, G. Kramer and J. Willrodt, DESY-Report 79/86, (1979). In their program the contribution due to 4-jet production is included. The virtual gluon correction due to 3-jet rate, however, is not included.

(17) R.D.Field, and R.P. Feynman, Nucl. Phys. B136,1 (1978).

(18) M. Kobayashi and T. Maskawa, Progr. Theor. Phys. 49,652 (1973).

(19) A.Ali et al., Heavy Quarks in e^+e^- Annihilation, DESY-Report 79/63 (1979).

(20) F.A. Berends et al., Phys. Lett. 63B,432 (1976);
F.A. Berends et al., Nucl. Phys. B68,541 (1974)
G. Bonneau and F. Martin, Nucl. Phys. B27,381 (1971)
Y.S. Tsai, Rev. Mod. Phys. 46,815 (1974)
L.W. Mo and Y.S. Tsai, Rev. Mod. Phys. 41,205 (1969).

(21) J.A.M. Vermaseren, CERN (to be published).

(22) H.G. Sanders, Diplomarbeit, Phys. Inst. Aachen, Report No. HEP 74/07 (1974) (unpublished).

(23) T.A. Gabriel and R.L. Bishop, Nucl. Instr. Methods 155,81 (1978) and references therein.

(24) G. Ripken, private communication
F.A. Berends and R. Kleiss, DESY-Report 80/66(1980).

(25) V.Alles-Borelli et al., Nuovo Cimento 7A,345 (1972);
H. Newman et al., Phys. Rev. Lett. 32,483 (1974)
J.-E.Augustin et al., Phys. Rev. Lett. 34,233 (1975)
L.J. O'Neill et al., Phys. Rev. Lett. 37,395 (1976).

(26) S.J. Brodsky and S.D. Drell, Annu. Rev. Nucl. Sci. 20,147(1970).

(27) ADONE Proposal INFN/AE-67/3 (March 1967), ADONE-Frascati (unpublished) and M.Bernardini et al., Nuovo Cimento 17A,383 (1973);
S. Orito et al., Phys. Lett. 48B,165 (1974)

(28) M. Perl et al., Phys. Rev. Lett. 35,1489 (1975)
G.Feldman et al., Phys. Rev. Lett. 38,117 (1977).

(29) J.Burmester et al., Phys. Lett. 68B,297 (1977)
J. Burmester et al., Phys. Lett. 68B,301 (1977).

(30) For a review of our present knowledge of the τ lepton, see G. Fluegge, Zeitschr. f. Physik C1, Particles and Fields, 121 (1979), and the references therein.
R.Brandelik et al., Phys. Lett. 92B,199 (1980).

(31) A. Böhm, 'Test of Quantum Electro Dynamics and models of the Electro-Weak Interaction', Invited talk at the High Energy Physics (Wisconsin) Conference, 1980; (Aachen Report PITHA 80/9, (1980)).

(32) R. Hofstadter, Proceedings of the 1975 Intern. Symposium on Lepton and Photon Interactions at High Energies (Stanford Linear Accelerator Center, STanford, CA., 1975),869.

(33) S.D. Drell, Ann. Phys.(N.Y.),4,75 (1958)
T.D. Lee and G.C.Wick, Phys. Rev. D2,1033 (1970).

(34) JADE: W. Bartel et al., Phys. Lett. 92B,206 (1980)
MARK-J: D.P. Barber et al., Phys. Rev. Lett 42,110 (1979); 43, 1915 (1979), Phys. Lett. 95B,149 (1980), Phys. Rev. Lett. 45,1904 (1980)
PLUTO: Ch.Berger et al., Z. Physik C4,269 (1980); Phys. Lett. 94B,87 (1980)
TASSO: R. Brandelik et al., Phys. Lett. 94B,259 (1980); Phys. Lett. 92B, 199(1980).

(35) M. Capdequi-Peyranere, G. Grunberg, F.M. Renard, M. Talon, Preprint PM/78/8 (1978), Departement Phys. Mathematique, Montpellier

(36) N.M. Kroll, Nuovo Cimento XLV (1966)65
K. Ringhofer, H. Salecker, Contribution to the 1975 Internat. Symposium on Lepton and Photon Interactions at High Energies, Stanford University, unpublished.

(37) A. Litke, Harvard University, Ph.D. Thesis (1970) unpublished.

(38) Ch. Berger et al., (PLUTO-Collaboration), Phys. Lett. 94B,87 (1980)

(39) W. Bartel et al., (JADE-Collaboration), Phys. Lett. 92B,806 (1980)

(40) R. Brandelik et al., (TASSO-Collaboration), Phys. Lett. 94B,259 (1980)

(41) C. Bacai et al., Lett. Nuovo Cim. 2,73 (1971)
G. Hanson et al., Lett. Nuovo Cim. 7,587 (1973)
B.L. Beron et al., Phys. Rev. Lett. 33,663 (1974)
E. Hilger et al., Phys. Rev. D15,1809 (1977) .

(42) D.P. Barber et al., Phys. Rev. Lett. 43,1915 (1979); 45,1904 (1980)

(43) PLUTO-Collaboration, G. Flügge, talk presented to Intern. Conf. on High Energy Physics (Geneva, 1979), DESY-Report 79/37 (1979).

(44) R. Brandelik et al. (TASSO-Collaboration), Phys. Lett. 92B, 199 (1980).

(45) F.J. Hasert et al., Phys. Lett. 46B,121 (1973)
J. Blietschau et al., Nucl. Phys. B114,189 (1976).

(46) Recent review of the subject include:
C. Baltay, Proc. 19th Int. Conf. on High Energy Physics, Tokyo, 1978, p. 882
K. Winter, Proc. Int. Symposium on Lepton and Photon Interactions, FNAL, Batavia, 1979, and CERN-EP/79-132
Fr.-W. Büsser, 19th Int. Universitätswochen für Kernphysik, Schladming, Styria, Austria, 1980, and
L.W. Mo, Proc. XVth Recontre de Moriond, Les Arcs-Savoie, France, 1980.

(47) L.M. Seghal, Proc. Int. Conf. on Neutrino Physics, Purdue Univ., W. Lafayette, Indiana,1978.

(48) P.Q. Hung and J.J. Sakurai, Phys. Lett. 69B,323 (1977)
P.Q. Hung and J.J. Sakurai, Phys. Lett. 88B,91 (1979).

(49) See Refs. 34 - 46. in Büsser's review listed in Ref. 46 above.

(50) C.Y. Prescott et al., Phys. Lett. 77B,347 (1978)
C.Y. Prescott et al., Phys. Lett. 84B,524 (1979).

(51) Looser constraints on g_V^2 and g_A^2 have been obtained using JADE date by: R. Marshall, Rutherford Lab. Report RL-80-29, May 1980.

(52) D.P. Barber et al., Phys. Rev. Lett. 42,1110 (1979)
D.P. Barber et al., Phys. Rev. Lett. 43,1915 (1979)
D.P. Barber et al., Phys. Rep. 63,7 (1980),337-391

(53) Accurate radiative corrections for the central detector are based on F.A. Berends and R. Kleiss, DESY-Report 80/66 (1980).
Also see:
F.A. Berends, K.J.F. Gaemers and R. Gastmans, Nucl. Phys. B57,381 (1973)
F.A. Berends, K.J.F. Gaemers and R. Gastmans, Nucl. Phys. B63,381 (1973)
F.A. Berends et al., Phys. Lett. 63B,432 (1976).

(54) E.H. DeGroot and D. Schildknecht, Univ. of Bielefeldt, BI-TP 80/08 (1980).

(55) R. Budny, Phys. Lett. 55B,227 (1975)

(56) The background for cosmic rays and beam-gas interactions is found to be $\leq$ 0.1 % from the vertex distribution of accepted Bhabha events in the range $\cos\theta \leq 0.8$. In this angular range they also find, from Monte Carlo studies, that the total contamination from other e^+e^- interactions is $\simeq$ 0.5 % of the measured Bhabha cross section. Contamination contributions are: 0.02 % from $e^+e^- \to$ hadrons, 0.35 % from $e^+e^- \to \tau^+\tau^-$, 0.15 % from $e^+e^- \to e^+e^-e^+e^-$, and $\sim \leq$ 0.01 % from $e^+e^- \to e^+e^-$ + hadrons.

(57) The global fit of the MARK-J data entails an assumption of e-μ-τ universality. The results are little affected by the $\tau^+\tau^-$ data, however, and e-μ universality would be sufficient to establish the conclusions of their result.

(58) H. Faissner, New Phenomena in Lepton-Hadron Physics (1979), ed. D.E.Fried and J. Wess (Plenum Publishing Corp., New York), p. 371;
H. Reithler, Phys. Blätter 35,630 (1979)
R.H. Heisterberg et al., Phys. Rev. Lett. 44,635 (1980)
L.W. Mo, Contribution to Neutrino 80, Erice (1980), and private communication H.Faissner and R. Reithler.
Different compilations of neutrino electron scattering data (see e.g. Büsser's review in Ref. 46 above) give contours which are slightly different from the one shown in Fig. 37. These differences do not, however, alter our conclusions.

(59) H. Georgi and S. Weinberg, Phys. Rev. D17,275 (1978)
J.D. Bjorken, Phys. Rev. D19,335 (1979).

(60) E.H. DeGroot, G.J. Gounaris, D. Schildknecht, Phys. Lett. 85B,399 (1979)
E.H. DeGroot, G.J. Gounaris, D. Schildknecht, Z. Physik C5, 127 (1980)

(60) ct'd. E.H. DeGroot, G.J. Gounaris, D.Schildknecht, Phys. Lett. 90B,427 (1980)
E.H. DeGroot and D. Schildknecht, Bielefeld preprint BI-TP 80/22 (1980).

(61) V. Barger, W.Y. Keung, and E. Ma, Phys. Rev.Lett. 44,1169 (1980)
V. Barger, W.Y. Keung, and E. Ma, Phys. Rev. D22,727 (1980)
V. Barger, W.Y. Keung, and E. Ma, Phys. Lett. 94B,377 (1980).

(62) The data from the JADE group was provided through the couresy of Dr. R. Marshall, also refer to Rutherford Lab. Report RL-80-29, May 1980.

(63) Ch. Berger, 'Two Photon Physics in the PLUTO Detector', Invited talk given at the Intern. Workshop on $\gamma\gamma$ Collisions, Amiens, April 8-12, 1980, Aachen Report PITHA 80/7 (1980).

(64) W. Wagner, '$\gamma\gamma$ processes at PETRA', Invited talk at the High Energy Physics (Wisconsin) Conference, 1980, USA.

(65) E. Hilger, 'Two Photon Results from TASSO', Invited talk at the Intern. Workshop on $\gamma\gamma$ Collisions, Amiens, April 8-12, 1980, DESY-Report 80/34 (1980) and BONN-HE-80-5.

(66) J.A.M. Vermaseren, private communication.

(67) H. Krasemann and J.A.M. Vermaseren, private communication.

(68) Ch.Berger et al. (PLUTO-Collaboration), Phys. Lett. 94B, 254 (1980).

(69) L.V. Fil'kov, JETP Lett. 5(67),153
G.M. Radutskiii, JETP Lett. 6(67)336; Sov. J. Nucl. Phys. 8(69)65
Kunzst et al., Dubna-Report E2-5424
B. Renner, Nucl. Phys. B30,634 (1971)
A. Bramon et al., Lett. Nuov. Cimento 2,522 (1971)
H. Kleinert et al., Nucl. Phys. B38,87 (1972)
G.Schierholz et al., Nucl. Phys. B40,125 (1972)
St. B. Berger et al., Phys. Rev. D8,3875 (1973)
V.N. Novikov et al., Sov. J. Nucl. Phys. 21,529 (1975)
D. Faiman et al., Phys. Lett. 59B,269 (1975)

(69) N. Levy et al., Phys. Rev. D13,2662 (1976)
ct'd. P. Grassberger et al., Nucl. Phys. B106,451 (1976)
J. Babcock et al., Phys. Rev. D14,1286 (1976)
M. Greco, Nuovo Cimento 42A,315 (1977)
M. Greco et al., Nuovo Cimento 43A,88 (1978)
V.M. Budnev et al., Phys. Lett. 86B,351 (1979)
W.N. Cottingham et al., J. Phys. G5,L155 (1979).

(70) R.Brandelik et al., (TASSO-Collaboration), Phys. Let. 79B,448 (1980).

(71) Ch. Berger et al., (PLUTO-Collab.), DESY preprint DESY 80/94.

(72) J. Field, Nucl. Phys. B168,477 (1980)

(73) A. Carimala, P. Kessler and J. Parisi, Phys. Rev. D20,1957 (1980), Phys. Rev. D20,2170 (1979), Phys. Rev. D21,669 (1980).

(74) W. Bartel et al., (JADE-Collab.), Phys. Lett. 88B,171 (1979)
S. Orito, Proc. Int. Symp. on Lepton and Hadron Interactions 1979, p. 52
D.P. Barber et al., (MARK-J-Collab.), Phys. Rep. 63,7 (1980), 337-391
Ch. Berger et al., (PLUTO-Collab.), Phys. Lett. 81B,410 (1989) 86B,413 (1979)
R.Brandelik et al.,(TASSO-Collab.), Phys. Lett. 83B,261 (1979) Z. Phys. C4,87 (198o).

(75) U.Timm, 'Total hadronic cross section, Multiplicity and Inclusive particle spectra from e^+e^- annihilation at PETRA', paper presented at the Third Warshaw Sym. on Element. Part. Phys., Jodlowy Dwor, Poland, May 1980; DESY-Preprint 80/70.

(76) D.Cords, Invited talk at the High Energy Conference (Wisconsin), 1980.

(77) J.L. Rosner, C. Quigg, H.B. Thacker, Phys. Lett. 74B,350(1978)
C. Quigg, contribution to the 1979 Intern. Symp. on Lepton and Photon Interactions, Fermilab
M. Greco, Phys. Lett. 77B,84 (1978)
T. Applequist and H. Georgi, Phys. Rev. D8,4000 (1973)

(77) A. Zee, Phys. Rev. D8,4038 (1973)
ct'd. M. Dine, J. Sapirstein, Phys. Lett. 43,152 (1979).
(78) R. Schwitters, Proceedings of the 1975 Intern. Symp. on Lepton and Photon Interactions, Fermilab, 5
G. Hanson et al., Phys. Rev. Lett. 35,1609 (1975)
G. Hanson, Talk at the 13th Recontre de Moriond, Les Arcs, France, (March 12-16, 1978), SLAC-PUB 2118 (1978).
(79) J.D. Bjorken and S.J. Brodsky, Phys. Rev. D1,176 (1970).
(80) E. Farhi, Phys. Rev. Lett. 39,1587 (1977)
S. Brandt et al., Phys. Lett. 12,57 (1964)
S. Brandt and H. Dahmen, Zeitschrift f. Phys. C1,61 (1979).
(81) Ch. Berger et al., (PLUTO-Collab.), Phys. Lett. 81B,410 (1978) 86B,413 (1979) and 86B,418 (1979)
R. Brandelik et al.,(TASSO-Collab.), Phys. Lett. 83B,261 (1979) 86B,243 (1979) and 89B,418 (1980).
(82) D.P. Barber et al., Phys. Rev. Lett. 42,1113 (1979)
D.P. Barber et al., Phys. Rev. Lett. 43,901 (1979)
D.P. Barber et al., Phys. Lett. 85B, 463 (1979).
(83) D.P. Barber et al., Phys. Rev. Lett. 45,1904 (1980).
(84) Y.S. Tsai, SLAC-Preprint, SLAC-PUB-2450, Dec. 1979.
Note that the τ branching ratios are taken from the compilations of world data in Ref. 30. The $\tau \to \mu\, \nu\nu$ branching ratio is taken as 17.0 %.
(85) Yu. A. Gol'fand and E.P. Likthman, JETP Letters 13,323 (1971)
J. Wess and B. Zumino, Nucl. Phys. B70,39 (1974)
For a review article, see:
P. Fayet and S. Ferrara, Phys. Reports 32C,249 (1977)
P. Fayet, Phys. Lett. 69B,489 (1977)
G.R. Farrar and P. Fayet,Phys. Lett. 76B,575 (1978), 79B,442 (1978)
P. Fayet, Phys. Lett. 84B,421 (1979)
G.R. Farrar and P. Fayet, Phys. Lett. 89B,191 (1980)
P. Fayet, Phys. Lett. 86B,272 (1979).

(86) F.B. Heiel et al., Nucl. Phys. B138, 189 (1978).

(87) W. Bartel et al., (JADE-Collab.), Z. Phys. C6, 295 (1980).

(88) S. Yamada, Invited Talk at the High Energy Conf. (Wisconsin),1980.

(89) D. Pandoulas, Invited Talk at the High Energy Conf. (Wisconsin), 1980.
R. Brandelik et al., (TASSO-Collab.), Phys. Lett. 94B, 444 (1980).

(90) C. Bacci et al., Phys. Lett. 86B, 234 (1979).

(91) J.L. Siegrist, Ph.D. Thesis SLAC-225 UC-34d (1980).

(92) Ch. Berger et al., (PLUTO-Collab.) Phys. Lett. 78B, 176 (1978).
R. Brandelik et al., (DASP-Collab.), Nucl. Phys. B148, 189 (1979).

(93) R.P. Feynman, Phys. Rev. Lett. 23, 1415 (1969).

(94) R. Brandelik et al., (TASSO-Collab.), Phys. Lett. 89B, 418 (1980).

(95) W. Furmanski, S. Pokorski, Nucl. Phys. B155, 253 (1979).
A. Bassetto, M. Ciafoloni, G. Marchesini, Phys. Lett. 83B, 207 (1978).
K. Konishi, Rutherford Preprint RL 79-035 T 241 (1979).

(96) R. Brandelik et al., (DASP-Collab.), Nucl. Phys. 81B, 410 (1979) and B63, 381 (1973).

(97) G.J. Feldman and M.L. Perl, Phys. Reports 33, 285 (1977).

(98) R. Baier, J. Engels and B. Peterson, 'University of Bielefeld Report', BI-TP 79/10 (1979).
W.R. Frazer and J.F. Gunion, Phys. Rev. D20, 147 (1979).

(99) Ch. Berger et al., Phys. Lett. 76B, 243 (1978).
J.K. Bienlein et al., Phys. Lett. 78B, 360 (1978).
C.W. Darden et al., Phys. Lett. 76B, 246 (1978).

(100) H. Meyer (PLUTO-Collab.), DESY-Preprint 79/81 (1979) and invited talk at the 1979 Intern. Lepton-Photon Symposium at FNAL.

(101) P. Duinker and D. Luckey, Comments in Nucl. and Part. Phys. 9, 123 (1980). Ch. Berger et al., (PLUTO Collab.), Phys. Lett. 82B, 449 (1979). D.P. Barber et al., (MARK-J Collab.), Phys. Lett. 85B, 463 (1979). R. Cashmore, P. Söding and G. Wolf, Proc. of the EPS Int. Conf. on High Energy Phys., Geneva. D.P. Barber et al., Phys. Rev. Lett. 43, 830 (1979). R. Brandelik et al., Phys. Lett. 86B, 243 (1979). Ch. Berger et al., Phys. Lett. 86B, 418 (1979). W. Bartel et al., Phys. Lett. 88B, 171 (1979). J. Ellis, TH-2817 - CERN (to be published in Comments on Nucl. and Part. Phys.).

(102) D.P. Barber et al., Phys. Lett. 89B,139 (1979)
H. Newman (MARK-J-Collab.), Invited talk given at the XXth Intern. Conf. on High Energy Phys., University of Wisconsin, Madison, 1980.

(103) A. DeRujula et al., Nucl. Phys. B138,397 (1978).

(104) H.L. Anderson et al., Phys. Rev. Lett. 40,1061 (1978)
P.C. Bosetti et al., Nucl. Phys. B142,1 (1978)
J.G.H. DeGroot et al., Zeitschr. f. Phys. C1, 143 (1979)
J.G.H. DeGroot et al., Phys. Lett. 82B,292 (1972)
J.G.H. DeGroot et al., Phys. Lett. 82B,465 (1979).

(105) M. Krammer and H. Krasemann, DESY-Report 78/66 (1978).

(106) Ch. Berger et al., Phys. Lett. 78B,176 (1978)
S.Brandt and H. Dahmen, Zeitschr. f. Phys. C1,61 (1979).

(107) V. Hepp (PLUTO-Collab.), 'PLUTO Resolts on Jets and QCD', Talk given at the XXth Intern. Conf. on High Energy Phys., University of Wisconsin, Madison, 1980
Ch. Berger et al. (PLUTO-Collab.), Phys. Lett. 97B,459(1980)
H.J. Daum et al., DESY-Report 80/101 (1980).

(108) K. Konishi, A. Ukawa and G. Veneziano, Phys. Lett. 80B,259(1979).

(109) G. Curci, M. Greco and Y. Srivastava, Phys. Rev. Lett.43,834 (1979), Nucl. Phys. B159,451 (1979).

(110) J. Ellis, M.K. Gaillard and G.G.Ross, Nuco. Phys. B11,253 (1976)

(111) S.L. Wu (TASSO-Collab.), Invited talk given at the XXth Intern. Conf. on High Energy Phys., University of Wisconsin, Madison, 1980.
R. Brandelik et al. (TASSO-Collab.), Phys. Lett. 94B,437(1980).

(112) J.D. Bjorken and S. Brodsky, Phys. Rev. D1,1416 (1970).

(113) S.L. Wu and G. Zobernig, Particles and Fields (Z. Phys. C)2, 107 (1979).

(114) R. Brandelik et al. (TASSO-Collab.) Phys. Lett. 79B,453 (1980).

(115) J. Ellis, and I. Karliner, Nucl. Phys. B148,141 (1979).

(116) J. Ellis, M.K. Gaillard, and G.G. Ross, Nucl. Phys. B111,253 (1976)
T.A. DeGrand, Y.J. Ng, and S.H. Tye, Phys. Rev. D16,3251 (1977)
A. DeRujula, J. Ellis, E.G. Floratos and M.K. Gaillard, Nucl. Phys. B138,387 (1978).

(117) W. Bartel and A. Peterson, DESY-Report 80/46 (1980)
W. Bartel et al. (JADE-Collab.), Phys. Lett. 91B,142 (1980)

(118) B. Anderson, G. Gustafson, Lund Preprint, LU TP79-2 (1979)
B. Anderson, G. Gustafson, Z. Physik C3,223 (1980)
B. Anderson, G. Gustafson, T. Sjöstrand, LUND-Report LU-TP 80-1 (1980)
B. Anderson, G. Gustafson, C. Peterson, Nucl. Phys. B135,273 (1978).